Computational Quantum Chemical Studies of Main Group and Transition Metal Molecules and Ions

Luke H. Thomas

A dissertation submitted in partial fulfillment
of the requirements for the degree of
Doctor of Philosophy
University of London

The Department of Chemistry
University College London

under the supervision of

Professor Nikolas Kaltsoyannis

September 2007

ProQuest LLC
789 East Eisenhower Parkway
P.O. Box 1346
Ann Arbor, MI 48106-1346

I, Luke H. Thomas declare that the work presented in this thesis is my own. Where information has been taken from the work of others sources, this is indicated, and the source given in the bibliography.

Signed:

Abstract

This thesis describes three computational studies; the decomposition of BCl_3^{2+}, the geometric and electronic structures of ferrocene and iron pentacarbonyl, and the electronic structure and spectra of the complexes $Th(\eta^8C_8H_8)_2$, $Pa(\eta^8C_8H_8)_2$, $Th(\eta^8C_8(CH_3)_4H_4)_2$ and $Pa(\eta^8C_8(CH_3)_4H_4)_2$.

The prediction and rationalisation of the decomposition products of BCl_3^{2+} has been achieved by a characterisation of the lowest energy singlet and triplet potential energy surfaces using *ab initio* methods. The $\mathscr{T}_1$ diagnostic has been used to assess the degree of multiconfigurational character in the coupled-cluster wavefunctions. The suitability of this method is determined by a partial re-characterisation of the system using multiconfigurational methods. The fragmentation products located are in good agreement with available experimental data provided by mass spectrometry.

The structures of ferrocene and iron pentacarbonyl are calculated using a variety of methods including coupled-cluster (CC) theory. CC from a Hartree-Fock reference produces good structures, but with $\mathscr{T}_1$ diagnostics that suggest single reference methods to be unreliable. CC from Kohn-Sham (KS) references return equally good structures, but with significantly reduced $\mathscr{T}_1$ values, suggesting that the $\mathscr{T}_1$ may not be a reliable indicator of multiconfigurational character in these systems. The single configurational nature of $Fe(CO)_5$ is confirmed by multiconfigurational calculations. Experimentally, $Fe(CO)_5$ is observed to have equatorial M-C bonds that are shorter than the axial; although the predicted structures agree well with experiment, this feature cannot be reproduced.

TD-DFT is used to calculate excitation spectra for thorocene, protactinocene and their methyl-substituted derivatives. The experimental UV-vis data for these species are extremely limited and previous theoretical studies give assignments of these data which are not consistent. The effects of the molecular structure and use of different exchange-correlation potentials on the spectrum are investigated for thorocene. Consistent excitation spectra for each species are calculated and assigned; these are used to suggest new assignments of the experimental data.

Acknowledgements

Although this thesis represents a number of years of research, it also represents the combined support that I have been afforded by my colleagues, friends and family. I must initially thank Nik; the research undertaken would not have been possible without the advice and inspiration that he has provided, and I consider myself extremely fortunate to have received such dedicated supervision. I must also thank the members of the group and of G19, both past and present, particularly Andy, Leif and Rosie. The working environment to which you have all contributed has been friendly, humourous and above all academically fruitful; it is this that has made the undertaking of this research especially enjoyable. Good friends are a valuable asset, and I feel particularly wealthy in this regard. I must thank all of you for your invaluable contributions, but particularly Andrea, Daniel, Kieran, Kieron and Stephen. Lastly, I must thank my Mother, Father, Sister and Grandfather. I feel privileged to have received the unconditional love and support of my family, which has been essential in so many ways; this thesis is dedicated to them.

Contents

List of Figures

List of Tables

Chapter 1

Theory Relevant to the Projects Undertaken

Contents

The following chapter gives a theoretical background for the types of calculation that have been used in the undertaking of the research presented in this thesis. These include the *ab initio* methods Hartree-Fock, Møller-Plesset perturbation theory, coupled-cluster, multiconfigurational self consistent field and multireference configuration interaction, as well as density functional theory of both the time-independent and time-dependent varieties. This chapter is not intended to provide a complete resource for the methods used, but to provide a theoretical framework for the projects undertaken.

1.1 The Born-Oppenheimer Approximation and the Molecular Wavefunction

The Hamiltonian for a system of charged particles, nuclei and electrons can be expressed as

$$\hat{H} = -\sum_{a} \frac{1}{2m_a}\nabla_a^2 + \sum_{a<b} \frac{q_a q_b}{|r_a - r_b|}, \tag{1.1}$$

where m_a are the masses and q_a the charges of the particles in the system, and the Laplacian is given by[1]

$$\nabla_a^2 = \left(\frac{\delta^2}{\delta x_a^2} + \frac{\delta^2}{\delta y_a^2} + \frac{\delta^2}{\delta z_a^2}\right). \tag{1.2}$$

Invoking the Born-Oppenheimer (BO) approximation allows the nuclear motion and the electronic motion to be separated out from one another. This is a good approximation due to the factor of 10^3 to 10^5 between the mass of the electrons and nuclei.[1] This assumption dramatically simplifies the problem to be solved since the nuclei are considered to be static, and this naturally leads to the introduction of potential energy surfaces where the energy is plotted as a function of the nuclear structure. The Hamiltonian is now rewritten in terms of the nuclear components ($\hat{T}_{nuc}$) and the electronic components ($\hat{H}_{el}$)

$$\hat{H} = \overbrace{-\sum_{\mu} \frac{1}{2m_\mu}\nabla_\mu^2}^{\hat{T}_{nuc}} \overbrace{-\sum_{i} \frac{1}{2}\nabla_i^2 - \sum_{\mu,i} \frac{Z_\mu}{|r_\mu - r_i|} + \sum_{i<j} \frac{1}{|r_i - r_j|} + \sum_{\mu<\nu} \frac{Z_\mu Z_\nu}{|r_\mu - r_\nu|}}^{\hat{H}_{el}}, \tag{1.3}$$

where the nuclei are given the indices μ and ν and the electrons the indices i and j.[1] At this point the nuclei are clamped, and the electronic motion can be considered around the rigid molecule. The electronic part still depends parametrically on the nuclear positions in the nuclear-electron term, and thus the nuclear-nuclear repulsion term is also included, although this is constant for a particular molecu-

lar arrangement.[1] With the nuclei fixed, the Schrödinger equation can be solved for the electronic part,

$$\hat{H}_{el}(r,R)\,\psi_{el}(r,R) = E_{el}(R)\psi_{el}(r,R)\,, \tag{1.4}$$

where the electronic wavefunction (ψ_{el}) depends upon the nuclear coordinates (R) and the electronic coordinates (r), but the electronic energy only depends upon the nuclear coordinates.[1] Under the Born-Oppenheimer approximation, we can write the total wavefunction of the system as a product of the nuclear and electronic wavefunctions[1]

$$\Psi_{BO}(r,R) = \psi_{nuc}(R)\,\psi_{el}(r,R)\,. \tag{1.5}$$

The total energy of the system can be found by solving the Schrödinger equation

$$\left\{\hat{T}_{nuc}(R) + E_{el}(R)\right\}\psi_{nuc}(R) = E_{tot}\psi_{nuc}(R)\,, \tag{1.6}$$

where the electronic motion is represented by the potential E_{el}, which is a function of R.[1] The potential energy surfaces presented in this thesis are nuclear potential energy surfaces and only consider the electronic component of the total energy. In this situation, although the nuclear-nuclear repulsion is considered in the energy, the component due to the nuclear motion ($\hat{T}_{nuc}$) is ignored.

Although the BO approximation is essential in simplifying the wavefunction to the point where it can be solved using the available methods, it does not introduce a significant error into the method, apart from under certain circumstances. An example of such a problem is where avoided crossings occur when potential energy surfaces of the same symmetry approach each other, such as for the dissociation of LiF.[2] At the equilibrium geometry the wavefunction is strongly ionic, but the dissociation products are neutral atoms. At the avoided crossing between the ionic and covalent surfaces the ground state wavefunction changes rapidly from being ionic to covalent.[2] By introducing the BO approximation we allow the separation of the nuclear from the electronic motion, by ignoring the terms where the nuclear and the electronic motion combine, and thus the dependence of the nuclear motion on the explicit electronic positions. These are also the terms that allow the interaction between different electronic configurations, and thus regions of potential energy surfaces where configuration mixing is expected are poorly represented.[2]

The separation of the wavefunction into a nuclear and an electronic component provides a dramatic simplification. The next approximation that can be made is to write the total wavefunction of the system (Ψ) as a product of one-electron functions, or orbitals. The simplest form of this is a Hartree product (Θ),[1]

$$\Theta(1,2,...,n) = \psi_1(1)\psi_2(2)...\psi_n(n). \tag{1.7}$$

For the wavefunction to obey the Pauli principle, it must change sign upon the interchange of a pair of electrons, because electrons are identical and fermionic. Therefore the wavefunction should obey the following condition

$$\hat{P}_{ij}\Psi = \Psi^{int} = -\Psi, \tag{1.8}$$

where $\hat{P}_{ij}$ is an operator that interchanges electrons i and j.[1] However, this is clearly not the case for a simple product wavefunction Θ, since

$$\Theta(1,2) = \psi_1(1)\psi_2(2) \tag{1.9}$$

$$\hat{P}_{1,2}\Theta(1,2) = \Theta(2,1) = \psi_1(2)\psi_2(1) \neq -\psi_1(1)\psi_2(2), \tag{1.10}$$

and therefore Θ is not a suitable choice for the wavefunction Ψ. A suitable wavefunction can be constructed from the Hartree product (Θ) by forming a Slater determinant.[1] The Slater determinant is a linear combination of all the Hartree products that can be constructed by interchange of all pairs of electrons, or, the determinant of a $n \times n$ matrix of n electron arranged in n orbitals. This process which symmetrises the wavefunction is represented by $\hat{A}$,

$$\Psi = \frac{1}{\sqrt{n!}}\hat{A}\Theta = \frac{1}{\sqrt{n!}}\Psi_{Sl}, \tag{1.11}$$

where

$$\Psi_{Sl} = det\begin{bmatrix} \psi_1(1) & \psi_1(2) \\ \psi_2(1) & \psi_2(2) \end{bmatrix} \tag{1.12}$$

$$= \psi_1(1)\psi_2(2) - \psi_1(2)\psi_2(1) \tag{1.13}$$

$$= \Theta(1,2) - \hat{P}_{1,2}\Theta(1,2) \tag{1.14}$$

$$= \Theta(1,2) - \Theta(2,1) \tag{1.15}$$

$$= |\psi_1(1), \psi_2(2)|\,. \tag{1.16}$$

The wavefunction can be written in a number of ways, and has been normalised by the $\frac{1}{\sqrt{n!}}$ factor. Acting on Ψ with $\hat{P}_{1,2}$ now gives the desired result

$$\hat{P}_{1,2}\Psi = \hat{P}_{1,2}\frac{1}{\sqrt{n!}}\left(\psi_1(1)\psi_2(2) - \psi_1(2)\psi_2(1)\right) \tag{1.17}$$

$$= \frac{1}{\sqrt{n!}}\left(\psi_1(2)\psi_2(1) - \psi_1(1)\psi_2(2)\right) \tag{1.18}$$

$$= -\Psi, \tag{1.19}$$

since the wavefunction has changed sign upon exchange of a pair of electrons.

1.2 Hartree-Fock Self Consistent Field Theory

Ab initio[a] techniques involve defining a many electron wavefunction for the system which is solved using the Schrödinger equation by making a series of approximations.[2] The most fundamental method considered here is the Hartree-Fock self consistent field technique (HF-SCF). The electronic Hamiltonian is as follows,

$$\hat{H}_{el} = \overbrace{-\sum_i \frac{1}{2}\nabla_i^2}^{T_e} \overbrace{-\sum_{\mu,i} \frac{Z_\mu}{|r_\mu - r_i|}}^{V_{ne}} \overbrace{+\sum_{i<j} \frac{1}{|r_i - r_j|}}^{V_{ee}} \overbrace{+\sum_{\mu<\nu} \frac{Z_\mu Z_\nu}{|r_\mu - r_\nu|}}^{V_{nn}} \tag{1.20}$$

where T_e is the kinetic energy of the electrons, V_{ne} the nuclear-electron attraction, V_{ee} the inter-electron repulsion and V_{nn} the internuclear repulsion, which is constant for a set arrangement of nuclei.[2] The equation is then rearranged into one and two electron terms[2]

$$\hat{H}_{el} = \sum_i^{N_{elec}} \hat{h}_i + \sum_{j>i}^{N_{elec}} \hat{g}_{ij} + V_{nn}, \tag{1.21}$$

where

$$\hat{h}_i = -\frac{1}{2}\nabla_i^2 - \sum_i^{N_{elec}} \frac{Z_a}{r_\mu - r_i} \tag{1.22}$$

and

$$\hat{g}_{ij} = \frac{1}{|r_i - r_j|}. \tag{1.23}$$

The energy associated with the wavefunction Ψ is then found variationally[2]

$$E = \left\langle \Psi \left| \hat{H}_{el} \right| \Psi \right\rangle \tag{1.24}$$

$$= \frac{1}{n!} \left\langle \Psi_{Sl} \left| \hat{H}_{el} \right| \Psi_{Sl} \right\rangle \tag{1.25}$$

$$= \frac{1}{n!} \left(\left\langle \Psi_{Sl} \left| \hat{h}_i \right| \Psi_{Sl} \right\rangle + \left\langle \Psi_{Sl} \left| \hat{g}_{ij} \right| \Psi_{Sl} \right\rangle \right) + V_{nn}. \tag{1.26}$$

Ψ_{Sl} has terms from all the possible arrangements of electrons in orbitals, i.e. all possible Hartree products. The one-electron operator, $\hat{h}_i$ acts only on the i^{th} electron of each wavefunction, and because the single electron functions ψ are chosen to form an orthogonal set, the $\hat{h}_i$ contribution to E only survives when it is acted upon by the same Hartree product both left and right.[2] For a two electron system, the following integrals are possible for electron one,

[a] *Ab initio* is a latin expression literally meaning "from the beginning".

$$\left\langle \Theta(1,2) \left| \hat{h}_1 \right| \Theta(1,2) \right\rangle = \left\langle \psi_1(1)\psi_2(2) \left| \hat{h}_1 \right| \psi_1(1)\psi_2(2) \right\rangle \tag{1.27}$$

$$= \left\langle \psi_1(1) \left| \hat{h}_1 \right| \psi_1(1) \right\rangle \left\langle \psi_2(2) | \psi_2(2) \right\rangle \tag{1.28}$$

$$= \left\langle \psi_1(1) \left| \hat{h}_1 \right| \psi_1(1) \right\rangle \tag{1.29}$$

$$\left\langle \Theta(1,2) \left| \hat{h}_1 \right| \Theta(2,1) \right\rangle = \left\langle \psi_1(1)\psi_2(2) \left| \hat{h}_1 \right| \psi_1(2)\psi_2(1) \right\rangle \tag{1.30}$$

$$= \left\langle \psi_1(1) \left| \hat{h}_1 \right| \psi_2(1) \right\rangle \left\langle \psi_2(2) | \psi_1(2) \right\rangle = 0 \tag{1.31}$$

$$\left\langle \Theta(2,1) \left| \hat{h}_1 \right| \Theta(2,1) \right\rangle = \left\langle \psi_2(1)\psi_1(2) \left| \hat{h}_1 \right| \psi_2(1)\psi_1(2) \right\rangle \tag{1.32}$$

$$= \left\langle \psi_2(1) \left| \hat{h}_1 \right| \psi_2(1) \right\rangle \left\langle \psi_1(2) | \psi_1(2) \right\rangle \tag{1.33}$$

$$= \left\langle \psi_2(1) \left| \hat{h}_1 \right| \psi_2(1) \right\rangle . \tag{1.34}$$

The first and third case are for identical Hartree products, and give the one-electron contribution to the energy of an electron in a specific orbital. The second case is zero, because the integral $\langle \psi_1(1) | \psi_2(1) \rangle$ is zero due to the orthogonality of the orbitals. For the two electron case, there will be four one electron integrals contributing to E, corresponding to permutations of two electrons and two orbitals. However, due to the normalisation constant, and since the two electrons in the system are identical, this simplifies to two interactions, one for the i^{th} electron in each orbital.

For the operator, $\hat{g}_{ij}$, a similar treatment is possible, except that now contributions are obtained from integrals with the same Hartree product $\langle \Theta | \hat{g}_{ij} | \Theta \rangle$ and those which differ from each other by only a single transposition of a pair of electrons, $\left\langle \Theta | \hat{g}_{ij} | \hat{P}_{ij}\Theta \right\rangle$.[2] Thus integrals are obtained of the form

$$\left\langle \Theta \left| \hat{g}_{ij} \right| \Theta \right\rangle = \left\langle \psi_i(1)\psi_j(2) | \hat{g}_{ij} | \psi_i(1)\psi_j(2) \right\rangle = J_{ij}, \tag{1.35}$$

and

$$\left\langle \Theta | \hat{g}_{ij} | \hat{P}_{ij}\Theta \right\rangle = \left\langle \psi_i(1)\psi_j(2) | \hat{g}_{ij} | \psi_j(1)\psi_i(2) \right\rangle = K_{ij}. \tag{1.36}$$

The first of these two-electron integrals (J_{ij}) is termed the Coulomb integral. It has a classical analogy, which is that it represents the electrostatic repulsion between the two occupied orbitals, with charge distributions $\psi_1(1)^2$ and $\psi_2(2)^2$.[2] The second integral (K_{ij}), is termed the exchange integral, it has no classical analogy, but arises as a direct consequence of the Pauli principle.[2] The result of these three integrals, h_i, J_{ij} and K_{ij} gives the general expression for the energy.[2]

$$E = \sum_{i=1}^{N_{elec}} h_i + \sum_{i=1}^{N_{elec}} \sum_{j>i}^{N_{elec}} (J_{ij} - K_{ij}) + V_{nn} \tag{1.37}$$

$$= \sum_{i=1}^{N_{elec}} h_i + \frac{1}{2} \sum_{i=1}^{N_{elec}} \sum_{j=1}^{N_{elec}} (J_{ij} - K_{ij}) + V_{nn} \tag{1.38}$$

$$= \sum_{i=1}^{N_{elec}} \left\langle \psi_i \left| \hat{h}_i \right| \psi_i \right\rangle + \frac{1}{2} \sum_{i=1}^{N_{elec}} \sum_{j=1}^{N_{elec}} \left(\left\langle \psi_j \left| \hat{J}_{ij} \right| \psi_j \right\rangle - \left\langle \psi_j \left| \hat{K}_{ij} \right| \psi_j \right\rangle \right) + V_{nn} \tag{1.39}$$

where

$$\hat{J}_{ij} |\psi_j(2)\rangle = \langle \psi_i(1) | \hat{g}_{ij} | \psi_i(1) \rangle |\psi_j(2)\rangle \tag{1.40}$$

and

$$\hat{K}_{ij} |\psi_j(2)\rangle = \langle \psi_i(1) | \hat{g}_{ij} | \psi_j(1) \rangle |\psi_i(2)\rangle. \tag{1.41}$$

By summing over all i and j the effect of each electron with all of the other electrons in the system is taken into account, thus including the inter-electron interaction twice. The factor of a half, together with the fact that the self interaction energy (i.e. $J_{ij} - K_{ij}$) is zero corrects for this problem.[2] The exchange and Coulomb integrals have been expressed more succinctly as operators (equations 1.41 and 1.40), where it should be noticed that the exchange operator effectively exchanges the i and j indices on the two particles before the integral is evaluated.[2]

The one-electron Fock operator ($\hat{F}_i$) is defined as[2]

$$\hat{F}_i = h_i + \sum_{j}^{N_{elec}} \left(\hat{J}_{ij} - \hat{K}_{ij} \right). \tag{1.42}$$

This is a contribution to the energy of the system for the i^{th} electron, representing its attraction to the nuclei of the system and the interactions with the other electrons.[2] It can be seen that the total Hamiltonian of the system is not just a sum of Fock operators; the Fock operator is arrived at by considering the variation of the energy.[2] The Fock operator acting on the i^{th} electron of the system, gives the energy ϵ_i, however, the total energy of the system is not simply a sum of the orbital energies ϵ_i, but

$$E_{tot} = \sum_{i}^{N_{elec}} \epsilon_i - \frac{1}{2} \sum_{ij}^{N_{elec}} \left(\hat{J}_{ij} + \hat{K}_{ij} \right) + V_{nn}, \tag{1.43}$$

where the second term corrects for the double counting included by summing the orbital energies.[2] Because the orbital energy describes the effect of the combined electronic field on the i^{th} electron, it only describes the inter-electronic forces in an average way, and thus is a mean-field approximation.[2]

In order to solve the problem to give an optimised HF wavefunction for a molecule, the molecular orbitals (MOs) ψ_i are written as a linear combination of atomic orbitals (χ) weighted by coefficients c_i, and these are inserted into the HF equation[2]

$$\hat{F}_i\psi_i = \epsilon_i\psi_i \tag{1.44}$$

$$\psi_i = \sum_k c_{ik}\chi_k \tag{1.45}$$

$$\hat{F}_i \sum_k c_{ik}\chi_k = \epsilon_i \sum_k c_{ik}\chi_k. \tag{1.46}$$

Each side is then multiplied by the complex conjugate of a member of the set, χ_l, and integrated,[2]

$$\int \chi_l^* \hat{F}_i \sum_k c_{ik}\chi_k d\tau = \int \chi_l^* \epsilon_i \sum_k c_{ik}\chi_k d\tau \tag{1.47}$$

$$\sum_k c_{ik} \overbrace{\int \chi_l^* \hat{F}_i \chi_k d\tau}^{F_{lk}} = \epsilon_i \sum_k c_{ik} \overbrace{\int \chi_l^* \chi_k d\tau}^{S_{lk}} \tag{1.48}$$

$$\sum_k c_{ik} \left(F_{lk} - \epsilon_i S_{lk}\right) = 0, \tag{1.49}$$

to give the secular equations (equations 1.49). One of the solutions to the secular equations is trivial, where $c_{ik} = 0$, and is not very useful, however, non-trivial solutions can found by solving the secular determinant[3]

$$|F_{lk} - \epsilon_i S_{lk}| = 0. \tag{1.50}$$

This gives an equation with i solutions ϵ_i, the orbital energies. Each ϵ_i is then used to solve the secular equations to give the coefficients c_{ik} which make up each MO.[3]

A problem arises at this point, because the secular equations are dependent on the MOs, and thus the coefficients c_{ik}, such that they must be known in advance, before the problem can be solved. The solution to this is an iterative approach, where the initial orbitals for the system are chosen by a "guess" calculation, typically using a lower level technique.[2] One way in which the guess orbitals can be formed is to calculate only the component for the core terms of the Hamiltonian, i.e. the one electron terms. These are trivial to calculate and do not involve an iterative solution.[2] This guess is used to form the secular equations, the secular determinant is then solved, and the secular equations then give the new values of c_{ik}. These are then used to calculate a new set of ϵ_i, and c_{ik}. Provided that the process converges, the iterative solution is reached when the MOs are (within a certain convergence criterion) unchanged by the process.[2]

There are three different formalisms of HF theory, which apply different constraints to the MOs. For a system at its equilibrium geometry with the same number of α and β electrons in a singlet configuration there is usually no require-

ment for one-electron orbitals with different spatial components. Thus a closed shell formalism can be used, which requires that the spatial component of the spin orbitals containing α and β electrons for a MO be the same. This is usually given the name restricted HF, or RHF.[2] Where there is an imbalance between the number of up and down spin electrons, or the wavefunction has unpaired electrons, there are two approaches that can be taken. The first is the unrestricted approach, where each electron occupies a spin-orbital with no restriction on the spatial wavefunction. This is usually termed unrestricted HF, or UHF.[2] The second is restricted open-shell HF, or ROHF. The double occupied orbitals are restricted to have the same spatial wavefunction for both α and β components, while the unpaired electrons are represented by spin-orbitals without restriction.[2]

The majority of the computational effort in calculating the HF energy is in evaluating the two-electron integrals, of which there are of the order of N^4 where N is the number of basis functions.[2] Because this is the step which scales the poorest it will dominate the calculation. The computational expense of HF therefore scales as N^4.[2] Various techniques such as orbital screening (which involves the neglect of the near-zero-valued and therefore unimportant integrals), and direct methods (where integrals are calculated as required) can be used to reduce the expense of the calculation to some degree.[2]

One of the major limitations of HF theory is that it does not include electron correlation; each electron only experiences the combined average effect of all of the other electrons.[2] This means that the position of each electron is independent of the position of each of the other electrons. The implication of this is that even with an infinite basis set, one cannot calculate an energy that is equal to the total electronic energy of the system; the most negative value that can be calculated, the HF limit, does not include the electron correlation energy (or the effects of relativity).[2]

For a more detailed treatment of HF theory the reader is directed to the text book "Introduction to Computational Chemistry" by Jensen.[2]

1.3 The Inclusion of Electron Correlation

The RHF method typically recovers 99 % of the total energy, despite its neglect of instantaneous electron-electron interactions.[2] Unfortunately, however, this 1 % of the energy is of the same order of magnitude as that relating to chemical processes, so really, from a chemical point of view, it is this remaining energy that is vital to the calculation of accurate energies.[2] In order to recover the remaining

1 % of the energy, it is necessary to consider the inter electronic interactions explicitly, or in other words, the electron correlation.[2] As a result this energy is usually called the correlation energy.

Electron correlation can be divided broadly into two types, dynamic and static (or non-dynamic), however, the boundaries between these classes are somewhat indistinct. Broadly, dynamic correlation can be envisaged as the attempt by the electrons in the same orbital to avoid each other on an instantaneous timescale, while static correlation involves altering the orbitals to better describe the ground state wavefunction, allowing the two electrons in different orbitals to avoid each other.[2] Electron correlation can be incorporated into *ab initio* methods in a number of different ways, of these the main methods are configuration interaction (CI), coupled-cluster (CC) and Møller-Plesset perturbation theory (MP). Multiconfigurational representations of the wavefunction through MCSCF (multiconfigurational self consistent field) and MRCI (multireference configuration interaction) can also be used, although these can in some ways be thought of as variants of CI.[2]

1.3.1 Configuration Interaction (CI)

CI is a fairly intuitive way of including electron correlation. Its main features will be discussed here in order to explain the concepts involved in some of the other methods, however, it will not be discussed in great detail. In order to account for the correlation energy, it is necessary to include the effects of excited state determinants in the wavefunction, as well as the Hartree-Fock configuration Φ_{HF}

$$\Psi_{CI} = a_0\Phi_{HF} + \sum_s a_1\Phi_s + \sum_d a_2\Phi_d + \sum_t a_3\Phi_t + ... = \sum_{i=0} a_i\Phi_i, \qquad (1.51)$$

where Φ_s are the singly excited states, individually weighted by a coefficient a_1, the importance of this configuration.[2] The logical extension of this method, full CI, includes the effects of *all* excited states.

There are really only two ways of improving the accuracy of an *ab initio* calculation. The first is to increase the size of the basis set, while the second is to consider more configurations. Full CI with an infinite basis will give the exact non-relativistic energy within the Born-Oppenheimer approximation.[2] This situation is represented in figure 1.1. Full CI is very expensive, and intractable, except for small molecules, although it is often the bench mark against which other methods are compared.[2] Often, truncated CI is used, usually at the CISD level, which includes the effects of single and double excitations from the HF reference wavefunction. The energy is then minimised variationally to optimise

the CI coefficients.[4] In the CI expansion all of the excitations are from the HF reference, using the set of MOs optimised with the HF method; these remain fixed throughout the calculation, since for full CI, at least, it is unnecessary to re-optimise the orbitals because all of the possible CSFs are considered.[4]

An approximation can be made to the energy of the quadruple excitations, by using the Davidson correction. This is given by

$$\Delta E_Q = \left(1 - a_0^2\right)\left(E_{CISD} - E_{HF}\right), \tag{1.52}$$

where the coefficient a_0 is the CI coefficient for the HF determinant in the CI expansion.[2] This correction is then added onto the CISD energy. It must be emphasised that this is only an approximation to the quadruple excitation energy; this is highlighted by the results of a calculation on a two electron system, where CISD is equivalent to full CI, yet ΔE_Q is not zero.[2]

CI is usually considered to include the effects of dynamical correlation, however, in the limit of full CI, all of the electron correlation is accounted for, including that originally considered to be static correlation. Truncated CI methods are not size extensive - the energy does not scale with the size of the system. This will be discussed in greater detail in the coupled-cluster section.[4]

1.3.2 Multiconfigurational Techniques

Truncated CI may suffer from the problem that the HF reference is poor, and hence its orbitals will not describe either the ground or excited determinants well. Another way of considering this problem is that the wavefunction cannot be adequately separated into a set of one-electron functions (orbitals) in such a way that these functions adequately represent the system. The solution to this problem is to move away from a single configurational technique. MCSCF can be viewed as a form of CI, where not only are the coefficients of the CI expansion optimised, but also the coefficients of the basis set expansion of the MOs.[2,b] This method really requires that the concept of one-electron orbitals be abandoned, because the orbitals are correct only for the full CI expansion[4] and not for the individual configurations in the same way as the HF orbitals are for the ground state configuration.

The complexity of full MCSCF is greater than that of full CI, and is as such formidable. In most practical cases, MCSCF is solved in a slightly different way from CI. Rather than truncate the CI expansion and consider only excited states

[b]MCSCF is multiconfigurational, but single reference, because all of the excited state determinants are generated from a single determinant, the HF determinant.

Figure 1.1: Diagrammatic representation of the two dimensional space for improving an *ab initio* calculation.

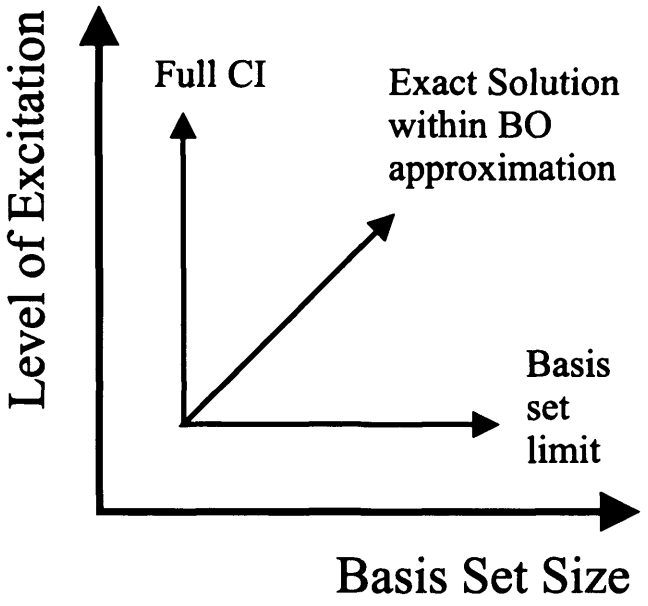

that are related by single and double excitations from the ground configuration (as in CISD), one considers *all* possible configurations inside a small subset of orbitals, termed the active space.[2] This type of MCSCF calculation is often referred to as a complete active space SCF (CASSCF) calculation, although in the results chapter of this thesis the term MCSCF is used to imply that a CASSCF calculation is being performed.

Initially the occupied and virtual MOs of the system are divided into four sets. The first set of orbitals, the core, have a fixed occupation of two electrons each, and their expansion in terms of basis functions is frozen to match the optimised orbitals from the calculation used to generate the reference, e.g. HF orbitals. The second region of orbitals are the closed set. Again, these remain doubly occupied throughout the calculation, however, the basis set coefficients for these orbitals are optimised variationally to reduce the total energy. The third region, the active orbitals, comprise some which were formerly doubly occupied, and some which were formerly virtual levels of the reference. The CASSCF calculation considers all of the determinants which can be generated by exciting the n electrons inside the active space into the N orbitals within the active space. The CI vectors which weight these determinants are optimised to reduce the energy, as are the basis function expansion coefficients which define these orbitals. The fourth region are the virtual levels. These are vacant in all determinants, and therefore do not

Figure 1.2: The division of the orbitals of the system into regions in the CASSCF procedure. The single and double headed arrows represent the one and two electron excitations in the MRCI procedure.

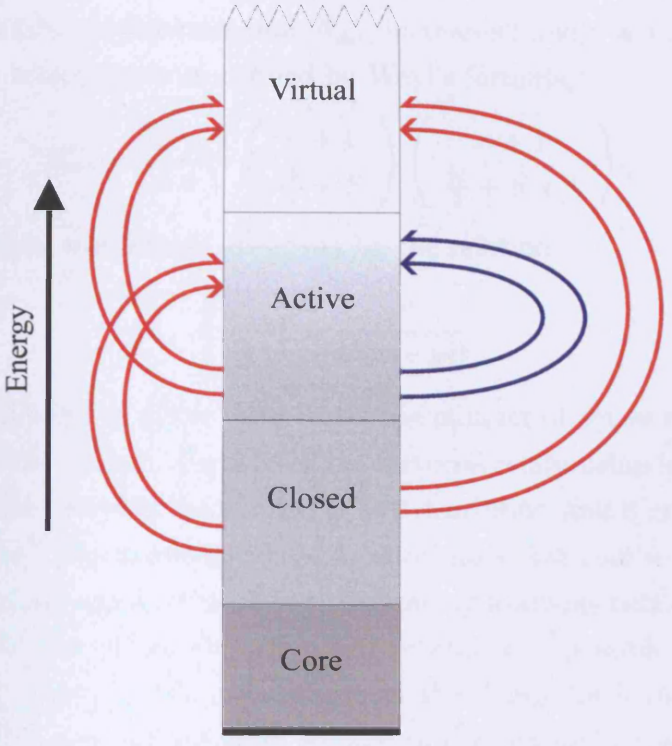

contribute to the energy. This means that the virtual orbitals are not optimised. Figure 1.2 represents diagrammatically the division of the orbitals into regions.

The choice of orbitals which go into the active space is the crux of an CASSCF calculation.[4] Suppose that in a HF calculation there is a small energy separation between the HOMO (highest occupied molecular orbital) and the LUMO (lowest unoccupied molecular orbital) levels such that if the LUMO were populated instead of the HOMO, this orbital would be stabilised to give a new *aufbau* configuration. The resulting calculation is likely to be poor, because the orbitals are only optimised on one of the two close lying configurations, and such it will be difficult to know which (if either), is the ground state configuration. A multiconfigurational approach where both of these orbitals are included in the active space is likely to be more reliable. The MCSCF wavefunction is written as a weighted linear combination of each of the configurations that can be generated by rearrangement of the electrons in the orbitals of the active space, and thus all the orbitals will be populated in at least one determinant. The optimisation of the

orbitals therefore considers all the determinants that expand the wavefunction, rather than the single determinant that is chosen in the HF calculation. This means that the orbitals are a better basis in which to expand the wavefunction.

Ideally, the active space would be chosen to include all the valence orbitals, however, the number of determinants, N_{det}, increases rapidly as more orbitals are included in the active space as defined by Weyl's formula,[1]

$$N_{det} = \frac{2S+1}{n+1}\begin{pmatrix} n+1 \\ \frac{N}{2}-S \end{pmatrix}\begin{pmatrix} n+1 \\ \frac{N}{2}+S+1 \end{pmatrix}, \tag{1.53}$$

where the binomial coefficients are given by the relation

$$\begin{pmatrix} x \\ y \end{pmatrix} = \frac{x!}{y!(x-y)!}. \tag{1.54}$$

where n is the number of active orbitals, N the number of active electrons, and S the total spin of the system. Because of the factorial relationship in equation 1.54, N_{det} strongly increases with the number of active orbitals, and is greatest for a half filled active space. The maximum number of orbitals that can be included in the active space is in the region of 12-13 with commonly available resources,[2] although for systems with more or less electrons than orbitals it is possible to increase this number slightly. Some of the calculations in this study have 16 orbitals in the active space. This may not be large enough to contain all of the orbitals of the valence space, and so a decision needs to be made about which orbitals to include. The choice of orbitals needs to be consistent for all of the stationary points of the system (e.g. all conformations and isomers on the surface); this adds an extra constraint when choosing the active space. Furthermore, the choice of active orbitals will certainly influence the results of a calculation, if the calculation even converges at all, which it may not if the orbitals have been chosen poorly. These factors make CASSCF calculations much more complex than single determinant methods such as HF, and MP; as a result CASSCF is often described as "not a black box method".[2]

MCSCF is usually considered to include the effects of static correlation, because the orbitals of the system are being improved to take into account electron correlation. However, if the active space is chosen to include all the orbitals, then all excited state determinants are included, and this is therefore equivalent to full CI.[4] All of the effects of correlation within the basis set limit, including those termed dynamic correlation, will be included in such a calculation.

The effects of dynamical correlation can also be incorporated into a multiconfigurational approach using multireference CI (MRCI). This is similar to regular

CI, except that single and double (and possibly higher) excitations are included from each configuration of the CASSCF wavefunction.[2] This allows many of the important remaining configurations to be included.[c]

In MRCI the system is divided into four regions, as it was in CASSCF. These may be chosen to match those from the CASSCF calculation, or the core may be made larger to reduce the number of orbitals in the closed region. Excitations are considered from the active space to the virtual levels, from the closed region to vacant orbitals of the active region, and from the closed region to the virtual region, as indicated by the red arrows in figure 1.2.

The computational effort can be reduced by considering only excitations from important determinants, those which contribute strongly to the MCSCF wavefunction.[2] This reduces the total number of determinants to be considered, but also gives rise to a new type of excitation, those from the occupied active orbitals to the virtual active orbitals and are indicated by blue arrows in figure 1.2. These excitations regenerate some of the determinants from the CASSCF calculation that were ignored as being too small to consider. A further reduction in complexity may be introduced by closing off some of the high lying virtual orbitals to avoid generating configuration state functions (CSFs) with extremely high energy.[4] The CI coefficients of these determinants are then determined variationally.[1]

If one finds that a particular CI coefficient relating to an excited determinant has a high weight, then this might indicate that the active space has been poorly chosen, and perhaps should have included the orbital to which this excitation took place. Further, if any of the single and double excitations which regenerate the determinants of the CASSCF calculation are large, then perhaps this determinant should have been included in the reference determinants from which the excitations took place.

1.3.3 Møller-Plesset theory

Møller-Plesset (MP) theory is based on Rayleigh-Schrödinger perturbation theory (RSPT), and was originally proposed in 1934.[5] In RSPT, rather than solving the Schrödinger equation for the true system, one modifies the result of a known problem by considering the effect of a small perturbation to the system.[2] The exact Hamiltonian for the system is expressed as the sum of the zeroth order

[c]MRCI is both multiconfigurational and multireference since the excited determinants are generated from more than one reference configuration. CI is only multiconfigurational, since the excited configurations are generated from the (usually) HF ground configuration.

Hamiltonian, and a perturbation λV,[2]

$$H = H^{(0)} + \lambda H'. \tag{1.55}$$

Provided that λ is small, the exact wavefunction, energy and Hamiltonian for the system can be considered as a Taylor expansion with the n^{th} order term weighted by a λ^n factor (as indicated by the superscripts),

$$\Psi_0 = \Psi_0^{(0)} + \lambda\Psi_0^{(1)} + \lambda^2\Psi_0^{(2)} + \ldots \tag{1.56}$$

$$E_0 = E_0^{(0)} + \lambda E_0^{(1)} + \lambda^2 E_0^{(2)} + \ldots, \tag{1.57}$$

where only the corrections to the ground state energy and wavefunction are considered, as indicated by the subscripts.[2] These are then inserted into the Schrödinger equation. In first order perturbation theory, only terms up to λ^1 are considered,

$$H\Psi_0 = E_0\Psi_0 \tag{1.58}$$

$$\left(H^{(0)} + \lambda H'\right)\left(\Psi_0^{(0)} + \lambda\Psi_0^{(1)}\right) = \left(E_0^{(0)} + \lambda E_0^{(1)}\right)\left(\Psi_0^{(0)} + \lambda\Psi_0^{(1)}\right). \tag{1.59}$$

When this is multiplied out, the terms in λ^2 are discarded,

$$H^{(0)}\Psi_0^{(0)} + \lambda H^{(0)}\Psi_0^{(1)} + \lambda H'\Psi_0^{(0)} = E_0^{(0)}\Psi_0^{(0)} + \lambda E_0^{(0)}\Psi_0^{(1)} + \lambda E_0^{(1)}\Psi_0^{(0)}, \tag{1.60}$$

and terms with equal powers of λ are equated

$$\lambda^0 : H^{(0)}\Psi_0^{(0)} = E_0^{(0)}\Psi_0^{(0)} \tag{1.61}$$

$$\lambda^1 : H^{(0)}\Psi_0^{(1)} + H'\Psi_0^{(0)} = E_0^{(0)}\Psi_0^{(1)} + E_0^{(1)}\Psi_0^{(0)}. \tag{1.62}$$

The first order perturbation in the wavefunction is then expanded in states of the unperturbed system, which are orthogonal,

$$\Psi_0^{(1)} = \sum_{n=0} a_n\Psi_n^{(0)}. \tag{1.63}$$

Combining equations 1.62 and 1.63, and rearranging this gives,

$$H^{(0)}\sum_{n=0} a_n\Psi_n^{(0)} + H'\Psi_0^{(0)} = E_0^{(0)}\sum_{n=o} a_n\Psi_n^{(0)} + E_0^{(1)}\Psi_0^{(0)} \tag{1.64}$$

$$\sum_{n=0} a_n\left(H^{(0)} - E_0^{(0)}\right)\Psi_n^{(0)} = \left(E_0^{(1)} - H'\right)\Psi_0^{(0)} \tag{1.65}$$

$$\sum_{n=0} a_n\left(E_n^{(0)} - E_0^{(0)}\right)\Psi_n^{(0)} = \left(E_0^{(1)} - H'\right)\Psi_0^{(0)}, \tag{1.66}$$

and then both sides are multiplied by $\psi_0^{(0)}$, and integrated,

$$\sum_{n=0} a_n \left(E_n^{(0)} - E_0^{(0)}\right) \left\langle \Psi_0^{(0)} | \Psi_n^{(0)} \right\rangle = E_0^{(1)} \left\langle \Psi_0^{(0)} | \Psi_0^{(0)} \right\rangle - \left\langle \Psi_0^{(0)} | H' | \Psi_0^{(0)} \right\rangle. \quad (1.67)$$

The left hand side of equation 1.67 equals zero since for $n = 0$ the energies cancel, and for $n \neq 0$ the integral becomes zero. This gives

$$0 = E_0^{(1)} - \left\langle \Psi_0^{(0)} | H' | \Psi_0^{(0)} \right\rangle, \quad (1.68)$$

and thus the first order correction to the energy is given by the expectation value of the first order correction to the Hamiltonian over the unperturbed ground state wavefunction.

$$E_0^{(1)} = \left\langle \Psi_0^{(0)} | H' | \Psi_0^{(0)} \right\rangle. \quad (1.69)$$

By setting the $\lambda = 1$, we obtain the energy and wavefunctions corrected to first order,

$$H = H^{(0)} + H' \quad (1.70)$$

$$E_0 = E_0^{(0)} + \left\langle \Psi_0^{(0)} | H' | \Psi_0^{(0)} \right\rangle. \quad (1.71)$$

In MP theory, the ground state Hamiltonian is chosen to be the sum over the Fock operators[2]

$$H^{(0)} = \sum_i \hat{F}_i. \quad (1.72)$$

Although there is some implicit error caused by this choice, specifically the double counting of the inter-electron interactions, the ground state problem needs to have a known solution, which is satisfied by this choice.[2] The exact Hamiltonian for the reference system is thus given by the following equation, where $\hat{F}_i$ is the Fock operator for the i^{th} electron in the system, and then the MP0 energy is simply the sum of orbital energies,[2]

$$E_0^{(0)} \Psi_0^{(0)} = H^{(0)} \Psi_0^{(0)} = \sum_i \hat{F}_i \Psi_0^{(0)} = \sum_i \epsilon_i \Psi_0^{(0)} \quad (1.73)$$

$$E_0^{(0)} = \sum_i \epsilon_i. \quad (1.74)$$

The first order correction to the Hamiltonian is given by the true electron-electron interaction, with Fock operator subtracted from it,

$$H' = H - H^{(0)} = H - \sum_i \hat{F}_i. \quad (1.75)$$

The first order correction to the energy given by,

$$E_0^{(1)} = \left\langle \Psi_0^{(0)} \left| H' \right| \Psi_0^{(0)} \right\rangle \quad (1.76)$$

$$= \left\langle \Psi_0^{(0)} \left| H - H^{(0)} \right| \Psi_0^{(0)} \right\rangle \quad (1.77)$$

$$= \left\langle \Psi_0^{(0)} \left| \frac{1}{r_{ij}} - \sum_i \hat{F}_i \right| \Psi_0^{(0)} \right\rangle, \tag{1.78}$$

and by using equations 1.35 and 1.36 this can be reduced to

$$E_0^{(1)} = \left\langle \Psi_0^{(0)} | \sum_i \sum_{i<j} (J_{ij} - K_{ij}) - \sum_i \sum_j (J_{ij} - K_{ij}) | \Psi_0^{(0)} \right\rangle \tag{1.79}$$

$$= -\left\langle \Psi_0^{(0)} | \sum_i \sum_j (J_{ij} - K_{ij}) | \Psi_0^{(0)} \right\rangle. \tag{1.80}$$

The MP1 corrected energy is then given by

$$E_0(MP1) = \sum_i \epsilon_i + E_0^{(1)} = E(HF). \tag{1.81}$$

It may be observed that the MP1 energy is essentially the Hartree-Fock energy; the first order correction to the energy corrects for the double counting of the interaction energy introduced by the choice of the unperturbed Hamiltonian.[2]

The second order perturbation to the energy depends on the sum over the levels of the unperturbed system,[2]

$$E_0^{(2)} = \left\langle \Psi_0^{(0)} | H' | \Psi_0^{(1)} \right\rangle, \tag{1.82}$$

but the first order correction can be expanded in terms of the states of the unperturbed Hamiltonian

$$\Psi_0^{(1)} = \sum_n c_n \Psi_n^{(0)}, \tag{1.83}$$

where the coefficients are given by

$$c_n = \frac{\left\langle \Psi_n^{(0)} | H' | \Psi_0^{(0)} \right\rangle}{E_0^{(0)} - E_n^{(0)}}. \tag{1.84}$$

This allows the second order energy to be simplified to

$$E_2^{(0)} = \sum_n c_n \left\langle \Psi_0^{(0)} | H' | \Psi_n^{(0)} \right\rangle \tag{1.85}$$

$$= \sum_n \frac{\left| \left\langle \Psi_0^{(0)} | H' | \Psi_n^{(0)} \right\rangle \right|^2}{E_0^{(0)} - E_n^{(0)}}. \tag{1.86}$$

The energy will converge quickly where there is a large spacing between the levels and the sum may be truncated without much effect. Only double excitations from the ground wavefunction can contribute toward the second order energy correction. This is because for single excitations the numerator of equation 1.86

would contain

$$\left\langle \Psi_0^{(0)} | H - H_0^{(0)} | \Psi_a^r \right\rangle = \left\langle \Psi_0^{(0)} | H | \Psi_a^r \right\rangle - \left\langle \Psi_0^{(0)} | \hat{F} | \Psi_a^r \right\rangle = 0, \qquad (1.87)$$

where Ψ_a^r represents a state generated by the excitation of a single electron from orbital a to orbital r. The first term is zero due to Brillouin's theorem,[d] while the second is zero because the spin-orbitals are eigenfunctions of the Fock operator. Thus they return an energy with the eigenfunction, which is orthonormal with $\Psi_0^{(0)}$ and thus zero.[2]

MP2 includes the effects of double excitations from the HF ground configuration; the effect of the third order correction to the energy is to include the correlation energy between pairs of electrons.[2] In order to calculate the second order energy correction, it is necessary to know the first order correction to the wavefunctions. Once these are known, the third order energy correction (MP3) can also be calculated.[2] Since no extra perturbations to the wavefunction are required, it can be deduced that, again, only the effects of double excitations are considered; and can be envisaged as the interaction between electron pairs, as opposed to MP2 which includes the interaction between pairs of electrons.[2] In order to calculate higher perturbation energy corrections, it is necessary to calculate the perturbation of the wavefunction to a higher level, and this makes the method more expensive.[2]

Since it is not necessary to calculate any more integrals than are required for a HF calculation this part of the calculation still scales as N^4, however, it is necessary to do a series of integral transformations in order to solve the problem. These integral transformations scale poorer than N^4, and therefore for large N it is these that dominate and represent the significant expense. MP2 recovers approximately 80-90 % of the total correlation energy, and scales as N^5, while MP3 recovers 90-95 % of the correlation energy, and scales as N^6.[2] MP4(sdq), including the effects of singles, double and quadruple excitations scales as N^6, while the inclusion of triples also in MP4(sdtq) scales as N^7 but recovers 95-98 % of the correlation energy.[2] This, however, is still competitive with CISD, which also scales as N^6, but only recovers 80-90 % of the correlation energy.[2]

MP perturbation theory is size extensive for all levels of theory. Brueckner showed this for the first few orders, and Goldstone showed, using a diagrammatic approach, that MP perturbation theory is size extensive for all orders.[6] This is not generally true for other forms of perturbation theory, and so Møller-Plesset

[d]Brillouin's theorem states that the matrix elements between the ground determinant and singly excited determinants are zero for HF orbitals.

Figure 1.3: The oscillating nature of MPn theory for a system well described by a HF wavefunction.

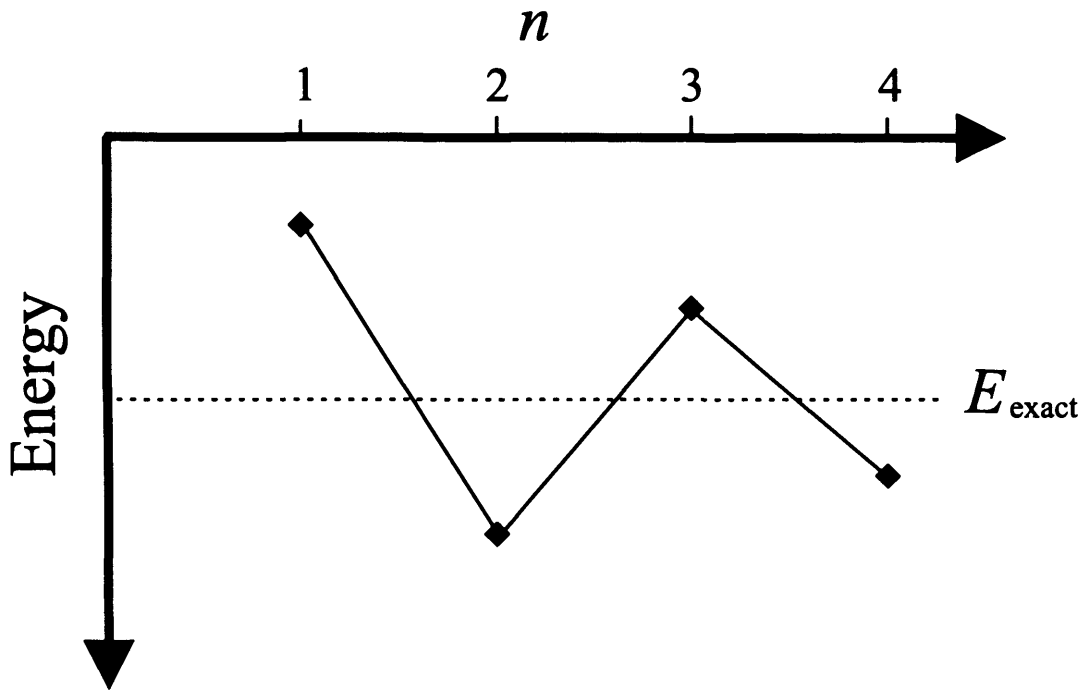

theory has become the most used form.[2]

The energy calculated by the Hartree-Fock method is an upper bound of the correct energy. This is ensured by the variational principle, such that the energy found is always less negative than the true energy, and this is also true for CI. For Møller-Plesset theory, there is no guarantee that this is the case because the method is non-variational.[2] Provided that we are interested in energy separations, this does not pose a serious limitation, because nothing can be inferred about the range of an energy difference between two variationally correct numbers (i.e. those with upper bounds).

The main assumption of perturbation theory in the calculation of the correlation energy is that the perturbation is small.[2] If the HF wavefunction is a particularly poor representation of the electronic structure of the system and so the perturbation is large, then the method may not converge.[2] However, other factors affect the convergence of MP methods, for instance the basis set chosen; the addition of diffuse functions may prevent convergence.[2]

Cramer and He proposed that for an ideal system with well separated pairs of electrons, a smooth convergence to a limiting value should be observed as terms are added to the perturbation series.[7] However, for most systems well

described by an HF wavefunction, an oscillating convergence is seen, such as in figure 1.3.[2] Typically the first term to include a type of excitation overestimates its effects. Thus MP2 over estimates the effect of correlating electron pairs, while MP4 overestimates the effects of singles and triples.[2] If the expansion is plotted and found to converge toward a limit, a good estimate of the correlation energy should be an average of the MP3 and MP4 energies. This would be MP∞ which is equivalent to full CI.[2] MP theory is a single reference method. If the system is not well described by a single reference wavefunction, then the MP series may not converge well. However, calculating each of the energies up to MP4 should show whether the system is well behaved, and allow an estimate of the full CI correlation energy.

1.3.4 Coupled-cluster theory

Coupled-cluster theory was originally developed by Coester and Kümmel in 1960, and was originally formulated for the study of nuclear physics.[8] In the 1960s, the theory was reformulated by Čižek and Paldus to make it suitable for the study of electronic structure.[9] Since then, it has become known as the "gold standard" technique for quantum chemical calculations.[4] One of the main benefits of coupled-cluster methodologies over more intuitively straight-forward techniques for including electron correlation, such as CI, is their size extensivity.[2]

Both CI and CC methods use the concept of an excitation operator, $\hat{T}$, which is expanded in terms of the number of electrons excited to generate a particular set of excited states[2]

$$\hat{T} = \hat{T}_1 + \hat{T}_2 + \hat{T}_3 + ... + \hat{T}_{N_{elec}}, \tag{1.88}$$

where $\hat{T}_1$ produces single excitations from the ground state, and $\hat{T}_{N_{elec}}$ excites all N electrons.[2] In CI, a linear *ansatz* is used,

$$\Psi_{CI} = (1 + \hat{T})\Phi_0 = (1 + \hat{T}_1 + \hat{T}_2 + \hat{T}_3 + ...)\Phi_0, \tag{1.89}$$

while in coupled-cluster an exponential *ansatz* is used, which is then expanded as a Taylor series[2]

$$\Psi_{CC} = e^{\hat{T}}\Phi_0 = (1 + \hat{T} + \frac{1}{2}\hat{T}^2 + \frac{1}{6}\hat{T}^3 + ...)\Phi_0 \tag{1.90}$$

$$= \left(\sum_{k=0}^{\infty} \frac{1}{k!}\hat{T}^k\right)\Phi_0. \tag{1.91}$$

If for a moment, we consider CCD, where only double excitations are included, then[2]

$$\hat{T} = \hat{T}_2 \tag{1.92}$$

$$\Psi_{CC} = \left(1 + \hat{T}_2 + \frac{1}{2}\hat{T}_2^2 + \frac{1}{6}\hat{T}_2^3 + ...\right)\Phi_0, \tag{1.93}$$

where

$$\hat{T}_2\Phi_0 = \sum_{i>j}^{occ}\sum_{a>b}^{vac} t_{ij}^{ab}\psi_{ij}^{ab}. \tag{1.94}$$

In comparison to CID, where

$$\Psi_{CI} = 1 + \hat{T}_2, \tag{1.95}$$

we observe that there are extra terms included in the CC wavefunction that are not included in the CI wavefunction. The terms with products of $\hat{T}_2$ are called disconnected, or product terms, and it is these that account for the size extensivity of coupled-cluster theory.[2,4]

Consider a hydrogen molecule, which is represented by a minimum basis. A CID calculation will give a wavefunction with two terms, the ground configuration, and the two-electron excited configuration; the energy of such a system we shall call E_{H_2}. If two hydrogen molecules are considered, initially at infinite separation, then one might expect that the total energy should equal $2E_{H_2}$.[2] However, for CID, this will not be the case, since it cannot represent the configuration where both H_2 molecules are simultaneously in the doubly excited state; this would be a quadruple excitation.[2] Thus the energy is deficient by this term, and this is an example of size non-extensivity. In the coupled-cluster approach, the product of double terms ($\hat{T}_2^2$) can represent the quadruply excited configuration in $2H_2$ and ensure that the energy scales with the size of the system.[2,e]

It is usual to include the effects of both single and double excitations in coupled-cluster theory, i.e. CCSD. The doubles contribution has the biggest effect, because the single excitations from the HF wavefunction do not contribute to the energy due to Brillouin's theorem.[2] However, once the double excitations are taken into account, it is not much more expensive to add the single excitation contributions, which can contribute because of their disconnected contributions, which would not be considered when performing what might be termed "CCS".[2]

Due to the highly non-linear nature of the exponential *ansatz*, it is not possible

[e]Møller-Plesset theory is also size extensive, however, while MP2 includes the effects of all excitations to the second order, CCD includes the effects of double excitations, but to an infinite order.

to calculate the energy using the variational procedure

$$E_{CC}^{var} = \frac{\left\langle \Psi_{CC} \middle| \hat{H} \middle| \Psi_{CC} \right\rangle}{\langle \Psi_{CC} | \Psi_{CC} \rangle} \tag{1.96}$$

$$= \frac{\left\langle e^{\hat{T}} \Phi_0 \middle| \hat{H} \middle| e^{\hat{T}} \Phi_0 \right\rangle}{\left\langle e^{\hat{T}} \Phi_0 | e^{\hat{T}} \Phi_0 \right\rangle}, \tag{1.97}$$

because the denominator does not terminate in a convenient way as in HF.[2] Instead, the energy is calculated by projecting the coupled-cluster Schrödinger equation (equation 1.98) onto the reference wavefunction.[2]

$$\hat{H} e^{T} \Phi_0 = E e^{T} \Phi_0 \tag{1.98}$$

$$\left\langle \Phi_0 \middle| \hat{H} e^{\hat{T}} \middle| \Phi_0 \right\rangle = E_{CC} \left\langle \Phi_0 | e^{\hat{T}} \Phi_0 \right\rangle \tag{1.99}$$

$$= E_{CC} \left\langle \Phi_0 \middle| \left(1 + \hat{T}_1 + \hat{T}_2 + ...\right) \Phi_0 \right\rangle \tag{1.100}$$

$$= E_{CC} \left\langle \Phi_0 | \Phi_0 \right\rangle + \left\langle \Phi_0 | \hat{T}_N \Phi_0 \right\rangle, \tag{1.101}$$

and due to the orthogonality of the states

$$\left\langle \Phi_0 | \hat{T}_n \Phi_0 \right\rangle = 0, \tag{1.102}$$

we have

$$E_{CC} = \left\langle \Phi_0 \middle| \hat{H} e^{\hat{T}} \middle| \Phi_0 \right\rangle. \tag{1.103}$$

$\hat{T}$ is now expanded, but since $\hat{H}$ is the Hartree-Fock Hamiltonian, which contains only one and two electron integrals, only the one and two electron terms from the expansion of $\hat{T}$ are kept, because matrix elements between the ground and excited determinants related by higher than a double excitation are zero.[2]

$$E_{CC} = \left\langle \Phi_0 \middle| \hat{H}(1 + \hat{T}_1 + \hat{T}_2 + \hat{T}_1^2) \middle| \Phi_0 \right\rangle \tag{1.104}$$

$$= \left\langle \Phi_0 \middle| \hat{H} \middle| \Phi_0 \right\rangle + \left\langle \Phi_0 \middle| \hat{H} \middle| \hat{T}_1 \Phi_0 \right\rangle \tag{1.105}$$

$$+ \left\langle \Phi_0 \middle| \hat{H} \middle| \hat{T}_2 \Phi_0 \right\rangle + \frac{1}{2} \left\langle \Phi_0 \middle| \hat{H} \middle| \hat{T}_1^2 \Phi_0 \right\rangle \tag{1.106}$$

$$= E_0 + \sum_{i}^{occ} \sum_{a}^{vir} t_i^a \left\langle \Phi_0 \middle| \hat{H} \middle| \Phi_i^a \right\rangle \tag{1.107}$$

$$+ \sum_{i<j}^{occ} \sum_{a<b}^{vir} \left(t_{ij}^{ab} + t_i^a t_j^b - t_i^b t_j^a\right) \left\langle \Phi_0 \middle| \hat{H} \middle| \Phi_{ij}^{ab} \right\rangle, \tag{1.108}$$

and since the second term is zero due to Brillouin's theorem,

$$E_{CC} = E_0 + \sum_{i<j}^{occ} \sum_{a<b}^{vir} \left(t_{ij}^{ab} + t_i^a t_j^b - t_i^b t_j^a\right) \left\langle \Phi_0 \left| \hat{H} \right| \Phi_{ij}^{ab} \right\rangle . \tag{1.109}$$

The coupled-cluster energy thus depends only upon the double excitations, the disconnected terms between single excitations, and the product terms of the single and double excitations. Provided that canonical HF orbitals are used this does not represent an approximation.[2]

In order to calculate the amplitudes for this equation, it is necessary to formulate and solve the coupled-cluster equations. Initially, the cluster expansion is terminated at a desired level. Since the single excitations on their own cannot contribute due to Brillouin's theorem, the first stage of approximation is CCD. The next stage of approximation that can be made is CCSD, and because there are many more doubly excited determinants than singly excited determinants, CCSD is not much more computationally demanding than CCD, and so this is usually where the truncation is made.[2]

For CCSD, $\hat{T} = \hat{T}_1 + \hat{T}_2$. The coupled-cluster equations involve integrals between a de-excited excited determinant and the Hamiltonian acting on an excited ground configuration.[2] Although the Hamiltonian only gives non-zero integrals for one and two electron integrals, the result of the coupled-cluster equations has terms containing single, double, product ($\hat{T}_1^2$), product triple ($\hat{T}_1\hat{T}_2$ & $\hat{T}_1^3$) and product quadruple ($\hat{T}_2^2$ & $\hat{T}_1^4$) excitations.[2] Thus, when the single and double amplitudes are calculated, these extra levels of excitation are taken into account.[2] The size extensivity of coupled-cluster theory is due to these extra connected terms, which do not appear in CISD.[2] The truncation of the coupled-cluster expansion results in approximate amplitudes being calculated, which leads to an approximate energy when they are used in equation 1.109.[2] The calculation of the CCSD energy involves a computational expense that scales on the order of N^6, where N is the number of basis functions.[4]

The consideration of the next term in the coupled-cluster expansion results in the CCSDT method. This is usually too computationally demanding, except for small systems, as it scales on the order of N^8.[4] The most important term which is excluded when comparing CCSD with CCSDT is the disconnected triples contribution, given by $\hat{T}_3$.[2] The extra four electron terms that also arise, such as $\hat{T}_1\hat{T}_3$ are expected to be small because the effect of the singles excitations is expected to be small,[2] since there is no direct energy contribution from the single electron excitations. Rather than calculating the full CCSDT energy the significant terms contributing to the energy can be calculated with MP theory using the coupled-cluster amplitudes, and these are then added to the CCSD energy.[2]

This technique is termed CCSD(T). This represents a significant reduction in the computational effort, since the method only scales to the order of N^7 instead of N^8.[1]

1.3.5 MP and CC theory in comparison

A comparison of coupled-cluster methodology with Møller-Plesset theory reveals a few interesting points. Since MP2 and MP3 include only double excitations, it is implicit that these are the most significant correction to the wavefunction, while single excitations are not introduced until MP4.[2]

Both Møller-Plesset and coupled-cluster theory rely on the HF wavefunction being a suitable reference from which to include correlation. In MP theory, if the reference wavefunction is poor, then a large perturbation must be considered in order to represent the true system, and the theory can tend to become unreliable.[2] CC theory tends to be more robust, because of the extra terms included in the expansion.[2] If the HF wavefunction is poor, one way of progressing is by a multi-configuration SCF calculation, where the wavefunction is improved by mixing in excited determinants when optimising the orbitals. A significant contribution to improving the wavefunction comes from the orbital relaxation caused by single excitations,[2] which can contribute to the energy because the MCSCF orbitals are not eigenfunctions of the Fock operator.

In methods based on a HF reference, such as CC and MP, there is no first order contribution to the energy from single excitations as the relevant integrals are formally zero by Brillouin's theorem.[2] They are however included to some extent in higher order terms through coupling interactions. If the singles amplitudes from solving the CC equations are large, this can be an indication that the HF wavefunction is poor, and is often taken as an indication of multiconfigurational character.[2] An equivalent way of looking at this is that if singles amplitudes are large, one might expect that they should be included as a first order effect!

1.3.6 The $\mathscr{T}_1$ diagnostic

The $\mathscr{T}_1$ diagnostic for a coupled-cluster wavefunction is defined as

$$\mathscr{T}_1 = \frac{1}{\sqrt{N_{elec}}}||t_1||, \tag{1.110}$$

where $||t_1||$ is the norm of the single excitation amplitudes.[10] $\mathscr{T}_1$ will therefore be large when the effect of single amplitudes is important, and is often taken as an indication that the system has significant multiconfigurational character.

Therefore it is often used as a measure of the reliability of a CC wavefunction.[2] The bigger the $\mathscr{T}_1$ value, the more likely the wavefunction is multiconfigurational, and hence the less reliable the single reference coupled-cluster method will be. There remains some debate as to the maximum acceptable $\mathscr{T}_1$, stemming partly from there being several different ways of calculating it, although the generally accepted upper limit is 0.02 for a closed-shell system.

The Gaussian[11,12] quantum chemical package uses the method of Lee and Taylor[10] to calculate $\mathscr{T}_1$ diagnostics for both closed-shell and open-shell systems. However it was pointed out by Rienstra-Kiracofe *et al.*,[13] that this method is formulated for use on closed-shell wavefunctions,[13] and more specifically "..closed-shell coupled-cluster wavefunctions that are based on a RHF reference function,..".[14] Thus it may not be ideally suited to open-shell wavefunctions.[13]

Jayatilaka and Lee formulated an alternative method for calculating the $\mathscr{T}_1$ diagnostic for open-shell systems.[14] This method takes into account that some of the amplitudes that are included in the closed-shell formalism should not be included in the open-shell approach, since they become the coefficients of doubly excited determinants. As the closed-shell $\mathscr{T}_1$ method includes these extra amplitudes when applied to open-shell systems, Jayatilaka and Lee concluded that $\mathscr{T}_1$ values calculated in this way would be significantly larger than those produced by their reformulated approach. This was also pointed out by Lee and Taylor when they formulated the closed-shell $\mathscr{T}_1$ diagnostic method.[10]

> *"It is not the purpose of this paper to provide numerous numerical examples of the open-shell $\mathscr{T}_1$ diagnostic, but mainly to give a definition for the open-shell $\mathscr{T}_1$ diagnostic that is consistent with the closed-shell quantity. It is apparent that a similar definition for $\mathscr{T}_1$ from previous open-shell coupled-cluster theories would include a contribution from the $t_{i\alpha}^{\alpha\beta}$ amplitudes. However since these amplitudes are considered coefficients of doubly excited determinants, it would appear that such a diagnostic would generally be quite a bit larger than the one proposed here and, more importantly, it would be inconsistent with the closed-shell $\mathscr{T}_1$ diagnostic."*[14]

Thus, a $\mathscr{T}_1$ diagnostic value for an open-shell system with an acceptable degree of multiconfigurational character will be larger than that for a closed-shell system when the method of Lee and Taylor[10] is applied to each. However, the method of Jayatilaka and Lee[14] as applied to open-shell systems should be comparable with the method of Lee and Taylor[10] as applied to closed-shell systems, suggesting that in both cases 0.02 is the upper limit for the $\mathscr{T}_1$ diagnostic.

In an attempt to further clarify the use of a $\mathscr{T}_1$ diagnostic, Rienstra-Kiracofe *et al.* applied the open-shell formalism of Jayatilaka and Lee[14] to the reaction of C_2H_5 with O_2.[13] They noted that although the $\mathscr{T}_1$ diagnostic for the HO_2 radical is 0.034 at the CCSD(T)/TZ2P level, coupled-cluster calculations accurately treat the system.[13] Calculations were also performed on the CN radical, which is renowned for having spin-contamination problems with unrestricted methodologies. However, CCSD(T) replicates well the experimental results, even with a $\mathscr{T}_1$ of 0.045.[13] Thus Rienstra-Kiracofe *et al.* suggested that the upper limit for the $\mathscr{T}_1$ diagnostic calculated with the open-shell procedure of Jayatilaka and Lee[14] should be 0.045,[13] and not 0.02.

Peiró-García and Nebot-Gil[15] used Gaussian 98 to calculate $\mathscr{T}_1$ diagnostics for the reaction of O_3 with OH. They accept the $\mathscr{T}_1$ value of 0.0481 as reliable[15] for the transition state with connectivity [HOOOO], since energy separations between CCSD(T) single points replicate experimental data reasonably well, and because it is not much larger than the value of 0.045 proposed by Jayatilaka and Lee.[14] Thus, it seems that some confusion has taken place, since these workers seem to be applying the limit (0.045) proposed by Jayatilaka and Lee[14] for the use of the open-shell $\mathscr{T}_1$ diagnostic on open-shell systems, despite using the method of Lee and Taylor to calculate the $\mathscr{T}_1$ for their open shell systems. This 'new' upper limit has been used in several papers,[15–17] although it unclear whether the limit has any real validity when used in this way.

In summary, the limit of the $\mathscr{T}_1$ diagnostic for an open-shell system computed using the open-shell formalism can be as high as 0.045.[13] Furthermore, the $\mathscr{T}_1$ diagnostic for the same system computed using the closed-shell method is likely to be even higher. This suggests that when using the Gaussian code on an open-shell system, the $\mathscr{T}_1$ diagnostic could be in excess of 0.045 without substantial multiconfigurational character. Certainly it seems unreasonable to look for $\mathscr{T}_1$ diagnostic results smaller than 0.02 when using the method of Lee and Taylor on open-shell systems.[10]

Chapters 2 and 3 will return to the subject of the $\mathscr{T}_1$ diagnostic, discussing both the maximum value that should be considered to indicate a reliable CC wavefunction, and situations where the $\mathscr{T}_1$ diagnostic may give misleading results.

1.4 Density Functional Theory

In the 1960s, Kohn and Hohenberg proved that the ground state properties of a system can be predicted entirely from a knowledge of the ground state electron

density;[18] this is the principle behind density functional theory (DFT). The total electronic energy can be written as a function of the density, kinetic energy (T), inter-electronic repulsion (V_{ee}) and electron-nuclear attraction (V_{ne})

$$E[\rho] = T[\rho] + V_{ee}[\rho] + V_{ne}[\rho]. \tag{1.111}$$

The problem is variational, so the energy obtained for an approximate density is always greater than that obtained for the true density[4]

$$E[\rho_{true}] \leq E[\rho_{approx}]. \tag{1.112}$$

Initially, a fictitious system is envisaged with the simplification of non-interacting electrons, which move in a potential $V(r)$ which represents the nuclear potential in a true system. The non-interacting wavefunction (Ψ_{NI}) is represented by a normalised Slater determinant of the one-electron functions

$$\Psi_{NI} = \frac{1}{\sqrt{n!}} |\psi_1, \psi_2, \psi_3, ..., \psi_n|, \tag{1.113}$$

which is acted on by the one-electron Hamiltonian ($\hat{h}_{NI}$) to give the one electron energies ϵ_i[1]

$$\hat{h}_{NI}\psi_i = \left(-\frac{1}{2}\nabla^2 + V(r)\right)\psi_i = \epsilon_i\psi_i. \tag{1.114}$$

These one electron functions are used to calculate the electron density of the system[4]

$$\rho = \sum_{i=1}^{n} |\psi_i(r)|^2. \tag{1.115}$$

In the non-interacting system, the kinetic energy, and total energy are given by the expressions[1,2]

$$T_{NI}[\rho] = \left\langle \Psi_{NI} \left| \sum_i^n \left(-\frac{1}{2}\nabla^2\right) \right| \Psi_{NI} \right\rangle \tag{1.116}$$

$$= \sum_i^n \left\langle \psi_i \left| -\frac{1}{2}\nabla^2 \right| \psi_i \right\rangle \tag{1.117}$$

$$\neq T_{true}[\rho] \tag{1.118}$$

$$E_{NI}[\rho] = T_{NI}[\rho] + V_{ne}[\rho] \tag{1.119}$$

$$= T_{NI}[\rho] + \int \rho(r) v_{nuc}(r) dr. \tag{1.120}$$

and given the one electron functions ψ_i, they are easy to calculate.

Knowing how to calculate the kinetic energy for the true system is one of the major problems for orbital free density functional theory. However, Kohn and Sham recast the problem by noticing that it was possible to use the kinetic energy

of the non-interacting system provided that the potential was modified to take this into account.[19] The total electronic energy is then written

$$E[\rho] = T_{NI}[\rho] + J[\rho] + E_{xc}[\rho] + V_{ne}[\rho] \tag{1.121}$$

$$E_{xc}[\rho] = T[\rho] - T_{NI}[\rho] + V_{ee}[\rho] - J[\rho], \tag{1.122}$$

where E_{xc} is a term that corrects for the difference between the true and non-interacting kinetic energy (sometimes called the kinetic correlation energy) and the difference between the Coulomb energy (J) and full electron-electron interaction.[1] The total energy of the real system is then given by the expression[2]

$$E[\rho] = T_{NI}[\rho] + J[\rho] + E_{xc}[\rho] + \int \rho(r) v_{nuc}(r) dr \tag{1.123}$$

So, it is possible to calculate the total energy, provided that we know the electron density of the true system. This is obtained from a one-electron Hamiltonian, with the electron experiencing a modified potential, V_{eff}, the Kohn-Sham potential,[4]

$$\hat{h}\psi_i = \left(-\frac{1}{2}\nabla^2 + V_{eff}(r)\right)\psi_i = \epsilon_i \psi_i \tag{1.124}$$

$$V_{eff}(r) = V_{nuc}(r) + \int \frac{\rho(r')}{|r - r'|} dr' + V_{xc}(r). \tag{1.125}$$

where equation 1.115 is then used to calculate the density. In order to solve the one-electron Hamiltonian (equation 1.124), V_{eff} must be known, which is obtained from the derivative of the exchange correlation functional with respect to density,[20]

$$V_{xc}(r) = \frac{\delta E_{xc}[\rho]}{\delta \rho(r)}. \tag{1.126}$$

Equations 1.115, 1.124, 1.125 and 1.126 are the Kohn-Sham equations. A guess set of orbitals is generated, and equation 1.115 is used to calculate the density. V_{eff} is then calculated using equations 1.126 and 1.125, and a new density is calculated using equations 1.124 and 1.115. This process is iterated to self consistency. The total energy of the system can then be calculated using equation 1.123.

In principle the process described above is exact, unlike the HF equations, where the mean-field approximation is required. However, although the Kohn-Sham theory states that an exact exchange-correlation functional (E_{xc}) *exists*, it does not indicate what its functional form might be![20] This is the goal of Kohn-Sham density functional theory, to find the true exchange-correlation functional, or, more realistically, to design exchange-correlation functionals to represent E_{xc}. Although the Kohn-Sham process is variational, this is only rigorously correct

with the exact E_{xc}. With approximate functionals, which are in practice all that are available, the process is no longer variationally correct.[4]

The electron density (ρ) is dependent only on three coordinates, the position in space.[2] However, when orbitals are introduced to the system, this dramatic simplification compared with HF is lost, since $3N$ coordinates are required to describe the orbitals. As a consequence KS-DFT formally scales as N^4 with the number of basis functions, however, it is possible to make the method slightly more economical by fitting the density to a linear combination of functions, and then using this fit when calculating the Coulomb integrals. This can reduce the computational expense of the method to N^3.[2]

1.4.1 Exchange Correlation Functionals

There are many different exchange-correlation functionals that have been designed and implemented in commonly used codes, and it is beyond the scope of this section to discuss them individually in any detail, however, an overview of the different types that have been used and their benefits will be given.

As already stated, the Kohn-Sham theorem states that a functional form for the exchange-correlation energy exists, but makes no inferences about what the functional form might be.[20] Unfortunately, the true form of the functional is entirely unknown, to the point that there is no clear understanding about how to improve a functional; the best that can be achieved is an approximation based on trial and error, and chemical intuition, although guidance exists in the form of properties that the functional should have such as the cusp condition when two electrons coincide in the same position.[20]

The simplest form of the exchange correlation functional is based on the local density approximation, a uniform electron gas is defined as a system in which electrons move in an electrically neutral environment, caused by a positively charged background potential.[20] This infinite volume of an infinite number of electrons has the density of a uniform electron gas.[20] For a metallic system, this may not be too poor an assumption, however, this is obviously not so for molecules, where the electron density is concentrated in the bonds. One major advantage of this strategy, however, is that it is the only system for which a functional form for E_{xc} is known.[20]

The exchange correlation functional can be written as

$$E_{xc}^{LDA}[\rho] = \int \rho(r)\epsilon_{xc}(\rho(r))\,dr, \tag{1.127}$$

where ϵ_{xc} is the energy per particle of the uniform electron gas (a function of the density), which is weighted by the probability of finding an electron occupying a certain volume of space, $\rho(r)$.[20] The energy per particle can be split into exchange and correlation components

$$\epsilon_{xc}\left(\rho(r)\right) = \epsilon_x\left(\rho(r)\right) + \epsilon_c\left(\rho(r)\right), \tag{1.128}$$

where

$$\epsilon_x^s = -\frac{3}{4}\sqrt[3]{\frac{3\rho(r)}{\pi}}, \tag{1.129}$$

and is termed the Slater exchange.[20] For ϵ_c, the functional form was derived from a fit to numerical simulations of the uniform electron gas. An example is the correlation functional of Vosko, Wilk and Nusair, which when combined with the Slater exchange functional gives the standard LDA method, SVWN.[20] The form of ϵ_c^{VWN} is not given because it is fairly complex. Although the LDA method makes a drastic assumption which clearly does not hold for molecules, the LDA method gives better results than HF, although it significantly over-binds molecules.[20]

The next step to improving the functional form can be made using the generalised gradient approximation, or GGA, where the exchange correlation functional depends not only on the charge density but also on the gradient of the density, $\nabla\rho(r)$.[20] This allows the charge density to vary and thus better represent the electron density in a molecular environment. GGA functionals are often described as non-local, in contrast to the local density approximation. While they include the effects of a non-constant density, this is calculated by an expansion of the local wavefunction. A better description of these functionals is therefore gradient corrected.[20]

GGA functionals can be written as

$$E_{xc}^{GGA}\left[\rho_\alpha, \rho_\beta\right] = \int f\left(\rho_\alpha, \rho_\beta, \nabla\rho_\alpha, \nabla\rho_\beta\right) dr, \tag{1.130}$$

where ρ_α and ρ_β are the densities of the up and down spin electrons respectively.[20] E_{xc}^{GGA} can then be divided into exchange and correlation contributions

$$E_{xc}^{GGA} = E_x^{GGA} + E_c^{GGA}, \tag{1.131}$$

and E_x^{GGA} is then written[20]

$$E_x^{GGA} = E_x^{LDA} - \sum_\sigma \int f\left(s_\sigma\right) \rho_\sigma^{4/3}(r) dr. \tag{1.132}$$

The argument of f, s_σ is the reduced density gradient for spin σ,

$$s_\sigma(r) = \frac{|\nabla \rho_\sigma(r)|}{\rho_\sigma^{4/3}(r)}, \tag{1.133}$$

and can be thought of as an inhomogeneity parameter, which takes into account the different regions and variations of density found in a molecular environment; for the homogeneous electron gas s_σ=0.[20]

Two classes of functional form exist for f. The first of these is parameterised, as in the case of the B88 functional of Becke

$$f^B = \frac{\beta s_\sigma^2}{1 + 6\beta s_\sigma \sinh^{-1} s_\sigma}, \tag{1.134}$$

where β is a parameter which is optimised on rare gas atoms, and has the value 0.0042.[20]

The second class of f are formed on a rational function expansion of s_σ. Examples are the P86 and PBE functionals. They do not contain any semi-empirical parameters. PBE can be written as

$$f^{PBE} = 1 + \kappa - \frac{\kappa}{4\mu s_\sigma^2/\kappa}, \tag{1.135}$$

where μ=0.21951 and κ=0.804.[21]

For the correlation functionals, both semi-empirically fitted examples exist, such as P86, and LYP, as do non-parameterised forms, such as the PW91 and PBE correlation functionals.[20] The functional forms of the correlation functionals are even more complex than their exchange counterparts, and thus are not given in this treatment, however, they are often based on a correction term to the LDA correlation functional. One exception to this is the popular LYP functional of Lee, Yang and Parr.[20] This functional is not based on the uniform electron gas, but on a fit to accurate *ab initio* calculations on helium atoms.[20] One problem with GGA functionals is that their form is motivated by achieving chemically sensible results, not from a comprehension of the physics of the system.[20]

The third major class of density functionals to be considered here are the hybrid density functionals. In the LDA and GGA functionals mentioned so far, the exchange and correlation contributions are approximated by a functional form. However, it is possible to calculate the exact exchange energy of a Slater determinant, so why not just use a functional form to calculate the correlation component? The reason why this methodology is not adopted is because the exchange and correlation components of exchange-correlation functionals are both calculated using a local mathematical approximation, gradient corrected or otherwise. This means that there is some complementary error cancellation which does not occur if exact exchange is used, because this has a non-local formulation.[20]

One method of circumventing this problem is to augment the density-functional exchange with some exact exchange. An example of this is given by the B3PW91 functional of Becke

$$E_{xc}^{B3PW91} = E_{xc}^{LSD} + a\left(E_{xc}^{\lambda=0} - E_{x}^{LSD}\right) + bE_{x}^{B88} + cE_{c}^{PW91}, \qquad (1.136)$$

where E_{xc}^{LSD} is the local density exchange-correlation functional, a is a parameter which allows the mixing of a proportion of exact exchange ($E_{xc}^{\lambda=0}$), b adds some gradient corrected exchange and c, a proportion of the gradient corrected correlation energy.[20] The three parameters are semi-empirically determined from atomisation data, and have values a=0.20, b=0.72 and c=0.81.[20] In fact, this method calculates the energies of molecules in the G2 set of atomisation energies to within 8-12 kJmol^{-1}.[20,f]

An adjustment to this functional was made by Stephens *et al.*,[22] such that the GGA correlation is provided by LYP rather than PW91.[20] Thus

$$E_{xc}^{B3LYP} = (1-a)E_{x}^{LSD} + aE_{xc}^{\lambda=0} + bE_{x}^{B88} + cE_{c}^{LYP} + (1-c)E_{c}^{LSD}, \qquad (1.137)$$

where the values of the parameters are chosen to match those determined for B3PW91.[20] B3LYP should probably be described as the most popular hybrid functional developed. Although the introduction of these parameters has added a semi-empirical nature to the functional, it has allowed energies of the desired chemical accuracy of about 8 kJmol^{-1} to be calculated, provided that one is working within the scope of the data set for which the parameters are determined. In fact, as will be evident from this study, and from previous studies,[23,24] B3LYP returns sensible results for species outside the scope of its parameterisation, such that it is often thought of as being universally applicable.

For a more detailed treatment of density functional theory the reader is directed to The Chemist's Guide to Density Functional Theory.[20]

1.4.2 Time-dependent DFT and the calculation of excitation energies

The calculation of excitation energies is essential for explaining many experimental phenomena such as those observed in photo-electron spectroscopy. The calculation of excitation energies with DFT has been achieved over the years using a number of different techniques, with varying success. Time-dependent

[f]The G2 set of molecules are a set of 50 species for which accurate experimental atomic data are available. For this reason they are often used for comparing the quality of theoretical techniques.[20]

DFT (TD-DFT) represents the current state-of-the-art method for calculating excitation energies.[25]

One way in which excitation energies can be approximated is by taking the energy differences between the Kohn-Sham orbital eigenvalues (or *pseudo*-orbital energies), however, because neither the orbitals, nor the eigenvalues have any real meaning, and because they are all calculated from the ground-state density, this method is not rigorously correct.[25] The only correct interpretation of the Kohn-Sham eigenvalues is for that of the HOMO, which gives the negative of the ionisation potential.[26]

Although normal DFT allows one to calculate the ground-state properties of a system from its ground-state density, with the introduction of molecular symmetry this can be achieved for the ground-state of each symmetry type. A comparison of the total energies thus indicates the first excitation energy of each symmetry species.[25] This method is obviously only of limited usefulness because of the number of excitations that can be calculated is severely restricted, and no guarantee can be made to the energy ordering of the excitations. In fact, if the lowest energy excitation is to a state of the same symmetry as the first excited state, then it may not even be possible to calculate the lowest energy excitation.

The calculation of excitation energies with TD-DFT may be achieved using a formulation of the theory based on linear-response theory. For calculations on systems involving strong LASER fields, it is necessary to use the more rigorous formulation of TD-DFT which does not depend on a perturbative approach,[25] however, this will not be discussed any further detail here.

The calculation of excitation energies using TD-DFT relies on the linear response of the system when an oscillating field is applied to it; when the frequency of the field matches the difference in energy between two states of the system resonance occurs.[27] The excitation energies can therefore be extracted from the susceptibility calculated for the ground-state density of the system calculated with the linear response theory. The oscillating linear electric field of frequency ω is written as

$$E = r\cos(\omega t), \tag{1.138}$$

and the frequency dependent polarisability

$$\langle\alpha\rangle_\omega = \sum_{i\neq 0}^{states} \frac{|\langle\Psi_0|t|\Psi_i\rangle|}{\omega - (E_i - E_0)}. \tag{1.139}$$

When the frequency ω is equal to the energy separation between two states, the denominator of equation 1.139 becomes zero, and this causes a pole in the frequency dependent polarisability. By calculating the position of these poles

using a propagator method, it is possible to calculate the electronic excitation energies without calculating the excited state wavefunctions.[4] In TD-DFT the Hamiltonian is written using various exchange integrals and KS orbital energies,[4] however the formulation is very complex and will not be given here.

If regular exchange-correlation functionals are used such as BPW91 or B3LYP, then care needs to be taken that only low energy excitation energies are calculated; high energy excitations may be inaccurate because of the poor quality of the high energy virtual KS orbitals.[4] This deficiency has been addressed by the development of exchange correlation potentials which have a correct asymptotic nature, such that they approach $-1/r$ as $r \rightarrow \infty$.[28] Two such functionals of this type are LB94[29] and SAOP.[30]

Casida *et al.* have suggested two rules of thumb for use when performing TD-DFT calculations to improve reliability. Firstly, the excitation energies that are being calculated should not exceed the ionisation potential for the molecule, as given by $-\epsilon_{HOMO}$. The second is that electron promotions should not take place to KS orbitals with positive eigenvalues.[31,32] Casida *et al.* also point out that because TD-DFT response theories are based on the ground state KS orbitals, it is possible to get multiconfigurational descriptions of the excitations arising, where an excitation comprises a mixture of orbital to orbital transitions.[33]

A study of the electronic excitation spectra of RuO_4 and OsO_4 shows mean absolute errors (MAEs) of 0.23 eV and 0.24 eV respectively for the first three excitations calculated with LB94 when compared with experiment.[34] This shows an improvement over the use of revPBE which gives an MAE over the first three bands of 0.47 eV for RuO_4, although the results for OsO_4 are similar to LB94.[34]

1.5 Basis Sets

The use of basis sets is central to the methods in which the majority of *ab initio* and density functional calculations are performed. The expansion of the wavefunction of a system in terms of a set of functions (the basis set) introduces an approximation into the calculation, because the basis set is not infinite.[2] The scaling of at least N^4 for *ab initio* methods and DFT methods (when using an atomic basis) means that a balance needs to be made between the size of the basis set and the difficulty of the calculation to be performed.[2] In one extreme the results will be extremely poor, while in the other, the calculation will be completely intractable.

Figure 1.4: A 1s orbital represented as a STO (black line) and several GTOs (red lines).

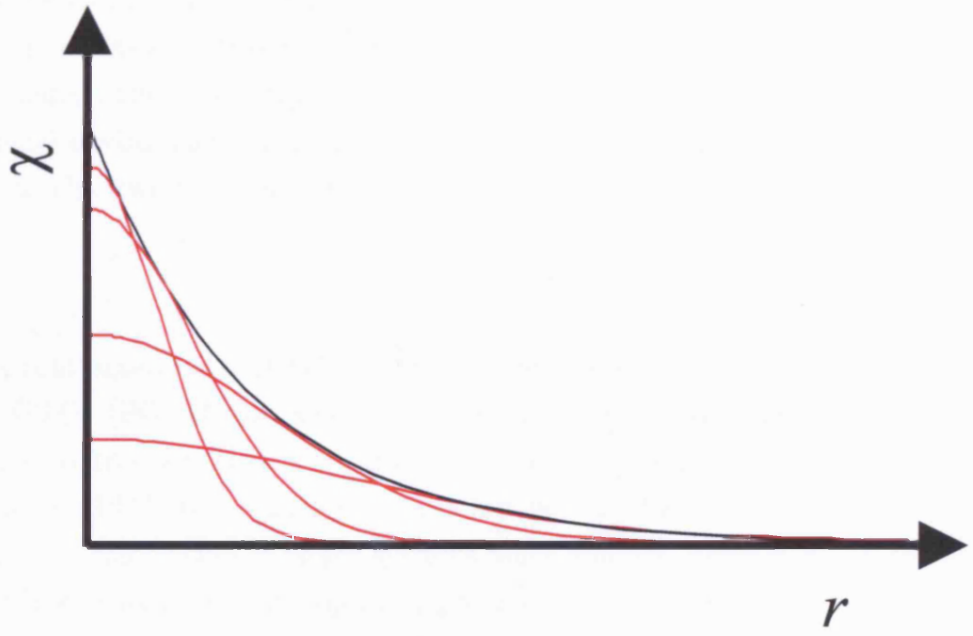

There are two types of commonly used basis functions for molecular calculations, the Slater type orbital (STO, equation 1.140) and the Gaussian type orbital (GTO, equation 1.141)

$$\chi_{\zeta,n,l,m}(r,\theta,\phi) = NY_{l,m}(\theta,\phi)r^{n-1}e^{-\zeta r} \tag{1.140}$$

$$\chi_{\zeta,n,l,m}(r,\theta,\phi) = NY_{l,m}(\theta,\phi)r^{2n-2-l}e^{-\zeta r^2} \tag{1.141}$$

where ζ is the exponent of the exponential function, n, l and m are the quantum numbers of the orbital being represented, N is a normalisation constant, Y are spherical harmonics, and θ, ϕ and r are the coordinates defining a point in space.[2]

Atomic orbitals have a cusp at the nuclei, where the gradient of the function becomes discontinuous. The STO reproduces this cusp like behaviour, while the GTO gives a continuous function at the nuclei, and also falls off too rapidly with increasing r due to the r^2 dependence of the exponential.[2] In order to better mimic atomic orbitals it is necessary to use approximately three times as many GTOs as STOs.[2] Figure 1.4 shows an atomic 1s STO and its representation using three GTOs.

However, GTOs have one major advantage in that they can be integrated analytically,[2] while STOs require numerical integration to solve the two electron integrals. The result of this is that GTOs are the most commonly used type of

basis function, the principal exception being the ADF package, which uses STOs. Neither GTOs or STOs have radial nodes so it is necessary to build these into the orbitals by using several GTOs or STOs.

Core orbitals contribute significantly toward the electronic energy of a system. Fortunately, the core orbitals for a particular atom are fairly independent of its chemical environment, and so the functions representing a core electron can be contracted down to a single function thus[2]

$$\chi^{CGTO} = \sum_{n=1}^{i} a_n \chi_n^{PGTO}. \tag{1.142}$$

A contracted-GTO (CGTO) has the contraction coefficients (a) of the i primitive-GTOs (PGTO) optimised, often in an atomic environment,[1] and are then fixed. Contraction always increases the energy of a system relative to the use of entirely PGTOs, because the basis has become less flexible, however, it also makes the calculation of larger systems much simpler, because it can reduce the number of variables to be optimised.[2] Two types of contraction scheme exist. The older type is termed *segmented contraction*, and this means that each PGTO is only present in one, or at most two adjacent CGTOs. The second, termed *general contraction* involves all of the PGTOs being present in all of the CGTOs of the basis, provided that they are of the correct angular momentum type.[2]

A minimal basis has a single contracted basis function per occupied orbital per atom of the neutral species, thus H and He will both have a single 1s function, a CGTO. For Li-Ne, it is conventional to have a 1s, 2s and 2p function for each atom.[2] A double-ζ (DZ) basis set has two basis functions per orbital per atom. This immediately gives the basis set a lot more flexibility.[2] An example of the requirement for this flexibility would be in the molecule ethyne (C_2H_2). Each carbon atom forms a σ bond with a hydrogen, and a π bond with the other carbon. Both types of bonding involve the 2p orbitals of carbon, however the p-orbitals involved in the σ and those involved in the π bond should have different radial extensions. A double-ζ basis (DZ) basis has two p-functions with different exponents to model this behaviour, while a minimal, or single-ζ basis (SZ) requires both of these p-orbitals to have the same exponent.[2]

As already mentioned, the core electrons behave essentially constantly for an atom in a molecule. Thus, it should not be necessary to represent them with as many basis functions as are required for the chemically important valence electrons.[2] A valence-DZ (VDZ) basis represents the core electrons with a single CGTO, and the valence orbitals with a pair of functions. Similarly, a VTZ basis uses three functions to represent the valence electrons.[2]

In order to represent polarised electron density, it is necessary to add functions of higher angular momentum than the highest angular momentum valence electron of the system.[2] These are termed *polarisation functions.* If a hydrogen atom has only s-functions to represent it, then it is not possible to have a different behaviour of the electron perpendicular to the bond compared with that along the bonding direction, which will probably be the case; thus, a set of p-functions is added.[2] Similarly, main group elements are polarised with a set of d-functions, and transition metals with a set of f-functions, although to polarise a system correctly it might be necessary to add even higher angular momentum polarisation functions.[2]

Polarisation also has a second critical rôle to play in describing electron correlation.[2] Two methods can be envisaged for this, termed in-out and angular correlation. The first involves the two electrons being at slightly different distances from the nucleus. Thus two functions are needed with different exponents to describe this, and so a DZ basis will give more flexibility compared with a SZ basis.[2] The second involves the two electrons being on the opposite sides of the nucleus. Thus a p-function is necessary to augment an s-function in order to describe this behaviour. Such functions are more correctly termed *correlation functions.*[2] These higher angular momentum functions are important for methods which include electron correlation but are not needed in HF or orbital based DFT calculations.[2] The exponents of basis functions are usually determined by a calculation on an atom with either HF, or a correlated method.[2] This procedure involves optimising the exponents variationally in order to minimise the energy.

Diffuse functions can also be added to a basis set. Usually, a basis function with a small exponent is added for each electron with a differing angular momentum. These are especially useful when performing calculations on anionic species, with diffuse outer electrons, since they improve the long range fall off of the basis set, and correct for the less accurate r^2 dependence of a GTO.[2] Care needs to be taken with large basis sets that include diffuse functions. Since these represent regions of space at significant distances from a nucleus, it is possible that the same region of space will also be represented by a basis function on a neighbouring nucleus.[2] This means that the basis set is larger than it needs to be, and in the extreme can cause the basis set to be nearly linearly dependent. This means that the overlap integral between the two basis functions that represent the same region of space will be close to unity. Part of the technique for solving the HF equations is to find the inverse of the S matrix, and since this becomes poorly defined when there are off-diagonal elements which have values close to

one, it can make the solutions to the HF equations inaccurate, or unobtainable.

Different parts of a molecule can be described by different basis sets, with the region thought to explain most of the chemistry represented with a larger basis. However, care needs to be taken that the calculation is not biased by this choice of partitioning. For instance, if a homonuclear diatomic is represented by a SZ basis at one end an a DZ at the other, then a dipole moment will be predicted; the end with the more basis functions per electron will attract the most electron density since it is better represented.[2] This problem gets less significant with larger basis sets because they have many more functions per electron, so the relative increase in the number of functions is smaller.[2]

1.5.1 Pople style basis sets

These basis sets were designed by Pople and co-workers. Two types will be considered. STO-nG basis sets are a minimal basis where each orbital is represented by a single STO to which is fitted a number of PGTOs which are then contracted to a single CGTO. It is not usually necessary to use more than 3 PGTOs since no real improvement is observed.[2]

A variety of basis sets exist of the form a-bcdG(x,y). They are split valence bases where the exponents of the s and p-functions are set to be the same, thus limiting their flexibility while reducing their computational cost.[2] The number of PGTOs contracted to a single CGTO in order to represent the core electrons is given by a. The number of PGTOs representing the valence electrons and their contraction scheme is indicated by b, c and d. For example a 6-31G basis uses 3 PGTOs contracted to a single CGTO and a further PGTO to represent each valence electron. It is a double split valence basis. A 6-311G basis uses an additional PGTO to represent the valence electrons.

Usually diffuse functions are only added for heavy atoms (indicated by a + before the G) however, diffuse functions can also be added for hydrogens, indicated by ++. Polarisation functions for the heavy atoms are represented by x, while y represents the polarisation functions for hydrogen, for instance 6-311++G(2df,2pd) indicates diffuse functions on all atoms, 2d and 1f polarisation functions on heavy atoms, and 2p and a d polarisation function on each hydrogen.

1.5.2 Correlation-consistent (cc) basis sets

These are basis sets designed to recover correlation in a systematic, consistent way from the smallest, cc-pVDZ[g] to the largest, cc-pV6Z. They are based on a general contraction scheme.[2] The energy correction made by the first set of f-polarisation functions is similar to that offered by the second set of d-functions, while the first set of g-functions make a similar contribution to the second set of f-functions and so on. Therefore, in order to make a consistent improvement to the accuracy of the basis set, when adding a new type of higher angular momentum functions, one should also add another set of each type of the lower angular momentum functions.[2] Furthermore, so that the error associated with an incomplete polarisation space does not get smaller than that associated with the occupied basis functions, when a new set of polarisation functions is added an extra ζ-function is added to the valence basis. Thus the cc-pVDZ basis has a d-polarisation function. The cc-pVTZ has 2d and an f, while the cc-pVQZ has 3d, 2f and a g-function.[2] The exponents of these polarisation functions are optimised by using CISD calculations on atomic systems.[2] Although this results in the bases becoming very large very quickly, with each step nearly doubling the number of functions, it ensures that the correlation energy is consistently recovered as one improves the basis set. For the Pople style basis sets this is not the case, because some are under, or over polarised by comparison with the cc bases, and also because the Pople bases are not constructed from a consistent set of PGTOs.[2] Diffuse functions can also be added to cc bases, usually one for each type of angular momentum function in the valence space.[2]

1.5.3 Ahlrichs-type basis sets

These basis sets, designed by Ahlrichs and co-workers are available in qualities from SVP (split valence polarised) to QZV (quadruple zeta valence). It should be noted that the number of basis functions of the s and p type are not immediately obvious from the label, the SVP having 3s2p, the TZV, 5s3p and the QZP 7s4p functions. The exponents and contraction coefficients are optimised variationally using HF, while the polarisation functions are added from the cc-pVxZ basis of equivalent quality.[2]

[g]Lower case letters have been used to avoid confusion with coupled-cluster theory which uses the acronym CC.

1.6 The Inclusion of Relativistic Effects

One of the major advancements in science at the beginning of the 20th century was made by Einstein in the development of the theory of special relativity in 1905. According to the theory of relativity, all frames of reference that travel with a constant velocity are equivalent, and thus the same physical laws should apply in each reference frame; in particular, one physical law that should apply to all of these frames is the speed of light, c, which is constant irrespective of the speed of the observer.[2] In order to describe the different frames of reference with the same physical laws, it is necessary to use four coordinates, three spatial, and one time coordinate.[2] One consequence of the constant speed of light, c, is that the mass of a particle increases with its speed v, such that

$$m = m_0 \left(\frac{1}{\sqrt{1 - \frac{v^2}{c^2}}} \right), \tag{1.143}$$

where m_0 is the rest mass of the particle.

It is clear that the effect is negligible except for particles that travel with a speed which is a good proportion of the speed of light. Unfortunately, the speed of an electron in a 1s orbital of an atom is equal to the nuclear charge Z in atomic units, while the speed of light in the same units is approximately 137.[2] The increase in the mass of the 1s electrons causes the contraction of the orbitals that they occupy, and because of the orthogonality of the orbitals, the s-orbitals of higher principal quantum shells also contract. The contraction of the s-shells increases the screening of the nuclear charge from the higher angular momentum orbitals, which penetrate the core less, and this results in the d and f-orbitals becoming less contracted.[2]

As well as altering the radial expansion of the orbitals of the system, the relativistic mass increase also alters the total energy. This is not significant for the first three rows of the periodic table, however, for the lanthanides, actinides and the third transition metal series, the relativistic correction to the energy is larger than the correlation energy,[2] and clearly cannot be ignored if accurate results are to be obtained.

The requirement that the same physical laws apply in all reference frames, or that the physical laws are invariant to a change of the coordinate system is not satisfied by the Schrödinger equation. Furthermore, the concept of spin is only introduced in an *ad hoc* way in order to produce a wavefunction that satisfies the Pauli principle, and thus phenomena which depend on the spin explicitly, for

instance spin-orbit coupling cannot be described.[2]

The formulation of a substitute for the Schrödinger equation that meets the requirement for relativistic invariance, has a usable mathematical form, is variationally stable and can be used in the available computational codes without the requirement to entirely recode them results in a considerable complexity that will not be discussed here, however, a useful treatment is given in the following source.[1] One way in which the relativistic Hamiltonian can be made to behave in a variationally stable way in regions that lie close to the nucleus is to make the regular approximation; this involves an expansion of the problematic term as a series, which is terminated at a specific point.[1] It is this termination that results in variationally stabilising the problem.[1] The method that is used in the present study involves terminating the expansion at zeroth order, resulting in the ZORA Hamiltonian which can be written as

$$\left[\frac{1}{2m}(\sigma \cdot p)\left(1 - \frac{V}{2mc^2}\right)^{-1}(\sigma \cdot p) + V\right]\psi^{ZORA}(r) = E\psi^{ZORA}(r), \qquad (1.144)$$

where p in the momentum of the electron, V its potential energy and σ are the Pauli spin matrices that incorporate electron spin into the equation.[1]

When performing calculations that make the ZORA to the relativistic wavefunction is necessary to use a basis set that is formulated to give reliable results. The Amsterdam Density Functional (ADF) package includes basis sets for this purpose which have functions with adapted core behaviour which are designed for use with the ZORA Hamiltonian.[28] These basis sets are available in a variety of qualities from SZ to QZ4P depending upon the atom considered.

1.6.1 Effective core potentials (ECPs)

Another problem caused by molecules with heavy atoms, for instance the lanthanides and actinides is that all electron calculations become expensive due to the large number of basis functions that are required to treat the core electrons, despite these having little influence on the chemistry.[2] It is necessary to include these electrons in the calculation because the valence electrons will only behave correctly if they experience both the correct nuclear charge and combined behaviour of the core electrons.[2]

There are two approaches that can be used to treat these core electrons. The first is to have a frozen core. The core electrons are optimised for the atom and then are assumed to be unaltered in a molecular environment.[2] This has the advantage that the valence electrons still interact with the core electrons. The

second approach is by introducing an ECP to model the core electrons. This method offers significant saving of computational effort for heavy atoms.[2] The construction of an ECP involves performing an initial high accuracy calculation using a HF, Dirac-HF or DFT calculation on an atom, with a regular basis set. The valence orbitals are then replaced by pseudo-orbitals, which have the correct nodal structure in the outer region, but lack the inner core nodal structure.[2] The core orbitals are replaced by a set of potentials (which can be polynomial or Gaussian functions), usually one for each angular momentum value. These potentials are then optimised such that the pseudo-orbitals best match the true valence orbitals in terms of functional form.[2]

One function of the radial nodes in orbitals is to ensure that they are orthogonal to one another. Since a large number of electrons have been removed from the system, and replaced by the ECP which mimics their *en masse* behaviour to the outer valence region, it is no longer required for the valence orbitals to be orthogonal to as many orbitals and thus not so many radial nodes are required. The introduction of ECPs has a second advantage. In heavy atoms, the core electrons can attain speeds close to the speed of light. Thus they begin to behave relativistically, and need to be treated so. The ECP can be designed to incorporate this, such that the relativistic nature of the core electrons can be implicitly included into the treatment of a molecule using a non-relativistic method,[2] for instance DFT. An ECP needs to be used with one of the basis sets for which it was designed.

1.7 The Optimisation of Molecular Geometries

The optimisation of molecular geometries in order to find minimum energy structures and transition states plays a major rôle in this thesis. The following section gives a brief overview of the methods used.

The potential energy surfaces of a molecule may have many stationary points, and many local minima of which the most energetically stable is termed the global minimum. Only optimisation to minima and transition states have been used in these studies. At a stationary point, the gradient of the energy, the force, is zero in every direction of the multi-dimensional molecular surface. For a minimum, the curvature of the surface (the second derivative) is positive in each direction. For a transition state (a first order saddle point), however, the second derivative matrix (or Hessian) will have a negative value in one specific direction, that which corresponds to the reaction coordinate. The presence of this negative

curvature in one direction is one reason why optimisation to transition states is more methodologically challenging than optimisation to a minimum.[2]

The square-root of the curvature of the surface can be used to calculate the vibrational frequencies of the molecule. A frequency analysis for a minimum will give $3N$-6 ($3N$-5 for linear species) normal vibrational modes, which will all be real, where N is the number of atoms in the molecule. A transition state will have a negative curvature in one direction, which will manifest itself as a single imaginary mode among the real modes, due to taking the square-root of a negative number. Thus frequency analysis may be used to identify the nature of a stationary point.

The optimisation of a structure to a minimum requires that the energy is minimised along each coordinate of the surface. The steepest descent method entails defining a vector in which direction the potential energy surface (PES) is the steepest.[2] Steps are taken in the negative direction of this vector, thus reducing the energy, until the energy again begins to rise. At the lowest energy point a new steepest descent direction is determined, and the process is repeated. Since the energy was minimised in the direction of the previous steepest descent vector, no further energy minimisation is possible in this direction, and so the new steepest descent vector is orthogonal to the previous one. The energy is successively lowered, although each step slightly degrades the effect of the previous one. This method ensures convergence to a local minimum, although the minimum will never actually be reached, just approached increasingly more slowly.[2]

For optimisation to a transition state, the situation is far less straightforward. This is because it is not desired to simply optimise the structure in the opposite direction to the steepest descent,[35] since this will eventually just locate a local maximum on the surface, where the curvature is negative in all directions. What is required is to find a stationary point which has a minimum in all directions except one.[35] The steepest descent method is only useful for optimising to a minimum, although a method termed the quadratic steepest descent method can be used for locating a transition state.[35] This involves calculating a quadratic image potential by mirroring the PES at a point close to the transition state. In this image potential, the transition state behaves as a minimum, such that the structure may be optimised to a transition state by using the steepest descent method.[35]

The Gaussian package uses the Berny algorithm, of Schlegel *et al.*[36,37] to optimise structures to both minima and transition states. This method uses a series of steps calculated from a knowledge of the Hessian, and a series of line

searches and polynomial fits to interpolate a new structure between two calculated points. The rational function optimisation (RFO) approach is used to ensure that a specific step does not exceed the trust radius of the calculation, i.e. that the calculated step is not too large such that it moves the next point an unreasonably large distance from the previous point.[38] The MOLPRO package uses this RFO approach for optimising to minima, and the quadratic steepest descent method for optimising to transition states. The ADF package uses a quasi-Newton method for optimisation of geometries.[39] This involves the expansion of the true function about a current point using the gradient of the surface.[2,28]

By default, these methods usually generate an initial Hessian using a valence force field type of approximation, and this Hessian is then updated using the first derivative information during the course of the optimisation. For optimisation to a transition state, this model Hessian will not be an acceptable initial guess, since these optimisations are very sensitive to the curvature of the surface.[38] The options available for a situation are to either calculate the initial Hessian using analytical second derivatives if they are available, e.g. for MP2, HF or DFT, or to calculate it numerically using a series of small displacements of the molecular framework.[38] This method can be very expensive for methods such as CCSD(T) and an alternative is to import a Hessian calculated analytically using a lower level technique.[38] Although this is an approximation it should at least have the correct number of negative eigenvalues necessary to guide the calculation to the transition state, and will be updated using the first derivatives at each optimised point, such that as the optimised geometry is approached the Hessian improves.

The Utilisation of the Theory in the Projects Undertaken

The following three chapters (2, 3 and 4) contain separate studies drawing on the methods that have been discussed in chapter 1.

Chapter 2 is a study of the fragmentation pathways by which the dication BCl_3^{2+} may decompose. This study employs HF, MP and CC theories, which have been used to characterise the potential energy surfaces using geometry optimisation and frequency analysis. The $\mathscr{T}_1$ diagnostic has been used to quantify the multiconfigurational nature of the CC wavefunctions and to assess the applicability of single reference methods. A further investigation of the multiconfiguration nature of the system has been achieved by a partial re-characterisation of the system using MCSCF and MRCI.

Chapter 3 considers the species ferrocene and iron pentacarbonyl, both of which are well known to present problems for poorly correlated methods such as HF theory. The structures of these species have been determined by using HF, MP, CC and DFT. The multiconfigurational character of the CC wavefunction has been assessed using the $\mathscr{T}_1$ diagnostic. Calculations using CC theory but from a KS reference have been performed, along with MCSCF and MRCI (for iron pentacarbonyl only) to demonstrate that neither system is significantly multiconfigurational.

Chapter 4 is a study of the electronic excitations of thorocene, protactinocene and their methyl substituted derivatives using TD-DFT at optimised geometries obtained using DFT. This study considers the effects of scalar relativistic effects using the ZORA Hamiltonian together with ZORA basis sets. Assignments of the available experimental spectra are made on the basis of the theoretical results.

Chapter 2

An *ab initio* Study of the Electronic Structure of BCl_3^{2+} and its Decomposition Pathways

Contents

2.1 Introduction

The study of doubly charged molecular cations (dications) has become increasingly popular since the early 1980s,[40-43] mainly due to the realisation that dications might be involved in the mechanisms of processes such as the industrial plasma etching of semiconductors.[44-49] Radio frequency (rf) plasmas based on boron trichloride can be used in the etching process of semiconductors based on aluminium and silicon and have generated considerable interest.[48] In this process, BCl_3 is ionised using rf radiation[46] to generate species which decay by a complicated series of reactions to produce a plethora of charged and radical species.[48] Both positive[49] and negative[50,51] ions are present in the plasmas, and neutral BCl is thought to be a particularly important etchant.[46] In order to gain a better understanding of how to adjust the plasma to give the best etching result (a

goal of great commercial importance) it is necessary to model the plasma process.[45] This, however, requires data on the chemical and physical properties of the species present in the plasma and unfortunately for many of these, reliable experimental data are not available.[45] For many species "...experimental studies are difficult, and only limited experimental results are available.",[48] and therefore several research groups have focused on characterising computationally molecules and ions thought to be present in the plasma process.[45,46,48] The resulting data can then be used to augment and verify the experimental data for use in the plasma modelling process,[48] or indeed to rationalise and correct the discrepancies between experimental data obtained by different groups.[46]

The aim of this work is to characterise the dication of BCl_3, and to explore its decomposition pathways and energetics using *ab initio* computational techniques. The data obtained are used to augment experimental studies previously carried out in this department.[52] This computational study has been published in an abridged form in the journal Physical Chemistry Chemical Physics.[53]

2.2 Dications, and systems related to BCl_3^{2+}

2.2.1 General Properties of Molecular Dications

Molecular dications have been described as "...highly energy-rich and reactive metastable species..."[41] and generally have few electronic states with long lifetimes.[42] Indeed most electronic states of dications are purely repulsive,[42] and if the species is generated in such a state, the molecule simply dissociates to products immediately, since there is no activation barrier to overcome. It is, however, generally believed that many small dications have at least one electronic state which is metastable with respect to dissociation into products, either by a neutral loss reaction, or a charge separation reaction.[41,42] Usually these species are experimentally studied using mass spectrometric techniques, and must therefore have a lifetime of at least the microsecond order.[54]

The existence of a metastable state arises from an activation barrier against separation into products being present in the potential surface of the dication.[42] The origin of this potential barrier is not unambiguous, however there are two theories that have been proffered. The first is that it is the product of an avoided crossing between the repulsive surface of two monocations and the attractive surface of a dication and a neutral species.[54] However a somewhat simpler approach has been postulated by O'Neil *et al.*; that the barrier can be modeled by adding a Coulombic repulsion to the normal bonding potential of the neutral species.[54]

Figure 2.1: Diagrammatic representation of decomposition by charge separation (a) and neutral loss (b) processes.

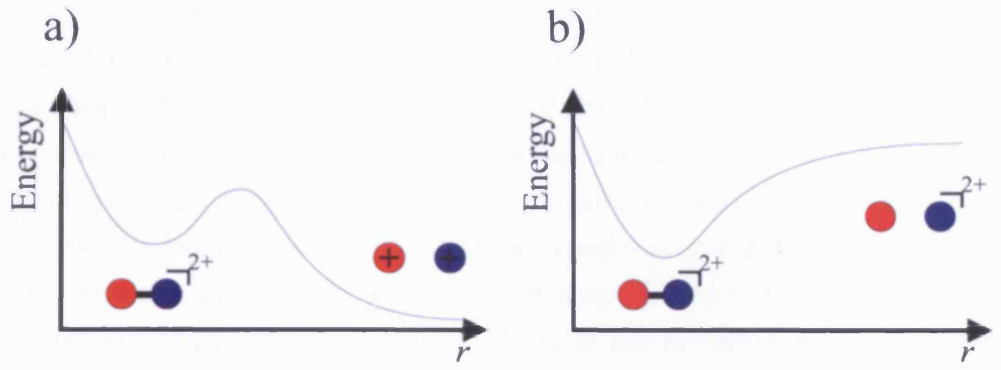

However, this theory has been shown to be inaccurate for some species.[54] The potential well of a typical metastable state is usually deep enough to contain several vibrational states, thus causing the species to have a significant lifetime.[42] However, if the molecule is in a sufficiently high vibrational state, then tunnelling may occur,[54] and the molecule may dissociate to an asymptote which is lower in energy than the minimum of the potential well (see figure 2.1 a).

Both experimental and computational work is being carried out to try to discover the relative stabilities of various charged species,[45] how they decay to products,[42] the associated energetics, and how they interact with other atoms and molecules.[41] Since the *geometry* of cations cannot be detected by mass spectrometry, this, as well as other molecular properties such as electronic structure, are often studied computationally.[41,49] Such a computational study is the focus of the present project.

2.2.2 Computational studies of related systems

Due to space restrictions, this is by no means a full account of all of the research that has been undertaken in this field. The examples chosen represent previous work that is pertinent to the particular system that I have studied, and the difficulties that I have encountered.

To date there has been very little computational work undertaken and reported in the literature on the dication of BCl_3. By comparison, the monocation has been studied significantly by computational methods such as *ab initio* coupled-cluster methodology, to calculate structures, vibrational modes and ionisation potentials in order to elucidate possible decomposition paths.[48] Heats of

formation have also been calculated by hybrid DFT techniques for the series of species BCl_n^+ (n=1-3).[49]

One particular computational study that was used successfully to correct the discrepancy between various experimental studies and previous computational results was that on BCl by Irikura *et al.*[46] They noted that previous experimental results obtained by various techniques gave different results for the adiabatic ionisation energy; mass spectroscopic results yielded a value between 9.9 and 12 eV,[46] while spectroscopic results from the extrapolation of two members of a Rydberg series gave a value of 9.03 eV.[55] Since these spectroscopic determinations usually produce very accurate results, this 1 eV difference seemed very large.[46] Irikura *et al.* characterised the species by using *ab initio* methodology and calculated the adiabatic ionisation energy to be (9.96±0.04) eV; their conclusion was that Verma had mis-assigned the Rydberg states used for the previous determination.[46]

There has been highlighted a number of problems with different computational methods in the characterisation of certain species; this is particularly apparent with BX_3 cations,[49,56] where X is a halide. Kaltsoyannis and Price noted that *ab initio* techniques find the minimum energy geometries of doublet BF_3^+, and valence iso-electronic species AlF_3^+, CF_3^{2+} and SiF_3^{2+} to be C_{2v}, with a slightly higher lying D_{3h} minimum.[56] The species were then characterised using B3LYP, which also found the two minima, of which the C_{2v} structure was the lower lying, except for BF_3^+, where no C_{2v} minimum could be found.[56] The use of pure DFT techniques also failed to find the C_{2v} minimum.[56]

Bauschlicher and Ricca also encountered this type of anomaly[49] for BF_3^+ and BCl_3^+. These workers noted that previous studies had found BF_3^+ to be C_{2v} and not D_{3h} in geometry,[49] while Baeck and Bartlett found BCl_3^+ to have three minima, two of which were C_{2v} (one with two long bonds, and one with two short bonds), and a D_{3h} structure.[48] The aim of Bauschlicher and Ricca was to clarify this by the use of B3LYP. They started their geometry optimisations from the previously found structures, and noted that they all converged to a D_{3h} structure, for both the chloride and the fluoride cations.[49] They also calculated the vibrational frequencies of the species using DFT, but these were found to be in poor agreement with experimental results.[49] In light of the above inconsistencies, they probed the system further using MP2 calculations.[49] These found a D_{3h} and two C_{2v} minima for both BCl_3^+ and BF_3^+; a geometry with 2 long and 1 short bonds (2L1S) was more stable for the chloride, while the 1L2S was found to be more stable for the fluoride.[49] A CCSD(T) calculation confirmed that a C_{2v} structure is most stable for BF_3^+, but was less conclusive for BCl_3^+; "For BCl_3^+ it

is clearly difficult to definitively determine the structure".[49]

Baeck and Bartlett thought it likely that the true ground state geometry of BCl_3^+ was in fact D_{3h}, and by drawing parallels with the chemistry of NO_3, suggested that including the effect of triple excitations in the coupled-cluster calculations was essential for this D_{3h} structure to be found.[48]

The potential energy surface of a species may be dependent on the computational method used, and it is often not clear why the computational methods give a different description. However it is clear that not all techniques are equally suitable for study of all areas of chemistry,[49] and particularly in cases where different minima lie very close together energetically, as is the case for the BF_3^+ and BCl_3^+ systems.[56]

Pierò-Garcìa and Nebot-Gil used MP2 and QCISD theory to computationally model the reaction of OH with O_3 to produce HO_2 and O_2.[15] When MP2 was used, two transition states were located in close proximity to each other, with an intermediate minimum between them. However, when these structures were re-optimised using QCISD, only one of the transition states could be found. When the extra transition state and minimum were used as initial structure for geometry optimisation, the calculation diverged toward the products.[15] They noted that this behaviour was also observed for the reaction of the iso-electronic NH_2 radical with ozone. It is clear that it will be necessary to consider this failing of MP2 when studying the BCl_3^{2+} system.

It is possible that there may be disagreements between the results obtained from different techniques used to study BCl_3^{2+}, similar to those that have been observed in studies of the monocation.[49,56] This is likely to complicate the computational study of these species. There is an absence of work published in this area which could be partially explained by the lack of experimental data on which a computational study could be based.

2.3 Computational Details

The majority of the calculations were performed with the Gaussian 98[11] and 03[12] codes, using three different basis sets. α is the Pople 6-311G(d) basis, while bases β and γ are the correlation consistent polarised valence triple zeta (cc-pVTZ) and its augmented form (aug-cc-pVTZ) respectively. Møller-Plesset second order perturbation theory (MP2) was employed, together with the more highly correlated coupled-cluster (CC) approach at both the CCSD and CCSD(T) levels. Geometry optimisations were performed at both the MP2/α and CCSD/β levels, and

the energies of the stationary points were refined using CCSD(T)/γ. Both MP2 and CC methods were used in both the restricted and unrestricted forms depending on the multiplicity of the electronic state in question. The closed-shell $\mathscr{T}_1$ diagnostic of Lee and Taylor[10] was calculated for the coupled-cluster wavefunctions at the optimised geometries, to assess the degree of multiconfigurational character in the wavefunction.

MP2 and CCSD frequency analyses were performed at the stationary points found by the geometry optimisations, both to determine the nature of the stationary points, and to calculate the zero-point vibrational energy. Intrinsic Reaction Coordinate (IRC) calculations were used to follow the reaction coordinate from the transition states located at MP2/α to determine the connectivity of the minima on the surface.

Multiconfigurational self consistent field (MCSCF) and multireference configuration interaction (MRCI) calculations were performed on selected structures using the MOLPRO 2006.1 program package.[57] MCSCF geometry optimisations were performed with an active space of 22 electrons in 16 orbitals (22/16). This active space was chosen to reflect the valence atomic orbitals 3s and 3p on chlorine, and 2s and 2p on boron. This calculation also optimised all of the doubly occupied orbitals. In order to reduce the computational expense, the species were all assumed to be planar, such that a C_s point group could be used; this reduced the number of CSFs to approximately 2.25x10^6. Basis set β was used for these calculations. MRCI single point Davidson corrected energies were calculated at the MCSCF stationary points, using the same active space as before, but with a core equivalent to the closed shell orbitals of the MCSCF calculation. Single and double excitations were considered from reference configurations of the MCSCF calculation with a CI coefficient of 0.02 or greater.

2.4 Experimental Observations of the Decay of BCl_3^{2+}

A brief summary of the experimental data obtained by Love and Price using time of flight mass spectroscopy (TOFMS) and ion-ion coincidence techniques[52] is now presented. The most abundant ion observed following the electron impact ionisation of BCl_3 is BCl_2^+, the parent ion BCl_3^+ being less abundant. The BCl_3^{2+} dication is not observed; the only dication detected is BCl_2^{2+}. The other ions detected are BCl^+, B^+, Cl^+, and Cl_2^+ although the peak due to Cl_2^+ is very small.

Figure 2.2: Schematic diagram of the experimentally observed decomposition products, and the fragmentation processes suggested by Love and Price.[52] The purple circles represent boron atoms, while the green circles represent chlorine atoms. The processes D1 and C2 will also produce neutral fragments, however these fragments are not shown since their identity cannot be inferred from the fragmentation scheme. Route C2 is suggested by Love and Price for formation of the $B^+ + Cl^+$ ion pair.[52] Route B3 is deduced from the theoretical treatment of the system by the present study.

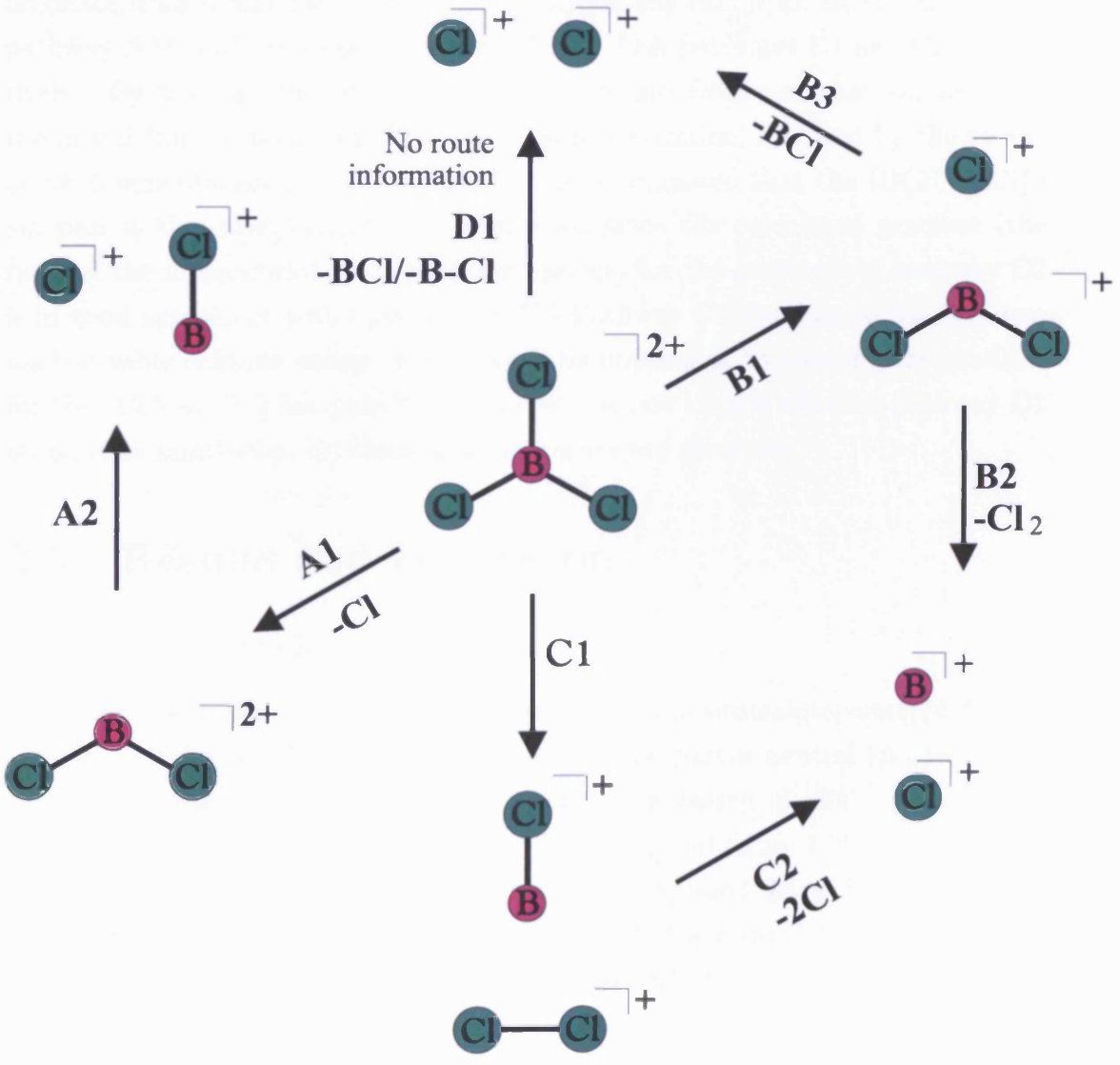

Coincidence studies show that the most abundant pair of ions is (BCl_2^+ + Cl^+), while (B^+ + Cl^+) is the second most abundant pair. Other pairs observed are (Cl^+ + Cl^+), (BCl^+ + Cl^+), and (BCl^+ + Cl_2^+), although only 16 counts are recorded for this last pair, compared with 1300 for the most abundant pair. The experimental results show that there is no dissociation of BCl_3 to form BCl_2,[52] and so the dication BCl_2^{2+} must come from the fragmentation of the parent dication BCl_3^{2+}, by the loss of a chlorine atom[52] (See figure 2.2, pathway A1).

The following fragmentation mechanisms are hypothesised by Love and Price for the production of these ion pairs, based on analysis of the experimental observations. They conclude that (BCl^+ + Cl^+), (BCl_2^+ + Cl^+) and (BCl^+ + Cl_2^+) originate from simple two body fragmentations; the first from BCl_2^{2+} (figure 2.2, pathway A2), and the second two from BCl_3^{2+} (via pathways B1 and C1 respectively). By contrast, the (B^+ + Cl^+) ion pair results from a mechanism involving the initial fragmentation of BCl_3^{2+} by charge separation, followed by the subsequent fragmentation of these products.[52] It is suggested that the (BCl^+ + Cl_2^+) ion pair is the intermediate in this process, since the calculated gradient (the ratio of the momenta of the separating species) for the products of pathway C2 is in good agreement with that observed.[52] Pathway C2 should also result in two unobservable chlorine atoms. It proved to be impossible to measure the gradient for the (Cl^+ + Cl^+) ion pair,[52] and hence it is not known whether pathway D1 is single or multi-step, or which neutral species are produced.

2.5 Results and Discussion

2.5.1 The Singlet Surface

The surface was initially explored, without symmetry constraints, using MP2 with basis set α. The minimum energy geometry of the parent neutral species (BCl_3) was used as the initial guess for a geometry optimisation of $^1BCl_3^{2+}$[a], and minimum energy structure min1 was located (table 2.1 and figure 2.3). The potential energy surface of the singlet dication was then explored using MP2/α starting from structure min1. Each stationary point located was then re-optimised at the CCSD/β level, and CCSD(T)/γ single point calculations were then performed at each CCSD/β stationary point.

Figure 2.3 shows the structure of each stationary point, while tables 2.1 and 2.2 give the energetic and geometric data respectively. Figure 2.4 defines the geo-

[a]Due to the large number of species discussed in this study, for brevity and clarity the multiplicity of the species is indicated throughout by a preceding superscript.

Table 2.1: The energies of the stationary points on the singlet surface with various methods and basis sets. The energies presented for MP2, CCSD and CCSD(T) are offset against the zero-point corrected energy of the D_{3h} neutral structure, calculated using the same method and basis set. $\mathscr{T}_1$ diagnostic results are shown for the CC methods. The numbers in parentheses after the CCSD(T) energies are the absolute differences between corresponding CCSD and CCSD(T) energies. All the MP2 structures are calculated in a C_1 point group, with the electronic symmetry A_1. The symmetry of the CCSD stationary points are given in the table. The CCSD(T) energies are from single points calculated at the same geometry and with the same symmetry as the CCSD optimised structures.

	Møller Plesset / α			Coupled-Cluster / β					Coupled-Cluster / γ	
	MP2 kJ mol^{-1}	ZPE	Imag modes σ / cm^{-1}	CCSD kJ mol^{-1}	ZPE	Imag modes σ / cm^{-1}	$\mathscr{T}_1$ Diagnostic	Electronic Symmetry	CCSD(T) kJ mol^{-1}	$\mathscr{T}_1$ Diagnostic
min1	2761	21.46	-	2884	14.97	-	0.0175	D_{3h} ^{1}A′	2814(70)	0.0173
min2	2744	19.30	-	2747	18.43	-	0.0151	C_{2v} ^{1}A$_1$	2742(5)	0.0150
min3	2777	18.45	-	2750	18.15	-	0.0168	C_s ^{1}A′	2749(1)	0.0168
ts1	2846	15.82	919i	2884	14.10	162i	0.0286	C_{2v} ^{1}A$_1$	2814(70)	0.0288
ts2	2780	17.60	146i	2762	16.94	219i	0.0166	C_s ^{1}A′	2758(4)	0.0166
ts3	2878	16.30	142i	2859	15.82	152i	0.0191	C_s ^{1}A′	2863(4)	0.0194
ts4	3036	13.38	143i	3018	12.70	94i	0.0358	C_s ^{1}A′	2911(107)	0.0356
ts5	3496	10.48	107i	3403	7.06	121i	0.0358	C_{2v} ^{1}A$_1$	3394(9)	0.0378

Figure 2.3: Diagrammatic representation of the structures of the stationary points on the singlet surface. The red circles indicate boron atoms, while the green circles indicate chlorine atoms.

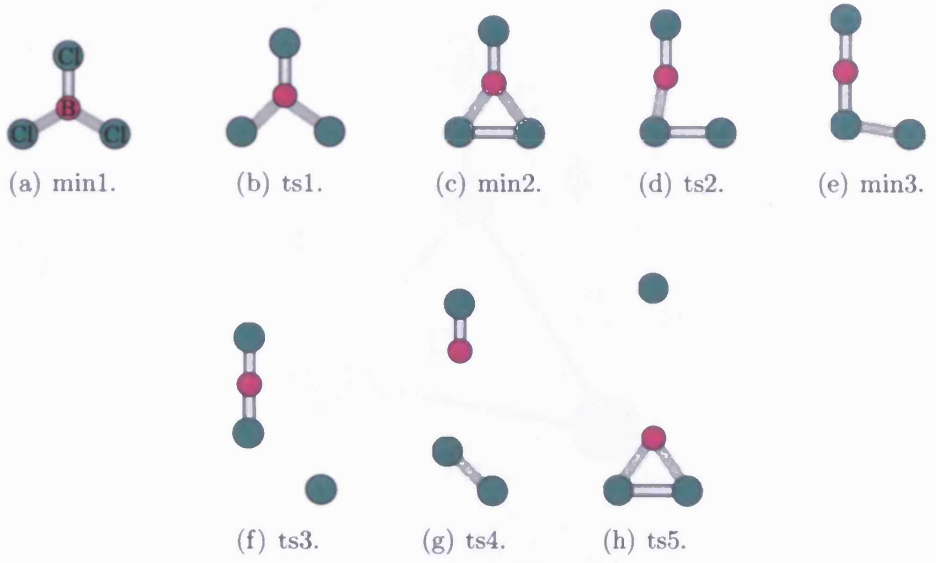

(a) min1. (b) ts1. (c) min2. (d) ts2. (e) min3.

(f) ts3. (g) ts4. (h) ts5.

metric parameters used in table 2.2. Figure 2.5 shows the zero-point corrected energies and connectivities for each stationary point obtained from MP2/α, together with the CCSD(T)/γ energies of each stationary point obtained at CCSD/β, including the zero-point correction at CCSD/β.

Vertical double ionisation from BCl_3 will initially populate the dication singlet surface in the geometric locale of the D_{3h} structure min1, because min1 has a similar geometry to the parent neutral species, which is D_{3h} with a bond length of 1.74 Å. However, structure min1 is found to be relatively unstable compared with the other minima on the singlet surface. By following the potential energy surface over transition state ts1 the singlet dication may form the more stable minimum energy structure min2. Structure min2 is the most stable structure on the singlet surface at both the CC and MP2 levels, perhaps because of the short inter-chlorine distance which is 2.09 Å (compared with 2.01 Å in Cl_2, table 2.7). However, the barrier for conversion of min2 to min3 via ts2 is not large (34 kJ mol^{-1} with MP2/α and 15 kJ mol^{-1} with CCSD(T)/γ), and proceeds by cleavage of one B-Cl bond in the trigonal unit. From min3 the dication may fragment in three ways. The cleavage of the inter-chlorine bond via transition state ts3 results in the ion pair ($^1BCl_2^+$(min41) + $^1Cl^+$) (asymptote 1a), where $^1BCl_2^+$ is formed in its linear ground state, while cleavage of the central B-Cl bond via ts4 allows

Figure 2.4: Definition of the geometric variables used in the tabulated data. The red circles indicate boron atoms, while the green circles indicate chlorine atoms.

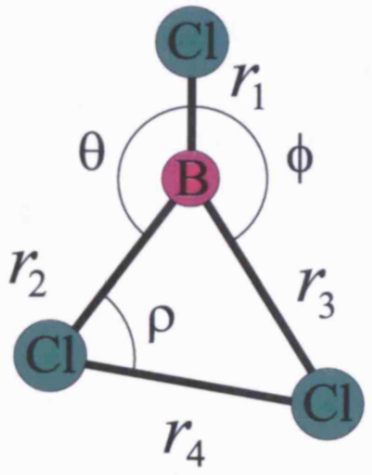

Table 2.2: The structures of the stationary points on the singlet surface of BCl_3^{2+} at MP2/α and CCSD/β. The geometric variables are defined in figure 2.4.

		Bond Lengths / Å				Bond Angles / degrees			
	Structure	r_1	r_2	r_3	r_4	θ	ϕ	ρ	dihedral
MP2/α	min1	1.746	1.746	1.746	-	120.01	120.01	-	180.00
	min2	1.601	1.853	1.851	-	145.21	145.24	-	179.96
	min3	1.574	1.734	-	2.097	177.68	-	99.10	179.99
	ts1	1.647	1.767	1.767	-	130.70	130.63	-	180.00
	ts2	1.578	1.729	-	2.097	173.74	-	81.81	179.48
	ts3	1.591	1.659	-	3.098	178.87	-	128.14	175.51
	ts4	1.594	3.124	-	1.902	173.39	-	124.50	164.46
	ts5	4.290	2.028	2.028	-	149.66	149.66	-	180.00
CCSD/β	min1	1.725	1.725	1.725	-	120.00	120.00	-	180.00
	min2	1.607	1.870	1.870	-	145.99	145.99	-	180.00
	min3	1.579	1.750	-	2.067	178.20	-	100.00	180.00
	ts1	1.704	1.736	1.736	-	123.29	123.29	-	180.00
	ts2	1.589	1.753	-	2.084	166.82	-	73.64	180.00
	ts3	1.597	1.666	-	3.075	177.45	-	125.37	180.00
	ts4	1.591	3.474	-	1.900	175.27	-	124.42	180.00
	ts5	3.878	2.083	2.083	-	150.78	150.78	-	180.00

Figure 2.5: Potential energy surface for decomposition of $^1BCl_3^{2+}$. The red curves indicates stationary points calculated at MP2/α including zero-point corrections, while the black curves indicate CCSD(T)/γ single point energies calculated at the CCSD/β optimised stationary points, corrected with CCSD/β zero-point energies. The curves connecting the stationary points are schematic. The energies on the surface are offset against the zero-point corrected energy for neutral BCl_3 calculated with the same method and basis set. The asymptote assignments on the right of the diagram are as follows: 1a) $^1BCl_2^+$(min41) + $^1Cl^+$, 4a) $^1BCl_2^+$(min43) + $^1Cl^+$ and 6a) $^2BCl^+$ + $^2Cl_2^+$.

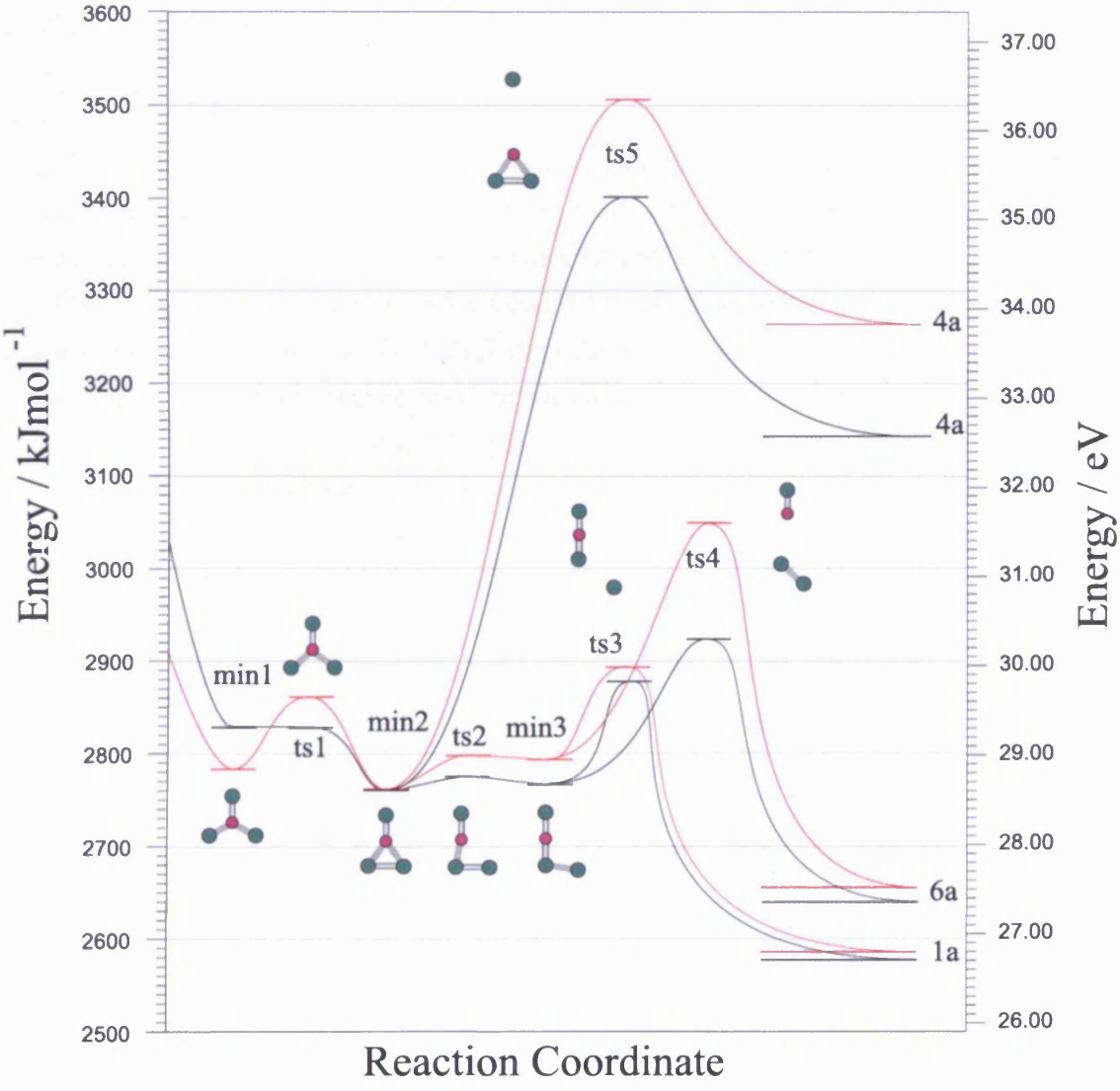

dissociation to ($^2BCl^+ + {}^2Cl_2^+$) (asymptote 6a). Cleavage of the terminal B-Cl bond via ts5 allows formation of the ion pair ($^1BCl_2^+$(min43) + $^1Cl^+$) (asymptote 4a), where the $^1BCl_2^+$ is formed in an excited electronic state with a triangular geometry.

Figure 2.5 reveals that both MP2 and CC give essentially the same general description of the surface, although there are some energetic differences. Of note is the barrier height for formation of the inter-chlorine bond, given by the energy separation between ts1 and min1. Møller-Plesset theory calculates this to be approximately 80 kJ mol^{-1}, while CCSD(T)/γ//CCSD/β suggests that the process is essentially barrierless when zero-point energies are taken into consideration.

The zero-point corrected activation barrier to fragmentation from min3 to ($^2BCl^+ + {}^2Cl_2^+$) (asymptote 6a) is 254 kJ mol^{-1} with MP2/α and 157 kJ mol^{-1} with CCSD(T)/γ// CCSD/β. For fragmentation to ($^1BCl_2^+ + {}^1Cl^+$) (asymptote 1a), the activation barrier from min3 is 99 kJ mol^{-1} with MP2 and 112 kJ mol^{-1} with CCSD(T)/γ// CCSD/β. Formation of the ion pair ($^1BCl_2^+ + {}^1Cl^+$) (asymptote 4a) via ts5 has an activation barrier from min2 of 743 kJ mol^{-1} at the MP2/α level, and 641 kJ mol^{-1} with CCSD(T)/γ// CCSD/β.

The closed-shell CCSD/β and CCSD(T)/γ $\mathscr{T}_1$ diagnostic values (table 2.1), calculated at the optimised CCSD/β structures, suggest that the minima on the singlet surface are well represented by single reference wavefunctions, since the values are less than the commonly used threshold of 0.02 for closed-shell wavefunctions. For the transition states the same may also be said for ts2 and ts3, although it is possible that transition states ts1, ts4 and ts5 have significant multiconfigurational character in their wavefunctions since their $\mathscr{T}_1$ values are higher than this threshold. This is perhaps not surprising given that these structures contain dissociating bonds.

In order to gain some measure of the extent of multiconfigurational character in the stationary point wavefunctions, a re-characterisation of the surface using the MCSCF and MRCI approaches was undertaken. The details of the active space used for these calculations is detailed in section 2.3. The assumption that the species are all planar is supported by the structures of the stationary points found with MP2. Table 2.3 gives the MCSCF and MRCI energies, and the breakdown of their wavefunctions by the number of CSFs with a specific weight. Also shown are the weights of the dominant excitations from the MRCI calculation. Table 2.4 gives the optimised stationary point structures from the MCSCF calculations. Figure 2.6 shows schematically the MCSCF and MRCI surfaces. These have been offset against min3 since this is the stationary point with the lowest

Table 2.3: The energies of the stationary points on the singlet surface with MCSCF and MRCI using basis set β. The composition of the multiconfigurational wavefunction is broken down into the number of CSFs which contribute a specific percentage to the total wavefunction. For the MRCI calculations, the Davidson corrected energy is given, along with the breakdown of the reference wavefunction. Also given is the percentage contribution to the total wavefunction of the most dominant internal excitation, and single and double external excitations. The energies are offset against min3, the most stable structure on the MCSCF surface.

	MCSCF						MRCI									CCSD $\mathscr{T}_1$
	Energy	Reference Configs / %					Energy	Reference Configs / %					Largest Excitation / %			Diag
	/kJ mol^{-1}	Dominant	$30 > x \geq 20$	$20 > x \geq 10$	$10 > x \geq 5$	$5 > x \geq 1$	/kJ mol^{-1}	Dominant	$30 > x \geq 20$	$20 > x \geq 10$	$10 > x \geq 5$	$5 > x \geq 1$	Internal	Ext. Single	Ext. Double	
min1	77	66	0	2	0	0	40	61	0	0	2	0	0.019	0.013	0.003	0.0173
min2	6	90	0	0	0	0	-10	79	0	0	0	1	0.024	0.008	0.004	0.0150
min3	0	91	0	0	0	0	0	80	0	0	0	1	0.029	0.018	0.003	0.0168
ts1	81	68	1	0	0	0	67	61	1	0	0	0	0.023	0.007	0.004	0.0288
ts2	17	90	0	0	0	1	8	80	0	0	0	1	0.028	0.074	0.023	0.0166
ts3	97	78	0	0	2	0	101	72	0	0	1	1	0.028	0.164	0.101	0.0194
ts4	155	71	0	1	0	0	180	64	0	1	0	0	0.022	0.073	0.028	0.0356

Table 2.4: The structures of the stationary points on the singlet surface of BCl_3^{2+} using MCSCF with basis set β. The geometric variables are defined in figure 2.4. All calculations were performed in the C_s point group.

		Bond Lengths / Å				Bond Angles / degrees			
	Structure	r_1	r_2	r_3	r_4	θ	ϕ	ρ	dihedral
MCSCF/β	min1	1.757	1.757	1.757	-	120.01	120.00	-	180.00
	min2	1.605	1.898	1.898	-	145.86	145.83	-	180.00
	min3	1.579	1.774	-	2.098	177.89	-	101.46	180.00
	ts1	1.633	1.872	1.872	-	130.35	130.35	-	180.00
	ts2	1.590	1.779	-	2.124	164.51	-	71.72	180.00
	ts3	1.594	1.687	-	2.914	177.16	-	122.27	180.00
	ts4	1.586	2.805	-	1.957	175.65	-	119.40	180.00

energy on the MCSCF surface. Unfortunately, due to the computationally demanding nature of these calculations, frequency analyses were not performed at the MCSCF level. Ts5 could not be found at the MCSCF level, this was attributed to the long B-Cl distance, which caused convergence problems with the MCSCF routine.

The orbitals inside the active spaces resulting from the MCSCF calculations were checked for consistency across the surface, by inspecting orbital plots from the optimised calculations. The suitability of the active space is also supported by the weights of the dominant excitations from the MRCI calculation. The largest of these is a single external excitation with weight of 0.164% for ts3. This indicates that there are no unoccupied orbitals significantly coupled to the active space, which should have been incorporated into it. The largest internal excitation is 0.029%, for min3, confirming that the consideration of excitations from only the CSFs of the MCSCF calculation with CI coefficients of 0.02 or greater is also sound. The highest energy closed shell orbital from the MCSCF calculation (with essentially boron 1s character) was found to be at least 6.5 H ($\approx$ 20,000 kJ mol^{-1}) more stable than the lowest energy orbital inside the active space. It is felt that this is sufficient ground for not considering excitations from the closed shell orbitals of the MCSCF calculation in the MRCI calculation, which would have been beyond our computational resources in any case.

The structural data obtained (table 2.4) indicate that much of the surface is very similar to that obtained with MP2 or CC, with most bond lengths agreeing with those from CC to within a few hundredths of an Ångstrom. The exceptions to this are ts1, which shows a more marked difference of 0.136 Å, and ts3 and ts4, where the the long interaction between the product fragments is reduced by

Figure 2.6: Potential energy surface for $^1BCl_3^{2+}$. The green curves indicates stationary points calculated at MCSCF/β, while the blue curves indicate MRCI/β single point energies calculated at the MCSCF/β optimised stationary points. Zero-point energy corrections are not considered. The curves connecting the stationary points are schematic. The energies on the surface are offset against the stationary point with the lowest energy from the MCSCF surface, min3.

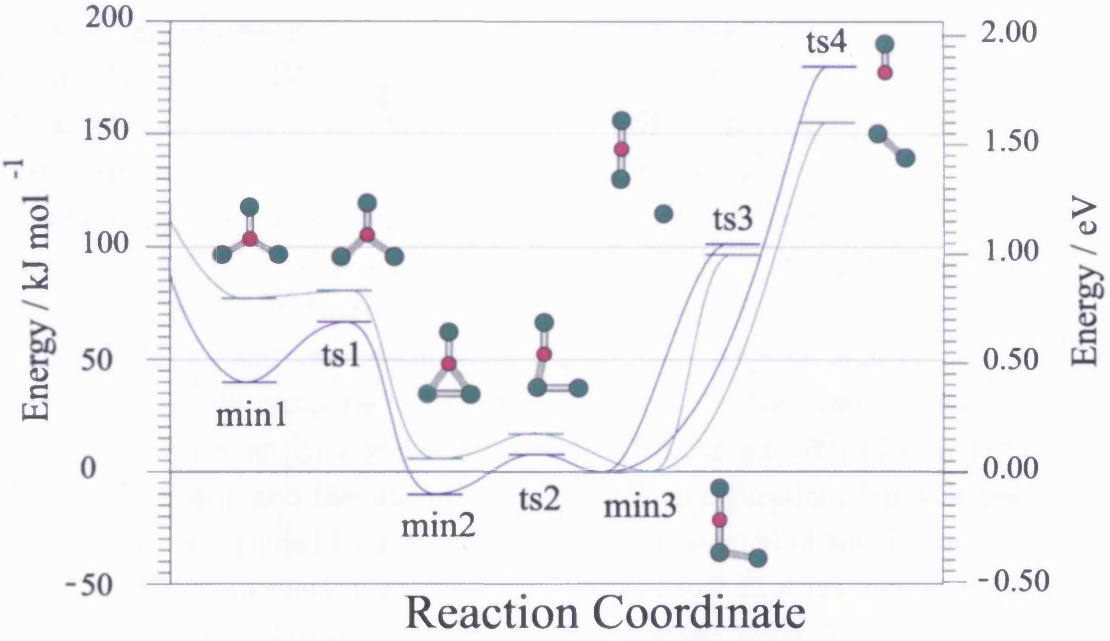

0.161 Å in ts3, and 0.669 Å in ts4, when comparing CCSD and MCSCF data.

Given the lack of dynamical correlation, it might be expected that the MCSCF surface (figure 2.6) would be energetically poorer than that calculated at the CCSD(T) level. However the general form of the MCSCF surface is energetically very similar to that calculated using coupled-cluster theories (and MP2). Comparing the non-vibrationally corrected energies, the barrier for conversion of min1 to min2 via ts1 (4 kJ mol^{-1}) is much closer to the CCSD(T) value (0 kJ mol^{-1}) than to the MP2 (85 kJ mol^{-1}). The activation barriers for fragmentation via ts3 (97 kJ mol^{-1}) and ts4 (155 kJ mol^{-1}) are also similar to the CCSD(T) values, 114 and 162 kJ mol^{-1} respectively, when zero-point corrections are ignored.

Inclusion of dynamical electron correlation with MRCI changes the form of the surface very little. The global minimum changes from being min3 to min2 and the barrier for conversion of min1 to min2 via ts1 increases by 23 kJ mol^{-1}, although this value is still closer to the CCSD(T) value than the MP2 value. The activation energies for fragmentation via ts3 and ts4 are also slightly increased, by

4 and 25 kJ mol^{-1} respectively. Since only the general form of the surface is being considered, it is not felt significant that the zero-point energy correction is being ignored, since it should be fairly consistent for each stationary point. From the CCSD data, the zero-point energy corrections only differ by 11 kJ mol^{-1} across the surface, reducing to 6 kJ mol^{-1} when ts5 is ignored.

Given the similarities between the MCSCF, MRCI and coupled-cluster surfaces, it was decided to examine the composition of the multiconfigurational wavefunctions at each stationary point, and to compare them with the $\mathscr{T}_1$ diagnostics obtained at the CCSD(T)/γ level. These data are shown in table 2.3, which gives the number of configuration state functions (CSFs) with a given weight at each stationary point and the weight of the dominant CSF.

In general, there is a reasonable inverse correlation between the size of the $\mathscr{T}_1$ and the weight of the dominant configuration. Min2, min3, ts2 and ts3 all have low $\mathscr{T}_1$ values and MCSCF dominant weights of >75%, while ts1 and ts4 have higher $\mathscr{T}_1$ values and lower dominant weights. The exception is min1, which has a dominant weight comparable with that of ts1, but a rather lower $\mathscr{T}_1$ diagnostic. Linear regression analysis yields a correlation coefficient (R^2) of 0.38 between the $\mathscr{T}_1$ diagnostic and the size of the dominant configuration, but this rises to 0.78 if min1 is excluded from the data set. If the weights of the dominant CSF from the MRCI calculation are used, R^2 increases to 0.82 when min1 is excluded from the data set. The dominant weights are slightly lower for the MRCI data compared with those from MCSCF. This takes into account the contribution to the wavefunction of the many low weighted single and double excitations.

An alternative gauge of the reliability of the CCSD(T) results is to examine the energy differences between corresponding CCSD and CCSD(T) calculations. If the triples contribution is large, it might be concluded that the coupled-cluster series is not converged and that there is potentially multiconfigurational character to the wavefunction. The absolute CCSD/CCSD(T) energy differences are given in table 2.1, and comparison of these data with those in table 2.3 shows that there is a very good inverse correlation between the magnitude of the CCSD/CCSD(T) energy difference and the size of the dominant weight in the MCSCF calculation.

So do the $\mathscr{T}_1$ diagnostic and CCSD/CCSD(T) energy differences indicate that single reference treatments are unsafe? In general, I believe that they do not, given that the form of the MCSCF surface, both structurally and energetically, is similar to the coupled-cluster surfaces. However, it is possible that some of the transition states are not well represented at the coupled-cluster level, especially ts4, which has one of the smallest dominant weights, a high $\mathscr{T}_1$ diagnostic, a

large CCSD/CCSD(T) energy difference and a large CCSD/MCSCF structural difference.

2.5.2 Triplet Surface

An initial survey of the triplet surfaces using MP2/α located 11 stationary points with C_{2v} symmetry. It rapidly became clear that the triplet surfaces are extremely complicated, and hence a more systematic approach to the location of the stationary points was adopted. Starting from the D_{3h} geometry of the parent neutral, the structure was slightly distorted so as to produce a C_{2v} geometry. This distortion was deemed necessary because (a) our initial MP2 survey had located many C_{2v} triplet minima and (b) the excitation of one or more electrons from the closed-shell electronic configuration of D_{3h} $^1BCl_3^{2+}$ will yield Jahn-Teller active ^3E states. The open-shell electronic configurations of the C_{2v} distorted BCl_3^{2+} as generated by the INDO and Harris guesses in Gaussian were then used as references, from which all the possible one and two electron promotions from the 12-n highest occupied MOs into the 10+n lowest virtual orbitals were performed, where n=0 for α orbitals and 2 for β orbitals.

The results from this procedure confirmed that the system is indeed very complex. Within the first 1000 kJ mol^{-1} from the lowest lying triplet electronic state, 41 new states were located. The close energetic spacing of these states posed a problem in that it was not obvious how many of them should be probed further. The energetic spread of stationary points on the singlet surface was therefore used as a guide to the number of triplet states that should be considered. The energy separation between ts5 and min2 at the CCSD(T)/γ level is 652 kJ mol^{-1}. Starting from the lowest energy triplet state generated by the orbital rotation process, the largest energy gap (80 kJ mol^{-1}) occurred between states 660 kJ mol^{-1} above the lowest state, and hence all the states below this energy (21 states) were considered further.

MP2/α optimisations performed on each of the these 21 triplet states (without symmetry constraints) resulted in the location of many minima and transition states. Hartree-Fock theory is a ground state theory, and hence in principle one can be confident only in those stationary points which are the lowest energy of a given state symmetry. As most of the minima located by the MP2/α search without symmetry constraints had geometries very close to those of higher point groups, these structures were re-optimised with symmetry constraints (in either C_s or C_{2v} symmetry). The geometries of these stationary points together with those obtained from CCSD/β optimisations, are given in table 2.5, and their ener-

gies and state symmetries are given in table 2.6, together with their CCSD(T)/γ $\mathscr{T}_1$ diagnostics. The energies and geometries of the re-optimised structures are in most cases essentially identical to those obtained without symmetry constraints. One or two of the stationary points located by the no-symmetry MP2/α searches have structures which are some way from C_{2v}, namely min15 and ts13 which, although planar, have three unique bond lengths and angles.

In some cases it was found that optimisations from two different initial electronic structures would converge on the same stationary point, resulting in fewer stationary points than initial electronic structures generated by the orbital rotation process. IRC calculations were performed from each of the transition states found, to deduce their connectivity to the true minima.

Fragmentation pathways were explored from each of the minima by the stretching of one of the B-Cl bonds (usually the unique bond) in a series of partial geometry optimisations. The connectivities of the dissociation transition states located by this technique were also verified by IRC calculations.

There may be regions of these potential energy surfaces which cannot be reached by a geometry optimisation from the starting geometry, because the route into these regions would initially involve increasing the energy of the system. This may be why some of the minima found by the unstructured search of the system were not found by the structured search using the orbital rotation method, although it is possible that the structured search would locate these stationary points if more than the first 21 states were considered.

Figure 2.7 shows the energies and connectivities on the stationary points in the triplet surface. Min11 is the lowest energy triplet structure, and can dissociate endothermically to ($^2BCl_2^{2+}$ + ^2Cl) (asymptote 5a), 229 kJ mol^{-1} above it at the MP2/α level, and 248 kJ mol^{-1} at CCSD(T)/γ //CCSD/β. This pathway has no transition state. Min12 can dissociate via ts11 to ($^1BCl_2^+$(min42) + $^3Cl^+$) (asymptote 3a) with the BCl_2^+ ion formed in an excited singlet electronic configuration. The activation energy for this pathway is 278 kJ mol^{-1} with both MP2/α and CCSD(T)/γ //CCSD/β. The process is exothermic by 4 kJ mol^{-1} at MP2/α but endothermic by 7 kJ mol^{-1} at CCSD(T)/γ//CCSD/β.

Min14a can dissociate to ($^1BCl_2^+$(min41) + $^3Cl^+$) (asymptote 2a) via transition state ts12 with an activation energy of 12 kJ mol^{-1} at MP2/α. This process forms the BCl_2^+ ion in its ground state and the process is exothermic by 499 kJ mol^{-1} at MP2/α. Min14a could not be located with CCSD, instead ts12 allows dissociation from min14b to ($^1BCl_2^+$(min41) + $^3Cl^+$) (asymptote 2a). This process has an activation barrier of 31 kJ mol^{-1} and is exothermic by 418 kJ

Figure 2.7: Potential energy surface for decomposition of $^3BCl_3^{2+}$. The red curves indicate stationary points calculated at MP2/α including zero-point corrections, while the black curves indicate CCSD(T)/γ single point energies calculated at the CCSD/β optimised stationary points, corrected with CCSD/β zero-point energies. The MP2 energy for min12 is zero-point corrected with the CCSD zero-point energy due to the apparent over-estimation of the zero-point energy with MP2. The curves connecting the stationary points are schematic. The energies on the surface are offset against the zero-point corrected energy for neutral BCl_3 calculated with the same method and basis set. The asymptote assignments on the right of the diagram are as follows: 2a) $^1BCl_2^+$(min41) + $^3Cl^+$, 3a) $^1BCl_2^+$(min42) + $^3Cl^+$ and 5a) $^2BCl_2^{2+}$ + ^2Cl.

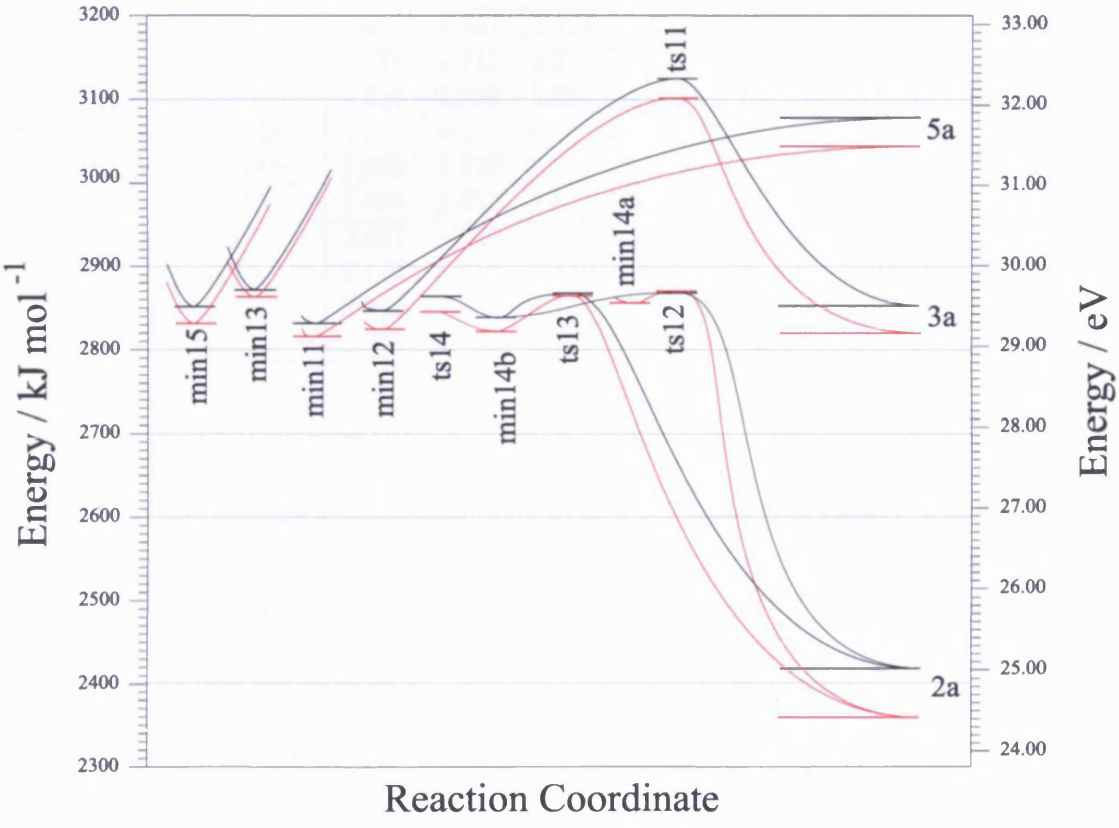

Table 2.5: Structures of the stationary points on the triplet surface of BCl_3^{2+} at MP2/α and CCSD/β. a - These structures were found by the unstructured search of the triplet surface. b - These structures were found by the structured search. c - These structures were found by the exploration of the surface subsequent to finding another point located on it. The definition of the geometric variables is given in figure 2.4.

		Bond Lengths / Å			Bond Angles / degrees		
	Structure	r_1	r_2	r_3	θ	ϕ	dihedral
MP2/α	min11[a,b]	1.822	1.714	1.714	126.04	126.03	180.01
	min12[a,b]	1.874	1.705	1.705	124.70	124.70	180.00
	min13[a]	1.614	1.852	1.852	135.82	135.82	180.00
	min14a[a]	1.891	1.686	1.686	107.14	107.15	180.00
	min14b[a,b]	1.648	1.833	1.833	120.27	119.87	180.01
	min15[a,b]	1.637	1.831	1.882	121.09	124.22	180.01
	ts11[c]	3.600	1.717	1.717	126.07	126.05	180.00
	ts12[c]	2.163	1.650	1.650	99.97	98.98	180.00
	ts13[c]	2.167	1.606	1.729	122.04	88.58	180.00
	ts14[b]	1.775	1.754	1.754	119.87	119.87	180.00
CCSD/β	min11	1.827	1.721	1.721	127.29	127.29	180.00
	min12	1.878	1.713	1.713	126.16	126.16	180.00
	min13	1.619	1.862	1.862	137.74	137.74	180.00
	min14a	-	-	-	-	-	-
	min14b	1.669	1.817	1.817	117.53	117.53	180.00
	min15	1.655	1.812	1.879	116.70	125.34	180.00
	ts11	3.861	1.725	1.725	126.93	126.93	180.00
	ts12	2.142	1.659	1.659	97.89	97.89	180.00
	ts13	2.142	1.614	1.753	123.68	88.04	180.00
	ts14	1.771	1.771	1.771	120.00	120.00	180.00

mol^{-1} at CCSD(T)/γ//CCSD/β.

Min14b has a structure with two long bonds and one short bond (2L1S), which can undergo an internal rotation process where a long bond and a short bond interchange. The activation energy for this process via ts14 is 25 kJ mol^{-1} at MP2/α, and 24 kJ mol^{-1} with CCSD(T)/γ//CCSD/β. A frequency analysis of ts14 with CCSD/β indicates that the structure has no imaginary modes, however, at MP2/α, a single imaginary mode is found. Analytic MP2 frequency analysis is likely to be more accurate on the energetically shallow surface than the numerical method employed with CCSD, and thus it is believed that ts14 is a transition state.

Min14b can dissociate to ($^1BCl_2^+$(min41) + $^3Cl^+$) (asymptote 2a) via ts13 at both the MP2 and CCSD levels of theory. Ts13 has a geometry which, again, cannot be idealised to C_{2v}, and offers a lower activation barrier compared with

Table 2.6: The energies of the stationary points on the triplet surface with various methods and basis sets. The energies presented for MP2, CCSD and CCSD(T) are offset against the zero-point corrected energy of the D_{3h} neutral structure, calculated using the same method and basis set. $\mathscr{T}_1$ diagnostic results are shown for the CC methods. The numbers in parentheses after the CCSD(T) energies are the absolute differences between corresponding CCSD and CCSD(T) energies. All the MP2 structures are calculated in a C_1 point group, with the electronic symmetry A_1. The symmetry of the CCSD stationary points are given in the table. The CCSD(T) energies are from single points calculated at the same geometry and with the same symmetry as the CCSD optimised structures.

	Møller Plesset / α			CoupledCluster / β					Coupled-Cluster / γ	
	MP2 kJ mol^{-1}	ZPE	Imag modes σ / cm^{-1}	CCSD kJ mol^{-1}	ZPE	Imag modes σ / cm^{-1}	$\mathscr{T}_1$ Diagnostic	Electronic Symmetry	CCSD(T) kJ mol^{-1}	$\mathscr{T}_1$ Diagnostic
min11	2791	25.27	-	2804	19.06	-	0.0182	C_{2v} $^3A_1$	2812(8)	0.0182
min12	2806	18.99	-	2820	18.99	-	0.0209	C_{2v} $^3A_2$	2827(7)	0.0209
min13	2844	19.76	-	2873	15.62	-	0.0209	C_{2v} $^3B_1$	2857(16)	0.0210
min14a	2822	36.19	-	-	-	-	-	-	-	-
min14b	2803	17.46	-	2809	15.31	88i	0.0301	C_{2v} $^3B_2$	2822(13)	0.0301
min15	2814	17.89	-	2821	16.24	-	0.0307	C_s $^3A''$	2835(14)	0.0307
ts11	3092	10.70	129i	3099	11.17	133i	0.0411	C_{2v} $^3A_1$	3113(14)	0.0433
ts12	2847	23.27	541i	2853	17.79	491i	0.0258	C_{2v} $^3B_2$	2851(2)	0.0260
ts13	2849	15.18	540i	2845	14.85	343i	0.0274	C_s $^3A''$	2852(7)	0.0276
ts14	2835	10.19	293i	2835	12.16	204(real)	0.0257	C_{2v} $^3B_2$	2849(14)	0.0258

the dissociation process via ts12 to asymptote 2a. The activation barrier for dissociation of min14b to asymptote 2a via ts13 is 44 kJ mol^{-1} at MP2/α and 30 kJ mol^{-1} at CCSD(T)/γ//CCSD/β, while the process is exothermic by 461 kJ mol^{-1} at MP2/α and 418 kJ mol^{-1} at CCSD(T)/γ//CCSD/β.

Two further minima were located, min13 and min15, from which it proved impossible to find a fragmentation route, or a route into one of the other minima from which fragmentation has already been discussed. The potential wells of these minima were found to be very steep, and cross several other potentials, onto which the electronic structure converges preferentially. Since BCl_3^{2+} is not observed as a product in the mass spectrum of the double ionisation of BCl_3 it must be concluded that either a) the surfaces connecting into min13 and min15 are repulsive at the geometry of BCl_3 at which the dication is formed, or b) that at least one pathway exists out of these minima which cannot be located computationally due to the tendency of the SCF convergence routines to locate preferentially the most stable electronic structure.

As discussed in section 1.3.6, it is likely that $\mathscr{T}_1$ diagnostics of up to 0.045 are acceptable for open-shell systems to be adequately described by a single reference wavefunction (and a strong case can be made that even this limit is conservative when using Gaussian to calculate open-shell $\mathscr{T}_1$ diagnostics). Table 2.6 shows that the largest $\mathscr{T}_1$ diagnostic for an optimised structure on the triplet surface is 0.043 (for ts11), and thus all of the $\mathscr{T}_1$ values are below the acceptable limit. Furthermore, as discussed in section 2.5.1, the CCSD/CCSD(T) energy difference can be used as a measure of multiconfigurational character. These data are given in table 2.6, and show only very small values. Thus the $\mathscr{T}_1$ diagnostics and CCSD/CCSD(T) energy differences are in agreement in suggesting that single reference treatments of the triplet surface are adequate.

2.5.3 Product Ion Fragmentation

Attention now turns to an analysis of the initial fragmentation products from singlet and triplet BCl_3^{2+} and exploring how these products can further fragment, with the aim of rationalising the experimental data of Love and Price.[52]

The geometry of all of the product ions resulting from the initial fragmentation processes A1, B1 and C1 (figure 2.2, contributing to asymptotes 1a-6a), have been optimised using both MP2/α and CCSD/β. The geometric data for these fragments are presented in table 2.7 and their energies in table 2.8, together with their CCSD(T)/γ single point energies and the CCSD/β and CCSD(T)/γ $\mathscr{T}_1$ diagnostics.

Table 2.9 collects the combined fragment energies for each asymptote, offset against the zero-point corrected energy of BCl_3 in its minimum energy structure. Experimental enthalpies of formation for each asymptote are also presented in table 2.9, offset against the enthalpy of formation of BCl_3. These have been collated from the NIST Scientific and Technical Data website.[58] Agreement between experiment and the CCSD(T)/γ energies is very good, suggesting that the CCSD(T)/γ description of the system is reliable.

The ion pair ($BCl_2^+ + Cl^+$) formed via route B1 (figure 2.2) can be produced by four different processes, two by the singlet dication fragmenting to asymptotes 1a or 4a (table 2.9, figure 2.5), and two from the triplet dication decomposing to asymptotes 2a or 3a (table 2.9, figure 2.7). ($BCl^+ + Cl_2^+$) formed in process C1 can result from the fragmentation of $^1BCl_3^{2+}$ to asymptote 6a. BCl_2^{2+} produced in route A1 is formed as $^3BCl_3^{2+}$ cleaves to asymptote 5a.

It is not possible, however, to explain all of the ion pairs observed by Love and Price[52] (figure 2.2) by considering only the initial fragmentation of BCl_3^{2+} in either its triplet or singlet states. It is necessary to consider a second fragmentation step in order to explain the formation of the ion pairs ($Cl^+ + BCl^+$) resulting from route A2, ($Cl^+ + Cl^+$) from route D1 and ($B^+ + Cl^+$) formed either via route B2 or C2.

Partial geometry optimisations were used to explore the fragmentation processes for the ions resulting from processes A1, B1 and C1. Since many of the ions from these initial processes carry only a single positive charge, most of the pathways to further fragmentation lack transition states. The asymptotes resulting from further fragmentation, and the sum of the fragment energies (1b, 2b & 4b-6b) are presented in table 2.9 and the optimised geometries and energies are collected in table 2.7 and table 2.8. Figure 2.8 shows the connectivity of the fragments resulting from processes A1, B1 and C1 with those from A2, B2 and C2 in the form of schematic potentials. The asymptotes on the left of the figure represent the products formed by the initial fragmentation of BCl_3^{2+}, while the asymptotes on the right result from a second fragmentation step. A fragmentation pathway could not be found for the $^1BCl_2^+$ (min42) ion formed by the separation of the dication to asymptote 3a.

Fragmentation of $^2BCl_2^{2+}$ (formed by decomposition of $^3BCl_3^{2+}$ in process A1) allows formation of the pair of ions ($^2BCl^+ + {}^3Cl^+$) via transition state ts44. This explains the presence of the ion pair resulting from route A2, in a two step process; initial fragmentation of $^3BCl_3^{2+}$ to asymptote 5a followed by fragmentation of $^2BCl_2^{2+}$ to asymptote 5b.

Figure 2.8: Schematic representation of the fragmentation pathways following the initial fragmentation of BCl_3^{2+}. CCSD(T)/γ//CCSD/β results are shown with black curves, while MP2/α data are shown with red curves. The horizontal axis is representative of the internal coordinates of the fragment species such that fragmentation occurs from left to right. The energy of the potential is offset against the energy of $^1BCl_3$ calculated at the same method.

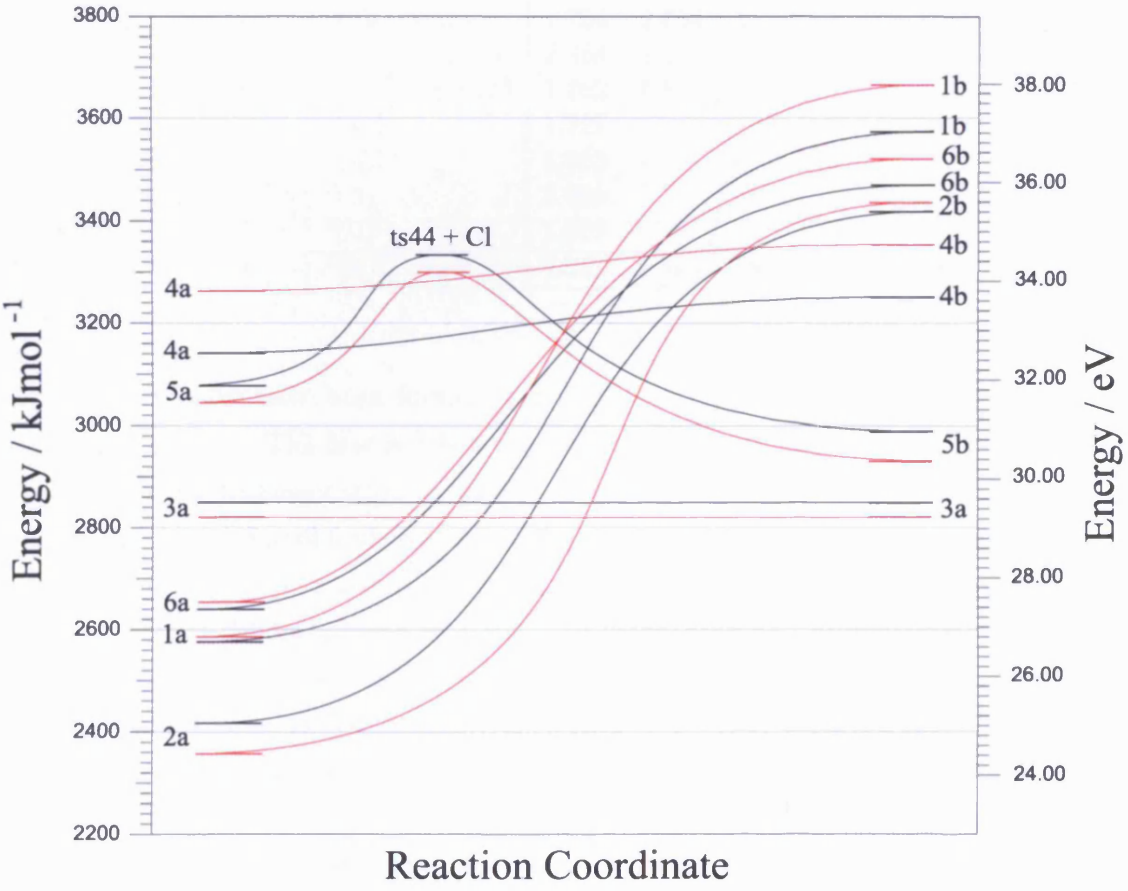

Table 2.7: The optimised structures of the triatomic and diatomic fragmentation products of BCl_3^{2+} calculated at MP2/α and CCSD/β.

		Structural Parameters		
	Structure	r_1/Å	r_2/Å	θ/°
MP2/α	$^1BCl_2^+$(min41)	1.611	1.611	120.00
	$^1BCl_2^+$(min42)	1.738	1.747	101.85
	$^1BCl_2^+$(min43)	2.237	2.237	54.04
	$^2BCl_2^{2+}$(min44)	1.760	1.572	179.98
	^1BCl	1.710	-	-
	$^2BCl^+$	1.597	-	-
	$^1Cl_2$	2.028	-	-
	$^2Cl_2^+$	1.935	-	-
	$^2BCl_2^{2+}$($ts44$)	2.838	1.579	181.00
CCSD/β	$^1BCl_2^+$(min41)	1.618	1.618	179.89
	$^1BCl_2^+$(min42)	1.754	1.754	98.81
	$^1BCl_2^+$(min43)	2.363	2.363	50.55
	$^1BCl_2^{2+}$(min44)	1.762	1.579	181.02
	^2BCl	1.727	-	-
	$^2BCl^+$	1.603	-	-
	$^1Cl_2$	2.009	-	-
	$^2Cl_2^+$	1.905	-	-
	$^2BCl_2^{2+}$(ts44)	3.043	1.584	181.19

Two pathways have been found to explain the (Cl^+ + B^+) ion pair, both via two step processes. The first involves the fragmentation of $^2BCl^+$ and $^2Cl_2^+$ formed from the initial fragmentation of $^1BCl_3^{2+}$ to asymptote 6a via route C1. This results in the formation of four atomic species on asymptote 6b after process C2 has taken place. The second route is via the fragmentation of $^1BCl_2^+$(min43), resulting from the initial decomposition of $^1BCl_3^{2+}$ to asymptote 4a. Since $^1BCl_2^+$(min43) has a triangular structure with an angle of 50.55° at boron (CCSD/β), it can fragment to ($^1Cl_2$ + $^1B^+$) in process B2 as there is already a partial inter-chlorine bond, causing the ion pair ($^1B^+$ + $^1Cl^+$) to be the charged fragments of asymptote 4b. Both of these processes are two step, with one ion resulting from each fragmentation. This implies that $^1B^+$ and $^1Cl^+$ will not have equal and opposite momentum. It is noted that asymptote 4b lies lower than 6b by the energy of a Cl-Cl bond, and thus process B1 + B2 would be energetically more favourable than C1 + C2. By considering processes C1 and C2 as separate consecutive events, theoretical prediction of the gradient of the ion pair agrees well with that experimentally measured,[52] and since processes C1 and C2 each have appreciable energy barriers it seems reasonable that they should occur consecutively.

Table 2.8: Total energy of the fragmentation products of BCl_3^{2+} calculated with MP2/α, CCSD/β and CCSD(T)/γ.

	Møller Plesset / α			Coupled-Cluster / β				Coupled-Cluster / γ	
	MP2	ZPE / 10^{-3}	Imag modes	CCSD	ZPE / 10^{-3}	Imag modes	$\mathscr{T}_1$	CCSD(T)	$\mathscr{T}_1$
	Hartree		σ / cm^{-1}	Hartree		σ / cm^{-1}	Diag	Hartree	Diag
$^1BCl_2^+$(min41)	-943.801235	5.541	-	-943.962453	5.372	-	0.0145	-943.994109	0.0143
$^1BCl_2^+$(min42)	-943.622381	2.669	-	-943.790521	4.004	-	0.0190	-943.823783	0.0190
$^1BCl_2^+$(min43)	-943.539573	2.323	-	-943.738540	1.970	$71i$	0.0139	-943.773461	0.0141
$^2BCl_2^{2+}$(min44)	-943.084436	4.776	-	-943.242339	4.415	-	0.0278	-943.272292	0.0276
^1BCl	-484.343059	2.017	-	-484.444927	1.920	-	0.0163	-484.463771	0.0163
$^2BCl^+$	-483.995598	2.726	-	-484.081590	2.614	-	0.0201	-484.098394	0.0199
$^1Cl_2$	-919.235781	1.227	-	-919.409188	1.281	-	0.0081	-919.437706	0.0086
$^2Cl_2^+$	-918.821433	1.345	-	-918.989921	1.506	-	0.0126	-919.017152	0.0131
$^1Cl^+$	-459.043789	-	-	-459.135027	-	-	0.0100	-459.146797	0.0100
$^3Cl^+$	-459.130582	-	-	-459.200572	-	-	0.0076	-459.206687	0.0076
^2Cl	-459.585137	-	-	-459.666282	-	-	0.0066	-459.676216	0.0066
$^1B^+$	-24.269565	-	-	-24.296454	-	-	0.0120	-24.296627	0.0120
$^2BCl_2^{2+}$(ts44)	-942.985447	3.103	$220i$	-943.147539	2.978	$210i$	0.0291	-943.174397	0.0297

Table 2.9: Energy of the fragmentation asymptotes of BCl_3^{2+}. The total energies are given in atomic units, and are also presented (in kJ mol^{-1}) offset against the zero-point corrected energy of the D_{3h} neutral structure, calculated using the same method and basis set. ΔH_f has been calculated for each asymptote from experimental data collated from the NIST Scientific and Technical Databases website.[58] These are presented offset against the experimentally determined $\Delta H_f(BCl_3)$.[58] The difference between the CCSD(T)/γ and experimental numbers is given in parenthesis after the experimental data.

Asymptote Number	Fragment Species	Total Energy / Hartree			Offset Energy / kJ mol^{-1}			
		MP2/α	CCSD/β	CCSD(T)/γ	MP2	CCSD	CCSD(T)	Experimental[58]
1a	$^1BCl_2^+$(min41) + $^1Cl^+$	-1402.839484	-1403.092109	-1403.135534	2587	2565	2577	2591(14)
2a	$^1BCl_2^+$(min41) + $^3Cl^+$	-1402.926276	-1403.157653	-1403.195424	2359	2393	2419	2452(33)
3a	$^1BCl_2^+$(min42) + $^3Cl^+$	-1402.750294	-1402.987089	-1403.030470	2821	2841	2853	-
4a	$^1BCl_2^+$(min43) + $^1Cl^+$	-1402.581040	-1402.871597	-1402.920258	3265	3144	3142	-
5a	$^2BCl_2^{2+}$ + ^2Cl	-1402.664797	-1402.904206	-1402.944093	3045	3058	3079	-
6a	$^2BCl^+$ + $^2Cl_2^+$	-1402.812959	-1403.067390	-1403.111426	2656	2630	2640	2636(4)
	$^2BCl_2^{2+}$(ts44) + ^2Cl	-1402.567482	-1402.810842	-1402.847635	3301	3303	3333	-
1b	^1BCl + $^1Cl^+$ + $^1Cl^+$	-1402.428621	-1402.713061	-1402.755445	3665	3560	3575	3574(1)
2b	^1BCl + $^1Cl^+$ + $^3Cl^+$	-1402.515413	-1402.778606	-1402.815335	3438	3388	3417	3435(18)
4b	$^1B^+$ + $^1Cl^+$ + $^1Cl_2$	-1402.547908	-1402.839387	-1402.879848	3352	3229	3248	3282(34)
5b	$^2BCl^+$ + $^3Cl^+$ + ^2Cl	-1402.708591	-1402.945829	-1204.978683	2930	2949	2988	3026(38)
6b	$^1B^+$ + $^1Cl^+$ + ^2Cl + ^2Cl	-1402.483629	-1402.764044	-1402.795855	3521	3426	3468	3526(58)

However, formation via pathway B1 + B2 can only have the experimentally determined gradient if the two processes occurred in a concerted, non-sequential event. Given that process B1 has a large activation energy, and the binding energy of $^1B^+$ to $^1Cl_2$ in min43 is very weak, it is suggested that fragmentation of the dication to asymptote 4a results in a concerted further fragmentation of $^1BCl_2^+$(min43) to asymptote 4b. This would result in a gradient different from that expected as a result of two isolated fragmentation processes.

Fragmentation of $^1BCl_2^+$(min41) via the loss of $^1Cl^+$ connects asymptote 1a to 1b or 2a to 2b depending upon whether the initial fragmentation occurred on the singlet or triplet surface. It is suggested that formation of the (Cl^+ + Cl^+) ion pair via process D1 is a two step process, B1 + B3, i.e. BCl_3^{2+} initially fragments on either the singlet or triplet surface to asymptote 1a or 2a respectively (process B1), followed by the cleavage of $^1BCl_2^+$ to asymptotes 1b and 2b (process B3). It is noted that the final asymptotes for (Cl^+ + Cl^+) formation are high in energy. Indeed asymptote 1b at the MP2/α level is the highest energy asymptote calculated.

Since fragmentation of the dication to asymptotes 1a-4a results in formation of BCl_2^+ in various electronic states which are indistinguishable mass spectrometrically, it is unsurprising that this ion is the most abundant observed.

2.6 Conclusions

The experimental data from the mass spectra obtained following double ionisation of BCl_3[52] have been successfully rationalised by *ab initio* characterisation of the potential energy surfaces of $^1BCl_3^{2+}$ and $^3BCl_3^{2+}$. The singlet surface is relatively straightforward, but the triplet surface is very complicated, with a large number of stationary points lying within a narrow energy range. Nevertheless, routes to all of the experimentally observed ion pairs, (BCl_2^+ + Cl^+), (B^+ + Cl^+), (Cl^+ + Cl^+), (BCl^+ + Cl^+), and (BCl^+ + Cl_2^+) and the dication BCl_2^{2+} have been found, and no products have been located that are not experimentally observed. Furthermore, since (BCl_2^+ + Cl^+) is the product of the fragmentation process with the smallest activation barrier for both the singlet and triplet systems, and can be formed by a total of four different fragmentation pathways, it is unsurprising that this should be the experimentally most observed ion pair. The quality of the CCSD(T)/γ data is indicated by the good agreement between the theoretical and experimental energies for the fragment asymptotes.

Dissociation pathways could not be located for min13 and min15 on the triplet surface; this might suggest that BCl_3^{2+} should be long-lived. However, the methodical search of the triplet surface of the dication also located at least one potential surface that was repulsive at the geometry of the neutral species. This is not indicated in diagram 2.7 because this surface was not fully investigated and the asymptote to which it connects was not conclusively determined. However, if this surface cuts through the other potential of the system, then it may be possible for an intersystem crossing to take place from a bound potential to a repulsive one. This would open up another mechanism for fragmentation of the dication, although the investigation of these processes is beyond the scope of this research.

An attempt has been made to gauge the multiconfigurational character of the singlet system through calculation of $\mathscr{T}_1$ diagnostic values, CCSD/CCSD(T) energy differences and a recharacterisation of the surface using MCSCF and MRCI calculations. The form of this surface is in overall good agreement with that calculated with the coupled-cluster method. There is a generally good inverse correlation between the weight of the dominant configuration in the MCSCF calculation and the $\mathscr{T}_1$ diagnostic, and also between the dominant weight and the CCSD/CCSD(T) energy difference. It is concluded that single reference treatments are adequate for most of the stationary points on the singlet surface, although ts4 in particular may be less well represented at this level.

For the triplet system, the majority of the $\mathscr{T}_1$ diagnostic values are larger than the traditional limit of 0.02. However, when using the closed-shell $\mathscr{T}_1$ diagnostic method of Lee and Taylor[10] with open-shell wavefunctions, one should expect larger $\mathscr{T}_1$ diagnostic values compared with those from closed-shell systems.[14] If the open-shell upper limit of 0.045 for a $\mathscr{T}_1$ diagnostic value of Rienstra-Kiracofe *et al.* is used,[13] then all of the optimised stationary points of $^3BCl_3^{2+}$ have acceptably single-reference wavefunctions. This conclusion is fully supported by the CCSD/CCSD(T) energy differences, which are very small in all cases.

Chapter 3

A Study of Ferrocene and Iron Pentacarbonyl using DFT and *ab initio* methods

Contents

3.1 Introduction

3.1.1 The Geometric and Electronic Structures of Ferrocene

The first reported syntheses of ferrocene ($FeCp_2$, Cp=η^5-C_5H_5) were by Pauson and Kealy,[59] and Miller, Tebboth and Tremaine[60] in 1951, and the D_{5h} structure of this sandwich complex was elucidated independently by two groups[61,62] in 1952. The bonding in ferrocene is predominantly between the 3d and 4p orbitals on iron, and linear combinations of the C $2p_z$ orbitals on the Cp rings. In order for the Cp rings to become aromatic, they must obtain an extra electron from iron, to complete their 4n+2(=6) electron complement. Therefore, the bonding can be thought of as between Fe^{2+} and $2Cp^-$, although this suggests that the bonding is purely ionic, which is not the case. The bonding is in fact largely covalent, and is expected to occur in the following way.

Figure 3.1 shows the π-combinations from the C $2p_z$ orbitals of the rings. These combine in the Cp_2^- ligand field to give a_1', a_2'', e_1', e_1'', e_2' and e_2'' orbitals. The 3d orbitals on iron span the a_1' and e_1'' and e_2' irreps under D_{5h}, while the 4p orbitals span the a_2'' and e_1' irreps. The e_2'' ring combinations have no symmetry match, and consequently form a non-bonding set of orbitals.

Although the ligands sit in an axial position relative to the metal, they are not expected to interact significantly with the $3d_{z^2}$ metal orbital. This is because the nodal cone of this orbital is oriented such that it lies along the direction of maximum electron density of the p-orbitals of the rings, and such most of the overlap cancels out. This leaves the $3d_{z^2}$ as largely non-bonding. The interaction of the metal e_2' set ($3d_{xy,x^2-y^2}$) with the ligand orbitals results in δ-back-bonding orbitals. These three orbitals are expected to be the highest occupied MOs, with the $3d_{z^2}$-like orbital being the HOMO. These orbitals are expected to contain the 6 d-electrons from iron. The LUMO is expected to be formed by the anti-

Figure 3.1: MO diagram showing the linear combinations of $2p_z$ carbon orbitals that make up the Cp ring orbitals.

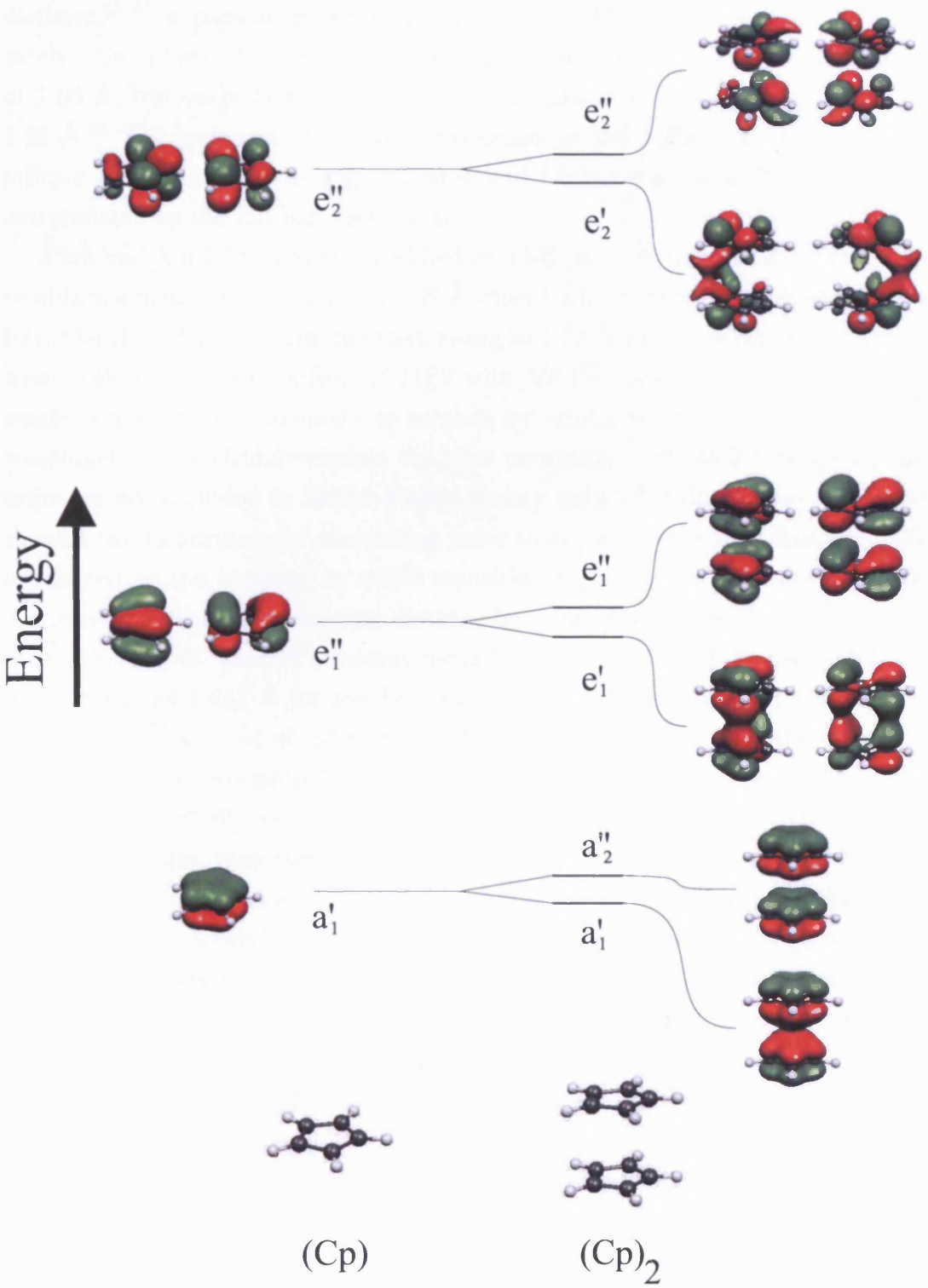

bonding combination of the e_1'' ring orbitals with the metal ($3d_{xz,yz}$) in a π-fashion. A schematic representation of the binding in ferrocene is given in figure 3.2.

Since its discovery, ferrocene has been the subject of many theoretical studies,[63-76] which have often focused on calculating the equilibrium metal to ring distance,[63-67] a parameter which is "notoriously difficult"[66] to compute accurately. Gas phase electron diffraction studies yield an Fe-Cp centroid distance of 1.66 Å, but early Hartree-Fock (HF) calculations found this distance to be 1.89 Å.[65] The inclusion of electron correlation at the MP2 level results in significant overcompensation, e.g. Klopper and Lüthi obtained 1.47 Å with MP2 extrapolated to the full basis set limit.[77]

Park and Almlöf[68] used the modified coupled pair functional (MCPF) method to obtain a metal-ring distance of 1.69 Å when both single and double excitations from the HF reference were included, rising to 1.72 Å when the single excitations were excluded.[68] Comparison of MP2 with MCPF data indicated clearly that single excitations are necessary to account for orbital relaxation of the reference wavefunction, which may explain the poor performance of MP2[68] (single excitations are not included in Møller-Plesset theory until 4^{th} order). This study also showed the importance of correlating more than just the 18 electrons normally attributed to the bonding in stable transition metal complexes; correlating 66 electrons shortens the metal-ring distance by as much as 0.1 Å.[68]

Pierloot *et al.* tackled ferrocene using CASSCF and CASPT2 calculations.[69] They obtained 1.643 Å for the Fe-Cp centroid distance, and their success was attributed by Koch *et al.* primarily to the inclusion of orbital relaxation effects in the CASSCF procedure.[66] Indeed, Koch *et al.* suggested that the ferrocene problem is essentially one of accounting for the dynamical correlation effectively.[66] To illustrate this, they used coupled-cluster (CC) theory with single and double excitations (CCSD) to optimise the metal-ring distance, correlating either 66 or all 96 electrons. Correlating more electrons, or improving the basis set, generally shortens the metal-ring distance, yielding 1.672 Å and 1.664 Å respectively when 66 or 96 electrons are correlated.[66] Using CCSD(T), and correlating 66 electrons, gives a metal ring distance of 1.660 Å. A recent study by Coriani *et al.* fully optimised the structure of ferrocene to give a metal-ring distance of 1.670 Å with CCSD and 1.655 Å with CCSD(T) when 66 electrons were correlated.[67]

Lüthi used the CCSD method, correlating 58 electrons,[63] to give a metal-ring distance of 1.633 Å, rising to 1.652 Å with CCSD(T). Interestingly, the $\mathscr{T}_1$ diagnostic calculated for a CC wavefunction was 0.049.[63] This is appreciably higher than the normally accepted limit of 0.02 for closed-shell species, as set out by Lee

Figure 3.2: MO diagram showing the interaction between the ring π-orbitals and the metal orbitals. The HOMO is indicated by the half arrows.

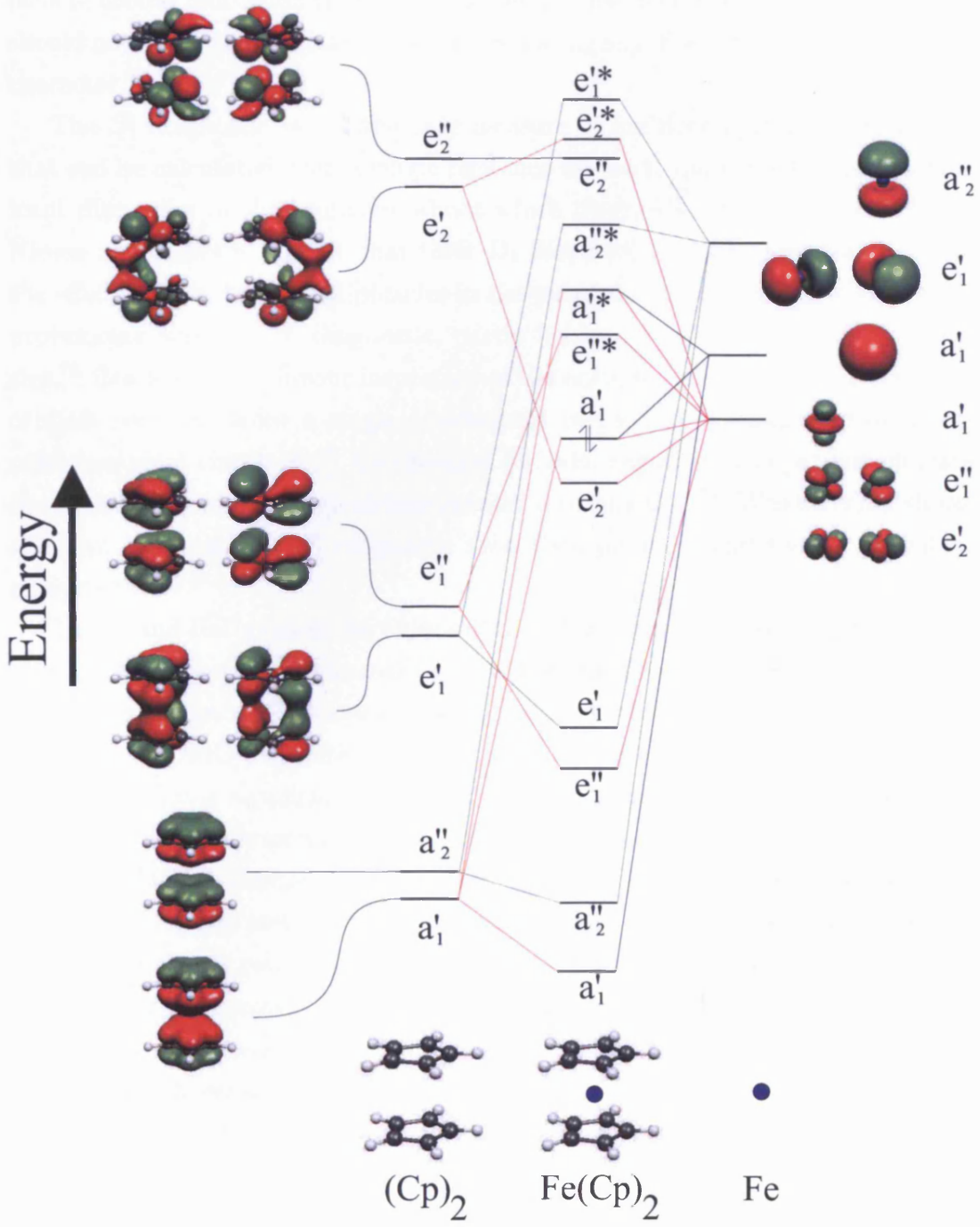

and Taylor,[10] above which one would usually consider single reference methods to be unreliable due to the onset of multiconfigurational character. However, given that there is expected to be only limited multiconfigurational character in ferrocene (e.g. the HOMO-LUMO gap calculated by Taylor and Hall is approximately 16 eV[70]) and that single excitations are important, it is likely that it is the effects of orbital relaxation that lead to a high $\mathscr{T}_1$ diagnostic. Hence high $\mathscr{T}_1$ values should not necessarily be interpreted as indicating significant multiconfigurational character.[63,66]

The $\mathscr{T}_1$ diagnostic is not the only measure of multiconfigurational character that can be calculated from a single reference method, and there has been significant discussion in the literature about which diagnostic tool is the best.[48,78,79] Niesen and Janssen suggest that their D_2 diagnostic, which takes into account the effects of the doubles amplitudes in the coupled-cluster expansion, shows improvements over the $\mathscr{T}_1$ diagnostic, partly because it is independent of system size.[79] Gordon *et. al.* favour inspection of the occupation numbers of the natural orbitals resulting from a single-determinant method as a diagnostic of multiconfigurational character;[78] non-integral (or even negative) occupations indicate the breakdown of the single-determinantal wavefunction.[78] Whatever its shortcomings, however, the $\mathscr{T}_1$ diagnostic remains a popular (and readily available) analysis tool[80–89,a].

Taylor and Hall probed the failure of the HF method by inspecting the molecular orbital structure,[70] particularly how the energies of the orbitals vary with metal-ring distance. The most striking feature is that the a_1' Fe $3d_{z^2}$-based orbital is the HOMO-5 at both the experimental geometry and at the HF optimised geometry. This is significantly different from the generally accepted orbital structure of sandwich compounds, which places the metal d_{z^2}-based level much closer to the HOMO, as discussed above. Ishimura *et al.*, in a more recent study of the ground and excited states of ferrocene, noted the particularly poor ordering of the molecular orbitals resulting from a HF calculation.[71] The Koopmans' ordering is very poor when compared with the photoelectron spectrum, although the use of symmetry adapted cluster CI (SAC-CI) from the HF orbitals gives ionisation energies which agree well with experiment.[71] However, considerable mixing of configurations is necessary to achieve this good agreement, probably because of the poor quality of the HF orbitals.

The use of density functional theory at the (LCGTO)Xα level found a metal-ring distance of 1.603 Å,[72] marginally better than contemporary CI calcula-

[a]The papers indicated are some of those published between January and June 2007.

tions,[70,73] but at much reduced computational expense. Delley *et al.* note that the Xα method "did not show many of the inadequacies of the Hartree-Fock model."[74] More recent DFT studies, including full geometry optimisations, have obtained remarkable results. BPW91 finds the metal-ring distance to deviate from experiment by less than a thousandth of an Ångstrom,[75] while the use of B3LYP, BLYP and BP86 gives metal-ring distances within 0.02 Å of the experimental structure.[76] Xu *et al.*, find the HOMO to be of e_2' symmetry with $3d_{xy}$ and $3d_{x^2-y^2}$ contributions from iron, while the HOMO-1 is of a_1' symmetry, with $3d_{z^2}$ character.[76] This is consistent with the photoelectron spectrum and generally accepted MO structure. A recent study by Bühl *et al.* using BP86, with an Ahlrichs split QZVP basis set reports the metal-ring centroid distance to be 1.651 Å.[90] The success of DFT in modelling the geometry of ferrocene may therefore be (partly) due to its correct modelling of the orbital structure, in contrast to HF theory. With *ab initio* methods, correlation treatments including single excitations are necessary to obtain the correct geometry, suggesting that the HF reference is poor.

3.1.2 The Geometric and Electronic Structures of Iron Pentacarbonyl

The bonding in Iron Pentacarbonyl (IPC) is an example of the synergic bonding in many transition metal complexes. Although the nature of the bonding is quite complex, in IPC it is possible to simplify the bonding mechanism by a group theoretical analysis.

The carbonyl ligand (CO) has a MO structure typical of the first row molecular diatomics. The carbon and oxygen 2s and $2p_z$ orbitals combine to form σ interactions, while the $2p_{x,y}$ orbitals form π interactions. The HOMO in CO is of σ-antibonding character, and is essentially a combination of the C and O $2p_z$ orbitals, although it is mainly carbon based. The LUMO is a degenerate pair of orbitals; the antibonding π-combination, and again is mainly carbon based. The HOMO from CO is responsible for donating electron density to iron through σ interactions with the metal orbitals of the correct symmetry. Each ligand donates two electrons, which allows iron to fill its 18 electron expanded octet. The LUMO of CO can receive electron density from iron, and thus back-bonding interactions are formed. This electron density pushed into the antibonding π-orbital of the CO ligand results in a weakening of the C-O bond with the strengthening of the M-C bond. The strength of the M-C bond can thus be quantified by the effect

it has on the carbonyl stretching frequency, which can easily be probed by IR spectroscopy.

The symmetry adapted linear combinations (SALCs) of the σ donating orbitals of CO under D_{3h} symmetry are a_1', a_2'', e' and a_1'. These combinations should have similar energies to the metal 3d orbitals, which transform as a_1', e', e''. As a result, the a_2'' combination is expected to be essentially non-bonding. These combinations are shown in figure 3.3. The higher lying CO back-bonding orbitals transform as a_2'', a_2', $2e'$ and $2e''$. The a_2' combination has no symmetry match with a metal orbital, and so forms a non-bonding pair. These back-bonding combinations are similar in energy to the 4p metal orbitals, which transform as a_2'' and e'. The higher lying e'' ligand combination does not have a close energetic match with a metal orbital of the correct symmetry, and so is expected to be essentially non-bonding.

Because it is not possible to completely separate out the forward and back-bonding orbital interactions (since they span, in part, the same irreps), the MO diagram for $Fe(CO)_5$ is fairly complex. A further complication is the π-bonding interactions of carbon with oxygen, which although not considered to have significant overlap with the metal orbitals, do contribute to the character of some orbitals because they also span the same irreps at similar energies. A schematic molecular orbital diagram is shown in figure 3.4.

The HOMO is expected to be formed from the $3d_{xy,x^2-y^2}$ metal orbitals, which can interact with the forward bonding, and back-bonding combination of ligand orbitals. The LUMO is expected to have largely ligand back-bonding character, however the many close lying levels make it difficult to predict the exact character. $Fe(CO)_5$ has a significant HOMO-LUMO gap, and is closed-shell. It is thus expected to be well represented by a single reference wavefunction, and so should be treated accurately by the more correlated *ab initio* methodologies, without the requirement for multiconfigurational techniques.

However, iron pentacarbonyl has been as difficult to study theoretically as ferrocene.[64,74,91–97] The experimental structure from gas phase electron diffraction studies show iron pentacarbonyl to have a D_{3h} structure with an axial M-C bond length of 1.807 Å and an equatorial bond length of 1.827 Å; the axial metal-carbon bonds are slightly shorter than the equatorial bonds by 0.02 Å.[98] In its solid form, x-ray crystallography indicates that the axial metal-carbon bonds are the longer.[99]

In an early study Pietro and Hehre used HF with an STO-3G basis set, calculated an equatorial bond length of 1.643 Å, and an axial bond length of 2.016

Figure 3.3: MO diagram of the carbonyl ligand showing the splitting into the symmetry adapted linear combination of orbitals under D_{3h} symmetry. Only the splitting of the orbitals considered to be involved in bonding, or back-bonding to the metal are considered.

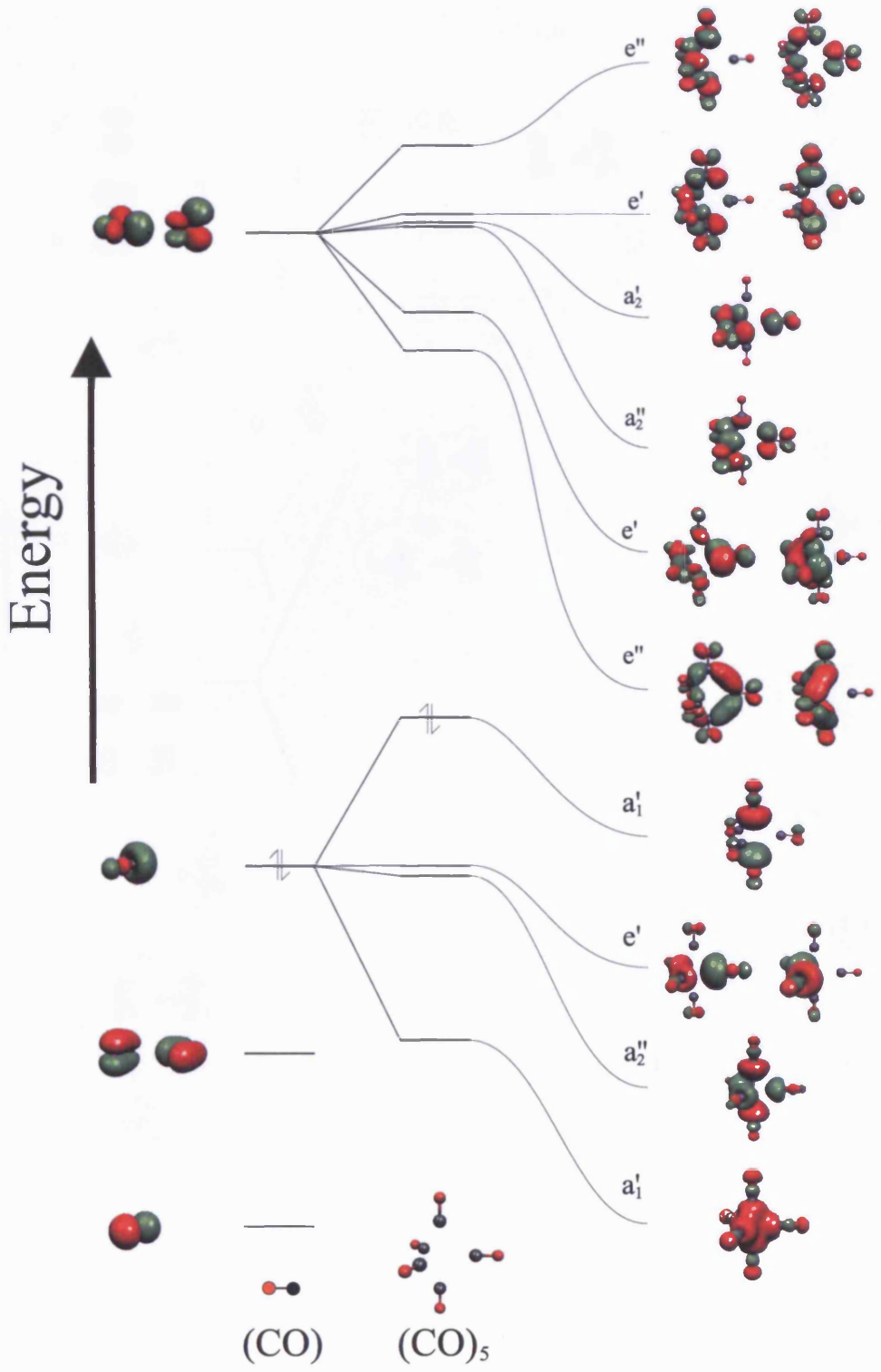

Figure 3.4: Schematic MO diagram for iron pentacarbonyl. Only the SALCs of the carbonyl ligands that take part in the bonding to the metal are considered. The higher lying orbitals of σ antibonding character are not shown, however these may interact with the metal 4p orbitals.

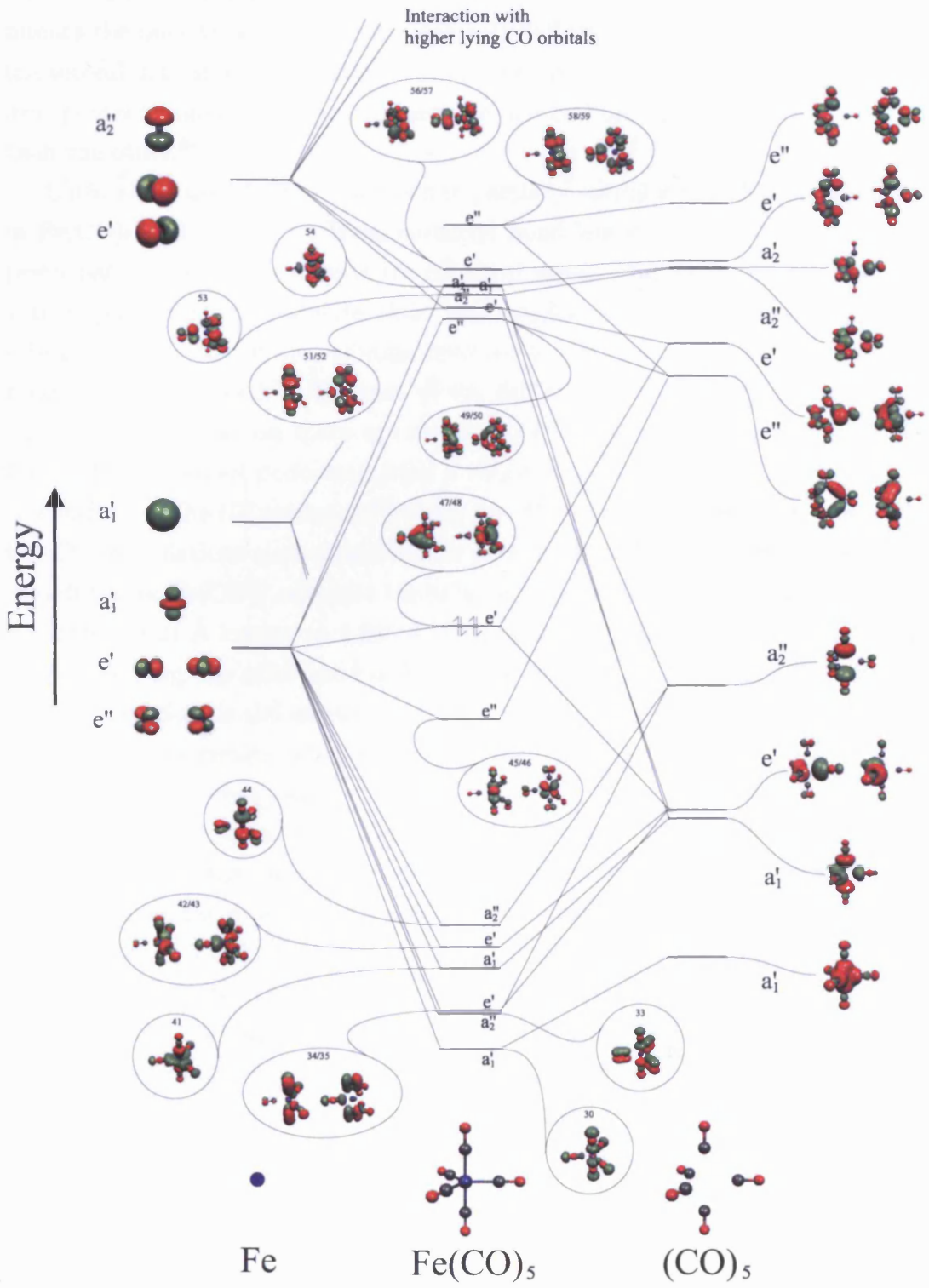

Å, thus each bond length is in error by approximately 0.2 Å and the calculation is seen to both under and over estimate bonds of the same type in the same molecule.[91] Demuynck *et al.* improved this result by calculating a HF structure in which the equatorial metal-carbon bond length matched well with experiment, but the axial bond was 0.15 Å longer than the equatorial bond.[92] This behaviour mimics the poor treatment of ferrocene with HF theory, except that in ferrocene the second indicator of performance is lacking, as it has no equatorial ligands; for iron pentacarbonyl HF seems to describe one carbonyl position more precisely than the other.[64]

Lüthi *et al.* used CCI calculations to partially optimise the M-C bond lengths in $Fe(CO)_5$, with fixed, identical carbonyl bond lengths.[64] This technique uses perturbation theory to estimate the effects of most of the single excitations. The active space used to calculate their best results correlated 10 electrons in 10 orbitals, thus some of the orbitals involved in the metal-carbonyl bonding interactions are ignored.[64] Because of the difficulties of performing an MCSCF calculation on an active space of this size with the resources they had available, the CCI was instead performed from a reference generated using an initial CCI calculation on the HF reference.[64] Using the HF reference as the sole reference for the CCI calculations gave structures as poor as those just using HF. Their best structures for $Fe(CO)_5$ calculate the axial M-C bond at 1.815 Å, and the equatorial bond 0.021 Å longer, at 1.836 Å.[64] Although both of these bond lengths are 0.01 Å too long, the axial bond is the correct amount shorter than the equatorial. What is not clear is the extent to which the incomplete treatment of the system influences these results; what would have happened to the structures if a bigger active space had been used?

Persson *et al.*, in a later study of $Fe(CO)_5$, used CASSCF and CASPT2.[93] They comment that the use of multiconfigurational treatments is necessary in systems where the d-orbitals are split into two sets (the double-shell effect) such as in $Fe(CO)_5$. Their treatment also uses a 10/10 active space, which correlated the 5 3d-orbitals, the CO axial σ-donating orbital with a_1' symmetry, and a pair of ligand e' and e'' orbitals.[93] Their CASPT2 calculation correlated the full valence space, freezing only the 1s orbitals on carbon and oxygen, and the 1s-3p orbitals on iron. The effects of basis set superposition error were included at the CASPT2 level. Again, this study assumes identical CO bond lengths, although these are optimised. CASPT2 gives M-C bond lengths of 1.792 Å and 1.798 Å for the axial and equatorial environments respectively.[93] The inclusion of the BSSE correction improves the agreement with experiment, giving 1.800 Å and 1.810 Å. Inclusion

of relativistic effects result in final values of 1.791 Å and 1.800 Å respectively.[93] These results are both about 0.02-0.03 Å too short, and they predict a shorter axial than equatorial distance. Although these results are of good quality, again, the whole system has not been treated in the active space, and it is unclear how this has influenced the results.

The multiconfigurational character of $Fe(CO)_5$ is not considered to be large. The CI calculations of Lüthi *et al.* gave dominant CI coefficients of approximately 0.9 for their equilibrium structure. The study of Persson *et al.* gave the natural occupations of the CASSCF wavefunction with a maximum of 0.15 of an electron in the vacant orbitals of the HF reference state. The system is therefore dominated by the HF reference, so the CC technique should well describe the system.

Lüthi *et al.* suggest a reason why the axial M-C bond length might be shorter than the equatorial. In a simple ligand field model the d^8 configuration of iron should have the d_{z^2} orbital vacant. This is more directionally localised along the z-axis of the molecule, and thus has a better overlap with the axial CO than with the equatorial ligands through the less directional torus.[64] The $3d_{xz,yz}$ e'' orbitals can form effective back-bonding interactions with both axial and equatorial ligands, but do not take part in the σ bonding. The $3d_{xy,x^2-y^2}$ orbitals can form both σ and π bonds with the equatorial ligands, but the π back-bonding must offset the charge donation from the σ interaction to the $3d_{xy,x^2-y^2}$ orbitals which are formally already occupied.[64] Consequently σ donation from the axial sites can be expected to be stronger, since it is not necessary to offset the charge donation to the unoccupied d_{z^2} orbital with π back-bonding, and thus the axial bond should be shorter.

Ab initio calculations using the multi-coupled pair functional (MCPF) were used to fully optimise the structure of iron pentacarbonyl.[97] These results are significantly better than those from the HF treatment, but the method still seems to perform better at predicting the equatorial metal-carbon bonds than the axial ones, predicting the axial bond to be longer than the experimental results. They comment that the refinement model used in the gas phase electron diffraction study of Beagley and Schmidling assumed the carbonyl bonds to all be the same length.[98] They wonder how the metal-carbonyl distances would have changed if the model was instead fully optimised.[97]

Other groups have attempted to study systems involving iron pentacarbonyl with *ab initio* methods. Apostolova *et al.* attempted to deduce the mechanism of thermolysis of iron pentacarbonyl using MP2.[100] The electron correlation effects

in this system are over estimated by MP2, in the same way as they are in ferrocene. The predicted metal-carbon distance is 1.67 Å for the axial, and 1.68 Å for the equatorial. Although both distances are significantly shorter than the gas phase model,[98] and the energy for removal of a single carbonyl ligand is over estimated by 3.5 times the expected amount, they point out that the environments are at least described such that the axial ligands have a shorter metal-carbon bond than the equatorial![100] Lüthi's study, using CCSD(T), gives very reasonable results, but like the majority of the other correlated methods (with the exception of MP2 and CI), the equatorial metal-carbon bond length is calculated accurately (within 0.001 Å of experiment) while the axial bond is over estimated.[63] Although the CCSD(T) structure is of "unexpectedly good quality",[63] it is accompanied by a $\mathscr{T}_1$ diagnostic larger than might be deemed acceptable, although the value is not given.

Density functional theory using the local density approximation also has problems describing the bonding in iron pentacarbonyl, calculating both metal-ligand bonds to be 1.77 Å, somewhat shorter than the experimental result.[94] This is typical of the over binding usually encountered with LDA.

Li *et al.* used gradient corrected DFT with a quasi-relativistic correction to study iron pentacarbonyl.[96] Their results agree well with experiment to 0.01 Å, and thus GGA functionals seem to perform as well as CASSCF,[64] except that their calculations also give the axial metal-ligand bonds to be longer than the equatorial, by 0.004 Å.[96] Delley, Wrinn and Lüthi, using B88-LYP, also overestimate the axial metal-ligand bond by 0.01 Å and underestimate the equatorial bond by an similar amount.[74] Matveev *et al.* calculated the geometry of iron pentacarbonyl with the PBE functional. Again, this reproduces the experimental results for the equatorial environments to within 0.007 Å, but the axial bond is too long, by about 0.02 Å.[95] A more recent DFT study by Bühl *et al.* with BP86 and a QZVP Ahlrichs basis set, calculated an axial metal-carbon bond length of 1.8080 Å, and an equatorial bond of 1.8079 Å.[90]

Due to the discrepancies between the structure of iron pentacarbonyl as predicted by various *ab initio* and DFT studies, and the electron diffraction result, it was decided by McClelland *et al.* to re-characterise iron pentacarbonyl experimentally. In their structural refinement model, they refined four variables under D_{3h} symmetry; the axial and equatorial metal-carbon bond lengths and the axial and equatorial carbonyl bond lengths. This model uses the rotational constants from the geometric structure as calculated with B3LYP as a refinement parameter to be compared with the experimental values from rotational spectroscopy.

This model also includes the effect of multiple scattering. The data from their best model structure gives the average iron-carbon bond length to be 1.829 Å, while the axial bond is shorter that the equatorial by 0.032 Å.[101] They claim that the statistical probability that the axial environment is longer is "absolutely negligible".[101]

If the wealth of theoretical data is considered, then it would seem that although the best single reference *ab initio* methods match well with experiment, none of them reflect the difference between the axial and equatorial metal-carbon bonds correctly. This trend is reflected by the CASSCF calculation, although in the study by Lüthi the carbonyl bond lengths are not individually optimised,[64] and it is not clear to what extent the incomplete treatment of the bonding by the choice of active space influences these results. Given the synergic nature of the bonding in iron pentacarbonyl, this is likely to place quite a constraint on the iron-carbon distances.

3.1.3 KS orbitals as a reference for further correlation treatments

In a CCSD(T) study of iron carbonyl species, Harvey and Aschi[102] highlight a general problem in using the $\mathscr{T}_1$ diagnostic as a measure of multiconfigurational character.[b] They find $\mathscr{T}_1$ diagnostics in the range 0.04-0.06, reminiscent of that calculated for ferrocene by Lüthi.[63] They imply that the coupled-cluster $\mathscr{T}_1$ diagnostic can be particularly misleading for systems where the HF reference is known to show fundamental inadequacies, e.g. in transition metal complexes. To demonstrate that the $\mathscr{T}_1$ diagnostics are large because of an underlying problem with the reference function, Harvey and Aschi performed coupled-cluster calculations from a density functional based reference (i.e. Kohn-Sham (KS) orbitals), arguing that since this reference will include some electron correlation, it is expected to be better than HF for coupled-cluster calculations. They were rewarded by $\mathscr{T}_1$ diagnostics in the range 0.02-0.025.[102]

In general, the technique of conducting coupled-cluster calculations from a density functional based reference has not been used extensively, probably because it shows little improvement compared with coupled-cluster from a HF reference, apart from in certain difficult systems.[103–105] A second reason may be that because the eigenfunctions which result from a density functional calculation do not describe a true "wavefunction" as they do in *ab initio* based methodologies, it

[b]Although this study reports energetic details for $Fe(CO)_5$, such as bond dissociation energies, it does not report any optimised geometries for this species.

is formally incorrect to use them as a reference for further correlation treatment. This is in much the same way that the spin contamination evaluated by DFT should really be calculated with a $\langle S^2 \rangle$ functional rather than from the eigenvalues of the Kohn-Sham orbitals. However, this is a commonly used technique because it produces chemically sensible results. If a DFT "wavefunction" can be used successfully in such a way, why should it not be possible to use it as a reference for higher level correlation treatments?

Villaume *et al.* have used CCSD and CCSD(T) from a KS reference to calculate the energy splitting between the electronic states of $NiCH_2^+$.[103] The poor performance of HF theory, due to spin contamination problems, causes the $^2A_2$-$^2A_1$(g.s.) splitting to be four times that calculated with CCSD, with either a HF or a KS reference. Although the choice of reference makes little difference to the CCSD energy, it does dramatically alter the spin contamination in the CCSD wavefunction, reducing $\langle S^2 \rangle$ from 2.43 with a HF reference to 2.09 with a KS reference.[103]

Beran *et al.* used CCSD with a BLYP reference to study a variety of diatomic radical systems. For these open-shell species it is known that HF and MP2 perform erratically, and these workers conclude that KS based coupled-cluster methods can offer cost effective methods to treat these difficult systems with near closed-shell accuracy.[104]

Graham *et al.* studied the activation of N_2 with molybdenum amine complexes using a variety of coupled-cluster based methods, including KS-CCSD(T), HF-CCSD(T) and OD(T).[c] They note that the use of these different methods provides qualitatively similar descriptions of the surface, but with significantly different energetics.[105] In complex transition metal systems, such as those studied, Hartree-Fock usually provides a poor description of the system, even qualitatively, due to the open-shell wavefunction breaking spin and spacial symmetry. They comment that because of the poor HF reference they expect HF-based Møller-Plesset perturbation results to be unreliable,[105] because the perturbation to the wavefunction cannot be considered small. Although OD(T) gave better results than HF-CCSD(T), it was found to be computationally too expensive to perform for the whole system.[105] KS-CCSD(T) and HF-CCSD(T) were both computationally accessible, and the KS-CCSD and KS-CCSD(T) results generally agree well with those from OD and OD(T) where these methods were used.[105]

[c]In OD(T) the (initially Hartree-Fock) reference wavefunction is optimised to minimise the CC energy, and so the triples contribution is more reliable, presumably because the perturbation is smaller.

KS orbitals have also been used as a reference for Møller-Plesset perturbation theory. Bouř studied a range of simple open and closed-shell species with the aim of demonstrating that the KS determinantal "wavefunction" can indeed be used as a reference for further correlation treatments.[106] However, this study concludes that at the MP2 level the KS reference leads to a less accurate result than the use of a HF reference.[106]

Overall, then, it appears that it is not unreasonable to use a KS reference as a starting point for higher level treatments of correlation, especially CC methods. Chemically sensible results can be obtained with computational costs similar to conventional techniques, but with the added benefit of better performance on difficult systems. Presumably this is because the reference is more robust in systems where the mean-field approximation is unable to adequately describe the system even qualitatively. Perturbation theory with a KS zero-order wavefunction appears not to perform quite so well. This may, however, only be the case for systems where the HF reference is adequate. If the perturbation is large, then this situation might be reversed. However, if KS-CC can be afforded, this is clearly preferable to KS-MP methods.

The aim of this project is to evaluate the performance of Kohn-Sham based coupled-cluster calculations on iron pentacarbonyl and ferrocene (both systems where the HF reference is poor), with the purpose of determining if (a) that when a KS reference is used for the coupled-cluster expansion that the $\mathscr{T}_1$ diagnostic is substantially reduced (to below the threshold where one might expect the onset of multiconfigurational character), and (b) that the KS-CC geometries are chemically sensible for these systems. The structure of $Fe(CO)_5$ is investigated in some detail, with both single reference and multiconfigurational methods, and the effect of a variety of different basis sets is considered. Particularly, will the KS-CC calculations compare well with experiment generally, and in particular improve on the iron pentacarbonyl geometry to give an axial metal-carbon bond shorter than the equatorial?

3.2 Computational Methodology

3.2.1 General *ab initio* and density functional calculations

The calculations were performed with the MOLPRO 2002.6 and 2006.1[57,107–118] program packages, using the Ahlrichs valence triple-ζ basis set on iron, supple-

mented with a set of f-functions with a radial exponent of 1.633, and the Ahlrichs polarised valence double-ζ basis set on carbon, oxygen and hydrogen. This basis set is similar to that used by Koch *et al.*[66]

Calculations were performed at the following levels of *ab initio* theory, HF, MP2, MP3, MP4(sdq), CCD, CCSD, and CCSD(T). Density functional calculations were conducted using the following functionals; VWN,[119,120] BLYP,[121–123] BP86,[121,124] B3LYP,[22] PBE,[21] PBE0,[125] PW91,[126] B97[127] and B97R.[128] The coupled-cluster calculations were performed from five different reference functions; the standard Hartree-Fock reference, and Kohn-Sham references generated by the B3LYP, BLYP, BP86 and PBE density functionals.

The coupled-cluster calculations employed a variety of different core sizes, although the majority of the calculations either used the standard core (core 5) where 54 electrons are correlated, or core 3, correlating 86 electrons. In the 86 electron treatment, there is no core present on the main group atoms. Table 3.1 details the core sizes. The Møller-Plesset calculations treated all of the electrons. Analytic gradients were employed for HF and the density functional techniques, while the remaining methods (including MP2) used numerical gradients.

For ferrocene, geometry optimisations were carried out using the aforementioned methods. Full optimisations were performed under D_{5h} symmetry constraints, and also partial optimisations in which the ring geometry was fixed at the experimental values, and only the metal-ring centroid distance (r_1) optimised. The effect of core size was gauged by performing partial geometry optimisations of the metal-ring centroid distance.

Fully optimised geometries were calculated for $Fe(CO)_5$ under D_{3h} symmetry, using the same set of density functionals and *ab initio* methods as for ferrocene. KS-CC calculations were, however, only performed using the B3LYP reference.

Table 3.1: The definition of the core sizes used, giving the breakdown into the functions on iron, carbon and oxygen.

Core Number	Atom		Number of Valence Electrons
	Iron	Carbon Oxygen	
1	-	-	96
2	1s	-	94
3	1s2s2p	-	86
4	1s2s2p	1s	66
5	1s2s2p3s3p	1s	54

Partial optimisations at fixed carbonyl bond lengths were used to investigate the constraint this imposes on the metal-carbon bond lengths. The calculations used B3LYP, PBE and CCSD (core 5) with the standard Ahlrichs basis set as described above.

$\mathscr{T}_1$ diagnostic values were calculated at the coupled-cluster optimised geometries using the method of Lee and Taylor,[10] using both HF and KS-based coupled-cluster wavefunctions.

3.2.2 Coupled-cluster calculations involving Kohn-Sham orbitals

Coupled-cluster calculations were performed from the Kohn-Sham references in the following way. Initially, a density functional single point calculation was performed, and the orbitals saved. These orbitals were then read into an HF calculation, set to perform zero iterations, and saved. The orbitals were then read into the closed-shell coupled-cluster code. Geometry optimisations were performed using the manual geometry optimisation routine, with the forces calculated by looping back to the initial density functional calculation each time, such that the gradient was calculated using the KS-CC technique rather than the HF-CC technique (which would be performed by the automatic optimisation routine). A final KS-CC single point was calculated at the optimised geometry.

Because of the infancy of this method, and its use by relatively few groups,[102–105] who all use different codes, and thus slightly different methods, I sought to confirm that the method that I am using is computationally robust. Professor Peter Knowles voiced two particular issues with the use of this technique, firstly that it may not be safe to rely on the use of the zero-iteration technique for treatment of the reference, because newer versions of the MOLPRO code may not behave in the same way, and secondly that the closed-shell CCSD(T) code makes the assumption that the reference orbitals diagonalise the Fock matrix, and that the restricted open-shell CC code (rCC) is more robust in this respect.[129] If the rCC code is used, then the CC calculation can be performed directly after the density functional calculation, and the zero iteration HF step is not required. However it is found that its presence makes no difference to the rCC energy, thus indicating that it really is a passive step.

For ferrocene it is found that although KS-CCSD and KS-rCCSD agree to $1\text{x}10^{-6}$ H (indeed HF-CCSD and HF-rCCSD agree to the same degree), the agreement between KS-CCSD(T) and KS-rCCSD(T) is less good, in the order of mH. This behaviour has also been noted by Jeremy Harvey, in that he finds the KS-

rCCSD(T) results for N_2 seem to give a better agreement with the results of Graham *et al.*[105] than KS-CCSD(T), although he notes that the difference he finds (.3 mH) is generally small enough to be within the errors expected of such calculations due to other factors.[130] It might be expected that this error would scale with the size of the system,[130] and indeed this seems to be the case, however, I expect it to remain fairly constant for similar geometries of the same species, such that the optimised geometry is less sensitive to this effect than the energy, because energy differences are being considered and this error would largely cancel.

Since the absolute energy of the system from different methods is not being compared, only used to calculate optimised geometries, I have chosen to use the KS-CCSD(T) code, because it represents a significant reduction in computational expense over the use of the KS-rCCSD(T) code. However, an attempt has been made to gauge the effect on the geometry of the error from using this "less robust" CC code, by optimising the metal-ring centroid distance in ferrocene using HF-CCSD, HF-CCSD(T), HF-rCCSD, HF-rCCSD(T), B3LYP-CCSD, B3LYP-CCSD(T), B3LYP-rCCSD and B3LYP-rCCSD(T). The HF-rCC and HF-CC results agree with each other to a thousandth of an Ångstrom for the metal-ring centroid distance (indeed the methods should be exactly equivalent), as is the agreement between KS-CCSD and KS-rCCSD. Upon the inclusion of triples (KS-CCSD(T) and KS-rCCSD(T)), a discrepancy of a few thousandths of an Ångstrom is seen for the metal-ring centroid distance, however, the potentials are of the same shape, with a fairly shallow gradient at the minimum energy structure, despite being offset by a couple of mH. I would argue, given the substantial reduction in the time taken to run the calculations, this difference in structure from using the closed-shell code over the restricted-open-shell code, is small enough to be acceptable.

3.2.3 Assessment of the effect of basis set

Gaussian 03[12] was used to assess the effect of basis set size on the structure of iron pentacarbonyl. Full geometry optimisations were performed using PBE, B3LYP and CCSD (core 5), with Pople style basis sets between 6-31G and 6-311+G(3df) on all atoms. Further optimisations were performed using the 6-311+G(2df) basis on iron, and Dunning's correlation-consistent basis sets on the main group atoms between cc-pVDZ and cc-pV5Z. The effect of adding diffuse functions was also investigated. To assess the effect of Slater type orbitals (STOs) and relativistic effects on the structure, the Amsterdam Density Functional (ADF)

2006.01 package[131–133] was used with ZORA basis sets between SZ and QZ4P to calculate optimised structures with BLYP and PBE. Further details of the basis set combinations are given in section 3.4.4.

3.2.4 Multiconfigurational calculations

$Fe(CO)_5$ represents a system of significant size for an MCSCF calculation, for to treat the system, one ideally would choose an active space that contained all five 3d metal orbitals, the five σ and 10 π SALCs from the ligands and perhaps the metal 4s and 4p orbitals. This represents a 18/24 system (or a 18/20 without the 4s and 4p orbitals), which is far beyond the scope of current hardware and time constraints!

In this study, the active space chosen is of 16/14 size, and includes the five 3d metal orbitals, the 4 σ ligand combinations with symmetries other than a_2'', and the two lowest lying pairs of π orbitals with e' and e'' symmetry. Finally, the 4s iron orbital was included. The a_2'' σ and π combinations are essentially non-bonding, while the a_2' orbital does not have a symmetry match on the metal. The higher lying e' and e'' π back-bonding combinations only interact weakly with the metal, having mainly ligand character. After the initial MCSCF calculation, the 14^{th} orbital was dropped from the active space, since it was found to be very contracted on the iron centre, and thus not involved in the metal-ligand bonding. This orbital also had an essentially zero natural occupation.

An MRCI calculation was used to introduce dynamical correlation into the system. Excitations were considered from 24 valence orbitals, including the 13 from the active space of the MCSCF calculation. This included the a_2'' carbonyl combination, and the 10 orbitals with π bonding combinations internal to the carbonyl ligands. During the geometry optimisation the structure was minimised on the Davidson corrected energy. Excitations were considered from reference states which contribute to the MCSCF wavefunction with weights greater than 0.1.

3.2.5 The RMS% difference measure for comparing theoretical and experiment structures

The difference between theoretical and experimental structures has been calculated as a root mean squared (RMS)% difference using the following equation:

$$RMS\% = \sqrt{\frac{1}{n}\sum_{1}^{n}\left(100\left(\frac{x_n^{theo} - x_n^{expt}}{x_n^{expt}}\right)\right)^2} \tag{3.1}$$

where n is the number of variables used in the optimisation and x_n is the value of that variable. Since the RMS% difference is dependent on the choice of variable in a system, it can only be used to compare the efficacy of different methods to reproduce a particular experimental structure, and because of the way that the quantity is normalised, it should not be used to compare between different structures. When n=1 the RMS% difference reduces to the absolute percentage difference, although, for consistency, the term RMS% difference is used irrespective of the value of n.

3.3 Results and Discussion - Ferrocene

3.3.1 Evaluation of the performance of *ab initio* and DFT methods

Initially a methodological survey was conducted using a variety of *ab initio* methods, and commonly used density functionals, using the Ahlrichs basis sets as described in section 3.2. Tables 3.2 and 3.3 gather together the geometric data obtained from optimisations of the metal-ring distance with the cyclopentadienyl rings held in the experimentally observed orientation,[134] and from full optimisation under D_{5h} symmetry. $\mathscr{T}_1$ diagnostic values were calculated for the optimised coupled-cluster wavefunctions, and are given in tables 3.2 and 3.3. Figures 3.6 shows the RMS% difference for these structures, for just the metal-ring distance from the partially and the fully optimised structures, and for all variables of the fully optimised structure respectively, as calculated with equation 3.1.

Inspection of figure 3.6, and the minimum energy structures in table 3.2 and 3.3, confirms the difficulty with which non-highly-correlated *ab initio* methods describe the geometry of ferrocene. HF predicts an over long metal-ring distance, with contracted cyclopentadienyl rings, while MP2 significantly underestimates the metal-ring distance, but with a better ring geometry. Increasing the order

to which the perturbation is considered, using MP3 and MP4(sdq), reveals the typical oscillation of the Møller-Plesset series,[2] except that the series appears divergent. MP3 overestimates the metal-ring distance by 0.08 Å, while MP4(sdq) underestimates it giving an even poorer result than MP2. MP4(sdq) suggests also that the hydrogen atoms should cant away from the metal, while all of the other methods used reflect the experimental structure with hydrogens that cant in towards the metal. MP4(sdq) includes the effects of single excitations, thought to be very important for the correct description of the wavefunction,[68] and so one might expect that the MP4 structure would be better than it is. However, it is likely that the failure of Møller-Plesset perturbation theory arises from a poor zero-order (HF) wavefunction, and so Møller-Plesset theory is inherently unreliable, even if performed to high orders, due to the perturbation to the zero-order wavefunction not being small.

By contrast to Møller-Plesset theory, all the coupled-cluster methods perform impressively, giving almost quantitative agreement with experiment. Our CC

Table 3.2: Structural and energetic data for the partial optimisation of ferrocene using a variety of different methods. The number in brackets after the CC methods indicates the core size used for these calculations (table 3.1). r_{FeX} is the metal to ring-centroid distance, and is defined in figure 3.5. The $\mathscr{T}_1$ diagnostic is given for the optimised coupled-cluster wavefunctions. a) The experimental geometry is that of Haaland *et al.*[134] The numbers in parentheses are the errors in the last digit of the quantity.

Method	r_{FeX} / Å	Energy/ Hartree	$\mathscr{T}_1$ Diag
HF	1.846	-1646.4650849	-
MP2	1.461	-1648.6564538	-
MP3	1.774	-1648.4979866	-
MP4(sdq)	1.371	-1648.8378066	-
CCD(C5)	1.656	-1648.1219902	-
CCSD(C5)	1.642	-1648.1774856	0.0459
CCSD(T)(C5)	1.631	-1648.2749342	0.0458
VWN	1.576	-1644.6464319	-
BP86	1.635	-1650.8048139	-
PW91	1.629	-1650.5309794	-
BLYP	1.671	-1650.4250387	-
B3LYP	1.668	-1650.1908958	-
PBE	1.632	-1650.0957223	-
PBE0	1.636	-1650.0972345	-
B97	1.662	-1650.3024793	-
B97R	1.664	-1650.3234974	-
Expt[a]	1.661(5)	-	-

Figure 3.5: The location of the geometric variables for ferrocene in the D_{5h} point group.

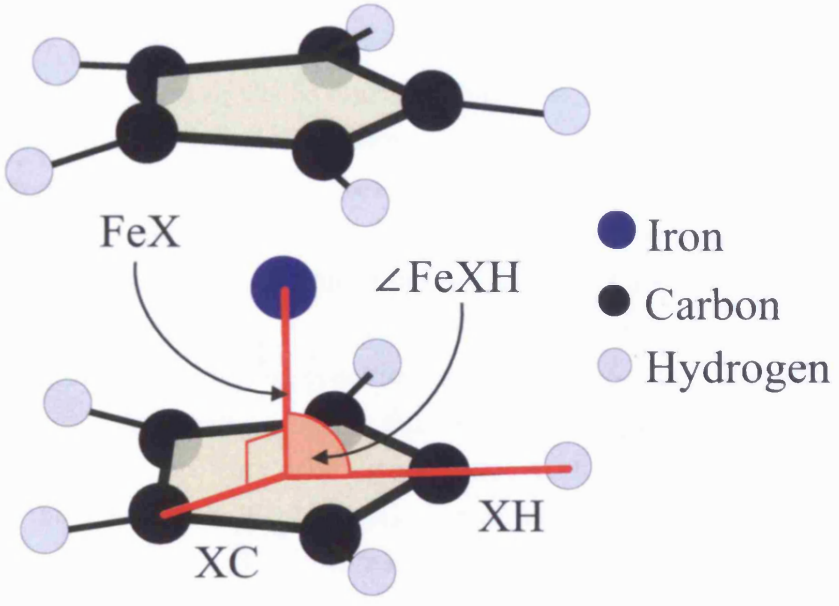

data also agree well with the previous studies of Koch *et al.*[66] and Coriani *et al.*,[67] with the metal-ring centroid distances agreeing to within three one-hundredths of an Ångstrom, when like methods are compared. This range of values is comparable with the error in the gas-phase electron diffraction structure of Haaland.[134] It is noticeable that the CCSD and CCSD(T) $\mathscr{T}_1$ diagnostic values are significantly above the limit of 0.02 as set out by Lee and Taylor,[10] as noted by previous workers.[63] This is discussed further in section 3.3.3.

By contrast to the HF and MP2 methods, density functional approaches perform remarkably well. The local density method underestimates the metal-ring distance, as might be expected, but the use of gradient corrected functionals improves the geometry such that the performance, as measured by the RMS structural difference, is as good as the coupled-cluster methods (figure 3.6).

3.3.2 The effects of core size on the coupled-cluster calculations

The effect of the core size used in the coupled-cluster expansion was investigated by optimising the metal-ring distance at the CCSD level with a variety of core sizes (table 3.1). For these calculations the rings were fixed in a planar HF optimised orientation. The difference between the Hartree-Fock and the experimental

geometry for the rings is not large, and we do not anticipate that the use of the former will make much difference to the core size analysis. The structural (r_1) and energetic data are collected in table 3.4, together with the $\mathscr{T}_1$ diagnostics, and figure 3.7 presents the r_1 and $\mathscr{T}_1$ data graphically. From figure 3.7 it can be seen that after inclusion of the 3s and 3p orbitals on iron in the correlation treatment (i.e. moving from core 5 to core 4), reducing the core size further makes increasingly smaller differences to the optimised metal-ring distance; removal of the 2s and 2p iron electrons from the core (i.e. core 3 to core 2) makes less than a one thousandth of an Ångstrom difference to r_1. There is a good correlation between the $\mathscr{T}_1$ diagnostic and the number of correlated electrons ($R^2 = 0.82$). This trend can be explained by considering orbital relaxation. The $\mathscr{T}_1$ diagnostic (equation 1.110) is normalised by the number of electrons included in the correlation treatment. As more core orbitals are included that do not require significant relaxation, the size of the $\mathscr{T}_1$ diagnostic is reduced.

Upon consideration of the data, I have chosen core 3 as the standard for fur-

Table 3.3: Structural and energetic data from the full optimisation of ferrocene using a variety of different methods. The number in brackets after the CC methods indicates the core size used for these calculations (table 3.1). The lengths and angles are defined in figure 3.5. The $\mathscr{T}_1$ diagnostic is given for the optimised coupled-cluster wavefunctions. a) The experimental geometry is that of Haaland *et al.*[134] The numbers in parentheses are the errors in the last digit of the quantity.

Method	r_{FeX} / Å	r_{XC} / Å	r_{XH} / Å	∠FeXH °	Energy/ H	$\mathscr{T}_1$ Diag
HF	1.857	1.200	2.279	89.87	-1646.4788773	-
MP2	1.459	1.226	2.315	89.76	-1648.6597826	-
MP3	1.782	1.208	2.295	89.49	-1648.5041542	-
MP4(sdq)	1.392	1.243	2.336	90.68	-1648.7510309	-
CCD(C5)	1.666	1.212	2.300	89.34	-1648.1262630	-
CCSD(C5)	1.649	1.215	2.305	89.63	-1648.1811205	0.0459
CCSD(T)(C5)	1.636	1.221	2.313	89.68	-1648.2774267	0.0462
VWN	1.583	1.215	2.315	89.55	-1644.6487685	-
BP86	1.637	1.224	2.322	89.78	-1650.8067529	-
PW91	1.632	1.223	2.318	89.77	-1650.5322859	-
BLYP	1.673	1.227	2.323	89.92	-1650.4273940	-
B3LYP	1.676	1.215	2.305	89.73	-1650.1947116	-
PBE	1.634	1.224	2.320	89.76	-1650.0968351	-
PBE0	1.645	1.212	2.300	89.57	-1650.1019112	-
B97	1.667	1.219	2.309	89.70	-1650.3054835	-
B97R	1.669	2.218	2.308	89.68	-1650.3264995	-
Expt[a]	1.661(5)	1.225(2)	2.328(8)	88.25(6)	-	-

Figure 3.6: The RMS% difference (equation 3.1) between the theoretical and experimental structures for ferrocence. The left hand side considers just the metal-ring centroid distance for each method used. The purple bars indicate the result if only the metal-ring distance is optimised and the cyclopentadienyl rings are held in their experimental geometry, while the green bars result from full optimisation, although only the metal-ring distance is used to calculate the bar length. The right hand side considers the RMS% difference taking into account the entire structure.

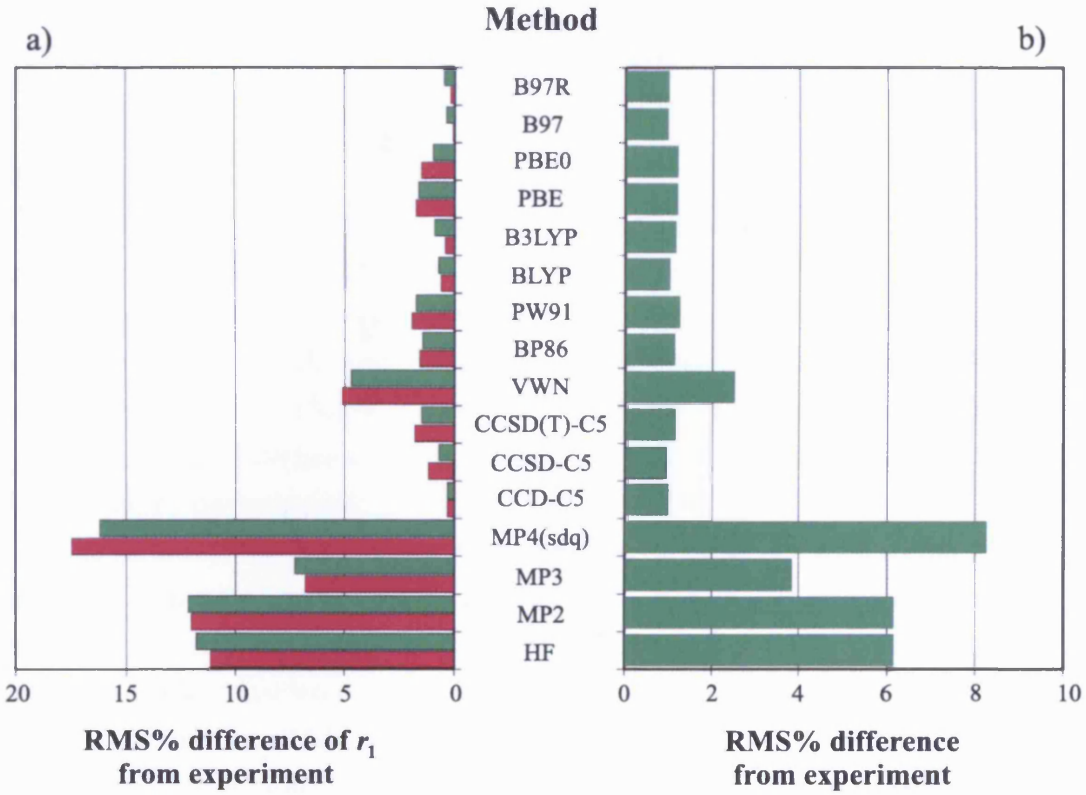

ther coupled-cluster calculations, as it best balances accuracy with computational speed. With this core 86 electrons are correlated, including all of the ligand-based electrons.

3.3.3 Kohn-Sham-based coupled-cluster calculations

We have chosen a subset of four functionals from those given in table 3.3 in order to generate the KS reference from which to perform a coupled-cluster expansion; these are BP86, BLYP, PBE and B3LYP. These were chosen not only because of their common use and general applicability to a wide variety of chemical systems, but also because they include examples of pure (BP86, BLYP), hybrid (B3LYP) and non-parameterised (PBE) functionals.

Table 3.4: Optimised metal ring-centroid distances, energies and $\mathscr{T}_1$ diagnostics for ferrocene using CCSD, with a variety of different core sizes. The core sizes are defined in table 3.1.

Core	r_{FeX} / Å	E/ Hartree	$\mathscr{T}_1$ Diag
1	1.6601	-1648.6128631	0.0352
2	1.6601	-1648.5759304	0.0356
3	1.6610	-1648.4883622	0.0373
4	1.6627	-1648.4600008	0.0426
5	1.6583	-1648.1774999	0.0407

Full geometry optimisations were performed, using CCD, CCSD and CCSD(T) from our chosen KS reference functions. For each optimised structure the $\mathscr{T}_1$ diagnostic was calculated. The results of these calculations are given in table 3.5 and figure 3.8, together with the results from coupled-cluster from a HF reference for comparison. Figure 3.8a shows the RMS% value for the whole structure (equation 3.1), while figure 3.8b considers only the metal-ring distance from the full geometry optimisation.

The results of the full geometry optimisations of ferrocene with coupled-cluster methods shown in figure 3.8 suggest that CCD from a HF reference reproduces experimental results slightly better than CCSD or CCSD(T) if just the metal-ring distance is considered (figure 3.8b), but CCSD performs slightly better if the entire structure is considered (figure 3.8a). The figures also show that the results of coupled-cluster from a KS reference are in all cases slightly worse than HF if equivalent methods are compared. However, all methods give results which are very close to experiment, and it could be argued that the differences between all of the geometries presented in table 3.5 are negligible. Indeed, a striking feature of figure 3.8a is how little difference in overall performance there is between the 15 methods employed - less than 0.3 separates the smallest RMS % difference from the largest.

Consideration of the $\mathscr{T}_1$ diagnostic (table 3.5) gives insight into the benefit of using a KS reference instead of the normal HF reference. Although the structural differences from experiment are very small independent of reference and method, a much smaller $\mathscr{T}_1$ diagnostic is observed for the coupled-cluster wavefunction from a KS reference. Two conclusions can be drawn from this. First, it is confirmed that the $\mathscr{T}_1$ diagnostics from the HF-based calculations do not give a true indication of the multiconfigurational character in the wavefunctions, since

Figure 3.7: The effect of the number of correlated electrons on the metal-ring centroid distance (r_1) and $\mathscr{T}_1$ diagnostic in ferrocene. The numbers next to the points on the graph are the core size numbers (table 3.1).

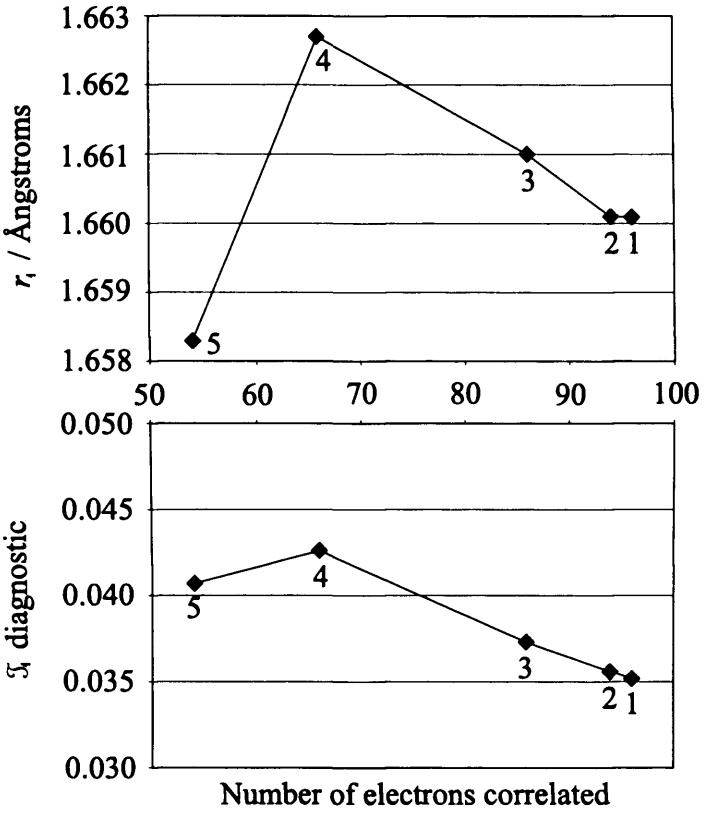

KS-CC is also an inherently single configurational method and gives acceptable $\mathscr{T}_1$ diagnostics. Second, if the large $\mathscr{T}_1$ from a HF coupled-cluster calculation is mainly a result of orbital relaxation due to the poor reference function, and for KS-CC these large singles amplitudes are not necessary to improve the reference (giving a much smaller $\mathscr{T}_1$ diagnostic value), then the KS reference is a better description of the MO structure. In order to probe this further I now turn to a comparison of the HF and B3LYP MOs, the latter being chosen because of the exceptionally low (0.0075) $\mathscr{T}_1$ diagnostics in the coupled-cluster calculations.

3.3.4 Comparison of the HF and B3LYP valence molecular orbitals

Figure 3.9 shows the relationship between the HF molecular orbitals and the B3LYP orbitals at the experimentally observed geometry. It can immediately be seen that the molecular orbital ordering is very different, in both the occupied and

Table 3.5: Structural and energetic data for ferrocene using coupled-cluster methods from a variety of different reference functions. The definition of the lengths and angles are given in figure 3.5. The $\mathscr{T}_1$ diagnostic is given for the optimised coupled-cluster wavefunctions. a) The experimental geometry is that of Haaland *et al.*[134] The numbers in parenthesis are the errors in the last digit of the quantity.

Method	r_{FeX} / Å	r_{XC} / Å	r_{XH} / Å	∠FeXH / °	Energy / Hartree	$\mathscr{T}_1$ Diag
HF-CCD	1.666	1.210	2.298	89.36	-1648.4348611	-
HF-CCSD	1.653	1.214	2.302	89.64	-1648.4913249	0.0378
HF-CCSD(T)	1.638	1.220	2.310	89.69	-1648.5966507	0.0381
BP86-CCD	1.636	1.212	2.299	89.51	-1648.4123994	-
BP86-CCSD	1.644	1.213	2.300	89.50	-1648.4575438	0.0127
BP86-CCSD(T)	1.636	1.220	2.311	89.67	-1648.5987452	0.0126
BLYP-CCD	1.636	1.212	2.299	89.51	-1648.4123994	-
BLYP-CCSD	1.644	1.213	2.300	89.50	-1648.4565704	0.0135
BLYP-CCSD(T)	1.636	1.220	2.311	89.67	-1648.5976545	0.0135
B3LYP-CCD	1.649	1.213	2.300	89.52	-1648.4462491	-
B3LYP-CCSD	1.649	1.213	2.301	89.52	-1648.4646120	0.0075
B3LYP-CCSD(T)	1.633	1.220	2.310	89.66	-1648.5970890	0.0075
PBE-CCD	1.634	1.213	2.300	89.54	-1648.4192081	-
PBE-CCSD	1.644	1.213	2.300	89.50	-1648.4575856	0.0129
PBE-CCSD(T)	1.636	1.220	2.311	89.66	-1648.5986569	0.0128
Experimental[a]	1.661(5)	1.225(2)	2.328(8)	88.25(6)	-	-

the virtual levels. The five highest energy occupied molecular orbitals are ordered entirely differently, with the HOMO for B3LYP having a strong contribution from the $3d_{xy}$ and $3d_{x^2-y^2}$ orbitals on iron, and the HOMO-1 having essentially $3d_{z^2}$ character. For the Hartree-Fock calculation these two molecular orbitals form the HOMO-2 and HOMO-4 orbitals respectively, while the HOMO consists of metal $p_{x/y}$ ring combinations and the HOMO-1 has a strong contribution from the $3d_{xz}$ and $3d_{yz}$ orbitals on iron. The ordering of the virtual orbitals is also significantly different. In particular, the LUMO for the B3LYP calculation has a strong contribution from the iron $3d_{xz}$ and $3d_{yz}$ orbitals, while this orbital in the Hartree-Fock calculation is significantly destabilised, forming the LUMO+6.

The generally accepted MO structure of metallocenes,[136] and other transition metal sandwich molecules,[137–139] is much closer to the B3LYP results than it is to the HF orbitals. Ligand field arguments and experiment (especially photoelectron spectroscopy) suggest that the HOMO of ferrocene is the largely non-bonding Fe $3d_{z^2}$-based orbital, while the HOMO-1 is a degenerate pair of Fe $3d_{xy,x^2-y^2}$-based orbitals which are δ-back-bonding with the carbocyclic ligands. These three or-

Figure 3.8: The RMS% difference (equation 3.1) between the theoretical and experimental structures for CCD, CCSD and CCSD(T) from each reference functional. The left hand side considers the entire structure, while the right hand side considers only the metal-ring centroid distance.

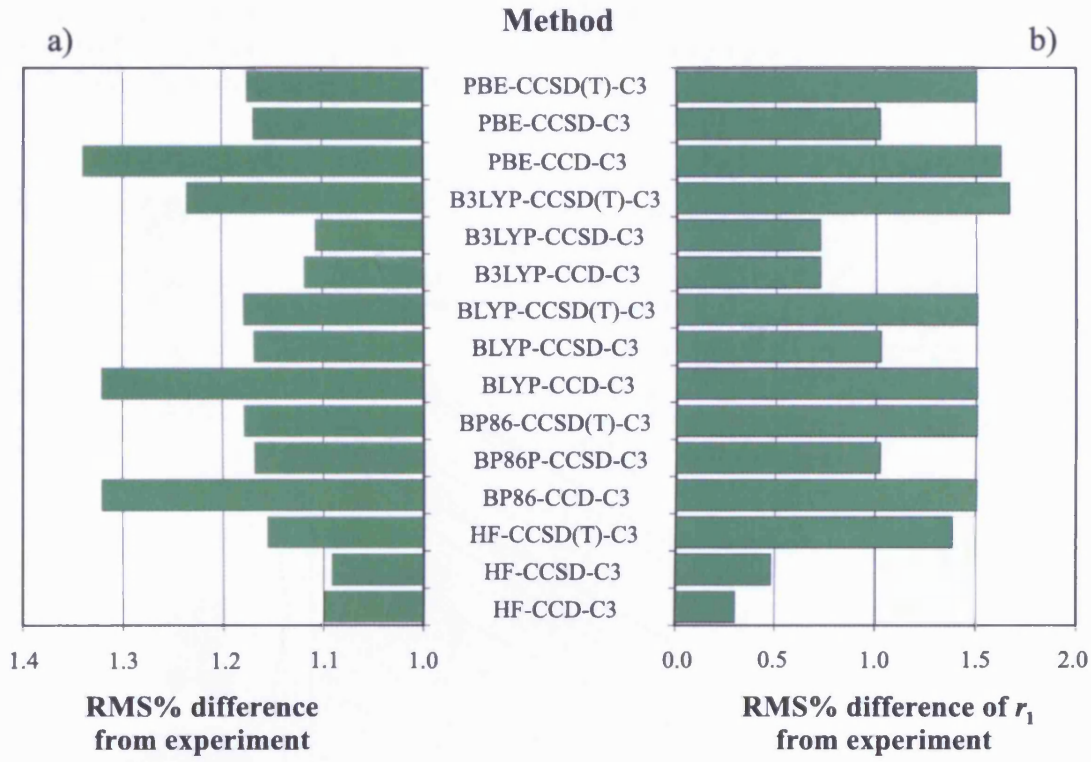

bitals contain the six Fe-based electrons expected for an Fe(II) system. The LUMO is anticipated to be the Fe $3d_{xz,yz}$-based metal-ring π^* orbitals. This description is close to the B3LYP molecular orbital structure, but is rather different from the ordering of the HF orbitals.

Figure 3.9: Correlation diagram showing the relative ordering of B3LYP orbitals and HF orbitals for ferrocene. The calculations are performed with the molecule in the experimentally observed orientation.[134] The colours of the lines indicate the irreducible representations of the molecular orbitals under D_{5h} symmetry. Red - a_1', Red dashed - a_2'', blue - e_1', blue dashed - e_1'', green - e_2', green dashed - e_2''. The lower part of the diagram shows the occupied orbitals, and the virtual levels are shown in the upper diagram. The spacial representations of the MOs are all from the HF reference, and show 0.05 isosurface, except for the LUMO which shows 0.035 isosurface. The orbital plots were generated using MOLDEN.[135]

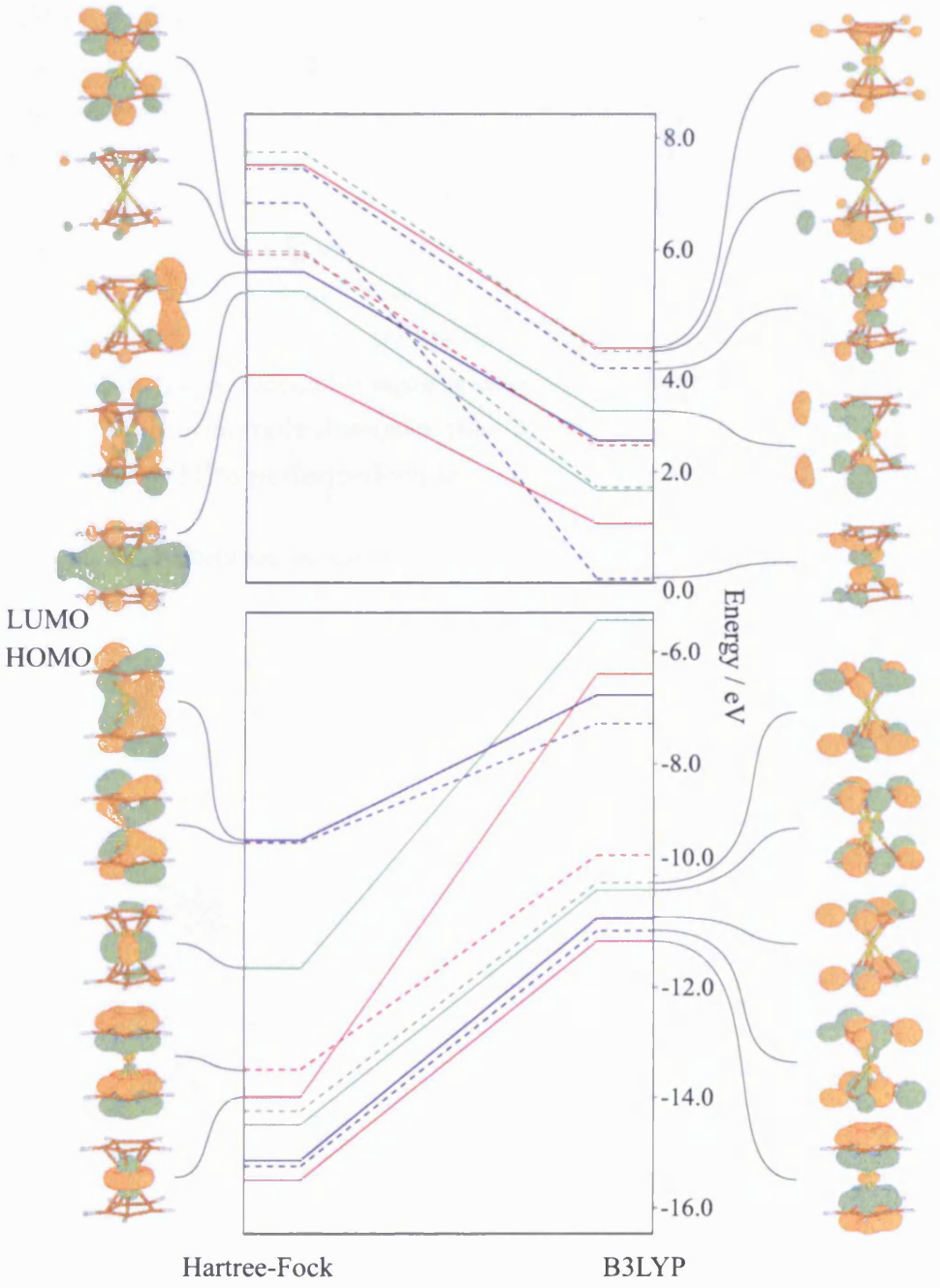

3.4 Results and Discussion - $Fe(CO)_5$

3.4.1 Evaluation of the performance of *ab initio* and DFT methodology

The structure of $Fe(CO)_5$ was fully optimised using the same set of *ab initio* methods and density functionals as used for ferrocene, using the Ahlrichs basis sets as described in section 3.2. The optimised parameters are given in table 3.6, while the geometric variables are defined in figure 3.10. Figure 3.11 gives the RMS% differences of the theoretical structures from the two experimental structure refinements as calculated with equation 3.1.

Consideration of the minimum energy structures from each method, both numerically (table 3.6) and graphically (figure 3.11) reveals similar trends to those observed for ferrocene. HF gives a very long axial M-C bond length, but an equatorial M-C bond which is in much better agreement with experiment. In contrast, MP2 gives an axial M-C bond which is ≈ 0.13 Å too short, and equatorial bonds which are ≈ 0.08 Å too short. MP3 gives the poorest performance for the axial M-C bond, but more reasonable equatorial bonds. It seems that the MP series for the axial bond is even more divergent than for the metal-ring centroid distance in ferrocene, where MP3 performed slightly better than MP2. An MP4(sqd) struc-

Figure 3.10: The location of the geometric variables for $Fe(CO)_5$ in the D_{3h} point group.

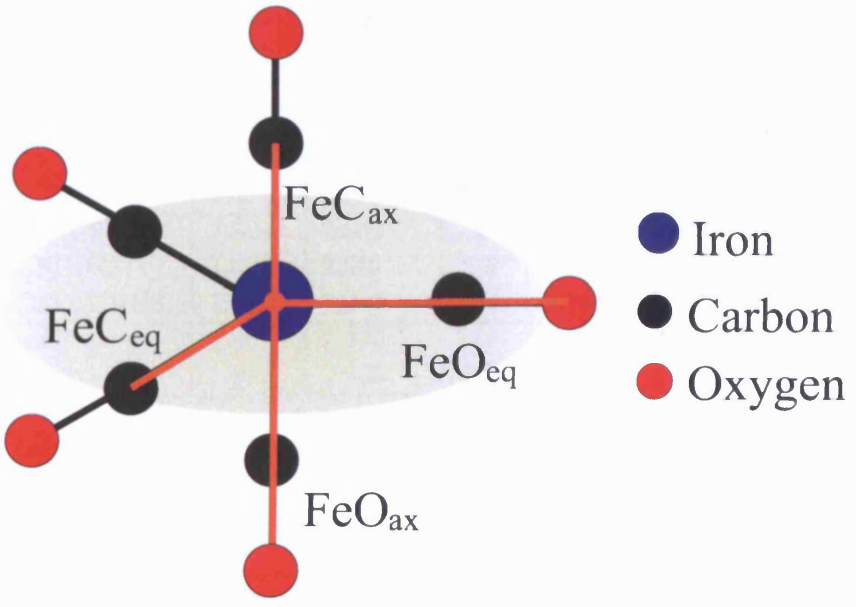

Table 3.6: Structural and energetic data for iron pentacarbonyl using a variety of different methods. The number in brackets after the CC methods indicates the core size used for these calculations (table 3.1). The definition of the lengths is given in figure 3.10. The $\mathscr{T}_1$ diagnostic is given for the optimised coupled-cluster wavefunctions. a) The experimental geometries are those of a) Beagley and Schmidling[98] and b) McClelland *et al.* (best model).[101]

Method	$r_{FeC_{ax}}$ / Å	$r_{FeO_{ax}}$ / Å	$r_{FeC_{eq}}$ / Å	$r_{FeO_{eq}}$ / Å	Energy / Hartree	$\mathscr{T}_1$ Diag
HF	2.049	3.155	1.852	2.970	-1825.43808178	-
MP2	1.682	2.851	1.767	2.924	-1828.06986992	-
MP3	2.426	2.546	1.792	2.930	-1827.47720197	-
CCD(C5)	1.812	2.949	1.795	2.935	-1827.29537112	-
CCSD(C5)	1.832	2.972	1.800	2.945	-1827.35318395	0.0399
CCSD(T)(C5)	1.813	2.962	1.802	2.954	-1827.47004745	0.0397
VWN	1.770	2.920	1.762	2.913	-1823.32522108	-
BP86	1.808	2.965	1.798	2.958	-1830.32947059	-
PW91	1.805	2.960	1.795	2.953	-1830.01659183	-
BLYP	1.830	2.987	1.820	2.981	-1830.05434762	-
B3LYP	1.827	2.969	1.809	2.955	-1829.65686216	-
PBE	1.807	2.964	1.797	2.956	-1829.52687962	-
PBE0	1.807	2.946	1.788	2.931	-1829.41619278	-
B97	1.819	2.963	1.802	2.950	-1829.71273837	-
B97R	1.820	2.963	1.802	2.949	-1829.75170137	-
B3LYP-CCD(C5)	1.821	2.960	1.796	2.939	-1827.30143204	-
B3LYP-CCSD(C5)	1.821	2.959	1.795	2.937	-1827.31721685	0.0106
B3LYP-CCSD(T)(C5)	1.818	2.967	1.805	2.958	-1827.46543944	0.0106
CCD(C3)	1.815	2.951	1.798	2.937	-1827.59558934	-
CCSD(C3)	1.835	2.973	1.801	2.945	-1827.65478664	0.0332
CCSD(T)(C3)	1.811	2.959	1.800	2.952	-1827.78263309	0.0329
B3LYP-CCD(C3)	1.824	2.961	1.798	2.940	-1827.60572666	-
B3LYP-CCSD(C3)	1.824	2.961	1.796	2.938	-1827.62558084	0.0088
B3LYP-CCSD(T)(C3)	1.819	2.967	1.805	2.957	-1827.78784446	0.0088
Experimental[a]	1.807	2.959	1.827	2.979	-	-
Experimental[b]	1.813	2.969	1.845	2.988	-	-

Figure 3.11: The RMS% difference (equation 3.1) for the optimised structures of $Fe(CO)_5$ with a variety of density functionals and *ab initio* methods. The red bars (darker) are relative to the structure of Beagley and Schmidling,[98] while the blue (lighter) bars are relative to the structure of McClelland *et al.*[101]

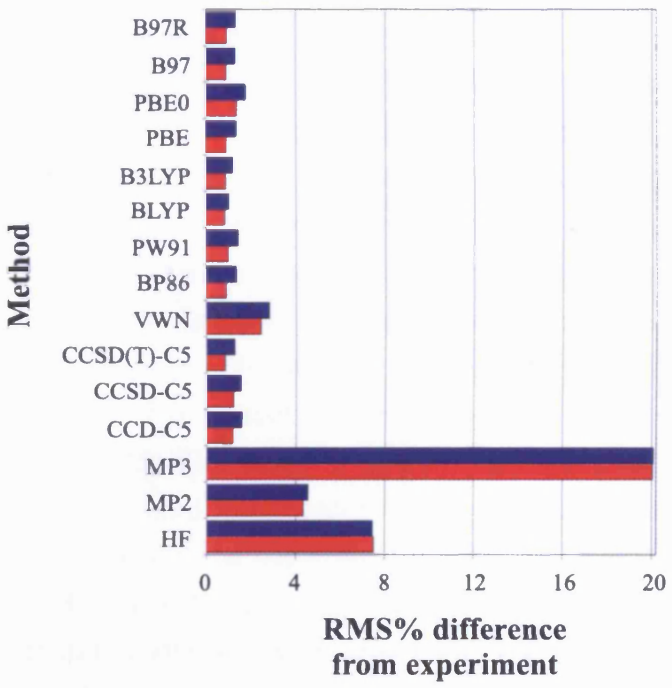

ture could not even be converged, confirming the unstable nature of MP methods with this system.

The carbonyl bond lengths show much less difference from experiment than the axial M-C bond. This indicates that the more poorly correlated methods are fairly robust for the treatment of the carbonyl bonding. This is supported by the observation that a longer C-O bond is observed for the carbonyl ligand which is more tightly bound to the metal (i.e. has a shorter bond), compared with the carbonyl ligands bound to the alternative sites. This is due to the back-bonding pushing electron density into the C-O antibonding orbital, as described in section 3.1.2.

The density functional methods all give much better agreement with experiment than HF and the MP methods, with VWN being the poorest, as expected, since it is not gradient corrected. By a short margin, B3LYP gives the best agreement with experiment. As for ferrocene, it is a surprise that the B97 and B97r functionals perform as well as the other functionals used, given that they are not refined for the energy of the system, but for magnetic shielding constants.

The coupled-cluster methods also show very good agreement with experiment; in fact, of all the methods used, CCSD(T) gives the best agreement with the structure of McClelland *et al.*.[101] The $\mathscr{T}_1$ diagnostic from the CC methods is found to be very large, 0.0397 for CCSD(T). This is taken to indicate that the reference is poor, rather than that the system is significantly multiconfigurational, as is also suggested by the poor HF structure.

Two conclusions can be drawn from the theoretically predicted minimum energy structures. Firstly, the agreement is generally better with the structural determination of McClelland *et al.*[101] for all the methods except HF and MP3, which have already been demonstrated as unreliable. This suggests that the structure of McClelland *et al.* is better than that of Beagley and Schmidling,[98] which is as expected from the fact that the former optimised both the axial and equatorial carbonyl distances individually rather than assuming them to be the same, as in the refinement model of the latter. Secondly, although all the methods (with the exception of HF, MP2, MP3 and VWN) give generally good agreement with experiment, they give an axial M-C bond that is longer than the equatorial M-C bond, by 0.01-0.034 Å, while the experimental structure of McClelland *et al.*[101] indicates that this should be the *shorter* metal-ligand bond, by 0.032 Å. MP2 is the only method found to give a shorter axial bond, but the effect is exaggerated (0.078 Å shorter) and this method also fails to give a sensible structure for the rest of the molecule.

In an attempt to improve the minimum energy structures from the CC calculations, the core size was reduced from size 5 to size 3 (see table 3.1). This reduced core includes only the 1s, 2s and 2p orbitals on iron, rather than the 1s orbitals on carbon and oxygen, and 1s-3p orbitals on iron. These structures are given in table 3.6, and the RMS% difference for all the CC methods is given in figure 3.12. The smaller core makes only small differences to the geometry, the largest difference made to any single variable is three one-thousandths of an Ångstrom.

From this I conclude that with the basis sets used, the core size makes no real extra improvement to the structure. The only slight improvement that is observed is the reduction in $\mathscr{T}_1$ diagnostics (from 0.0397 to 0.0329 with CCSD(T)). This indicates that the 1s ligand and 3s and 3p metal orbitals do not require as significant orbital relaxation as the valence orbitals, so they dilute the $\mathscr{T}_1$ diagnostic, because it is normalised by the number of electrons correlated.

Figure 3.12: The RMS% difference (equation 3.1) for the optimised structures of $Fe(CO)_5$ from coupled-cluster calculations using both cores 3 and 5 (see table 3.1) and from both HF and B3LYP reference functionals. The red bars (darker) are relative to the structure of Beagley and Schmidling,[98] while the blue (lighter) bars are relative to the structure of McClelland *et al.*[101]

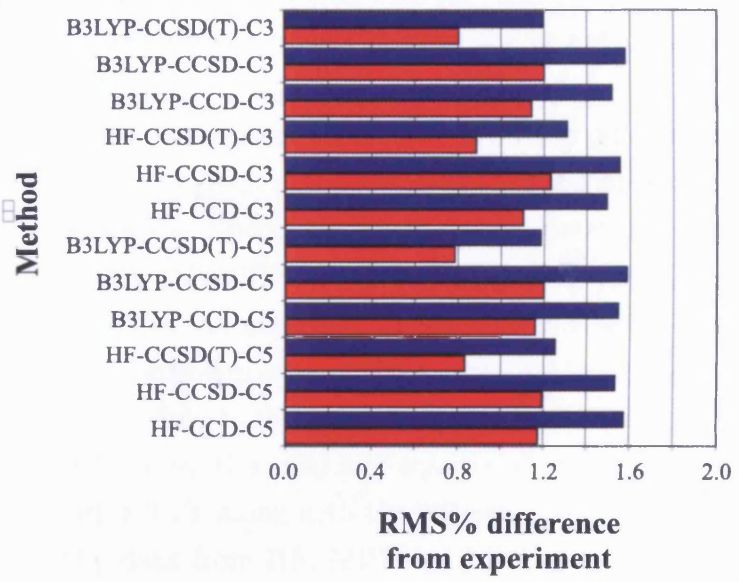

3.4.2 KS-based Coupled-Cluster Calculations

The structure of $Fe(CO)_5$ was fully optimised using KS-CC calculations with B3LYP to generate the reference, because this method gave the smallest $\mathscr{T}_1$ diagnostic for the CC calculations on ferrocene. The calculations were performed with both core sizes 3 and 5 to gauge any effect of core size on the structure. The results of these calculations are given numerically in table 3.6 and graphically by RMS% difference in figure 3.12.

From figure 3.12 it is easy to draw the conclusion that using B3LYP as a reference makes little difference to the minimum energy structures given by the CC calculation; certainly no improvement to the structure is observed. It is noted that all the CC methodologies fall within the range 0.7 - 1.3 RMS% difference from the structure of McClelland *et al.*,[101] and in an even closer range from the structure of Beagley and Schmidling,[98] 1.1 - 1.6. Equivalent levels of CC give structures which agree to 0.2 RMS% difference depending upon core size and reference. One conclusion from these observations is that CC is insensitive to the reference chosen, and for this system, also to the core size. The latter suggests

that much of the correlation occurs within the valence orbitals, or that the basis set used is not effective at correlating the core orbitals.

One improvement of KS-CC over HF-CC is the size of the $\mathscr{T}_1$ diagnostic. This has been reduced substantially with B3LYP as the reference, and then again slightly when using the smaller core; the smallest value (0.0088) was obtained with B3LYP-CCSD and B3LYP-CCSD(T). This indicates that B3LYP is a better reference functional than that generated with HF, and that less orbital relaxation in the form of single excitations is necessary in the calculation, resulting in the smaller $\mathscr{T}_1$ diagnostic.

Although all of the theoretical structures are in good agreement with the structures determined experimentally, they all predict the equatorial M-C bond to be shorter and most the axial bond longer than those determined experimentally, although in some cases this difference is as small as a few thousandths of an Ångstrom. This results in the axial bond being longer than the equatorial bond in all cases where the method gives a sensible structure, and suggests that all the methods used favour binding to the equatorial environment over the axial in some way. The difference between the axial and equatorial M-C bond lengths (Δ_{ax-eq}) is summarised in figure 3.13, along with the difference from the two experimental determinations. The data from HF, MP2 and MP3 are not shown because the structures are not considered to be sensible. The best agreements for Δ_{ax-eq} are seen for VWN, PBE and CCSD(T) in rank order. The general structure from VWN is however not as good as that from PBE or CCSD(T). A reduction of 0.04 Å in Δ_{ax-eq} would be required to match the experimental results of McClelland *et al.*.[101]

3.4.3 Comparison of the HF and B3LYP valence molecular orbitals

Figure 3.14 shows the correlation between the HF and B3LYP MOs at the experimentally determined geometry of McClelland *et al.*[101] The HOMO-LUMO gap is larger for HF than B3LYP, as expected, due to the failure of the orbitals from density functional theory to obey Koopmans' theorem. Unlike for ferrocene, the HF structure of $Fe(CO)_5$ is fairly sensible, and does not show significant reordering of the MOs when compared with the B3LYP orbitals.

The only reordering that occurs for the occupied levels is the $3d_{z^2}$ based orbital which is slightly less stable in the HF description. The virtual orbitals show a slightly greater re-ordering; this does not change the LUMO, which is still π-back-bonding in character, however, the LUMO+1 for HF (which is $3d_{z^2}$

Figure 3.13: The difference between the axial and equatorial metal carbon bond lengths (Δ_{ax-eq}) for all the methods investigated in this study. The values are shown for the experimental determinations of Beagley and Schmidling[98] and McClelland *et al.*[101]

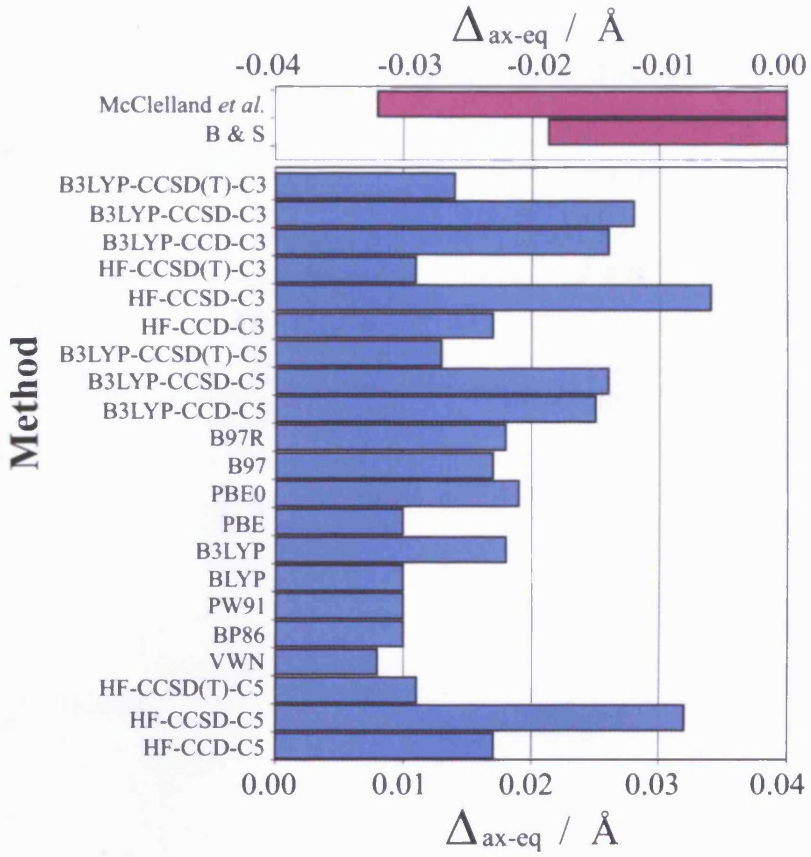

based), becomes the LUMO+7 for B3LYP, while the LUMO+4 for B3LYP (also $3d_{z^2}$ based), correlates with the LUMO+7 in the HF description. If the $\mathscr{T}_1$ diagnostic is only large for HF-based CC due to orbital relaxation effects, then it seems strange that the HF-CC $\mathscr{T}_1$ diagnostic for $Fe(CO)_5$ is larger that that for ferrocene, despite the apparently largely correct ordering of the MOs for $Fe(CO)_5$. Given the significantly greater re-ordering necessary to correlate the B3LYP and HF orbitals for ferrocene, one might expect this reordering to require more orbital relaxation, which should result in a larger $\mathscr{T}_1$ diagnostic. It seems unlikely that the $3d_{z^2}$ based orbitals can account for the entirety of the re-ordering effect and the large $\mathscr{T}_1$ value for $Fe(CO)_5$. It seems more likely that the orbital relaxation in $Fe(CO)_5$ affects a lot of orbitals approximately equally (while treating the $3d_{z^2}$ based orbitals differently), so that only minor reordering is observed.

Figure 3.14: Correlation diagram showing the relative ordering of B3LYP orbitals and HF orbitals at the geometry of McClelland *et al.*.[101] All the MO plots are from the B3LYP calculation irrespective of their position on the diagram. The red lines indicate orbitals of a_1', symmetry, the red-dashed lies of a_2'', blue lines of e', blue-dashed of e'' and green lines of a_2' symmetry. The spacial representations of the MOs are all from the HF reference, and show 0.05 isosurface, except for the HF LUMO+1 which shows 0.035 isosurface. The orbital plots were generated using MOLDEN.[135]

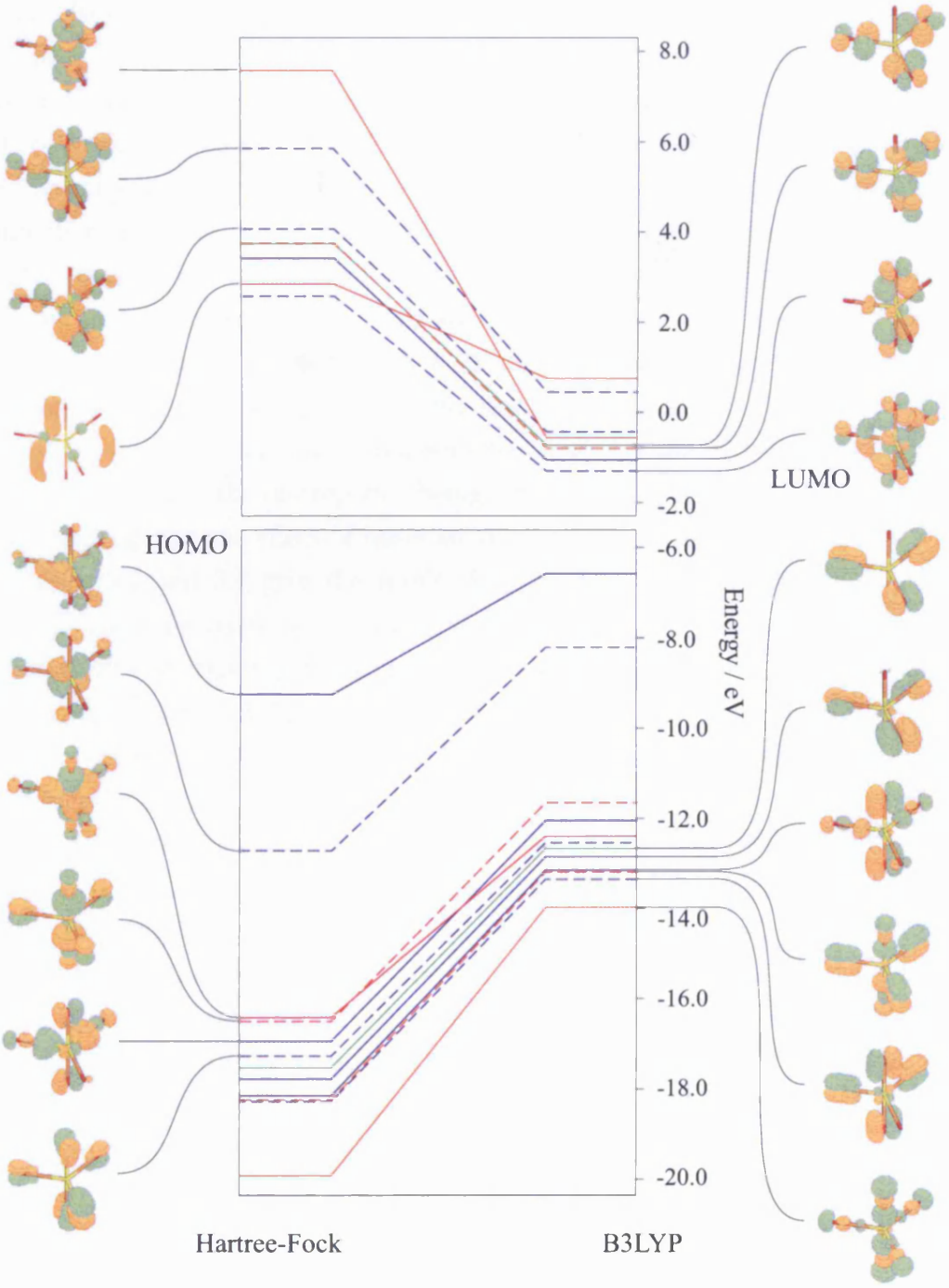

3.4.4 The variation of geometry with basis set

All the methods used up to this point (with the exception of HF, MP2, MP3 and VWN) give good structures for $Fe(CO)_5$. However, despite these good agreements, typically to within a few hundredths of an Ångstrom, all the theoretical structures have a longer axial than equatorial metal-carbon bond length. It might be valid to question the accuracy of the electron diffraction structure determination. However, this issue has already been addressed by McClelland *et al.*,[101] who have recalculated the molecular structure from a new x-ray experiment with this particular problem in mind. Their refinement model also included the effects of rotational distortion and multiple scattering, in an attempt to clarify the question of which of the environments has the longer metal-carbon bond. They claim that the chance that the axial M-C bond is longer than the equatorial is "utterly negligible" for their preferred model structure,[101] the results from which are used in the present study. This structure gives the axial M-C bond length to be shorter than the equatorial by 0.032 Å, even shorter than that determined by Beagley and Schmidling.[98] It seems that the theoretical structures must be at fault, although it should be remembered that the theoretical structures are very good and that the discrepancy being investigated is very small. This section attempts to gauge the effect of basis set size on calculated structures.

Tables 3.7 and 3.8 give the results from PBE, B3LYP and CCSD (core 5) calculations using basis sets of the style 6-31G(x), 6-31+G(x), 6-311G(x) and 6-311+G(x) respectively,[d] where x are polarisation functions. Figure 3.15 shows the variation of the RMS% difference from the structure of McClelland *et al.* and the variation in the difference between the axial and equatorial metal-carbon bond lengths (Δ_{ax-eq}) with the number of basis functions.

The trends for the Pople style basis sets are divided into double and triple-ζ and polarised and un-polarised groups to aid analysis. The trends for the RMS% difference in figure 3.15 show a general decrease with increasing basis set size. B3LYP is consistently slightly better than PBE, while CCSD performs better than PBE, but worse than B3LYP. The triple-ζ basis sets perform better than the double-ζ equivalents when few polarisation functions are included, but with larger basis sets, this difference is smaller, especially with B3LYP. The large step in the plot between the 3d and 2df bases suggests that the extra d-function is preferable to an f-function; with 3df polarisation functions added, the result is approximately as good as 2df. When diffuse functions are present, this trend is

[d]For the CCSD calculations, the largest basis set usable before system resources were exhausted was 6-311G(2d)

Table 3.7: The effect of basis set on the structure of iron pentacarbonyl using double-ζ Pople style basis sets, and a variety of different method. The geometric variables are defined in figure 3.10.

	Basis Set		No. Functs	$r_{FeC_{ax}}$ / Å	$r_{FeO_{ax}}$ / Å	$r_{FeC_{eq}}$ / Å	$r_{FeO_{eq}}$ / Å	Energy / H	$\mathscr{T}_1$ Diag
B3LYP	6-31G	A	119	1.8121	1.1654	1.7945	1.1697	-1830.0889439	-
	6-31+G	B	172	1.8223	1.1657	1.8106	1.1698	-1830.1484817	-
	6-31G(d)	C	186	1.8129	1.1474	1.7994	1.1514	-1830.3201555	-
	6-31+G(d)	D	239	1.8280	1.1478	1.8187	1.1518	-1830.3722140	-
	6-31G(2d)	E	253	1.8116	1.1411	1.8002	1.1452	-1830.3702999	-
	6-31+G(2d)	F	306	1.8226	1.1406	1.8167	1.1447	-1830.4128630	-
	6-31G(3d)	G	320	1.8200	1.1413	1.8122	1.1452	-1830.4001172	-
	6-31G(2df)	H	332	1.8106	1.1407	1.7997	1.1446	-1830.3882018	-
	6-31+G(3d)	I	373	1.8221	1.1420	1.8155	1.1459	-1830.4168143	-
	6-31+G(2df)	J	385	1.8214	1.1404	1.8161	1.1444	-1830.4284253	-
	6-31G(3df)	K	399	1.8173	1.1401	1.8102	1.1439	-1830.4175623	-
	6-31+G(3df)	L	452	1.8188	1.1411	1.8132	1.1448	-1830.4331925	-
PBE	6-31G	A	119	1.7948	1.1806	1.7855	1.1839	-1829.3313009	-
	6-31+G	B	172	1.8042	1.1808	1.7994	1.1838	-1829.3895081	-
	6-31G(d)	C	186	1.7947	1.1615	1.7882	1.1647	-1829.5409253	-
	6-31+G(d)	D	239	1.8078	1.1620	1.8050	1.1648	-1829.5922432	-
	6-31G(2d)	E	253	1.7943	1.1557	1.7889	1.1589	-1829.5883232	-
	6-31+G(2d)	F	306	1.8033	1.1553	1.8036	1.1583	-1829.6296193	-
	6-31G(3d)	G	320	1.8015	1.1558	1.7998	1.1585	-1829.6171164	-
	6-31G(2df)	H	332	1.7930	1.1553	1.7878	1.1584	-1829.6047050	-
	6-31+G(3d)	I	373	1.8029	1.1566	1.8028	1.1593	-1829.6343311	-
	6-31+G(2df)	J	385	1.8020	1.1551	1.8024	1.1580	-1829.6438662	-
	6-31G(3df)	K	399	1.7989	1.1546	1.7976	1.1573	-1829.6328489	-
	6-31+G(3df)	L	452	1.7998	1.1558	1.8004	1.1583	-1829.6491522	-
CCSD	6-31G	A	119	1.8457	1.1675	1.8139	1.1740	-1826.8538167	0.0466
	6-31+G	B	172	1.8604	1.1691	1.8334	1.1750	-1826.9575869	0.0464
	6-31G(d)	C	186	1.8207	1.1465	1.7973	1.1517	-1827.6565094	0.0411
	6-31+G(d)	D	239	1.8404	1.1481	1.8206	1.1530	-1827.7377084	0.0416
	6-31G(2d)	E	253	1.8206	1.1380	1.7999	1.1430	-1827.8778311	0.0396

Table 3.8: The effect of basis set on the structure of iron pentacarbonyl using triple-ζ Pople style basis sets and a variety of different method. The geometric variables are defined in figure 3.10.

	Basis Set		No. Functs	$r_{FeC_{ax}}$ / Å	$r_{FeO_{ax}}$ / Å	$r_{FeC_{eq}}$ / Å	$r_{FeO_{eq}}$ / Å	Energy / H	$\mathscr{T}_1$ Diag
B3LYP	6-311G	M	169	1.8173	1.1615	1.7980	1.1658	-1830.3441563	-
	6-311+G	N	221	1.8233	1.1609	1.8144	1.1652	-1830.3848796	-
	6-311G(d)	O	226	1.8189	1.1388	1.8044	1.1428	-1830.5763250	-
	6-311+G(d)	P	278	1.8278	1.1389	1.8209	1.1430	-1830.6091858	-
	6-311G(2d)	Q	283	1.8245	1.1373	1.8120	1.1413	-1830.6055697	-
	6-311+G(2d)	R	335	1.8301	1.1371	1.8222	1.1411	-1830.6252934	-
	6-311G(3d)	S	340	1.8267	1.1363	1.8196	1.1401	-1830.6221591	-
	6-311G(2df)	T	362	1.8216	1.1366	1.8104	1.1405	-1830.6231209	-
	6-311+G(3d)	U	391	1.8284	1.1368	1.8216	1.1408	-1830.6348764	-
	6-311+G(2df)	V	414	1.8268	1.1365	1.8203	1.1404	-1830.6424812	-
	6-311G(3df)	W	419	1.8254	1.1357	1.8190	1.1394	-1830.6403505	-
	6-311+G(3df)	X	471	1.8264	1.1361	1.8203	1.1400	-1830.6524884	-
PBE	6-311G	M	169	1.7976	1.1772	1.7867	1.1804	-1829.5822291	-
	6-311+G	N	221	1.8037	1.1765	1.8013	1.1795	-1829.6222204	-
	6-311G(d)	O	226	1.7987	1.1537	1.7914	1.1564	-1829.7900223	-
	6-311+G(d)	P	278	1.8065	1.1538	1.8060	1.1566	-1829.8231711	-
	6-311G(2d)	Q	283	1.8042	1.1522	1.7988	1.1551	-1829.8176570	-
	6-311+G(2d)	R	335	1.8077	1.1521	1.8067	1.1549	-1829.8377666	-
	6-311G(3d)	S	340	1.8051	1.1511	1.8046	1.1537	-1829.8335181	-
	6-311G(2df)	T	362	1.8013	1.1515	1.7972	1.1542	-1829.8338123	-
	6-311+G(3d)	U	391	1.8063	1.1518	1.8062	1.1546	-1829.8474899	-
	6-311+G(2df)	V	414	1.8048	1.1513	1.8049	1.1541	-1829.8535985	-
	6-311G(3df)	W	419	1.8036	1.1505	1.8038	1.1531	-1829.8503407	-
	6-311+G(3df)	X	471	1.8042	1.1510	1.8048	1.1537	-1829.8636875	-
CCSD	6-311G	M	169	1.8415	1.1626	1.8053	1.1692	-1827.1674976	0.0450
	6-311+G	N	221	1.8521	1.1630	1.8275	1.1692	-1827.2511525	0.0454
	6-311G(d)	O	226	1.8248	1.1369	1.7977	1.1421	-1828.0084759	0.0400
	6-311+G(d)	P	278	1.8414	1.1375	1.8223	1.1425	-1828.0661297	0.0409
	6-311G(2d)	Q	283	1.8338	1.1349	1.8102	1.1399	-1828.1687258	0.0395

Figure 3.15: The variation of the RMS% difference from the structure of McClelland *et al.* and the variation of the difference between the axial and equatorial metal-carbon bond lengths (Δ_{ax-eq}) with the number of basis functions for 6-31G(x) and 6-311G(x) (solid lines) and 6-31+G(x) and 6-311+G(x) (dashed lines) style Pople basis sets. The double-ζ basis sets are shown on the left. These basis sets are defined in tables 3.7 and 3.8. The red lines indicate the B3LYP results, the blue lines PBE results and the black lines CCSD.

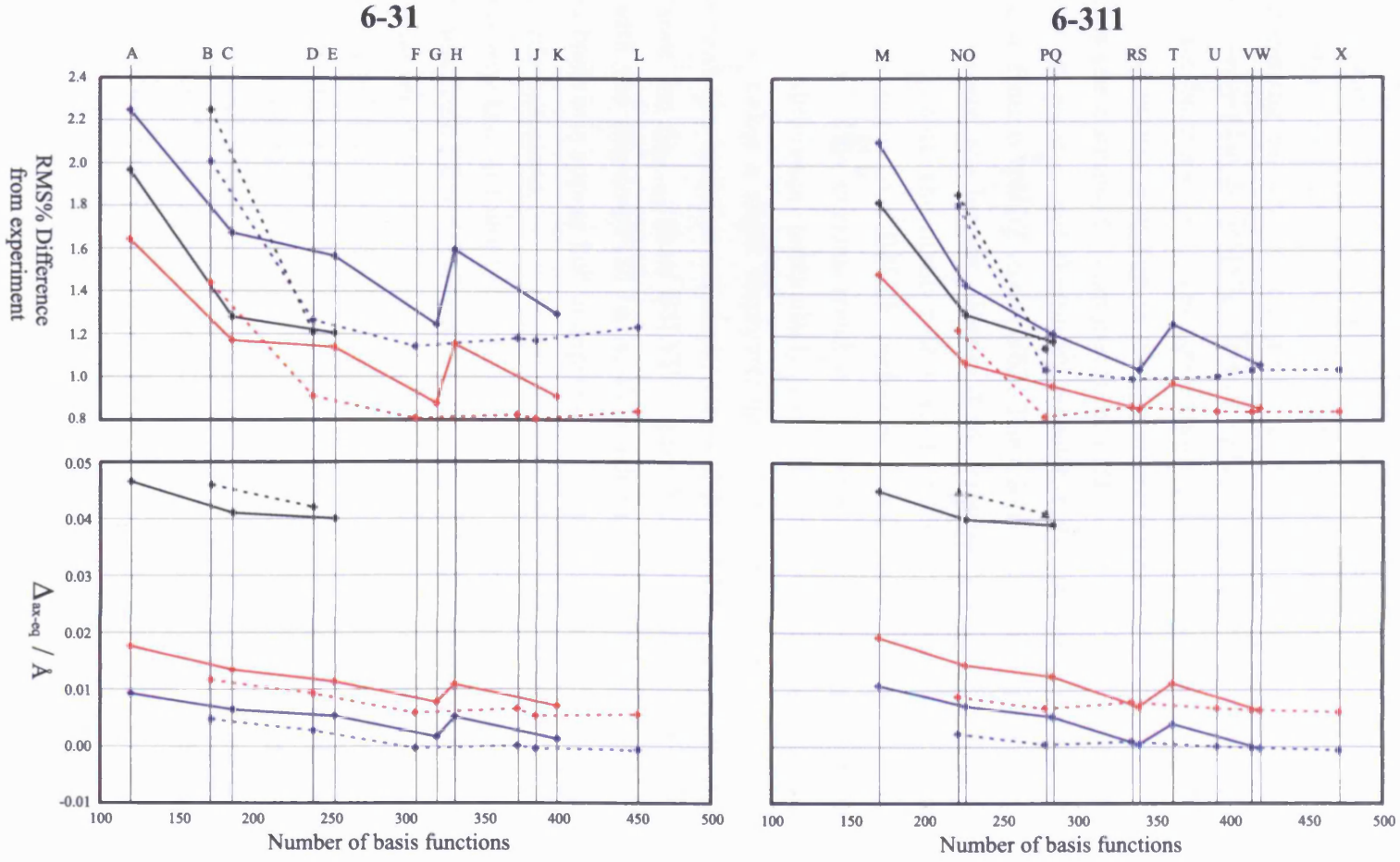

significantly less noticable. One general feature indicated by the plots is that the basis set saturates quite quickly, certainly by 6-31+G(2d) and 6-311+G(2d).

Although B3LYP gives a structure closer to experiment than PBE, the latter gives a slightly negative value of Δ_{ax-eq} for a number of basis sets (although Δ_{ax-eq} is still slightly too large), while CCSD gives the poorest agreement for Δ_{ax-eq}. It is interesting to note similar trends in the variation of Δ_{ax-eq} with basis set size as observed for the RMS% difference plots, especially the saturation of Δ_{ax-eq} with larger basis sets, which suggests that replicating the experimental value of Δ_{ax-eq} is not simply a matter of using a large enough basis set.

Table 3.9 gives the optimised structures from PBE and B3LYP using the 6-311+G(2df) basis set on iron and Dunning's correlation consistent basis sets on carbon and oxygen, from cc-pVDZ to cc-pV5Z. The effect of diffuse functions was considered for all except the largest. Figure 3.16 gives the variation of RMS% difference and Δ_{ax-eq} with the number of basis functions respectively. These calculations indicate again that B3LYP performs slightly better than PBE for the RMS% indicator. One curious trend is that the smallest basis set gives the smallest RMS% difference, particularly, for PBE. It appears that the use of diffuse functions makes a slight improvement, however the main indication of these data is that the basis set saturates very quickly. PBE gives a slightly better performance for Δ_{ax-eq} than B3LYP (figure 3.16); the best match for experiment is with the aug-cc-pVDZ basis, although this value is only slightly negative. Larger basis sets appear not to improve the situation, another similarity with the Pople style basis sets.

Table 3.10 collects the optimised structures from the geometry optimisations using STO basis sets from SZ to QZ4P with ADF, using BLYP and PBE.[e] Figure 3.16 gives the variation of the RMS% and Δ_{ax-eq} values with the number of basis functions respectively. The optimised structures indicate that BLYP performs better than PBE for the RMS% difference test (figure 3.16). Although the SZ basis set is seen to perform very poorly, after the DZ basis is used, saturation occurs very quickly, and gives similar RMS% values to those observed for the other basis set classes. The Δ_{ax-eq} value is positive for all the basis sets, and again saturates very quickly, such that it appears that it will not be possible to replicate the experimental value.

The inclusion of relativistic effects by Persson *et al.*[93] in their study of $Fe(CO)_5$ made a correction of approximately a hundredth of an Ångstrom to the ligand

[e]It was not possible to use B3LYP, because the ADF package does not support the use of this functional for geometry optimisations.

Table 3.9: The effect of basis set on the structure of iron pentacarbonyl using both the B3LYP hybrid density functional and the unparameterised PBE functional with a Pople style basis set on iron, and a correlation-consistent Dunning basis set on carbon and oxygen. The geometric variables are defined in figure3.10.

	Basis Set		No. Functs	$r_{FeC_{ax}}$ / Å	$r_{FeO_{ax}}$ / Å	$r_{FeC_{eq}}$ / Å	$r_{FeO_{eq}}$ / Å	Energy / H
B3LYP	cc-pVDZ	α	214	1.8294	1.1453	1.8220	1.1492	-1830.4925729
	aug-cc-pVDZ	β	304	1.8262	1.1448	1.8200	1.1489	-1830.5243348
	cc-pVTZ	γ	374	1.8267	1.1375	1.8204	1.1413	-1830.6546999
	aug-cc-pVTZ	δ	534	1.8266	1.1371	1.8203	1.1410	-1830.6624691
	cc-pVQZ	ϵ	624	1.8260	1.1354	1.8194	1.1393	-1830.7010172
	aug-cc-pVQZ	ζ	874	1.8265	1.1355	1.8197	1.1394	-1830.7035218
	cc-pV5Z	θ	984	1.8261	1.1354	1.8194	1.1392	-1830.7146595
PBE	cc-pVDZ	α	214	1.8073	1.1601	1.8066	1.1627	-1829.7114066
	aug-cc-pVDZ	β	304	1.8049	1.1597	1.8053	1.1625	-1829.7440924
	cc-pVTZ	γ	374	1.8045	1.1523	1.8048	1.1549	-1829.8655610
	aug-cc-pVTZ	δ	534	1.8046	1.1520	1.8048	1.1547	-1829.8739441
	cc-pVQZ	ϵ	624	1.8040	1.1504	1.8039	1.1531	-1829.9134465
	aug-cc-pVQZ	ζ	874	1.8043	1.1505	1.8042	1.1533	-1829.9162521
	cc-pV5Z	θ	984	1.8039	1.1503	1.8039	1.1530	-1829.9284434

Table 3.10: The effect of basis set on the structure of iron pentacarbonyl using BLYP and PBE with a basis set of Slater type orbitals. The geometric variables are defined in figure 3.10. The binding energy presented is that relative to the atom fragments.

	Basis Set	No Functs	$r_{FeC_{ax}}$ / Å	$r_{FeO_{ax}}$ / Å	$r_{FeC_{eq}}$ / Å	$r_{FeO_{eq}}$ / Å	Energy / H
BLYP	SZ	68	1.7227	1.2230	1.6507	1.2265	-3.5923061071
	DZ	138	1.8299	1.1752	1.8212	1.1548	-2.7790064893
	TZP	232	1.8272	1.1557	1.8244	1.1588	-3.0563150762
	TZ2P	309	1.8246	1.1516	1.8218	1.1548	-3.0859976112
	QZP	518	1.8249	1.1507	1.8232	1.1540	-3.0944629506
PBE	SZ	68	1.7085	1.2179	1.6407	1.2209	-3.7119740545
	DZ	138	1.8011	1.1735	1.7979	1.1766	-2.9103730102
	TZP	232	1.7996	1.1545	1.7955	1.5272	-3.2086277045
	TZ2P	309	1.7961	1.1508	1.7925	1.1535	-3.2378711751
	QZP	518	1.7978	1.1501	1.7950	1.1529	-3.2469744213

Figure 3.16: The variation of the RMS% difference from the structure of McClelland *et al.* and the difference between the axial and equatorial metal-carbon bond lengths (Δ_{ax-eq}) with the number of basis functions for Dunning's correlation consistent basis sets with (solid lines) and with out diffuse functions (augmentation, dashed lines) and ZORA basis sets of Slater type functions. These basis sets are defined in tables 3.9 and 3.10. The red lines indicate the B3LYP results, the blue lines PBE results and the purple lines, BLYP results.

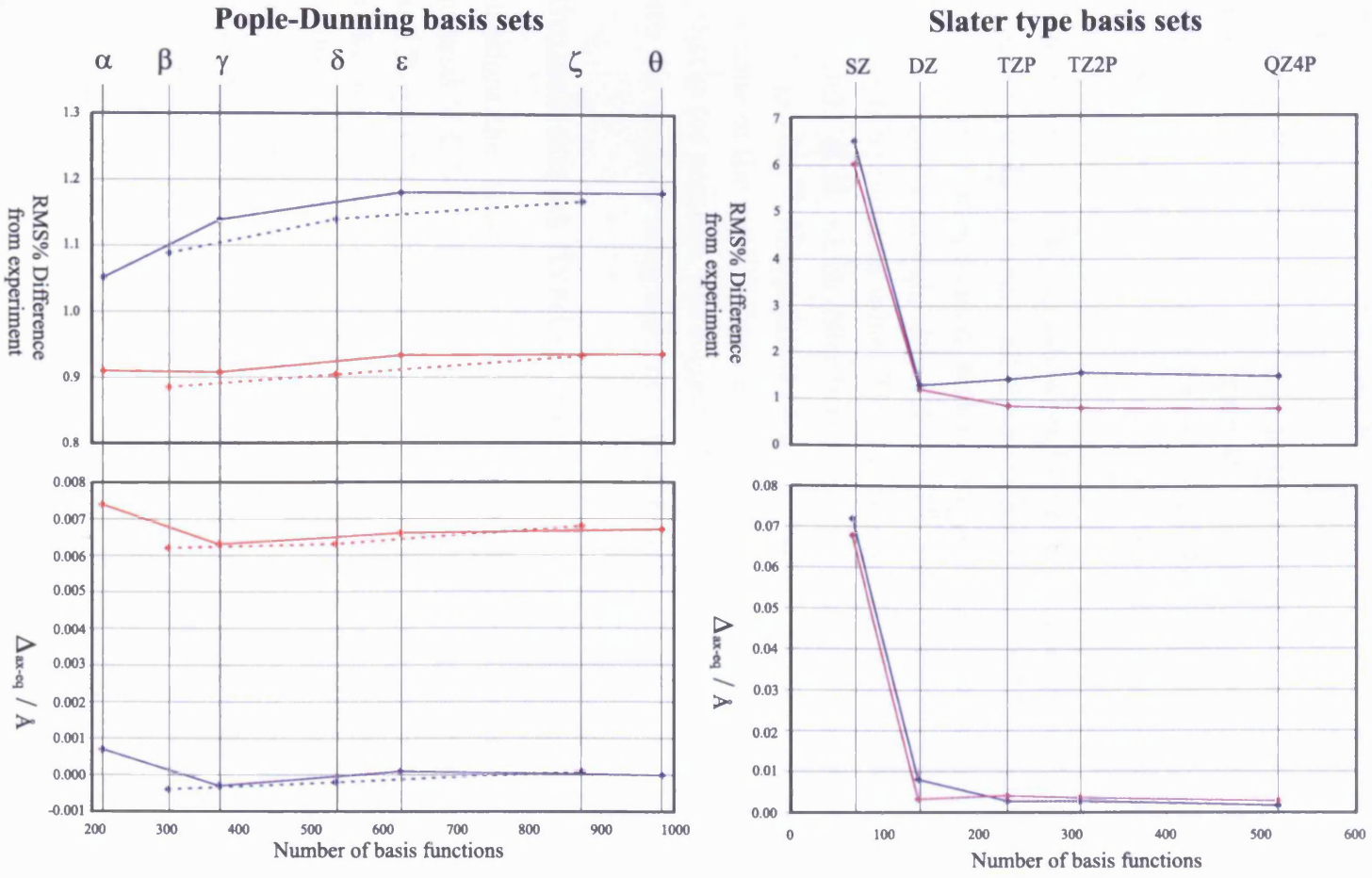

axial bond length, causing a slight contraction. These effects were included using first order perturbation theory at the CASSCF level. The present study also predicts the effects of relativity to be small, based on a comparison of the structures optimised with the ZORA basis sets compared with those from the other basis sets used. The PBE M-C bond lengths from the largest basis set calculation of each style provide the best comparison between methods. These structures vary by less than a thousandth of an Ångstrom for the Pople and Pople/Dunning calculations. The results from the calculations with the ZORA Slater type orbital basis differ from the non-relativistic results by approximately 0.007 Å, comparable with the results of Persson *et al.*

In summary, the RMS% and Δ_{ax-eq} values tend to saturate quickly for all the basis set classes investigated. Although all the basis set classes can be used to give structures that are in good agreement with experiment, none of them give a Δ_{ax-eq} value which is negative enough, although in a few cases is was possible to at least achieve a (slightly) negative value! These results are in good agreement with the results of Bühl *et al.*, which differ from the PBE results by only a few thousandths of an Ångstrom.[90] Although it is noted that the discrepancy is small, it is curious that none of the method/basis set combinations used so far give a value of Δ_{ax-eq} that is *too* negative, this suggests that the failure, although small is a problem with the methods being used, not just the basis set.

3.4.5 Optimisations at fixed carbonyl bond lengths

Of all the calculations that have been performed in past studies, the only two that predict the axial M-C bond length to be shorter than the axial are those of Lüthi *at al.*[64] and Persson *et al.*,[93] using multiconfigurational methods. However both of these studies assume the axial and equatorial carbonyl bond lengths to be identical. Given the synergic nature of the bonding in $Fe(CO)_5$, what constraint does this impose on the M-C bond lengths? Further, is it possible to replicate the correct value of Δ_{ax-eq} by introducing this constraint into the present study?

Table 3.11 gives the partially optimised structures, at fixed, identical carbonyl bond lengths using PBE, B3LYP and CCSD (core 5). Figure 3.17 shows the variation of bond lengths, Δ_{ax-eq} and energy with carbonyl bond length.

The variations of the M-C bond lengths are found to be negatively correlated to the carbonyl bond length. This is as expected from the discussion of the bonding in these complexes, where a stronger, shorter M-C bond results in the weakening of the carbonyl bond. Although the variation induced in the length of the M-C bond is of the same order of magnitude as Δ_{ax-eq}, both axial and

Table 3.11: Partialially optimised geometries for $Fe(CO)_5$ at fixed, identical carbonyl bond lengths, using CCSD, PBE and B3LYP with the standard Ahlrichs basis set as defined in section 3.2. The coupled-cluster calculations used core size 5 (see table 3.1).

	$r_{(C-O)}$ / Å	$r_{(Fe-O)_{ax}}$ / Å	$r_{(Fe-O)_{eq}}$ / Å	Energy / H	Δ_{ax-eq} / Å
PBE	1.06	1.8148	1.8069	-1829.1230425	0.0079
	1.08	1.8124	1.8043	-1829.1716277	0.0081
	1.10	1.8101	1.8019	-1829.2166124	0.0082
	1.12	1.8080	1.7995	-1829.2296754	0.0085
	1.14	1.8060	1.7973	-1829.2422007	0.0087
	1.16	1.8042	1.7952	-1829.2455614	0.0090
	1.18	1.8026	1.7932	-1829.2410216	0.0094
	1.20	1.8011	1.7914	-1829.2295418	0.0097
	1.22	1.7998	1.7897	-1829.2120421	0.0101
	1.24	1.7986	1.7881	-1829.1893506	0.0105
	1.26	1.7976	1.7866	-1829.1621846	0.0110
B3LYP	1.06	1.8386	1.8215	-1829.5602631	0.0171
	1.08	1.8350	1.8182	-1829.6028554	0.0168
	1.10	1.8317	1.8151	-1829.6319323	0.0166
	1.12	1.8286	1.8121	-1829.6491797	0.0165
	1.14	1.8259	1.8094	-1829.6560299	0.0165
	1.16	1.8232	1.8067	-1829.6538298	0.0165
	1.18	1.8205	1.8040	-1829.6437484	0.0165
	1.20	1.8183	1.8018	-1829.6268104	0.0165
	1.22	1.8163	1.7995	-1829.6039385	0.0168
	1.24	1.8143	1.7974	-1829.5759591	0.0169
	1.26	1.8125	1.7954	-1829.5435947	0.0171
CCSD	1.06	1.8425	1.8120	-1827.2590927	0.0305
	1.08	1.8393	1.8091	-1827.3016650	0.0302
	1.10	1.8364	1.8063	-1827.3304208	0.0301
	1.12	1.8336	1.8037	-1827.3470496	0.0299
	1.14	1.8311	1.8012	-1827.3530508	0.0299
	1.16	1.8288	1.7989	-1827.3497569	0.0299
	1.18	1.8266	1.7967	-1827.3383572	0.0299
	1.20	1.8246	1.7946	-1827.3198928	0.0300
	1.22	1.8228	1.7926	-1827.2953165	0.0302
	1.24	1.8211	1.7908	-1827.2654614	0.0303
	1.26	1.8196	1.7890	-1827.2310752	0.0306

Figure 3.17: The variation of the M-C bond lengths (solid - axial, dashed - equatorial), the difference between these bond lengths and the total energy with carbonyl bond length. Red indicates the B3LYP results, black, CCSD and blue, PBE. The B3LYP and PBE energies are offset by +1829 H, and the CCSD by +1827 H.

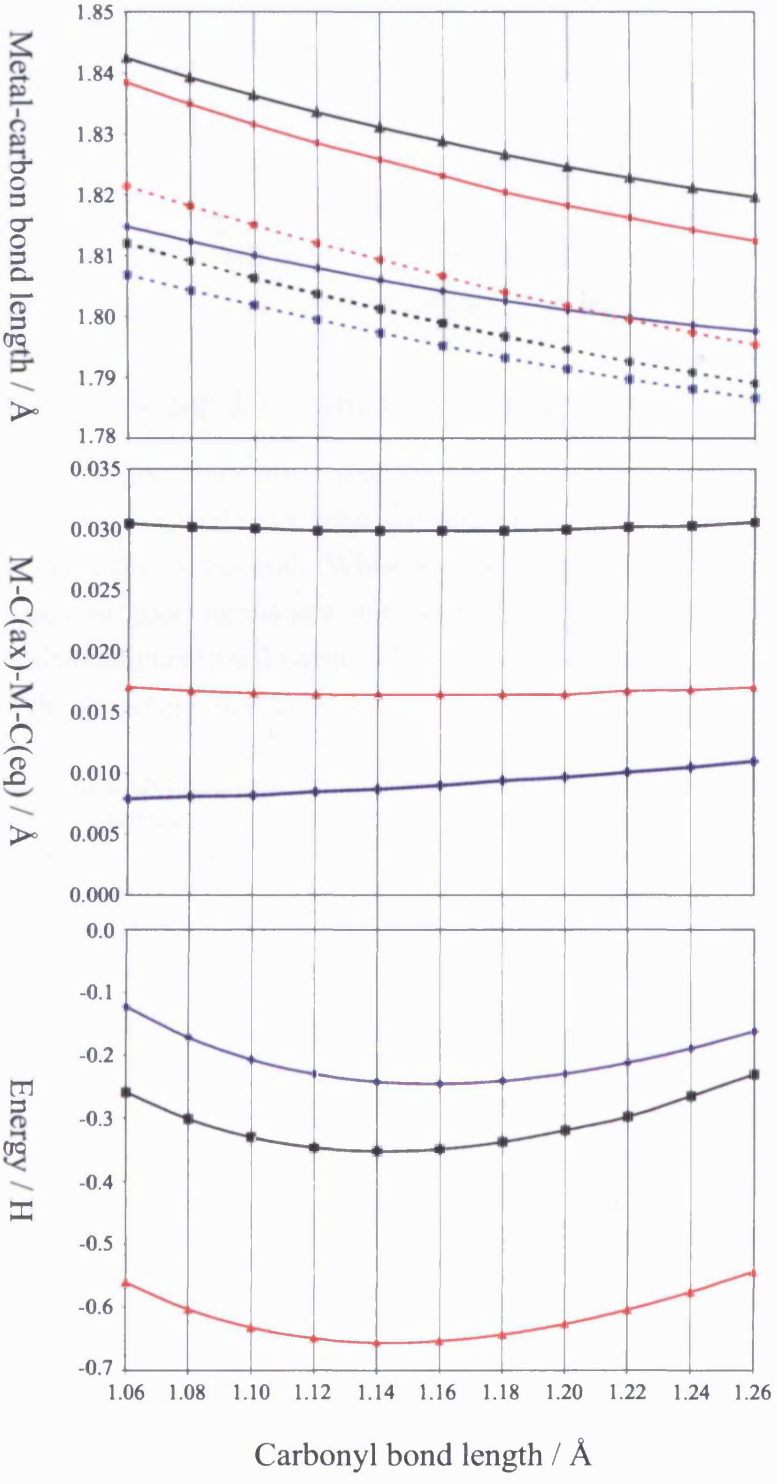

equatorial environments are affected approximately equally, so Δ_{ax-eq} is fairly constant. The minimum in the energy profiles is at the point expected from the full optimisations. The fact that the carbonyl bond lengths in the fully optimised structures are virtually identical simplifies this analysis.

The conclusion from these calculations is that a "better" match with experiment cannot be induced into the present study by fixing the carbonyl bond lengths at an arbitrary, sensible distance. It is not clear exactly what effect fixing the carbonyl bond lengths has on the calculations of Lüthi *et al.*,[64] or Persson *et al.*;[93] however, the effect would appear to be small, provided that these studies treat the axial and equatorial environments without bias (as in the CC calculations) introduced by the choice of the active space, which, due to computational necessity, does not include all of the metal-ligand bonding orbitals.

3.4.6 The treatment of multiconfigurational character

MCSCF and MRCI geometry optimisations were performed with the aim of improving the structure, specifically with the aim of calculating an axial M-C distance shorter than the equatorial. While is is appreciated that the CC calculations are already in good agreement with experiment, it is hoped that treating the limited multiconfigurational nature of the wavefunction might make the small alteration to the structure that is desired.

Table 3.12: Structural and energetic data for iron pentacarbonyl using a variety of single and multi-reference methods. The definition of the lengths is given in figure 3.10. The parentheses after the coupled-cluster methods indicates the core size used for those calculations. The cores are defined in table 3.1. a) The experimental structures are those of a) Beagley and Schmidling[98] and b) McClelland *et al.* (best model).[101]

Method	$r_{FeC_{ax}}$ / Å	$r_{FeO_{ax}}$ / Å	$r_{FeC_{eq}}$ / Å	$r_{FeO_{eq}}$ / Å	Energy / Hartree
HF	2.049	3.155	1.852	2.970	-1825.43808178
MP2	1.686	2.854	1.764	2.921	-1827.56814246
CCD(C3)	1.815	2.951	1.798	2.937	-1827.59558934
CCSD(C3)	1.835	2.973	1.801	2.945	-1827.65478664
CCSD(T)(C3)	1.811	2.959	1.800	2.952	-1827.78263309
MCSCF	1.875	2.988	1.842	2.960	-1825.75596310
MRCI	1.842	2.964	1.820	2.945	-1826.58006857
Experimental[a]	1.807	2.959	1.827	2.979	-
Experimental[b]	1.813	2.969	1.845	2.988	-

Figure 3.18: The RMS% difference (equation 3.1) for the multiconfigurational methods used, compared with those from HF and the CC calculations with core 3.

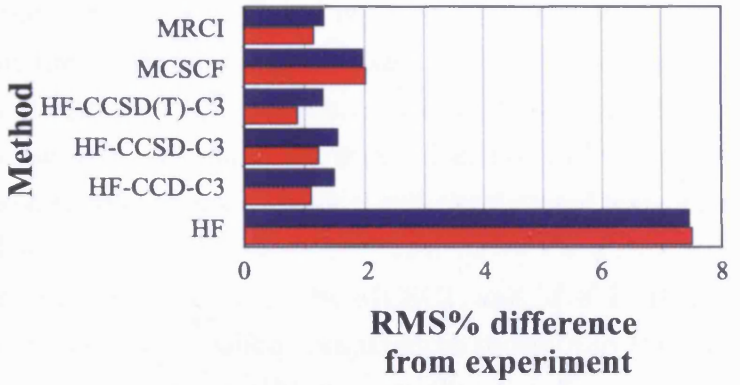

The optimised structures are given in table 3.12, while the RMS% differences are given in figure 3.18. For ease of comparison, the CC and HF results are repeated. The inclusion of static correlation with MCSCF can be seen to offer a dramatic improvement over the HF results. This can be thought of as a direct consequence of the inclusion of much of the orbital relaxation with this method. Inspection of the natural orbitals from the calculation indicated that there were no orbitals outside the active space with the character of the metal-ligand bonding interactions that it had been intended to include in the active space. The lowest active orbital was seen to have essentially metal s-character, however, it was decided to keep this orbital as active, since removing it caused the σ donating all-in-phase a_1' orbital to appear in the doubly occupied levels, which it had been intended to include as active.

The MRCI calculation makes a further improvement to the structure. Inclusion of single and double excitations, and the estimated Davidson cluster energy, gives a structure which is comparable to the CC results with core 3. This structure has an axial M-C bond some 0.03 Å too long and an equatorial bond 0.025 Å too short, thus, again failing to predict the experimental trend that the axial environment should be the shorter. The MCSCF wavefunction is found to be dominated by a single CSF, with a weight of approximately 85%, with the next largest CSF contibuting 1.2%. The MRCI wavefunction is also dominated by a single CSF (80%), while the next most significant contribution has a weight of 3%. The dominant CSF is the HF configuration in both MCSCF and MRCI wavefunctions, however, both methods show some multiconfigurational character, with a contribution from lots of low weight CSFs.

Unfortunately, the complex bonding mechanism exhibited by $Fe(CO)_5$ due to the synergic nature of the bonding means that a large active space is required to treat the system without bias. The active space used in this treatment includes all of the σ bonding and anti-bonding combinations of the ligands with the metal, and the most significant π combinations. It is larger than that used in the studies of Lüthi *et al.*[65] and Persson *et al.*,[93] and hopefully deals with all the major interactions. Although the study does not include a BSSE correction, it is not envisaged that this will have a sufficiently significant effect as to alter the optimised structure.

The optimised structures from the MCSCF and MRCI calculations, and especially the value of Δ_{ax-eq} when compared to those from the earlier studies of Persson *et al.*[93] and Lüthi *et al.*[65] suggest that the system is extremely sensitive to the choice of active space, and rather asks the question: "which active space is more appropriate". The past studies get a "better" answer, but the present study uses a larger active space, and gets a result of approximately the same quality as the CC results. This suggests that a careful interpretation of the results is required before drawing any conclusion about which theoretical study gives the best results. In other words, it is not inconceivable that the previous multiconfigurational studies[65,93] get the right answer for the wrong reasons.

3.5 Summary and Conclusions

The present study uses both *ab initio* and density functional methods, especially HF and KS-based coupled-cluster theory, to study the electronic and geometric structure of both the iconic sandwich molecule ferrocene, and a typical metal-carbonyl compound, iron pentacarbonyl. In agreement with previous workers, I find that HF theory performs badly for both the geometry and orbital structure of both systems. Møller-Plesset theory also performs poorly, which is perhaps not surprising, as it relies on the perturbation to the HF reference wavefunction being small.

It is clear from my results and past theoretical work,[63,66,67,102] that coupled-cluster theory can accommodate a poor reference function to generate good structures, but at the expense of significant relaxation of the molecular orbitals. The $\mathscr{T}_1$ diagnostic from HF based coupled-cluster theory is therefore large. The $\mathscr{T}_1$ diagnostics from B3LYP-based (and other DFT-based) coupled-cluster calculations are found to be much smaller, which we attribute to the B3LYP reference

being much closer to the expected MO structure, i.e. orbital relaxation is less significant.

The large $\mathscr{T}_1$ diagnostics from HF-based coupled-cluster calculations can be attributed to the poor reference wavefunction. Since coupled-cluster calculations from better references (i.e. KS orbitals) return equally acceptable geometries, yet significantly smaller $\mathscr{T}_1$ diagnostics, it can be confirmed that neither ferrocene nor iron pentacarbonyl are dominated by multiconfigurational wavefunctions. This is contrary to what might be concluded if the $\mathscr{T}_1$ diagnostic from HF-based coupled-cluster theory were used as the sole indicator of multiconfigurational character. This is supported by the large HF HOMO-LUMO gaps of approximately 13 eV and 12 eV for ferrocene and $Fe(CO)_5$ respectively.

For $Fe(CO)_5$, multiconfigurational calculations indicate that the HF reference dominates the wavefunction (accounting for 80%) while the remaining 20% is accounted for by many other CSFs, with the largest of these accounting for only 3% of the wavefunction. The minimum energy structure from this calculation is comparable with that from CCSD(T), indicating that this single reference method is capable of treating the system accurately, a further indication that the multiconfigurational character is not as large as might be construed from the HF-CC $\mathscr{T}_1$ diagnostic.

The present calculations suggest that the KS-CC approach may be a useful tool in situations where single reference behaviour is anticipated, yet the $\mathscr{T}_1$ diagnostics from regular coupled-cluster theory are high. Under such circumstances it is likely that the HF reference is poor, and that regular coupled-cluster expansions result in significant orbital relaxation. Perhaps the KS-CC $\mathscr{T}_1$ diagnostic could be a useful addition to the arsenal of indicators of multireference character, because it appears to be less sensitive to the often misleading effects of orbital relaxation than the HF-CC $\mathscr{T}_1$ diagnostic.

CC and DFT methodologies give good results for the structure of $Fe(CO)_5$, agreeing with the experimental structure to within a few hundredths of an Ångstrom. However, an exact agreement with the experimental structure is found to be particularly difficult to achieve. In fact, all of the single reference methods used (except MP2) are found to be in error, giving a longer axial than equatorial metal ligand bond lengths. A study of the system with various basis sets up to 6-311+G(3df), cc-pV5Z and STO-QZ4P quality finds the molecular structure, and Δ_{ax-eq} to become saturated quite quickly and it is concluded that the problem of the longer axial bond cannot be solved by varying the basis set size. The effects of the larger basis sets with the CC methodology have not been fully investigated

because of the limitation on available system resources. It is possible that it is necessary to simultaneously use a large basis set, a well correlated method and to consider relativistic effects in order to further improve the theoretical structure; this is beyond the scope of this study.

Multiconfigurational calculations have been used to probe the effect of the small (but not insignificant) contribution to the wavefunction due to multiconfigurational character. With the active space used it is found that the geometry is slightly poorer than those calculated using CC methods. It is clear from a comparison of this study with earlier studies that the choice of active space can make a difference to the structure predicted. More specifically, it appears that a smaller active space gives a structure that is in better agreement with experiment than that predicted when a larger active space is used. No attempt was made to repeat the calculations with the smaller active spaces used in the previous studies, because it was not clear exactly which orbitals were included in these active spaces. Unfortunately, the bonding mechanism involved in $Fe(CO)_5$ results in contributions to the orbitals affecting the metal-ligand bonding from all of the atoms in the system; i.e. many of the important molecular orbitals have atomic contributions from all the atoms of the molecule. This means that a very large active space would be required to include all of these orbitals, making such a calculation unfeasible.

It is unclear why it is not possible to reproduce the structure of $Fe(CO)_5$ exactly, particularly the correct value of Δ_{ax-eq}. It seems most unlikely that the experimental structure is in error; however, there may be a slight disparity between what is being measured in the experiment and the results of the calculations performed. The electron diffraction experiment involves the expansion of gaseous $Fe(CO)_5$ through a nozzle at 300 K.[101] This results in a cooling of the gas, and decreases the number of collisions between molecules significantly. This process effectively removes the mechanism for vibrational relaxation of the system, which is through quenching (i.e. collisions between molecules), and as such each molecule should have a similar amount of vibrational energy as it had at 300 K, before it was expanded. The removal of collisions results in a much cleaner electron diffraction pattern, because the measurements are being made of species with a fixed partitioning of the vibrational energy between vibrational states.

Due to the anharmonic nature of bonds, as higher vibrational states are populated the vibrationally averaged bond length (r_a) diverges from the equilibrium bond length (r_e), ultimately with the result that the bond can dissociate; even

the zero-point averaged bond length is slightly different from r_e. It is the vibrationally averaged structure that is being measured in the electron diffraction experiment. However all of the structures calculated in the present study (and in the past studies that are considered) are at equilibrium, free from vibrational motion, which will be slightly different from that measured. An important question is the size of this effect at the temperature of the experiment. It is not considered to be large, however, the disagreement between the experimental structures, and the predicted structures is only small, of the order of a few hundredths of an Ångstrom! For $FeCl_2$, the bond length from electron diffraction using a nozzle temperature of 981 K is reported to be 2.151 Å, while the equilibrium bond length from a anharmonic cubic potential is calculated to be 0.023 Å shorter, at 2.128 Å.[140]

$Fe(CO)_5$ has 27 normal vibrational modes. A B3LYP calculation with Gaussian using a 6-31+G(2d) basis set indicates that although the symmetrical stretch has a frequency of 2179 cm^{-1}, it also has 4 modes with frequencies under 100 cm^{-1}, and a further 3 at approximately 100 cm^{-1}. Thus, at 300 K (which corresponds to $\approx$ 210 cm^{-1}) there should be a significant population of the excited states of many of these vibrational modes. It is most certainly not straightforward, however, to estimate the effect on the bond lengths in such a system, or even if the axial and equatorial environments will undergo the same degree of vibrational expansion. With Gaussian, I have calculated the anharmonic vibrational frequencies and the resulting zero-point thermally averaged structure. This shows an extension of the metal-ligand bonds by approximately 0.7 thousandths of an Ångstrom. Unfortunately, Gaussian does not allow the calculation of vibrationally averaged structures at specific temperatures.

In the absence of another explanation for the small disparity between the theoretical and experimental structures, it is suggested that the effect of vibrational averaging should be considered as a possible cause. It is beyond the scope of the present study to consider the effect of vibrational averaging quantitatively, although I suggest that this effect should be investigated in further attempts to improve upon these calculations.

Chapter 4

TD-DFT Studies of the Electronic Absorption Spectra of the Actinocenes of Thorium and Protactinium

Contents

4.1 Introduction

The first actinide-carbocyclic ligand sandwich compound - bis(cyclooctatetraenyl) uranium (U(COT)$_2$, COT=η^8-C_8H_8) - was synthesised by Streitwieser and Müller-Westerhoff in 1968,[141] and dubbed uranocene due to the structural similarity to the metallocenes of the d-block transition metals[a]. The synthesis of further actinocenes soon followed, with thorocene, by Yoshida and Streitwieser in 1969,[142] and protactinocene by Stark *et al.* in 1973.[143]

Thorocene and uranocene were found to have D_{8h} structures by x-ray analysis,[142] however, due to the extreme rarity of protactinium[b], a full x-ray diffraction

[a]The term metallocene in its formal sense implies a metal bound to two five membered cyclopentadienyl (Cp) rings to form a sandwich compound, however, the term actinocene (or sometimes actinidocene) is not taken to imply Cp rings.

[b]Protactinium-234 was first discovered in 1913 as a decay product of ^{238}U, and Pa-231 in 1916.[144] Although it occurs naturally as a few ppm in ores, such as pitchblende, the world's main supply of pure protactinium was separated by the UK Atomic Energy Authority from 60 tons of waste in 1960, yielding 130 grams.[145]

pattern was unachievable, although the data available showed it to be structurally similar to its neighbouring analogues;[146] the exact structure, including the metal-ring centroid distance remains unknown.

The effects of adding substituent groups to the rings in metallocene complexes is to stabilise them both kinetically and thermodynamically.[147] This is because the substituents generally shield the metal centre,[147] and because in the case of alkyl substituents, the inductive effect causes the ring orbitals to be a better energy match with the metal orbitals, thus allowing a stronger covalent bond to form. $Th(TMCOT)_2$ (TMCOT=η^8-$C_8(CH_3)_4H_4$) was first synthesised by Levanda and Streitwieser in 1981,[148] and the protactinium analogue, $Pa(TMCOT)_2$ by Solar *et al.* in 1980.[146]

One of the main efforts in the theoretical study of actinocenes is to understand the nature of the metal-COT bond.[145] In particular the balance between ionic and covalent bonding, and the extent to which the f-orbitals are involved in the bonding.[149] The second main interest in studying actinocene species is to gain a better knowledge of the behaviour of the f-electrons in complexes. The typical experimental means of determining electronic structure (e.g. optical spectroscopy), generally give data which are very difficult to interpret for actinide species, an effect which is attributed to the nature of the 5f electrons; a possible exception to this is for highly symmetrical systems, such as uranocene and thorocene.[150]

Due to the nature of the M-COT bond, the extra two electrons present in uranocene compared with thorocene are expected to occupy an orbital that is essentially non-bonding. Due to the weak interaction of these electrons with the ligand field, the uranium atom in uranocene can be thought of as having an f^2 configuration; the interaction of these electrons results in extremely complex behaviour, which makes spectroscopic assignment difficult. In fact, it is not clear from experiment exactly which orbitals contain the unpaired electrons.[150] Similarly, thorocene has an effective f^0 configuration; all its valence electrons are involved in ring bonding. Since the complexity of the electronic spectra of these species is attributed to the f-electrons, thorocene should have a much simpler electronic absorption spectrum than uranocene, since there should be no transitions originating from orbitals with strong metal f-character. The importance of the study of protactinocene in the quest for understanding the complex nature of the f-electrons stems from this fact. Protactinocene, with an f^1 configuration should provide the most direct evidence for the nature of the f-electrons, because, in some respects it allows for the study of an individual f-electron, which interacts with the ligand field only and not with any another metal based f-electrons. Under-

standing the electronic properties of protactinocene thus represents an important step in the quest for a better understanding of the behaviour of f-electrons.

TD-DFT has been shown to be a generally useful tool for calculating the electronic excitations of many species, especially transition metal complexes.[151] It is more versatile than calculating excitations using Slater's transition state method, because it allows for configuration mixing, which helps correct for the orbitals of the ground state (g.s.) not being representative of the orbitals of the excited states.[151] TD-DFT to the best of my knowledge has not been used to study actinocene systems, and it is hoped that it will prove a useful tool in furthering the understanding of the electronic structure of these species.

4.2 The Electronic Structure of Actinocenes

4.2.1 Unsubstituted actinocenes of D_{8h} symmetry

Cyclooctatetraene (COT) forms particularly stable covalent bonds with the early actinides, due to a number of electronic and structural factors. The larger ring diameter in COT compared with smaller carbocyclic ligands (such as benzene), forces the metal atom to sit closer to the ring plane for the same metal-carbon distance. This increases the overlap between the metal and ring orbitals. The COT ligand donates electron density to the metal through interactions of the p-orbital combinations on the rings with the metal d- and f-orbitals, which are of a good energy match. The eight carbon atoms in each ring allow π-combinations to be formed which can interact with the metal to form σ, π, δ and ϕ bonds with the d- and f-orbitals (see figure 4.1). The π-combinations formed on the rings are shown in figure 4.2.

Figure 4.3 depicts schematically the interaction of the d- and f-orbitals of thorocene with the p-orbital ring combinations formed by the COT sandwich. The COT ligand requires two electrons to become aromatic, and such it can be viewed as occupying two metal valencies. The actinide atom can thus be thought of as being in its 4+ oxidation state in the complex.

The high symmetry of these systems has the effect that the d- and f-orbitals cannot mix in bonding interactions with the rings,[152] the former being *gerade* parity while the latter are *ungerade*. This facilitates analysis of the contributions to the bonding. The d-orbitals can interact with the a_{1g}, e_{1g} and e_{2g} ring orbitals forming σ, π and δ interactions respectively. The f-orbitals can interact with the a_{2u}, e_{1u}, e_{2u} and e_{3u} ring orbitals forming σ, π, δ and ϕ interactions. The extent of

metal-ring mixing between orbitals of the same symmetry type, depends strongly upon having a good energy match.

In the 3d metallocenes, it is the dπ interactions with the rings which stabilises the system, the interaction of the dδ orbital with the rings is weak.[149] Streitwieser and Müller-Westerhoff originally proposed that the main stabilising interactions in thorocene were of the metal f-orbital (the HOMO) with the e_{2u} ring π-orbitals, in a δ-fashion, since these orbitals project directly into the ring plain.[141] This is analogous to the bonding in ferrocene of the HOMO (e_{1g}) with the rings.[153] It was soon realised that this description of the bonding was too simplistic, and could not predict the photo-electron (PE) spectrum for uranocene, or thorocene.[154]

Clark and Green recorded the PE spectra for these species and noted that the ordering of the e_{2g} and e_{2u} orbitals matched that expected for the interaction between the rings in the absence of the metal (i.e. e_{2g} more stable than e_{2u}), except that the splitting of approximately 1 eV was much greater than one would expect from the ring-ring interaction alone.[150]

Figure 4.1: The e_{2u}, e_{2g}, e_{1u}, e_{1g} bonding orbitals, the weakly bonding e_{3u} orbital and the a_{2u} non-bonding orbitals of thorocene.

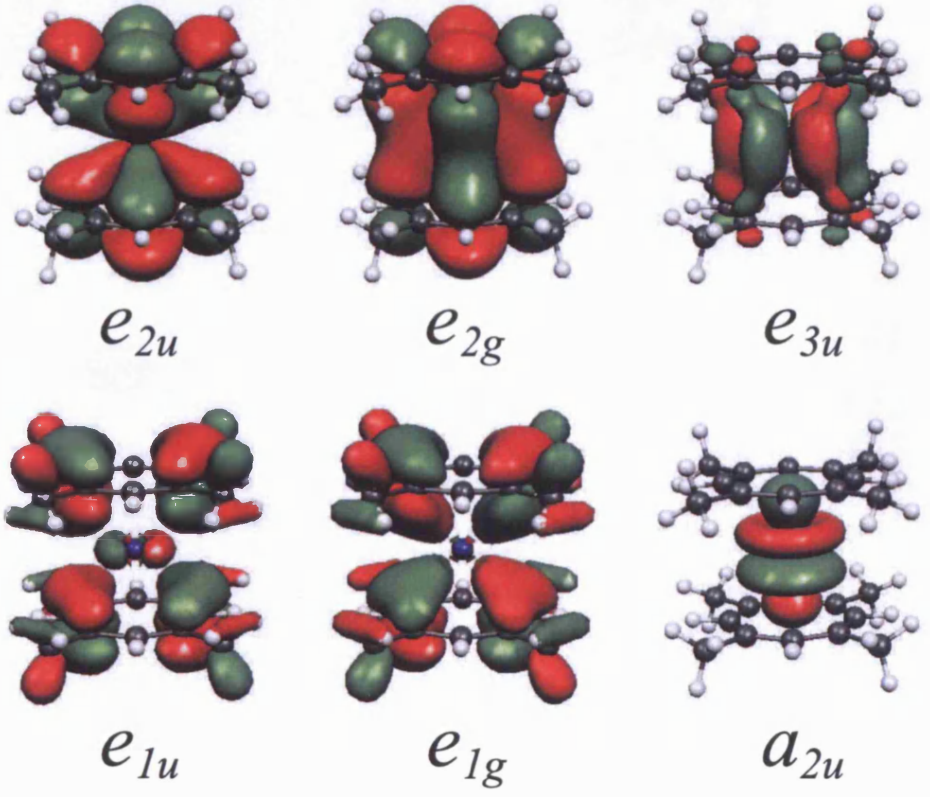

Figure 4.2: Qualitative molecular orbital diagram showing the π-orbitals of COT and their interaction to form the frontier MOs of $(COT)_2$.

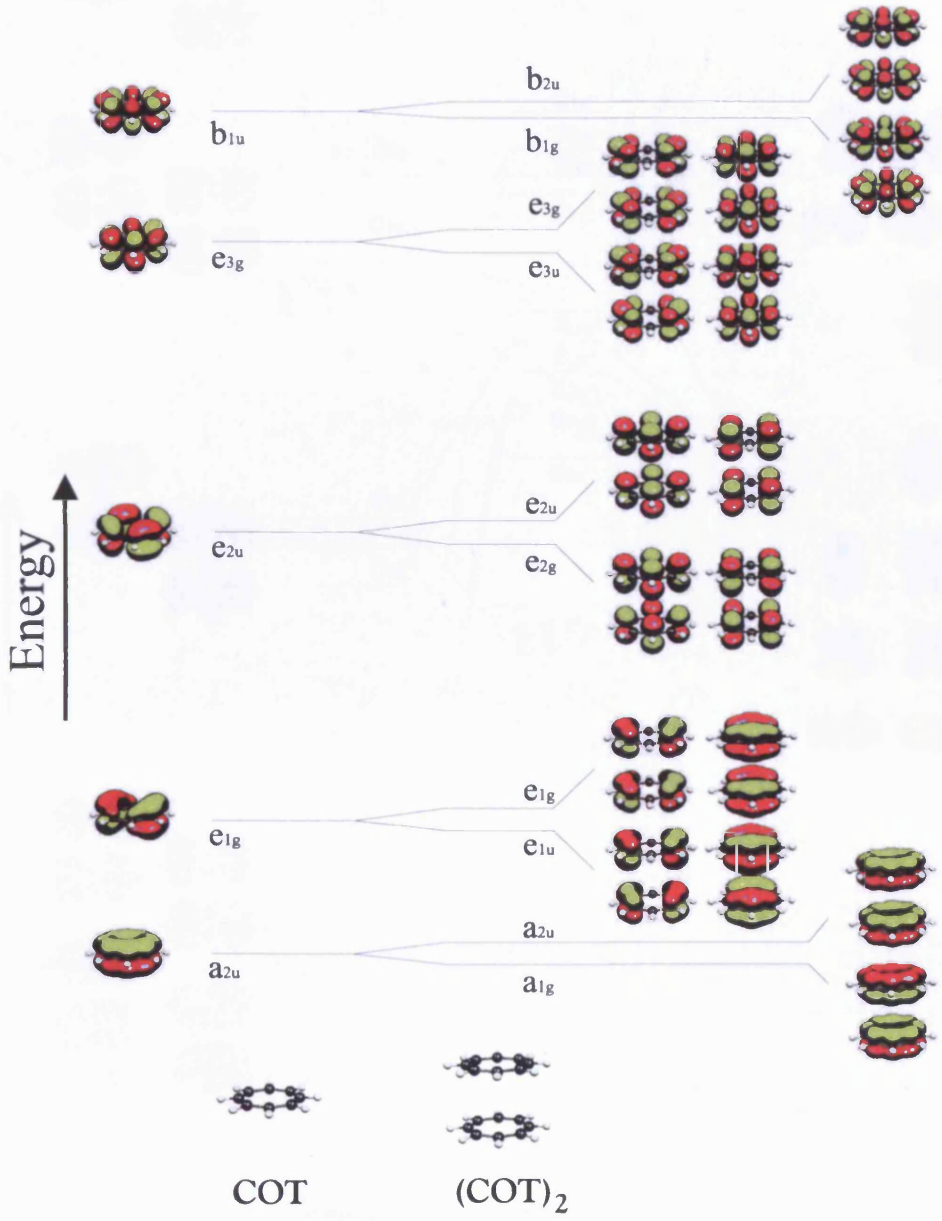

Figure 4.3: Molecular orbital diagram showing the interaction of the d- and f-orbitals of thorium with the conjugated π-system of the rings. The half arrows indicate the electrons in the HOMO of $Th(COT)_2$.

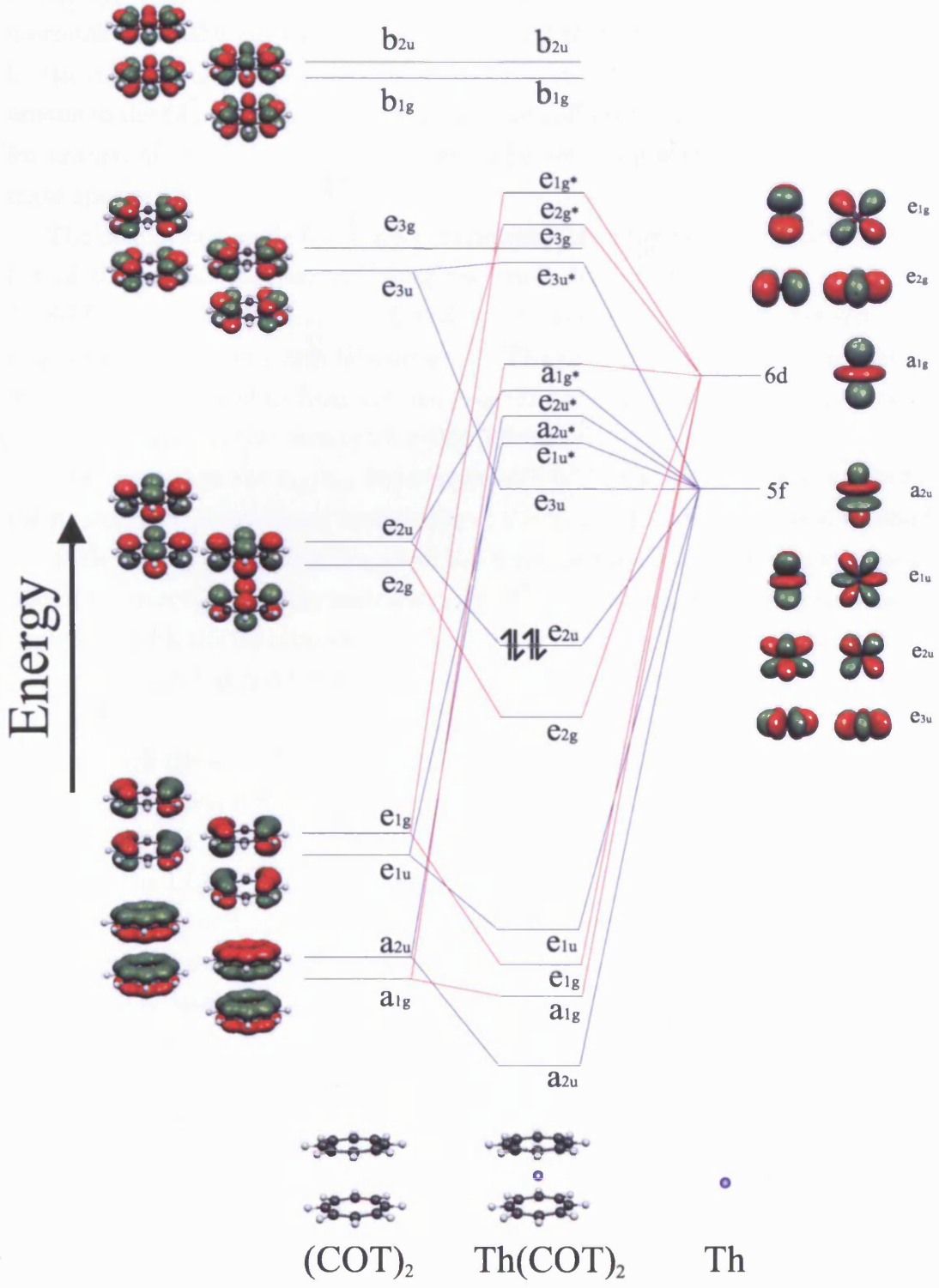

The interaction of the e_1 and e_2 type orbitals between the rings should be roughly equivalent, however, experimentally the e_{1u}/e_{1g} splitting is smaller than the e_{2u}/e_{2g} splitting in the complex. If the only interaction of the metal was of the $f_{e_{2u}}$ type, one would expect the e_{2u}/e_{2g} to be the smaller due to the stabilisation of the e_{2u} orbitals.[150] Thus the PE spectral data indicate involvement of the d-orbitals with the e_{2g} ring combinations, and that this interaction is likely to be the major source of covalent bonding in these species. The $f_{e_{2u}}$ interaction is unique to the f-block and the extra stabilisation afforded (which should be greater for uranocene than thorocene) is likely to be very important to the stability of these species.[150]

The deductions made from this experimental study were confirmed by a number of theoretical studies, including the study by Boerrigter *et al.* using the HFS-LCAO method,[149] and Rösch and Streitwieser using Xα scattered wave calculations on thorocene and uranocene.[153] The earlier study of Hayes and Edelstein excluded d-orbitals from the analysis, thus failing to predict the importance of the d-orbitals in the covalent bonding interaction.[155]

The reversal of the e_{1g}/e_{1u} ordering in $M(COT)_2$ compared with the $(COT)_2$ dimer indicates a significant interaction of the rings with the 6dπ metal orbitals, but little mixing of the metal-e_{1u} f-orbital with the rings (although the symmetry match is correct, the energy match is poor).[149] The 5f orbitals are very contracted compared with the 6d orbitals, thus 5f-ring interactions are only significant when the energy match is good; the 6d-ring interactions are less sensitive to this energy match.[149]

Although the e_{3u} orbital has a symmetry match with a ring combination, this metal f-orbital has little radial extension along the principal molecular axis, and thus should not interact significantly with the ring orbitals; this non-bonding orbital is the LUMO for thorocene.

The e_{3g}, b_{1g} and b_{2u} ring orbitals have no symmetry match with the metal, requiring g- and h-metal functions. The metal a_{1g} d-orbital and a_{2u} f-orbital interact only weakly with the ring π system in the pseudo-axial environment of actinocenes, because there is very little overlap (see figure 4.4). These metal orbitals can be expected, however, to interact more strongly with the σ framework of the rings, and this effect, although not shown in figure 4.3, is likely to cause a slight re-ordering of the low lying virtual orbitals, depending upon the energy match with the ring system.

Although the interactions of the 6pπ orbitals with the e_{1u} orbitals is expected to be small, since the energy match is poor, it is thought to be exchange re-

pulsion between these occupied orbitals which prevents the metal-ring centroid distance becoming small enough to allow significant f-orbital overlap with the ring orbitals.[149]

Protactinocene can be expected to have a similar molecular orbital structure to thorocene, however the effect of the open-shell electronic configuration needs to be considered. In thorocene, the closed shell electronic structure can be treated with a restricted methodology where each MO is occupied by two electrons. Thus the up- and down-spin components of the molecular orbitals can be considered to have the same space function and are degenerate. In protactinocene, the open-shell configuration means that there is one more up-spin than down-spin electron. Thus, in an unrestricted methodology the degeneracy between the up- and down-spin components of the same MO is lifted. The largest α-β splitting is expected for the orbital with the 'single' electron and the vacant orbital of the same spatial type, however all the f-orbitals will exhibit this α-β splitting since the up- and down-spin components are orthogonal, and so the down-spin orbitals will 'see' one less electron than the up-spin orbitals.

The f-orbitals are fairly contracted and are not expected to interact strongly with the ligand orbitals, thus they will have similar orbital energies to each other. For a species with a single electron in nearly degenerate orbitals, we would expect a multiconfigurational wavefunction. However if the electron is forced to occupy a single orbital, as in a single determinantal wavefunction, then we might expect it to occupy the a_{2u}, or the e_{3u} f-orbital, because these should interact to the least extent with the pseudo-axial ligand field. Indeed Li and Bursten predict $Pa(COT)_2$ to have an $^2A_{2u}$ electronic ground state.[156]

One important observation from the electronic structures predicted by Kaltsoyannis & Bursten[157] and Li & Bursten[156] is that the MOs are much more evenly spaced out in terms of energy, and this results in a smaller HOMO-LUMO gap than seen for thorocene. Of course, due to the close spacing of the f-based orbitals, the HOMO-LUMO gap is expected to be very small for protactinocene. Due to the close energetic spacing of the f-orbital based levels, Kaltsoyannis and Bursten found it necessary to employ a thermal spreading factor, resulting in the partial occupation of two metal-f based MOs.[157]

Kaltsoyannis and Bursten used DFT with spin-orbit (SO) corrections to study $Pa(COT)_2$. They confirm the importance of the interaction between the 5fδ metal orbitals and the e_{2u} ring orbitals as being a major source of the covalency in the metal-ring interaction, but also note the important participation made by the 6d orbitals.[157] This observation is consistent with the observation of Boerrigter *et*

Figure 4.4: Schematic representation of the interaction between the ring p-orbitals and the metal d_{z^2} orbital; in D_{8h} mixing can only occur between the a_{1g} ring orbital and the d_{z^2} metal-orbital. For simplicity only a slice through the molecule (which contains the principal molecular axis) is shown in the diagram. The dashed line represents the nodal-cone of the d-orbital, bisecting the region of greatest electron density on the rings.

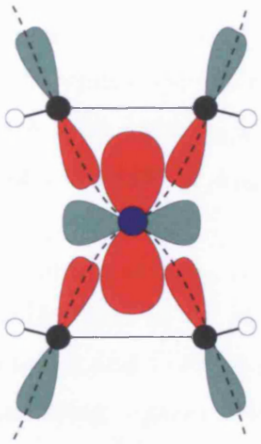

al.,[149] that relativistically, the 6d orbitals contribute significantly to the metal-ring δ- and π-bonds. The MO structure is found to have a region in which the f-orbital based MOs lie in very close energetic proximity, except for the 5fδ based-orbital - the anti-bonding component of the ring-metal δ bond, which is significantly destabilised. This was taken to support the notion that it is only this f-orbital that is significantly involved in the ring-metal bond.[157]

The 6dσ orbital was found to lie above this manifold of f-metal based levels, having essentially non-bonding character with no significant interaction with the pseudo-axial ligand environment.[157] The reason suggested for this is that the lobes of the p-orbitals on the rings bisect the nodal cone of the d_{z^2} orbital, thus giving minimal overlap (figure 4.4).[157] The inclusion of relativistic effects in the system, using SO coupling have the main effect of lifting the degeneracy of the e-orbitals. The metal-6p orbitals are stabilised, and so interact less with the ring orbitals; a similar stabilisation is noted for the $6d_{z^2}$-based orbital, moving it into the same energy range as the metal f-orbital based levels.[157] This does not, however, alter the ground state configuration from being f^1, but does imply a low lying f→d transition.

4.2.2 Substituted actinocenes of D_{4h} symmetry

$Th(TMCOT)_2$, where the COT rings have each been substituted with four methyl groups, has a slightly modified MO structure compared with the unsubstituted species for two main reasons. Firstly, the substituent orbitals on the rings cause the MOs to lie at slightly higher energy, and thus the ligand orbitals are expected to be a better energy match with the metal orbitals. Secondly, the descent in symmetry from D_{8h} to D_{4h} causes an alteration of the symmetry properties of the ligand field. Upon the descent in symmetry, the orbitals of the $e_{2u/g}$ irreducible representation (irrep) in D_{8h} are split into $b_{1u/g}$ and $b_{2u/g}$ components in D_{4h} (table 5.3, section 5.1), while the orbitals of $e_{1u/g}$ and $e_{3u/g}$ symmetry in D_{8h} span the same irrep in D_{4h}, $e_{u/g}$.

On lowering the symmetry, the b_{1g} and b_{2u} ring π combinations translate to a_{1g} and a_{2u} symmetry respectively, and so all of the ring π-combinations have symmetry matches with the metal d- and f-orbitals. However this does not imply significant mixing of the higher lying ligand orbitals with the metal orbitals, because these may still not be of a good energy match. Figure 4.5 represents diagrammatically the effects on the MO structure caused by the alteration of the ligands, and accompanying change in the framework symmetry.

Upon the substitution of protactinocene to form $Pa(TMCOT)_2$, it is expected that the same splitting that occurred in thorocene should occur to both the α and β-orbitals of protactinocene, thus further removing degeneracy from the system.

4.2.3 Experimental UV-vis data

There are very few experimental data available in the literature for the electronic spectra of the species under investigation, and unfortunately there are no experimental electronic excitation data available for protactinocene at all. For $Th(COT)_2$ and $Th(TMCOT)_2$ the energy of the lowest energy band is published, while for $Pa(TMCOT)_2$ the lowest energy band, and a shoulder are reported. These data are given in table 4.1. Unfortunately no actual spectra are shown for any of these compounds, which could aid with the assignment of the experimental bands to a theoretically calculated excitation.

It is clear that the experimental data available for the compounds studied are scant, but it also appears that the data for $Pa(TMCOT)_2$ are inconsistent with the data available for the thorium compounds, since they do not fit in with a simple explanation of these systems using molecular orbital theory.

Figure 4.5: Molecular orbital diagram showing the interaction of the d- and f-orbitals of thorium with the conjugated π system of the rings after the descent in symmetry from D_{8h} to D_{4h} caused by the methyl substitution to the rings. The half arrows indicate the electrons in the HOMO of $Th(COT)_2$.

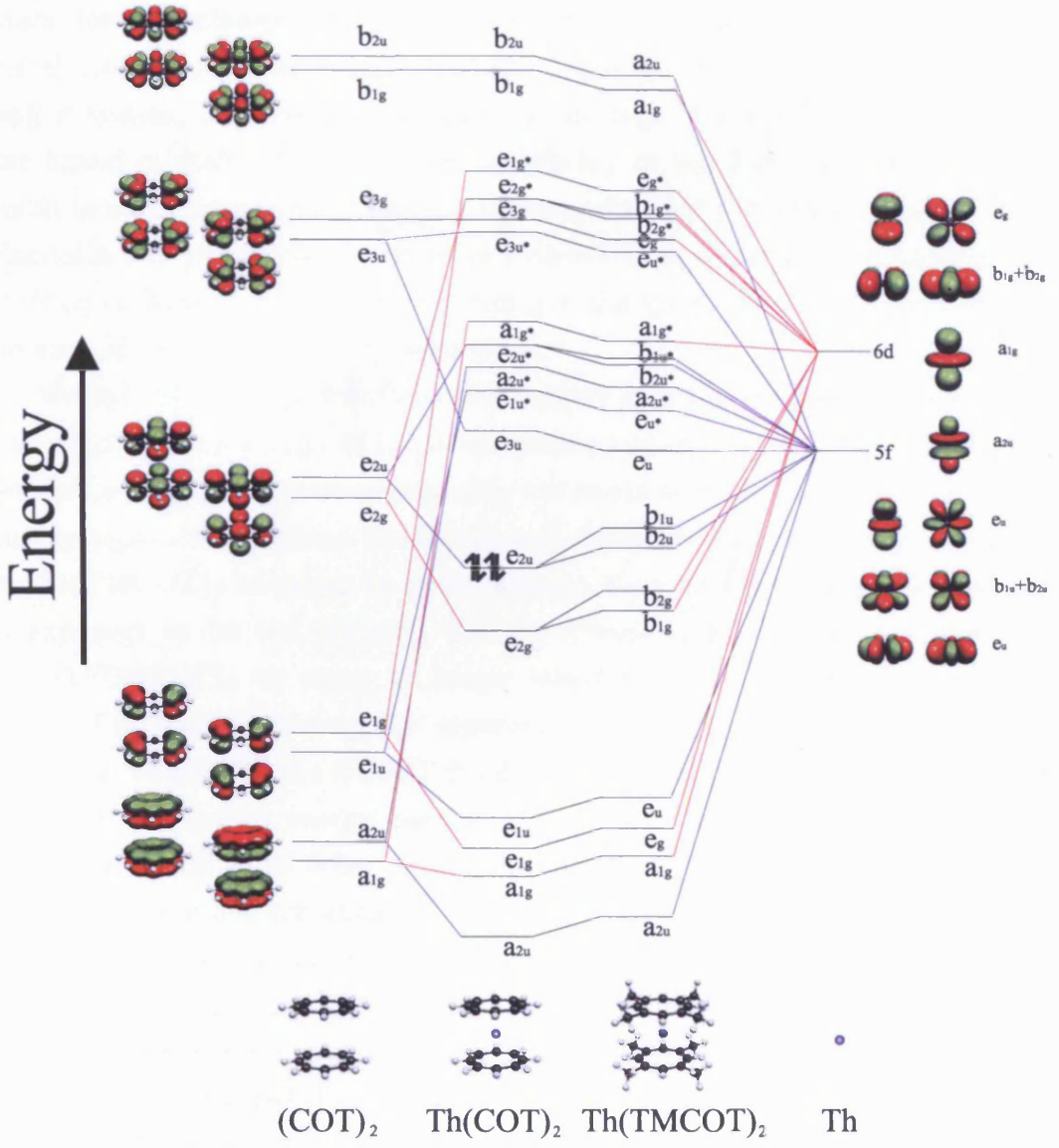

Table 4.1: Available experimental UV-vis data for the species studied.[146]

Compound	Wavelength / nm
$Th(COT)_2$	450
$Th(TMCOT)_2$	480
$Pa(TMCOT)_2$	380, 490(sh)

As one progresses across the actinocenes, the metal orbitals become more contracted, and are stabilised, however the f-orbitals contract more quickly than the other orbitals due to the poor shielding of the f-orbitals from the nucleus by the other electrons (leading to the actinide contraction). For thorium the metal d-orbitals lie below the f-orbitals, but this situation is reversed for uranium; for protactinium one would expect them to lie very close together. These metal orbitals occur at a higher energy than their symmetry matches with the ring π system, and the general stabilisation improves their energy match with the ligand orbitals. This improves the efficacy of the bonding, and should also result in a smaller energy separation between the ligand and metal based orbitals. Excitations in protactinium compounds should thus occur at lower energies than their equivalents in thorium compounds (i.e. the spectrum should be red-shifted), because of this smaller energy separation.

Methyl substituents push electron density into the ring system (the inductive effect), which results in the destabilisation of the ring orbitals[c], and so they become a better energetic match with the metal d- and f-orbitals. The smaller energy separation between the ligand and metal orbitals causes the transitions in $Th(TMCOT)_2$ to occur at lower energies than in $Th(COT)_2$; the spectrum is expected to be red shifted. The experimental data shows the first band for $Th(TMCOT)_2$ to occur at longer wavelengths by 30 nm compared with $Th(COT)_2$, thus supporting this argument.

In $Pa(TMCOT)_2$ the HOMO should be of f-orbital character; one would expect that the lowest energy band in the spectrum of $Pa(TMCOT)_2$ would be from this f-orbital, to other close lying metal or ring based orbitals. Thus if one assigns the 490 nm shoulder to this f-electron transition, then the natural assumption would be for the 380 nm band to have the equivalent assignment as the highest energy band in $Th(TMCOT)_2$. This clearly does not match with our simple description of the system - the band has been blue shifted by 100 nm, not red-shifted as expected. If the 490 nm band is assumed to be the equivalent of the highest band in $Th(TMCOT)_2$, it contradicts the idea that the HOMO should have f-electron character, unless transitions originating from this orbital are missing from the spectrum (i.e. they occur at too low energy, or have no intensity). The 380 nm band is unlikely to be the lowest energy transition originating from the HOMO f-based orbital since it would then occur at a higher energy than the ligand-to-metal charge transfer (LMCT) transition. It seems that we should treat the $Pa(TMCOT)_2$ data with suspicion, and I tentatively suggest that the

[c]i.e. the extra electron density in the rings makes ionisation from the orbitals easier.

bands appearing are not equivalents of the bands observed for $Th(COT)_2$ and $Th(TMCOT)_2$.

4.2.4 Previous assignments of electronic spectra

4.2.4.1 $Th(COT)_2$

Rösch and Streitwieser, using the Xα scattered wave methodology, assigned the experimentally observed band at 450 nm to a LMCT transition with $\pi_{e_{2g}} \rightarrow 5f_{e_{3u}}$ character.[153] This was based on the difference between orbital energies, their theoretical band occurring at 409 nm. This method, of course, ignores orbital relaxation effects, and calculates the excitation energy purely from g.s. properties.

Dolg *et al.*, using MRCISD, calculate the $^1A_{1g}$ g.s. to be $5f^0\pi^4_{e_{2u}}$, with a good energy separation to the first excited state, which they calculate to lie 2.45 eV above the g.s.[158] The first excited state corresponds to a $6d^1_{a_{1g}}\pi^3_{e_{2u}}$ configuration with $^3E_{2u}$ symmetry. This gives a vertical transition energy of 454 nm.[158] Dolg *et al.* also calculate the $\pi_{e_{2g}} \rightarrow 5f_{e_{3u}}$ transition suggested by Rösch and Streitwieser[153] to occur at 230 nm in their study, and estimate that the $\pi_{e_{2u}} \rightarrow 6d_{a_{1g}}$ transition occurs at 577 nm in the study of Rösch and Streitwieser.[158]

This analysis agrees with the study of Boerrigter *et al.*, who calculate that non-relativistically the lowest lying vacant orbitals in thorocene are f-based, with a higher lying dσ-orbital.[149] However, when relativistic effects are included, a differential stabilisation of the f and d-orbitals is caused, such that the f-orbitals are preferentially destabilised; the LUMO thus becomes metal dσ instead of M-f based.[149]

4.2.4.2 $Pa(COT)_2$ and $Pa(TMCOT)_2$

Chang *et al.* used CI calculations to predict the lowest energy excitation of protactinocene, including the effects of spin-orbit (SO) coupling.[159] The g.s. is predicted to be $E_{5/2u}$, which is essentially e_{3u} based. They calculate the lowest energy excited states to be $5f^1$ based, however, the $6d^1$ level, with d_{z^2} character lies between the lower 5f levels and the higher lying $5f_{e_{2u}}$ level, which is destabilised by interactions with the ring orbitals.[159] The $5f_{e_{3u}}$ orbitals are predicted to be lowered by the slight interaction with the ring e_{3u} orbitals.[159] The 6d orbitals are predicted to be split more significantly than the 5f, due to more significant interactions with the rings, except for the $6d_{a_{1g}}$, which is essentially non-bonding.[159] Their lowest energy allowed transition is at 338 nm and is of $\pi \rightarrow$d character,

although the exact character of the orbitals involved in this transition are unclear.[159]

Kaltsoyannis and Bursten[157] used DFT with a spin-orbit (SO) corrected wavefunction to investigate the electronic transitions of $Pa(COT)_2$, using Slater's transition state method. The formal g.s. from both non-relativistic and relativistic calculations is predicted to be f^1, although the M-dσ based level lies at only a slightly higher energy once relativistic effects are considered. At the relativistic level, the lowest energy allowed transition was found to have f→d character occurring at 911 nm which may mask two transitions from the metal-f levels to antibonding levels with largely metal-ring e_{2u}-character at 886 and 736 nm.[157] These are observed to be of too low energy to explain the experimental spectrum. The lowest energy charge transfer (CT) transitions are of LMCT character and occur at 467 and 360 nm; these occupy the low lying vacant metal-f based levels from the ring based e_{2u} and e_{2g} bonding orbitals respectively. A further transition at 351 nm is of MLCT character, populating the ring e_{3u} anti-bonding orbitals from the Pa-f manifold of levels.[157]

Since no spectrum is available for $Pa(COT)_2$, these theoretical transitions are compared with those for $Pa(TMCOT)_2$, although the effects of the bathochromic shift expected upon substitution of the COT rings for TMCOT are not considered.[157] The similarity between the spectra of $Th(COT)_2$ and $Pa(TMCOT)_2$, as observed by Solar *et al.*, is interpreted by Kaltsoyannis and Bursten as good evidence that the spectrum of $Pa(TMCOT)_2$ is dominated by the only transitions which can occur in $Th(COT)_2$ - those of charge transfer character. They suggest that the shoulder and band observed experimentally at 490 and 360 nm should be interpreted in terms of the theoretical LMCT bands at 467 and 360 nm and the MLCT band at 359 nm.[157] Since the f→d transition at 911 nm occurs at an energetically sensible energy in comparison with that in uranocene, it is deduced that this band was not observed in the experimental data, since it occurs in the IR.[157]

Li and Bursten studied various properties of protactinocene, including its geometry and electronic transitions.[156] Their scalar-relativistic calculations predict the electronic g.s. to be of $^2A_{2u}$ symmetry, with the single electron in the f_{z^3}-orbital. With the inclusion of spin-orbit effects, they calculate the g.s. to be $E_{5/2u}$, corresponding to the outer configuration $(e_{5/2u})^1$, which corresponds predominantly to the $f\phi^1$ configuration.[156]

The lowest energy transitions from the $f\phi^1$ outer configuration are $E_{5/2u}\rightarrow E_{5/2g}$ and $E_{5/2u}\rightarrow E_{7/2g}$, which both occur at 397 nm; these correspond to populating

the $3e_{3g}$ orbital, which has antibonding character between the rings.[156] The second allowed transition ($E_{5/2u} \rightarrow E_{3/2g}$) occurs at 368 nm, and the dominant orbital transition character is the formation of an excited state with a $d\delta^1$ outer configuration.[156]

Only two electronic transitions from the ligand based orbitals were found to occur in the visible region of the spectrum, the remainder occurred in the UV part of the spectrum. These LMCT transitions occur at 435 and 430 nm and correspond to transitions from the $5e_{5/2u}$ and $7e_{3/2u}$ orbitals to the $8e_{1/2g}$ orbital respectively.[156] These relate to transitions from the $3e_{2u}$ ligand-based orbitals to the Pa-dσ based MO.

Solar *et al.* suggested that the band occurring in the spectrum of $Pa(TMCOT)_2$ at 380 nm should occur at 365 nm in $Pa(COT)_2$, based on the bathochromic shift observed when COT is replaced with TMCOT in other actinocene complexes.[146] Li and Bursten assign the band predicted to occur at 365 nm to the transition with f$\phi \rightarrow$dδ character at 368 nm and suggest that the two LMCT bands at 435 and 430 nm could be the origin of the shoulder in the spectrum of $Pa(TMCOT)_2$ (490 nm[146]), once the effect of a hypsochromic shift has been considered.[156] They further suggest that it is these bands that give $Pa(COT)_2$ its characteristic golden-yellow colour, since these bands absorb in the violet region of the spectrum.[156]

The aim of this study is to calculate the electronic excitations of $An(COT)_2$ and $An(TMCOT)_2$ (An = Th, Pa) using TD-DFT, and to use these results to confirm, or reinterpret the previous assignments[149,156–159] of the available experimental UV-vis spectral features for these species. A comparison of the results of this study with the previous studies should lead to a more thorough understanding of the electronic structure of these species, but will also extend the range of systems for which TD-DFT has been used, hopefully reinforcing its general applicability.

4.3 Methodology

4.3.1 Computational Methodology

The structures of $An(COT)_2$ and $An(TMCOT)_2$ (An = Th, Pa), were determined using the TZP ZORA basis sets on thorium, protactinium and carbon, and the DZP ZORA basis set on hydrogen, using the VWN,[119,120] BLYP,[121–123] OLYP,[122,123,160] BP86,[121,124] PW91,[126] PBE,[21] KT1 and KT2[161] density functionals with the Amsterdam Density Functional (ADF) 2006.01 package.[131–133]

TD-DFT with VWN, BLYP, OLYP, BP86, PW91, PBE, KT1, KT2, SAOP,[30] LB94[29] and GRACLB[162] was used to calculate the lowest allowed electronic transition energy for $Th(COT)_2$, and this was compared with experiment, to determine the best method for calculating the electronic spectra. For the LDA and GGA functionals the electronic spectra were calculated at the geometry optimised with the same functional, while a variety of optimised geometries were chosen at which to calculate the excitation energies with the model potentials. The calculations used an integration grid value of 5, and a geometry convergence criterion of $1x10^{-4}$ on the gradient of the energy.

The electronic spectra for $Th(TMCOT)_2$, $Pa(COT)_2$ and $Pa(TMCOT)_2$ were calculated with the method which gave the best agreement with experiment for thorocene.

These results were augmented with Gaussian 03[163] calculations using the Stuttgart ECP60SEG basis sets for thorium and protactinium with the ECP60-MWB relativistic core potentials of Dolg.[164,165] Dunning's cc-pVTZ basis set was used for carbon, but with the f-functions omitted, while the cc-pVDZ basis set was used for hydrogen. The BLYP and B3LYP[22] density functionals were used to optimise geometries and calculate excitation energies using TD-DFT.

For the ADF calculations MO plots were calculated with Molekel,[166] and the UV-vis spectra were visualised with ADFSpectra.[167] For the Gaussian calculations, Gaussview[168] was used to plot the molecular orbitals, while GaussSum[169] was used to plot the spectra. All the molecular orbital plots used a space value of 0.02.

4.3.2 Analysis Methodology

4.3.2.1 Electronic spectra

The output from the TD-DFT calculation gives the dipole allowed molecular electronic excitations in order of energy, along with their calculated oscillator

strengths. The quantitative breakdown of each excitation into electronic transitions between orbitals is indicated by weighting coefficients similar to those from a CI calculation, with the labels of the MOs involved.

These data have been used to plot the electronic spectrum, and each of the band envelopes above 200 nm has been assigned a letter. Where a band envelope (for instance band A) contains more than one overlapping molecular excitation, they have been tabulated as A1, A2, A3 etcetera. Any excitations with oscillator strengths of less than (1/10)x that of the dominant excitation of the band have been neglected. A molecular excitation may be comprised of several electronic orbital transitions; these are tabulated along with the percentage weight they contribute towards the excitation. Only transitions which contribute at least 5% towards an excitation are tabulated. The character of the transition is also tabulated, where R and M indicate ring and metal based orbitals respectively. These transitions are indicated on the MO diagrams by vertical lines between the relevant orbitals. The width of the line indicates the proportion of the excitation with that character and the colour indicates the nature of the transition in terms of the MOs involved, to allow comparison between diagrams. Only transitions which contribute at least 10% towards an excitation are marked on the diagram.

4.3.2.2 Selection rules

Transitions must span either the E_{1u} or A_{2u} irreps in the D_{8h} point group, and E_u or A_{2u} in the D_{4h} to be dipole allowed, because the cartesian coordinates span these irreps, and therefore the direct product of the irreps of the initial and final states must contain one of these irreps. This of course implies the laporte (g/u) selection rule.

Since the l-quantum number is not a good quantum number in molecular systems, the $\Delta l = \pm 1$ selection rule must be considered more carefully. The angular momentum of the MOs is influenced by all their atomic components, and will not necessarily be integral. However, we might expect transitions between orbitals dominated by metal orbitals where $\Delta l = 1$ to have a stronger oscillator strength than other metal-based transitions.

4.4 Computational Results for $Th(COT)_2$

4.4.1 Geometric structure

The structure of thorocene was optimised with a variety of density functionals under D_{8h} symmetry. Table 4.2 gives the optimised parameters while figure 4.6 defines the geometric variables. The experimental metal-ring centroid distance, C-C and Th-C bond lengths as determined by single crystal x-ray diffraction are also given.[170]

The agreement of the theoretical results with the x-ray data is within 0.1 Å of experiment for the metal-ring centroid and Th-C distance, and rather better for the C-C bond length. The best method appears to be VWN, while the poorest is BLYP. Curiously, the KT1 and KT2 functionals work as well as the other functionals used at predicting the structure, which is slightly surprising since they are not parameterised for geometries, but for calculating shielding constants! The hydrogen atoms bend inward towards each other for all of the methods investigated. This can be explained by the p-orbitals on the carbon atoms which make up the π-system having better overlap with the metal orbitals if this orientation is adopted. This explanation was first suggested by Hodgson and Raymond for $U(COT)_2$.[171]

Table 4.2: The structure of thorocene as determined by a variety of density functionals. The experimental data are from single crystal x-ray diffraction.[170] The definition of the geometric parameters is given in figure 4.6.

	VWN	BLYP	OLYP	BP86	PW91	PBE	KT1	KT2	Expt
Th-X / Å	1.998	2.106	2.043	2.057	2.042	2.043	2.033	2.013	2.004 Å
X-C / Å	1.836	1.857	1.850	1.853	1.851	1.852	1.862	1.842	-
X-H / Å	2.929	2.947	2.936	2.943	2.940	2.943	2.952	2.920	-
Th-X-H / °	88.10	88.39	88.09	88.25	88.15	88.16	88.01	88.02	-
Th-C / Å	2.713	2.808	2.756	2.769	2.756	2.758	2.757	2.729	2.701(4)
C-C / Å	1.405	1.422	1.416	1.418	1.417	1.418	1.425	1.410	1.386(9)
C-H / Å	1.096	1.091	1.090	1.093	1.091	1.093	1.093	1.081	-
H def / °	84.91	84.84	84.84	85.28	85.01	85.05	84.62	84.64	-

Table 4.3: The energy of the first allowed excitation for thorocene as calculated with TD-DFT using a variety of different methods at a selection of geometries. The GRACLB model potential requires the 1^{st} ionisation potential as a parameter. This has been calculated theoretically, from the energy difference between the neutral and cation at the same geometry, and obtained experimentally from PE spectroscopic data.[150] All of the transitions are of E_{1u} symmetry

Method		Excitation Energy	
TD-DFT	Geometry	eV	nm
VWN	VWN	4.103	302
BLYP	BLYP	3.634	341
BP86	BP86	3.862	321
OLYP	OLYP	3.811	325
PW91	PW91	3.930	315
PBE	PBE	3.634	341
KT1	KT1	4.068	305
KT2	KT2	4.050	306
SAOP	BLYP	4.312	288
	OLYP	4.426	280
	PBE	4.412	281
	VWN	4.534	270
	PW91	4.420	280
LB94	BLYP	2.641	469
	OLYP	2.900	428
	PBE	2.888	429
	VWN	3.105	399
	PW91	2.898	432
GRACLB	BLYP	3.705	335
theoretical	OLYP	3.935	315
1^{st} IP	VWN	4.103	302
GRACLB	BLYP	3.705	335
experimental	OLYP	3.934	315
1^{st} IP	VWN	4.103	302
Experimental		2.76	450

Figure 4.6: The definition of the geometric variables for unsubstituted actinocenes. AnX is the metal to ring-centroid distance, XC and XH are the distances from the centroid to the carbon and hydrogen atoms respectively, and angle AnXH is the angle subtended by the XH and AnX distances. H-def is the deflection angle measured from a vector through the carbon atom to which the hydrogen atom is bonded, parallel to the AnX distance. Angles less than 90° indicate that the hydrogen atoms bend inwards towards those on the opposite ring.

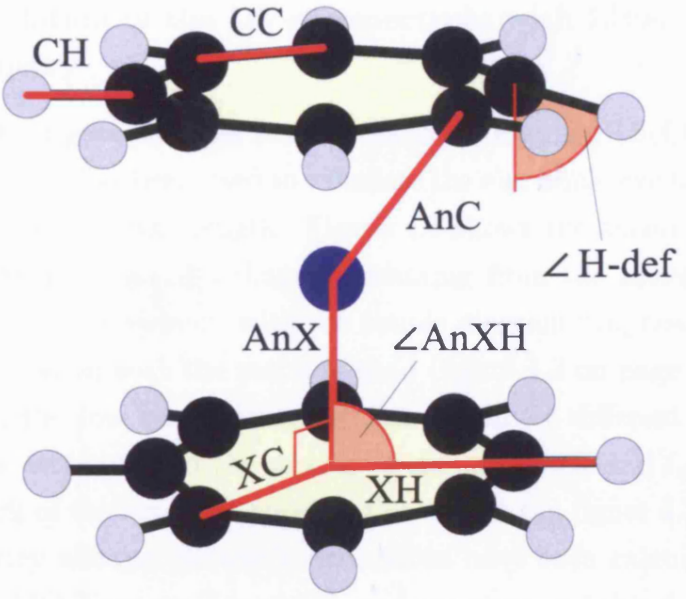

4.4.2 The use of ADF to calculate the UV-vis spectrum with TD-DFT

4.4.2.1 A general methodological comparison

Table 4.3 gives the energy of the first allowed electronic excitation with a variety of functionals and model potentials. For the GRACLB model potential, it is necessary to supply, as a parameter, the first ionisation potential. This has been calculated from the energy separation between the neutral and cation ground states at the neutral geometry, and has also been obtained from PE spectroscopy.[150] The calculations using the model potentials were performed at a number of different optimised geometries, while excitations from the VWN and the GGA functionals were calculated at the optimised geometry using the same method.

Comparison of the calculated first excitation energy with the experimental data indicates that the excitation energies are extremely dependent on the method used, and to a lesser extent also on the geometry. The poorest agreement with

experiment is seen for SAOP at the VWN geometry, while the best is for LB94 with a BLYP geometry. In fact, although the VWN geometry agrees well with experiment, it gives the poorest first excitation energy for all of the TD-DFT methods used, while the TD-DFT results at the BLYP geometry gives the best agreement when a model potential is used, although the BLYP geometry was, by a small margin, the poorest from all the methods used.

4.4.2.2 Calculation of the UV-vis spectrum with LB94 at the BLYP geometry

The method which gave the best first excitation energy for $Th(COT)_2$, LB94 at the BLYP geometry, has been used to calculate the electronic excitation spectrum for bands > 200 nm in wavelength. Figure 4.7 shows the theoretical electronic excitation spectrum. The MO diagram resulting from the LB94 calculation is shown in figure 4.8. Agreement with the simple diagram proposed for the interaction of the π-system with the metal is good (figure 4.3 on page 144), however, the ordering of the low lying virtual orbitals is subtly different from that expected. This is attributed to the mixing of the metal d_{z^2} and f_{z^3} orbitals with the σ-framework of the rings, an effect not considered in figure 4.3.

The symmetry allowed electronic excitations have been calculated and overlayed on to the MO diagram (figure 4.8), and are given in table 4.4. As expected from our simple model, the destination of the lowest energy excitations are metal-based orbitals that interact weakly with the ring orbitals. Since these orbitals have *ungerade* symmetry, transitions to these orbitals cannot originate from the HOMO, as this also has *ungerade* symmetry. The two lowest energy bands (A&B in figure 4.7) each comprise two transitions from the HOMO-1 ($7e_{2g}$ which has strong ring character), to the LUMO+1 ($5e_{3u}$) and LUMO+2 ($11e_{1u}$) orbitals, which are metal-f based. Band C populates the slightly higher lying metal-f based orbital with $6e_{2u}$ symmetry (LUMO+4). These bands are ring to metal charge transfer (LMCT) bands. Band D is formed of two transitions from the HOMO and HOMO-1 orbitals to the LUMO+7 and LUMO+6 orbitals respectively. Both of these orbitals have strong ring character, however, one is slightly ϕ antibonding with the metal.

The spectrum in the region 200 - 250 nm contains many excitations. Bands E, F, G, I & J all involve transitions from lower lying ring-based orbitals to metal based orbitals, while bands H, I and J involve transitions from the HOMO and HOMO-1 orbitals to higher lying ring-based orbitals. The low energy bands from the HOMO and HOMO-1 to the metal based f-orbitals, and low lying vacant ring

Figure 4.7: Theoretical electronic excitation spectrum for $Th(COT)_2$ using LB94 at the BLYP geometry. Each of the bands in the spectrum has been assigned a label to aid in identification.

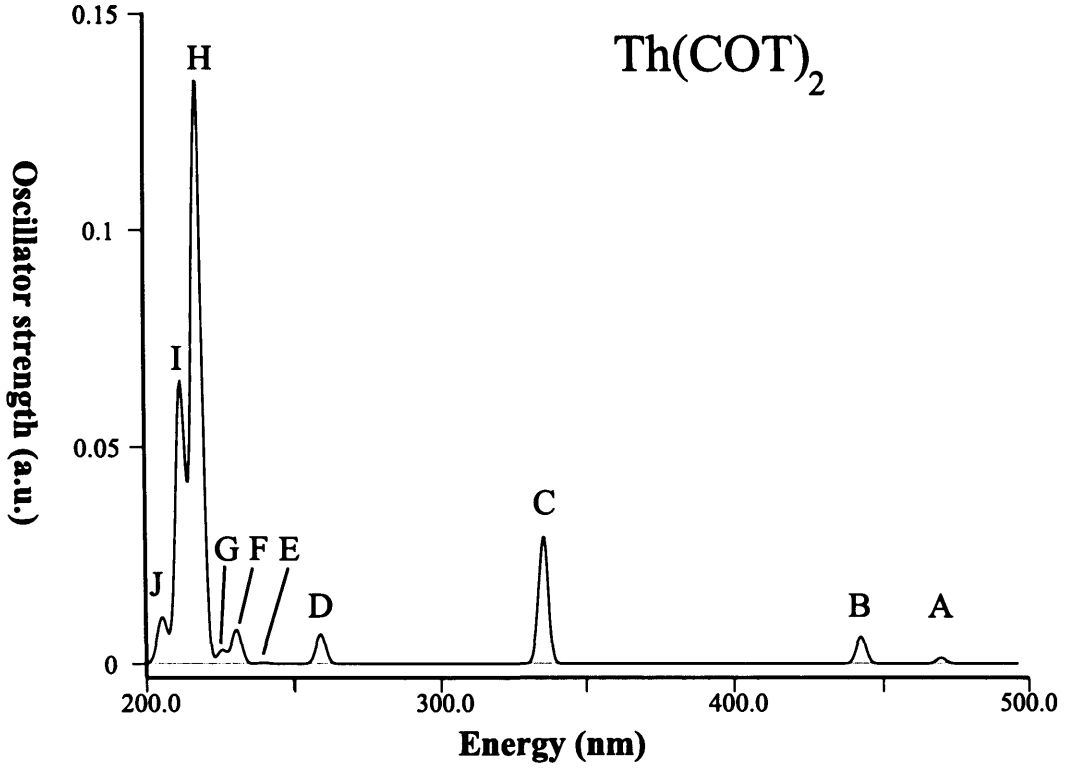

MOs are well resolved, and do not overlap with neighbouring bands due to the the reciprocal energy scale; it is anticipated that analysis of the bands equivalent to these in the spectra of $Pa(COT)_2$ and the substituted species will yield the most information about the electronic structure.

The experimental band recorded at 450 nm falls between bands A&B in the theoretical spectrum. Band B has the larger oscillator strength, however, it is not clear which of the bands should be assigned to the experimental band since the actual spectrum is not available. Perhaps broadening in the spectrum would indicate a single band in this region of which A&B are the major components.

4.4.2.3 SAOP vs. LB94

Although it is clear that LB94 with a BLYP geometry gives the best agreement with experiment for the first electronic excitation energy, it would be useful to understand why the different methods give significantly different results, and to understand how the rest of the spectrum is affected. Is it purely shifted to higher

Figure 4.8: MO diagram from an LB94 calculation of $Th(COT)_2$ at the BLYP geometry. The half arrows indicate the HOMO. Overlayed on the diagram are the calculated excitations using TD-DFT; details of how to interpret these data are given in section 4.3.2.1. Table 4.4 gives this information in numerical form.

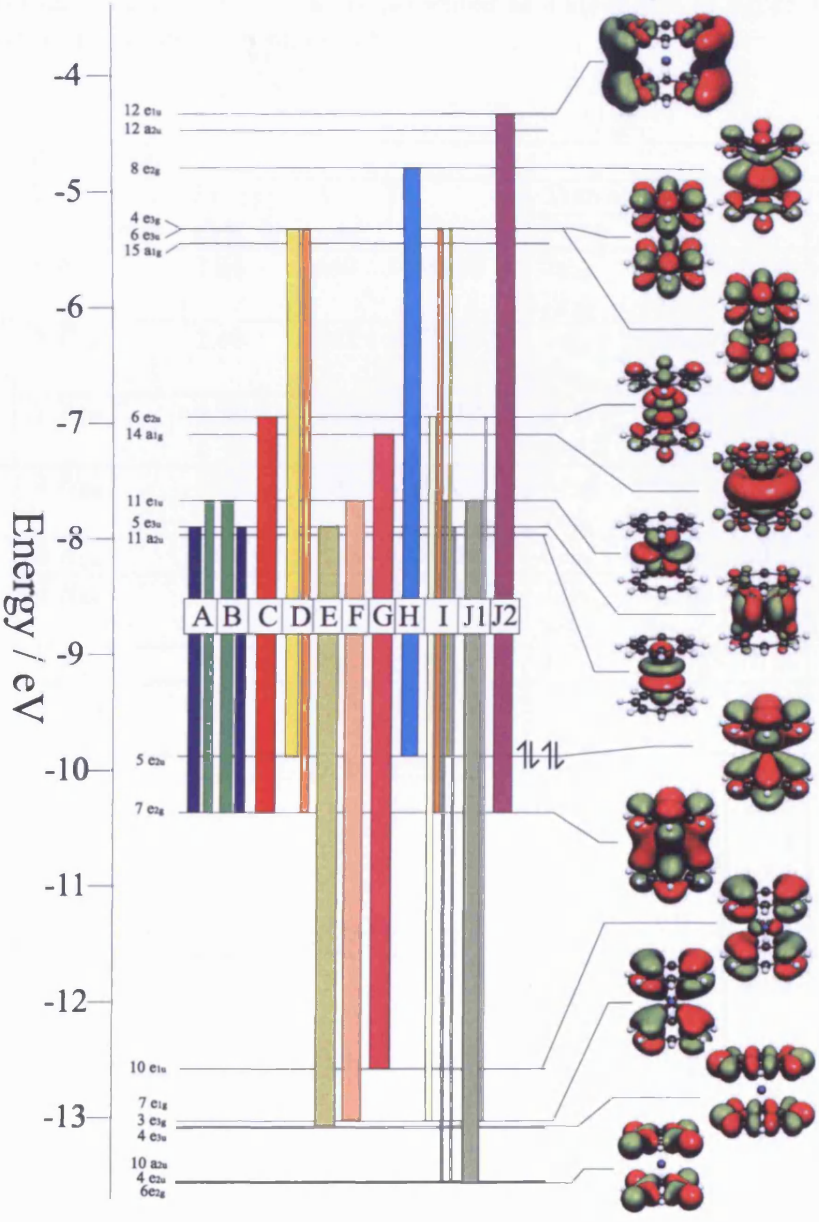

Table 4.4: Tabulated electronic excitation data for $Th(COT)_2$ calculated with LB94, at the BLYP geometry using ADF. Details of the interpretation of these data may be found in section 4.3.2.1. These data are presented as a spectrum in figure 4.7, and are overlayed on a MO diagram in figure 4.8.

Feature on Spectrum	Excitation				Transition			
	Transition Symmetry	Energy eV	λ nm	f	From	To	%	Character
A	1 E_{1u}	2.64	469	$5.38\text{x}10^{-3}$	$7e_{2g}$	$5e_{3u}$	57.6	Rπ→M-f
					$7e_{2g}$	$11e_{1u}$	41.8	Rπ→M-f
B	2 E_{1u}	2.80	442	$2.47\text{x}10^{-2}$	$7e_{2g}$	$11e_{1u}$	58.0	Rπ→M-f
					$7e_{2g}$	$5e_{3u}$	40.5	Rπ→M-f
C	1 A_{2u}	3.70	335	$1.17\text{x}10^{-1}$	$7e_{2g}$	$6e_{2u}$	94.4	Rπ→M-f
					$5e_{2u}$	$8e_{2g}$	5.1	Rπ→M-f
D	3 E_{1u}	4.79	259	$2.70\text{x}10^{-2}$	$5e_{2u}$	$4e_{3g}$	61.7	Rπ→Rπ
					$7e_{2g}$	$6e_{3u}$	37.7	Rπ→Rπ
E	2 A_{2u}	5.18	239	$1.06\text{x}10^{-3}$	$3e_{3g}$	$5e_{3u}$	99.7	Rσ→M-f
F	3 A_{2u}	5.38	230	$3.11\text{x}10^{-2}$	$7e_{1g}$	$11e_{1u}$	92.3	Rπ→M-f
					$5e_{2u}$	$8e_{2g}$	7.2	Rπ→Rπ
G	5 E_{1u}	5.50	225	$1.26\text{x}10^{-2}$	$10e_{1u}$	$14a_{1g}$	97.6	Rπ→M-d
H	4 A_{2u}	5.70	218	$5.32\text{x}10^{-1}$	$5e_{2u}$	$8e_{2g}$	80.4	Rπ→Rπ
					$7e_{1g}$	$11e_{1u}$	7.3	Rπ→M-f
I	8 E_{1u}	5.85	212	$2.52\text{x}10^{-1}$	$7e_{1g}$	$6e_{2u}$	32.2	Rπ→M-f
					$7e_{2g}$	$6e_{3u}$	25.0	Rπ→Rπ
					$6e_{2g}$	$11e_{1u}$	12.4	Rσ→M-f
					$5e_{2u}$	$4e_{3g}$	12.4	Rπ→Rπ
					$6e_{2g}$	$5e_{3u}$	10.3	Rσ→M-f
J1	9 E_{1u}	6.01	206	$1.92\text{x}10^{-2}$	$6e_{2g}$	$11e_{1u}$	20.1	Rσ→M-f
					$7e_{1g}$	$6e_{2u}$	10.4	Rσ→M-f
					$7e_{2g}$	$12e_{1u}$	6.8	Rπ→Rσ
J2	10 E_{1u}	6.05	205	$2.76\text{x}10^{-2}$	$7e_{2g}$	$12e_{1u}$	90.4	Rπ→Rσ

energies, is there reordering of the bands, or does the character of the excitations change entirely? In order to determine this, the spectrum of the best method (LB94//BLYP, figure 4.7), and the worst method (SAOP//VWN, figure 4.9) have been compared for thorocene. One thing that is immediately apparent from figure 4.9 is that energies of the excitations for SAOP are extremely contracted on the wavelength scale, with the excitations occurring at higher energies. However, what is not clear from a simple visual inspection is if the ordering of the bands remains constant, or even if all the bands are present.

Comparison of the MO diagram from the SAOP calculation (figure 4.10) with that from the LB94 calculation (figure 4.8) indicates that the HOMO-LUMO gap is much greater when calculated with SAOP, 3 eV, compared with ≈1.8 eV for LB94, thus the transitions, and consequently excitations for SAOP occur at higher energies. This is the major factor causing the spectrum from SAOP to be very contracted on the energy scale. The second difference between the two MO diagrams is in the ordering of the virtual orbitals, which is completely altered. The LUMO with LB94 ($11a_{2u}$), becomes the LUMO+3 with SAOP, while the LUMO for SAOP ($14a_{1g}$) is the LUMO+3 for LB94. The e_{1u} and e_{2u} f-based MOs are strongly destabilised, moving from LUMO+2 and LUMO+4 with LB94 to LUMO+4 and LUMO+7 with SAOP respectively. The ordering of the ring-π ϕ-bonding orbitals is reversed with SAOP. If the interaction of the metal $f_{e_{3u}}$ orbital with the ring orbital of the same symmetry is weak, then one would expect the ordering of the $6e_{3u}$ and $4e_{3g}$ MOs (which have strong metal ring character), to match that when the two rings are in close proximity, with the metal absent (i.e. $6e_{3u}$ more stable than $4e_{3g}$, see figure 4.2). However, the interaction of the metal $f_{e_{3u}}$ orbital seems to be significant in the case of SAOP, and this has caused significant destabilisation of the anti-bonding $6e_{3u}$ orbital, such that it occurs about 1 eV higher than the $4e_{3g}$ MO. With LB94 they are virtually degenerate, although the $6e_{3u}$ MO is the lower in energy.

These alterations in the MO structure translate to significant alterations to the transitions which make up the excitations. The ordering of the excitations which have clear equivalents between SAOP and LB94 is significantly altered. The closest equivalent excitation is J2 in LB94, which becomes E3 in SAOP. All of the other excitations have significantly different characters; for instance, there is no excitation in LB94 with the character (i.e. broken down into roughly the same proportion of equivalent transitions) of excitation A in SAOP.

Table 4.5: Tabulated electronic excitation data for $Th(COT)_2$ calculated with SAOP, at the VWN geometry using ADF. Details of the interpretation of these data may be found in section 4.3.2.1. These data are presented as a spectrum in figure 4.9, and are overlayed on a MO diagram in figure 4.10.

Feature on Spectrum	Excitation				Transition			
	Transition Symmetry	Energy eV	λ nm	f	From	To	%	Character
A	1 E_{1u}	4.53	273	$2.07\text{x}10^{-2}$	$7e_{2g}$	$5e_{3u}$	71.1	Rπ→M-f
					$5e_{2u}$	$4e_{3g}$	28.2	Rπ→Rπ
B	2 E_{1u}	5.38	231	$6.77\text{x}10^{-3}$	$7e_{2g}$	$11e_{1u}$	93.0	Rπ→M-f
					$5e_{2u}$	$4e_{3g}$	5.0	Rπ→Rπ
C	3 E_{1u}	5.50	225	$4.80\text{x}10^{-3}$	$5e_{2u}$	$8e_{1g}$	99.0	Rπ→Rσ
D	4 E_{1u}	5.84	212	$3.88\text{x}10^{-1}$	$10e_{1u}$	$14a_{1g}$	27.9	Rπ→M-d
					$5e_{2u}$	$4e_{3g}$	32.3	Rπ→Rπ
					$7e_{2g}$	$12e_{1u}$	14.0	Rπ→Rσ
					$7e_{2g}$	$5e_{3u}$	12.8	Rπ→M-f
					$7e_{2g}$	$6e_{3u}$	6.5	Rπ→Rπ
E1	5 E_{1u}	5.95	208	$9.14\text{x}10^{-2}$	$10e_{1u}$	$14a_{1g}$	70.0	Rπ→M-d
					$7e_{2g}$	$12e_{1u}$	12.5	Rπ→Rσ
					$5e_{2u}$	$4e_{3g}$	9.4	Rπ→Rπ
E2	1 A_{2u}	6.03	206	$1.80\text{x}10^{-1}$	$5e_{2u}$	$8e_{2g}$	69.4	Rπ→Rπ
					$7e_{2g}$	$6e_{2u}$	27.5	Rπ→M-f
E3	6 E_{1u}	6.11	203	$2.98\text{x}10^{-1}$	$7e_{2g}$	$12e_{1u}$	73.1	Rπ→Rσ
					$5e_{2u}$	$4e_{3g}$	11.4	Rπ→Rπ
					$7e_{2g}$	$5e_{3u}$	5.9	Rπ→M-f
					$7e_{2g}$	$6e_{3u}$	5.8	Rπ→Rπ
F	2 A_{2u}	6.40	194	$4.14\text{x}10^{-1}$	$5e_{2u}$	$9e_{2g}$	53.0	Rπ→Rσ
					$7e_{2g}$	$6e_{2u}$	39.5	Rπ→M-f
					$5e_{2u}$	$8e_{2g}$	6.6	Rπ→Rσ
G	3 A_{2u}	6.72	184	$3.23\text{x}10^{-1}$	$10a_{2u}$	$14a_{1g}$	25.1	Rπ→M-d
					$5e_{2u}$	$9e_{2g}$	36.5	Rπ→Rσ
					$7e_{2g}$	$6e_{2u}$	22.8	Rπ→M-f
					$5e_{2u}$	$8e_{2g}$	13.4	Rπ→Rσ
H1	4 A_{2u}	6.99	177	$2.07\text{x}10^{-1}$	$10a_{2u}$	$14a_{1g}$	73.5	Rπ→M-d
					$7e_{2g}$	$6e_{2u}$	8.7	Rπ→M-f
					$5e_{2u}$	$9e_{2g}$	7.7	Rπ→Rσ
					$5e_{2u}$	$8e_{2g}$	7.0	Rπ→Rπ
H2	8 E_{1u}	7.08	175	$5.55\text{x}10^{-1}$	$7e_{2g}$	$6e_{3u}$	70.5	Rπ→Rπ
					$10e_{1u}$	$15a_{1g}$	5.0	Rπ→Rσ
					$5e_{2u}$	$4e_{3g}$	7.3	Rπ→Rπ
					$5e_{2u}$	$9e_{1g}$	6.4	Rπ→Rσ

Figure 4.9: Theoretical electronic excitation spectrum for $Th(COT)_2$ from a TD-DFT calculation using SAOP at the VWN geometry.

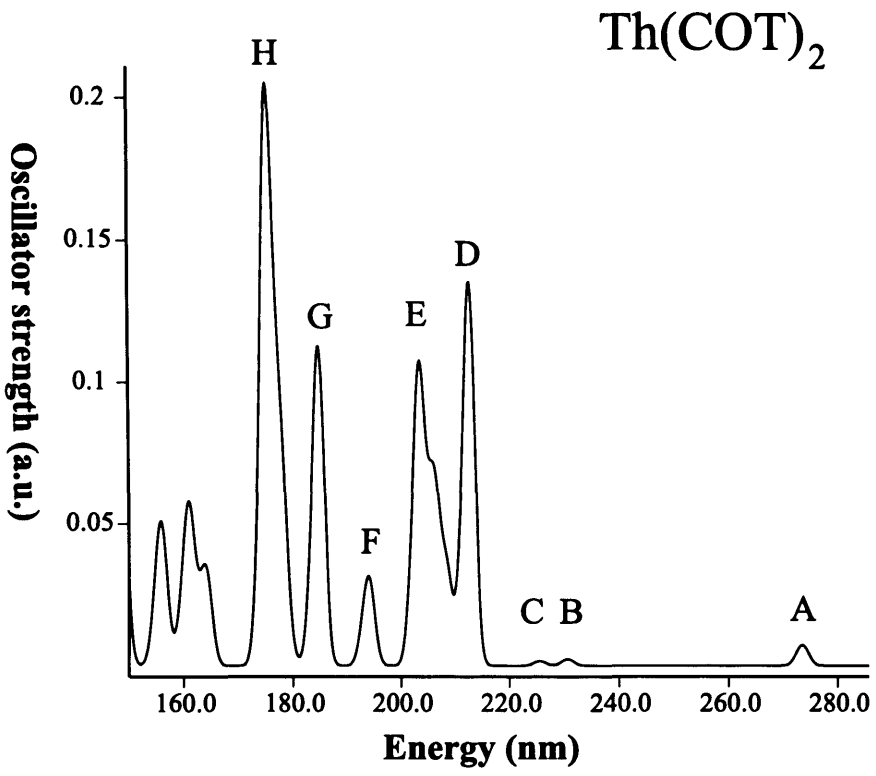

4.4.3 TD-DFT with B3LYP - ADF vs. Gaussian

Although Gaussian does not support the LB94 functional, one can use hybrid functionals, which are supported in Gaussian for all types of calculation. One can perform a single point calculation using a hybrid functional with ADF, however, hybrid functionals cannot be used for geometry optimisations, or for TD-DFT. The low energy transitions for $Th(COT)_2$ have been calculated with BLYP and B3LYP with Gaussian, the former for comparison with a BLYP spectrum calculated using ADF. Initially the use of BLYP to calculate the electronic excitations of $Th(COT)_2$ is investigated. A comparison between the BLYP spectra calculated with Gaussian and ADF is then made, followed by a comparison of the BLYP and B3LYP results calculated with Gaussian.

4.4.3.1 ADF BLYP vs. LB94

Figure 4.11 shows the theoretical excitation spectrum from a BLYP calculation with ADF. Table 4.6 gives the breakdown of these bands into their various exci-

Figure 4.10: MO diagram from an SAOP calculation at the VWN geometry for $Th(COT)_2$. The half arrows indicate the HOMO. Overlayed on the diagram are the calculated excitations using TD-DFT; details of how to interpret these data are given in section 4.3.2.1. Table 4.5 gives this information in numerical form.

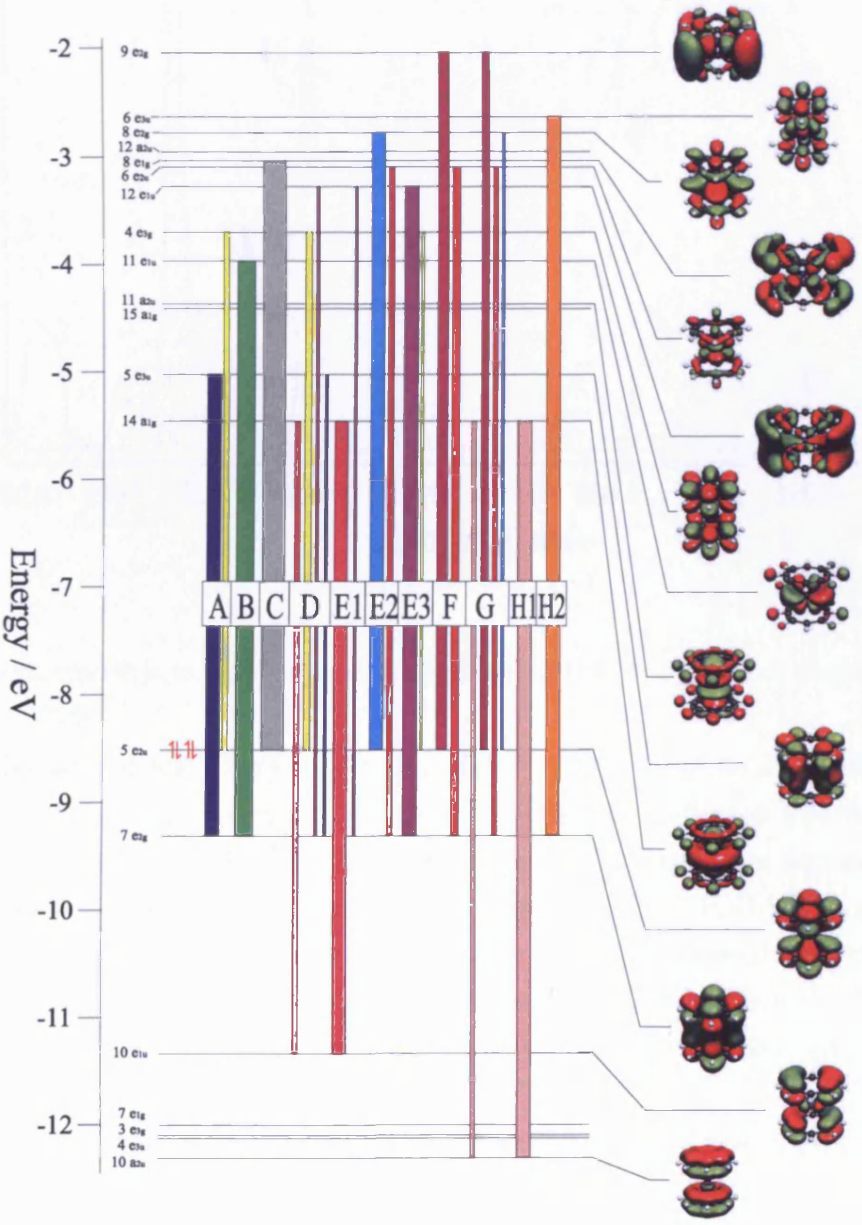

Figure 4.11: Theoretical electronic excitation spectrum calculated with TD-DFT using BLYP at the optimised BLYP geometry, using ADF.

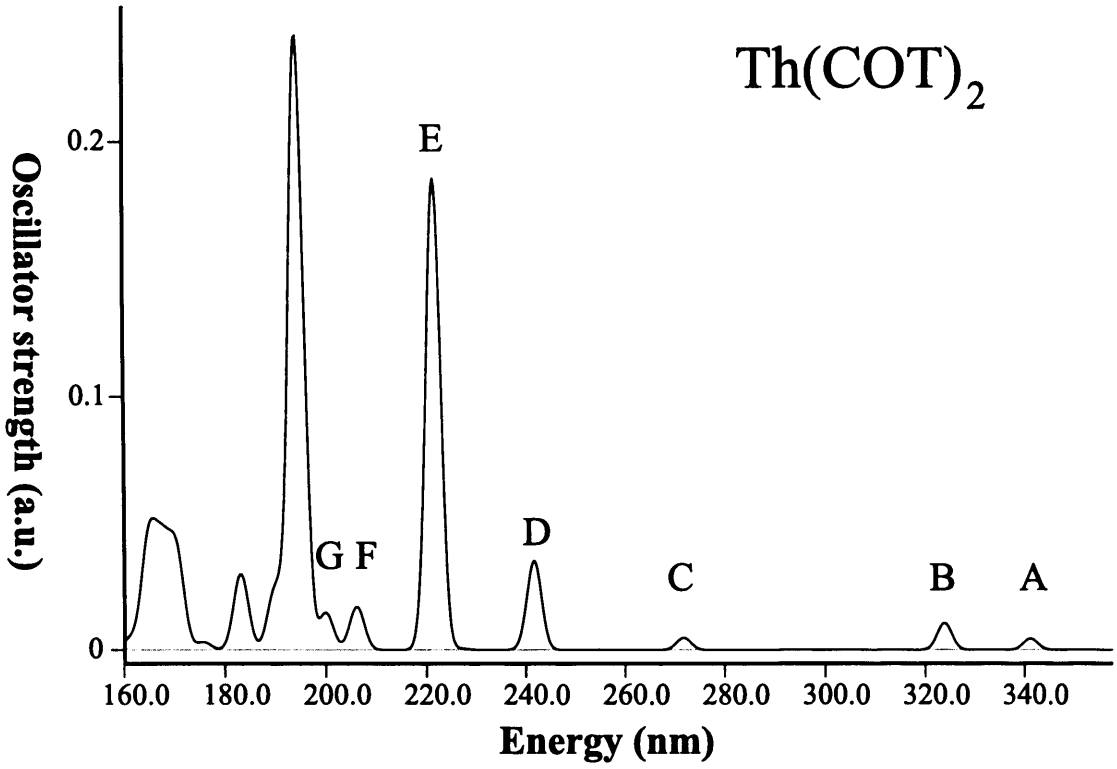

tations and transitions, while figure 4.12 presents this information diagrammatically.

Comparison of the BLYP spectrum (figure 4.11) with the LB94 spectrum calculated at the same geometry (figure 4.7, page 160) indicates the differences between the two methods. The features on the BLYP spectrum are all shifted to lower wavelengths; this is attributed to the larger HOMO-LUMO gap with BLYP ($\approx$ 2.6 eV) compared with LB94 ($\approx$ 1.8 eV). From a visual inspection it is fairly obvious that bands A&B are equivalent in both spectra, however comparing the relative intensity of bands C&D between spectra suggests that either bands C(BLYP) and D(LB94) are equivalent, as are C(LB94) and D(BLYP) (i.e. their relative position has changed), or that the intensity of the bands is not consistent between the methods. Comparison of the tabulated data (tables 4.4 and 4.6, pages 162 and 169) indicates that bands A-D have the same character in both spectra, while band E(BLYP) matches with band H(LB94). Bands G&I (BLYP) do not have equivalents in the range of energies studied in the LB94 spectrum. The differences between the spectra are attributed to alterations in the general

Figure 4.12: MO diagram from a BLYP calculation at the BLYP geometry for $Th(COT)_2$, calculated with ADF. The half arrows indicate the HOMO. Overlayed on the diagram are the calculated excitations using TD-DFT; details of how to interpret these data are given in section 4.3.2.1. Table 4.6 gives this information in numerical form.

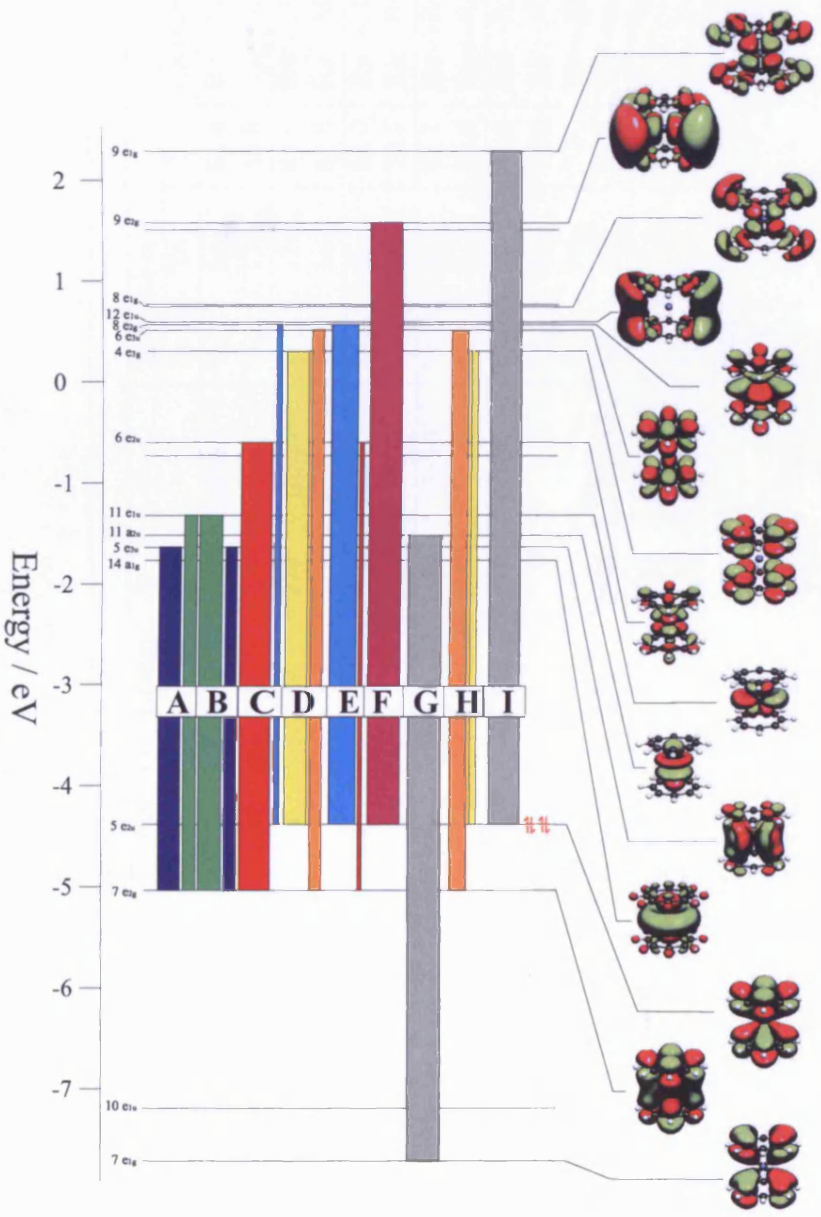

Table 4.6: Tabulated electronic excitation data for $Th(COT)_2$ calculated with BLYP, at the BLYP geometry using ADF. Details of the interpretation of these data may be found in section 4.3.2.1. These data are presented as a spectrum in figure 4.11, and are overlayed on a MO diagram in figure 4.12.

Feature on Spectrum	Excitation				Transition			
	Transition Symmetry	Energy eV	λ nm	f	From	To	%	Character
A	$1E_{1u}$	3.63	341	$1.56\text{x}10^{-2}$	$7e_{2g}$	$5e_{3u}$	61.4	Rπ→M-f
					$7e_{2g}$	$11e_{1u}$	35.6	Rπ→M-f
B	$2E_{1u}$	3.83	324	$3.76\text{x}10^{-2}$	$7e_{2g}$	$11e_{1u}$	63.9	Rπ→M-f
					$7e_{2g}$	$5e_{3u}$	31.6	Rπ→M-f
C	$1A_{2u}$	4.56	272	$1.69\text{x}10^{-2}$	$7e_{2g}$	$6e_{2u}$	86.0	Rπ→M-f
					$5e_{2u}$	$8e_{2g}$	13.7	Rπ→Rπ
D	$3E_{1u}$	5.13	242	$1.23\text{x}10^{-1}$	$5e_{2u}$	$4e_{3g}$	62.1	Rπ→Rπ
					$7e_{2g}$	$6e_{3u}$	33.0	Rπ→Rπ
E	$2A_{2u}$	5.60	221	$6.61\text{x}10^{-1}$	$5e_{2u}$	$8e_{2g}$	75.4	Rπ→Rπ
					$7e_{2g}$	$6e_{2u}$	10.8	Rπ→M-f
					$5e_{2u}$	$9e_{2g}$	7.5	Rπ→Rσ
F	$3A_{2u}$	6.01	206	$6.08\text{x}10^{-2}$	$5e_{2u}$	$9e_{2g}$	90.8	Rπ→Rσ
G	$7E_{1u}$	6.20	200	$5.22\text{x}10^{-2}$	$7e_{1g}$	$11a_{2u}$	93.1	Rπ→M-f
H	$8E_{1u}$	6.38	194	$8.56\text{x}10^{-1}$	$7e_{2g}$	$6e_{3u}$	47.2	Rπ→Rπ
					$5e_{2u}$	$4e_{3g}$	19.2	Rπ→Rπ
					$7e_{1g}$	$11a_{2u}$	5.6	Rπ→M-f
					$5e_{2u}$	$9e_{1g}$	7.0	Rπ→Rσ
					$7e_{1g}$	$6e_{2u}$	5.8	Rπ→M-f
I	$10E_{1u}$	6.77	183	$1.08\text{x}10^{-1}$	$5e_{2u}$	$9e_{1g}$	87.1	Rπ→Rσ
					$7e_{1g}$	$6e_{2u}$	8.0	Rπ→M-f

structure of the virtual MOs (i.e. their ordering and spacing).

As stated, the HOMO-LUMO gap is $\approx$ 0.8 eV larger, and the unoccupied orbitals with strong metal-f character have a similar energy spacing (although the $14a_{1g}$ orbital becomes the LUMO with BLYP), however, the MOs then get much more closely spaced. For LB94 the highest energy MO ($12e_{1u}$) on figure 4.8 (page 161) is $\approx$ 3.7 eV above the LUMO, but with BLYP the equivalent orbital occurs $\approx$ 2.25 eV above the LUMO. Thus, although the HOMO-LUMO gap has increased with BLYP, the $12e_{1u}$ orbital has a smaller separation from the HOMO; the lower lying virtual orbitals have been destabilised relative to the HOMO, while the higher lying virtual orbitals have been stabilised. Perhaps this is indicative of increased radial extension of the f-orbitals, and thus greater interaction with the ring orbitals compared with LB94.

The energy of the lowest energy transition, and thus the only experimental datum, is a fair indication of the methods ability to correctly attain the HOMO-LUMO gap, because (ignoring selection rules), it is a transition from the highest lying occupied orbitals to the lowest lying virtual orbitals across the HOMO-LUMO gap. It is assumed that the method which gives the best first transition energy also represents the rest of the spectrum correctly, however, there is neither further evidence to support this supposition, nor extra data with which to improve upon this situation. The lower energy end of the spectrum is dominated by transitions from the HOMO-1 to the metal f-based anti-bonding orbitals. Apart from the position of these excitations on the energy scale, these bands seem to retain fairly constant character between methods. The higher energy portion of the spectrum is much more method dependent, more complex and generally less dependent on the size of the HOMO-LUMO gap. In conclusion, it seems to be sensible to concentrate the discussion to the low energy section of the spectrum, which is simpler, more consistent in character between methods, and more importantly, is better supported by the extremely limited experimental data. This should make comparison between the different species, different methods and experimental data simpler.

4.4.3.2 ADF-BLYP vs. G03-BLYP

The BLYP spectrum calculated with Gaussian is given in figure 4.13, while the excitations are presented graphically and in tabulated form in figure 4.14 and table 4.7. Only the low energy excitations have been calculated due to the computational expense of the use of Gaussian type orbitals. Figures 4.11 and 4.12 and table 4.6 give the ADF results for comparison.

Table 4.7: Tabulated electronic excitation data for $Th(COT)_2$ calculated with BLYP, at the BLYP geometry using Gaussian. Details of the interpretation of these data may be found in section 4.3.2.1. These data are presented as a spectrum in figure 4.13, and are overlayed on a MO diagram in figure 4.14.

Feature on Spectrum	Excitation							
	Transition Symmetry	Energy eV	λ nm	f	Transition			
					From	To	%	Character
A	$21/22E_{1u}$	3.68	337	$2.50\text{x}10^{-2}$	$68/69e_{2g}$	$73/74e_{3u}$	67.8	Rπ→M-f
					$68/69e_{2g}$	$76/77e_{1u}$	23.8	Rπ→M-f
B	$28/29E_{1u}$	3.89	319	$2.64\text{x}10^{-2}$	$68/69e_{2g}$	$76/77e_{1u}$	74.6	Rπ→M-f
					$68/69e_{2g}$	$73/74e_{3u}$	17.6	Rπ→M-f
C	$39A_{2u}$	4.69	265	$2.51\text{x}10^{-2}$	$68/69e_{2g}$	$79/80e_{2u}$	85.7	Rπ→M-f
					$70/71e_{2u}$	$88/89e_{2g}$	12.7	Rπ→Rπ
D1	$50A_{2u}$	5.06	245	$1.30\text{x}10^{-3}$	$68/69e_{2g}$	$81/82e_{1u}$	96.8	Rπ→Rσ
D2	$54/55E_{1u}$	5.20	238	$1.55\text{x}10^{-1}$	$68/69e_{2g}$	$85/86e_{3u}$	33.8	Rπ→Rπ
					$70/71e_{2u}$	$83/84e_{3g}$	56.2	Rπ→Rπ
D3	$58/59E_{1u}$	5.54	224	$4.00\text{x}10^{-4}$	$66/67e_{1u}$	$72a_{1g}$	97.1	Rπ→M-d
D4	$66/67E_{1u}$	5.62	220	$4.00\text{x}10^{-4}$	$70/71e_{2u}$	$90/91e_{1g}$	97.3	Rπ→Rσ
E	$77A_{2u}$	5.88	211	$6.72\text{x}10^{-1}$	$68/69e_{2g}$	$79/80e_{2u}$	39.1	Rπ→M-f
					$70/71e_{2u}$	$88/89e_{2g}$	35.6	Rπ→Rπ
					$59a_{2u}$	$72a_{1g}$	6.1	Rπ→M-d

A comparison of the Gaussian data with the ADF data indicates that the four bands calculated with Gaussian are positioned within 7 nm[d] of each of the first four bands calculated with ADF. The relative intensities of these bands are roughly equivalent (figures 4.11 and 4.13), and the transitions comprising the dominant excitations are the same (figures 4.12 and 4.14). The spacing of the MOs is roughly equivalent, although there are a number of MOs which are not ordered consistently, for instance the $12e_{1u}$ orbital in figure 4.12, lies $\approx$ 0.6 eV closer to the LUMO in the Gaussian calculation. The HOMO-LUMO gap is $\approx$ 0.1 eV bigger in the Gaussian calculation, however, since the LUMO $d_{a_{1g}}$-based orbital is not involved in any of the intense transitions, this difference does not manifest itself in the spectra calculated here.

The results of the BLYP calculations on $Th(COT)_2$ with ADF and Gaussian

[d]Only the dominant excitation has been considered for band D (D2) (see table 4.7). This is >100 times the intensity of all of the other excitations comprising this excitation.

Figure 4.13: Electronic excitation spectrum for $Th(COT)_2$ from a TD-DFT calculation using BLYP at a BLYP optimised geometry, with Gaussian.

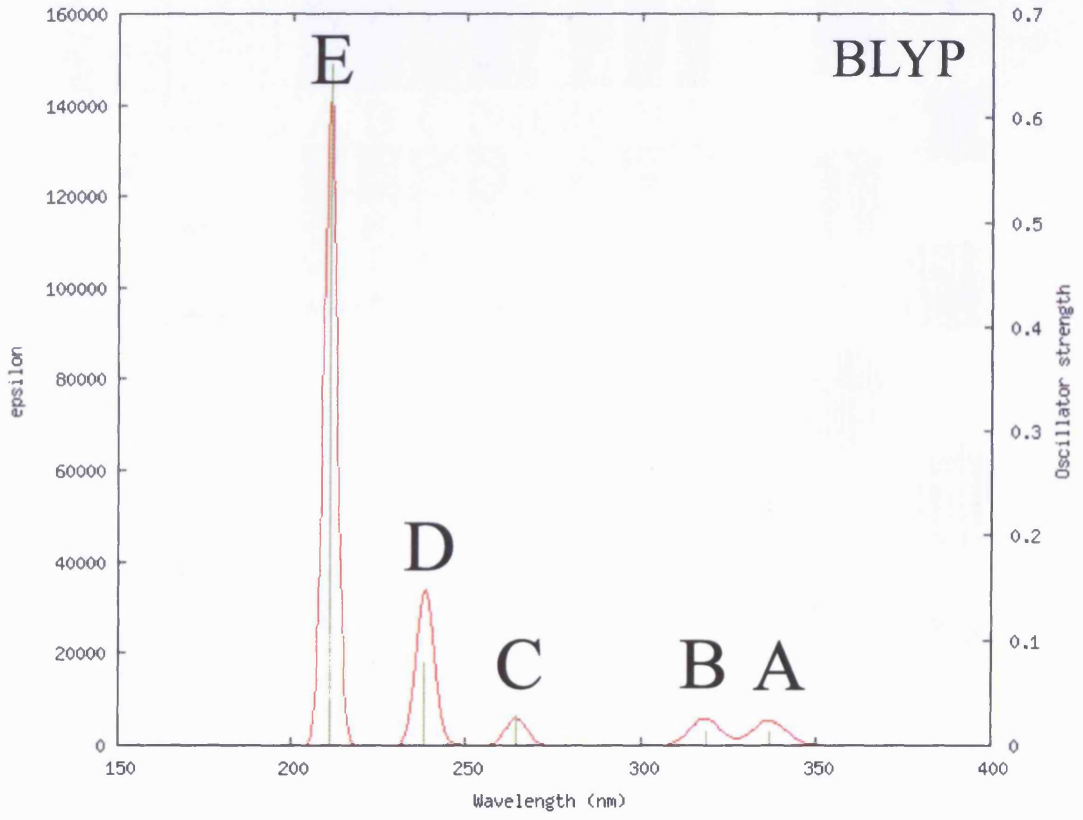

Figure 4.14: MO diagram from a BLYP calculation at the BLYP geometry for $Th(COT)_2$, calculated with Gaussian. The half arrows indicate the HOMO. Overlayed on the diagram are the calculated excitations using TD-DFT; details of how to interpret these data are given in section 4.3.2.1. Table 4.7 gives this information in numerical form.

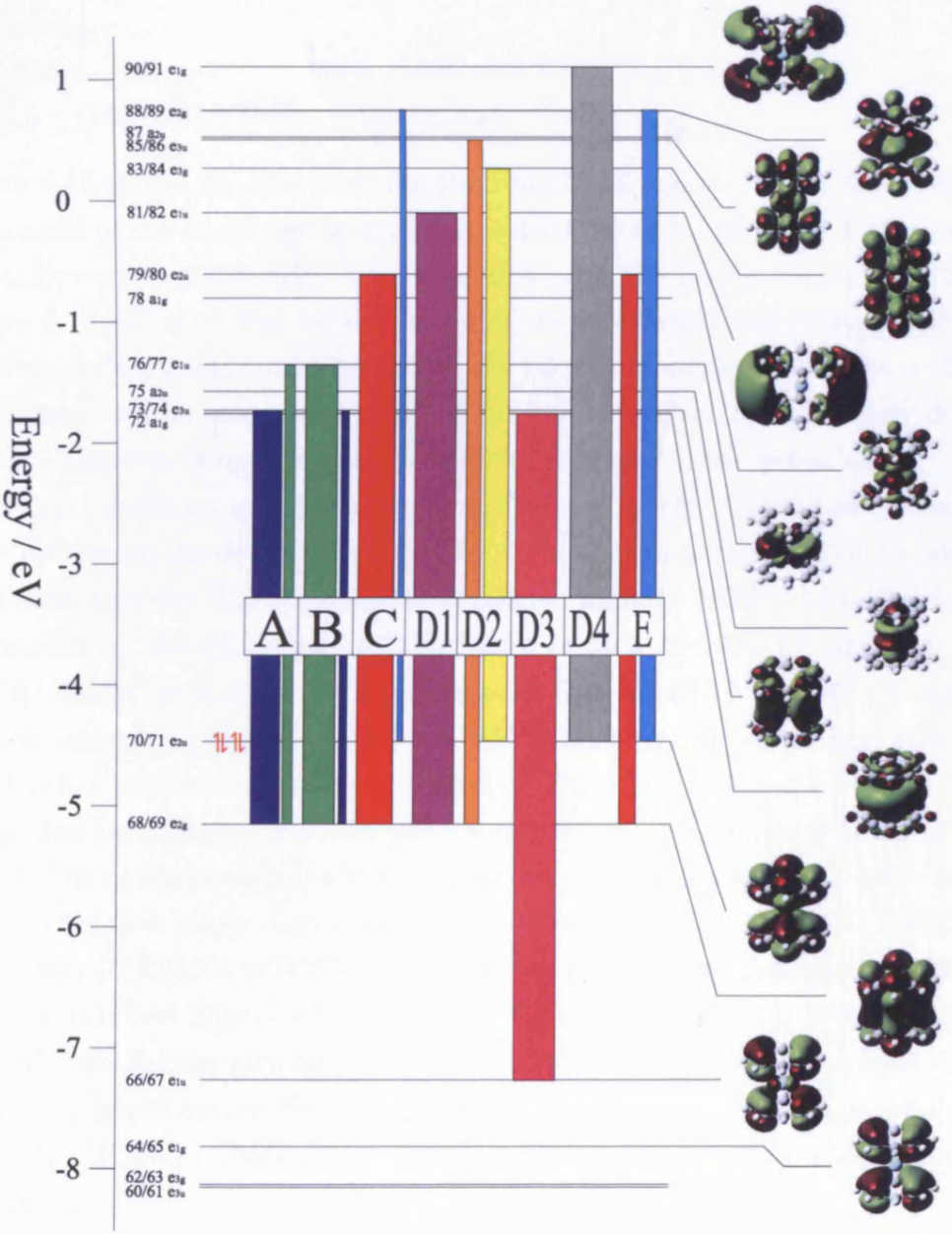

indicate that the two codes give essentially identical results given the differences in the basis sets used. We therefore have access to a wider range of computational techniques through the use of both codes, with results that should be comparable. The Gaussian calculations, due to the use of large Gaussian type basis sets, were time consuming, and beyond our computational resourses for all but the first few allowed excitations. The ADF calculations are more economical, since they use Slater type orbitals. Since ADF and Gaussian give essentially the same results with BLYP, it clearly makes sense to use ADF for calculations using pure functionals.

4.4.3.3 G03-B3LYP vs. G03-BLYP

Figure 4.15 shows the spectrum for the B3LYP calculation, table 4.8 gives the breakdown of the bands into excitations and transitions, and figure 4.16 presents this information graphically, for comparison with the BLYP data presented in figures 4.13 and 4.14 and table 4.7. All of the calculated excitations are shown for these calculations, independent of the oscillator strength, so that a direct comparison can be made between all of the available data. Unfortunately due to limited resourses, it has not been possible to calculate more excitations.

Visual inspection of the two spectra (figures 4.13 and 4.15) shows an immediate difference; the first band in the B3LYP spectrum is blue-shifted by 60 nm, compared with the BLYP band. The tabulated data for BLYP shows five bands dominated by the excitations A,B,C,D2&E. In fact, the B3LYP data are very similar; bands A&B are direct equivalents of those in BLYP. Band C comprises two excitations, equivalent to C&D1 in BLYP, with roughly equivalent intensity. Band D has the same character as excitation D2 in BLYP. Band E for B3LYP is dominated by a single excitation (E3), which matches in character to band E in BLYP. The bands in each spectra are thus direct equivalents of each other in the character of their major component, however the minor excitations (D1,D3&D4 in BLYP and C2,E2&E1 in B3LYP) although equivalent, now form part of different bands; this is best illustrated by comparing figures 4.14 and 4.16. It is well known that HF calculations give larger HOMO-LUMO gaps than DFT calculations, so perhaps it is not surprising that the inclusion of some HF exchange should increase the HOMO-LUMO gap (by $\approx$1eV in this case), and cause blue-shifting of the bands.

One objective for the comparison of BLYP with B3LYP was to determine if the calculated first excitation energy is a better match with the experimental data upon the inclusion of some exact exchange. The data presented here suggest

Table 4.8: Tabulated electronic excitation data for $Th(COT)_2$ calculated with B3LYP, at the B3LYP geometry using Gaussian. Details of the interpretation of these data may be found in section 4.3.2.1. These data are presented as a spectrum in figure 4.15, and are overlayed on a MO diagram in figure 4.16.

Feature on Spectrum	Excitation							
	Transition Symmetry	Energy eV	λ nm	f	Transition			
					From	To	%	Character
A	$21/22E_{1u}$	4.45	279	$5.56\text{x}10^{-2}$	$68/69e_{2g}$	$73/74e_{3u}$	71.7	Rπ→M-f
					$68/69e_{2g}$	$77/78e_{1u}$	16.4	Rπ→M-f
B	$28/29E_{1u}$	4.74	262	$3.18\text{x}10^{-2}$	$68/69e_{2g}$	$77/78e_{1u}$	80.8	Rπ→M-f
					$68/69e_{2g}$	$73/74e_{3u}$	11.3	Rπ→M-f
C1	$42A_{2u}$	5.51	225	$7.30\text{x}10^{-3}$	$68/69e_{2g}$	$81/82e_{2u}$	82.4	Rπ→M-f
					$70/71e_{2u}$	$86/87e_{2g}$	15.5	Rπ→Rπ
C2	$47/48E_{1u}$	5.59	222	$5.00\text{x}10^{-3}$	$68/69e_{2g}$	$79/80e_{1u}$	95.8	Rπ→Rσ
D	$54/55E_{1u}$	5.99	207	$4.39\text{x}10^{-1}$	$70/71e_{2u}$	$83/84e_{3g}$	65.1	Rπ→Rπ
					$68/69e_{2g}$	$88/89e_{3u}$	16.9	Rπ→Rπ
					$66/67e_{1u}$	$72a_{1g}$	5.5	Rπ→M-d
E1	$60/61E_{1u}$	6.15	202	$7.60\text{x}10^{-3}$	$70/71e_{2u}$	$90/91e_{1g}$	89.5	Rπ→Rσ
E2	$62/63E_{1u}$	6.20	200	$1.58\text{x}10^{-2}$	$66/67e_{1u}$	$72a_{1g}$	87.9	Rπ→M-d
E3	$67A_{2u}$	6.32	196	$8.99\text{x}10^{-1}$	$70/71e_{2u}$	$86/87e_{2g}$	71.9	Rπ→Rπ
					$68/69e_{2g}$	$81/82e_{2u}$	12.1	Rπ→M-f

that for $Th(COT)_2$, B3LYP is in fact poorer than BLYP, since the bands are blue-shifted, making the agreement with experiment poorer. This indicates that, at least on the basis of comparison with experiment, there is no advantage to using the B3LYP method. Therefore the remaining calculations in this study are performed using ADF.

Figure 4.15: Electronic excitation spectrum for $Th(COT)_2$ from a TD-DFT calculation using B3LYP at a B3LYP optimised geometry, with Gaussian.

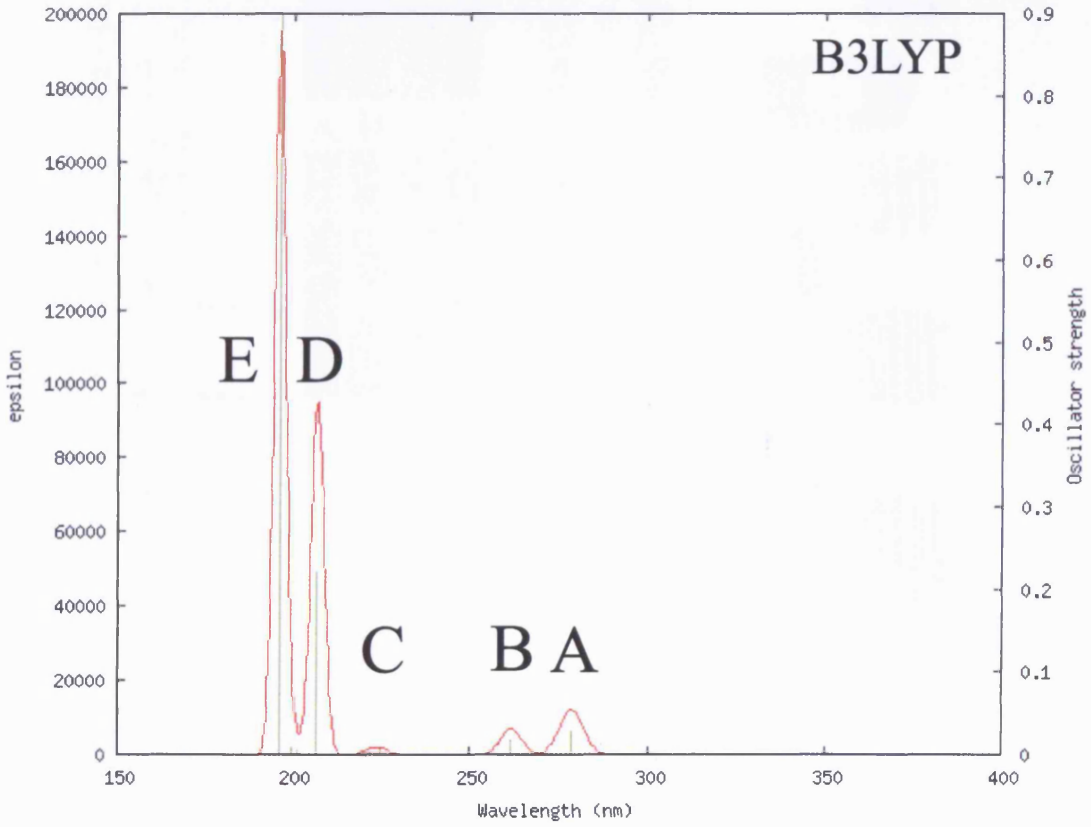

Figure 4.16: MO diagram from a B3LYP calculation at the B3LYP geometry for $Th(COT)_2$, calculated with Gaussian. The half arrows indicate the HOMO. Overlayed on the diagram are the calculated excitations using TD-DFT; details of how to interpret these data are given in section 4.3.2.1. Table 4.8 gives this information in numerical form.

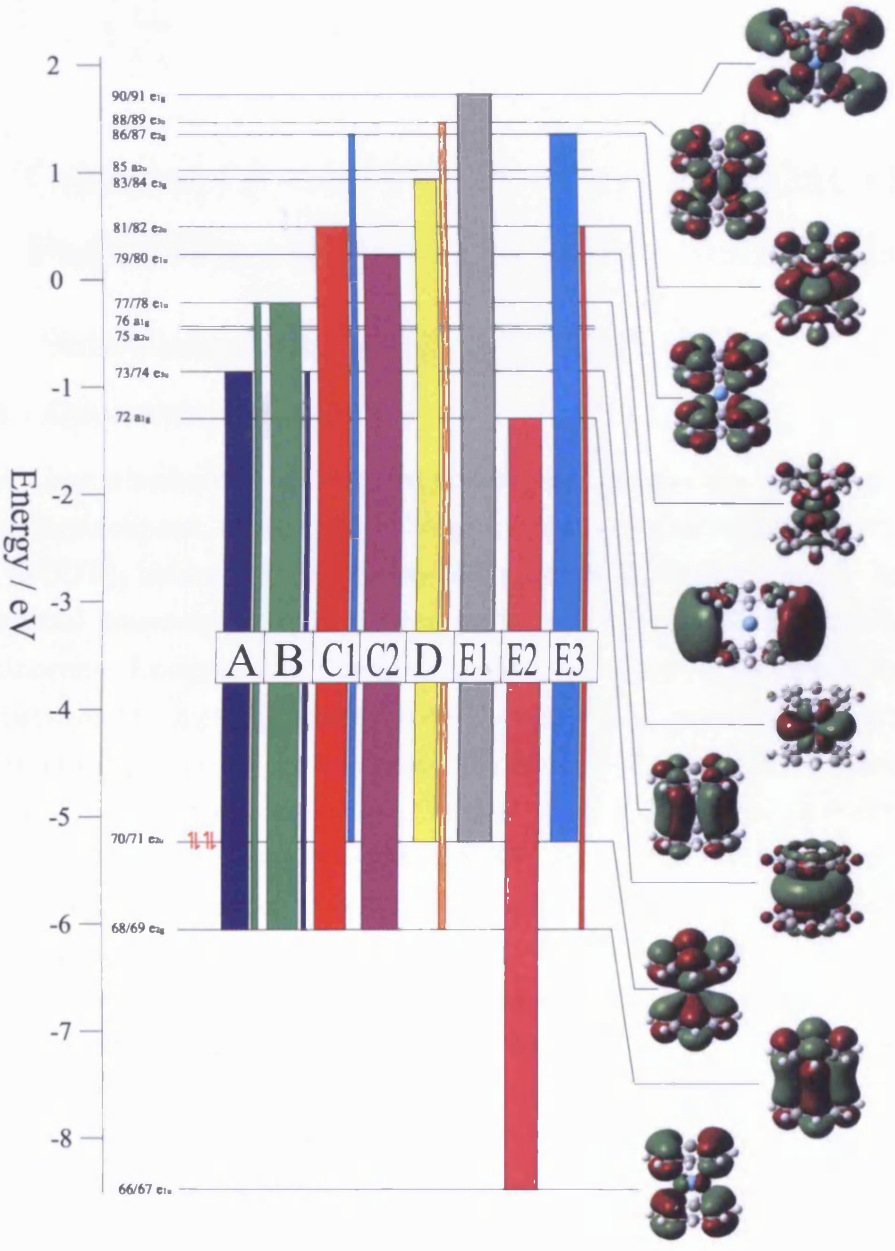

Table 4.9: Total bonding energy for each of the isomers of $Th(TMCOT)_2$. α is the dihedral angle between the unique C-H methyl bonds and the thorium-ring centroid distance. $\alpha = 0.0°$ indicates that the unique methyl-hydrogen atoms on opposite rings point in towards each other, while $\alpha = 180.0°$ indicates that they project out of molecule.

Point Group	$\alpha°$	Bonding Energy / kJ mol^{-1}
D_{4h}	0.0	+23.53
D_{4h}	180.0	0 (-31118.91)
D_{4d}	0.0	+26.24
D_{4d}	180.0	+8.24

4.5 Computational Results for $Th(TMCOT)_2$, $Pa(COT)_2$ and $Pa(TMCOT)_2$ using ADF.

4.5.1 Substituted thorocene - $Th(TMCOT)_2$

4.5.1.1 Geometric structure

It is not clear whether the substituted species should have the methyl groups on the two rings eclipsed, or staggered. Single crystal x-ray structure determination on $U(TMCOT)_2$ indicates both isomers to be present in the structure,[171] however, no structural determinations have been performed for substituted thorocene, or protactinocene. Hodgson and Raymond suggest that there is no significant interaction between the methyl groups between rings, so any preference for a specific structure must be due to the resulting stability of the metal-ligand interaction. A further structural consideration is whether the methyl groups should be positioned on the rings such that the unique methyl-hydrogens project towards those on the opposite ring, or towards the outside of the molecule, where the closest approach of the hydrogens on the opposite rings would be slightly reduced.

In the absence of any conclusive experimental evidence for the most stable structure, BLYP optimisations on the two possible D_{4h} and D_{4d} structures have been used to predict the structure of the most stable isomer. These data indicate that the D_{4h} isomer with the unique methyl hydrogens projecting outwards to be slightly lower in energy (table 4.9), although only by about 8 kJ mol^{-1}. From this point on, for brevity, all references to $Th(TMCOT)_2$, and $Pa(TMCOT)_2$ assume this structure.

Table 4.10 gives the results of geometry optimisations performed on $Th(TMCOT)_2$ with a variety of functionals. Comparison of the optimised structures for

$Th(COT)_2$ and $Th(TMCOT)_2$ indicates that the methyl substituents on the rings makes a difference of only hundredths of an Ångstrom to the thorium-ring centroid distance. Thus it appears that the extra stabilisation caused by the better energetic match between the metal and ligand orbitals caused by the inductive effect of the methyl groups cancels with any interaction between the methyl groups on the upper and lower rings. Unfortunately there are no experimental data available with which to compare these optimised geometries.

The optimised geometries show that the C_8 rings are slightly puckered, but essentially planar for all functionals investigated, however, different methods show the rings puckering in opposite directions. The hydrogen atoms attached to the rings (i.e. in the unsubstituted ring positions) are deflected towards the centre of the molecule with all methods. The carbon atoms of the methyl groups are deflected to a lesser extent than the hydrogen atoms, indeed with some methods they are deflected away from the centre of the molecule (e.g. BLYP or OLYP).

Table 4.10: Results from geometry optimisations on $Th(TMCOT)_2$ using a variety of density functionals under D_{4h} symmetry. The definition of the geometric variables is given in figure 4.17. Although optimised, the lengths and angles within the methyl groups are not given.

	VWN	BLYP	OLYP	BP86	PW91	PBE	KT1	KT2
Th-X / Å	1.991	2.108	2.056	2.062	2.047	2.047	2.025	2.007
X-C(RH) / Å	1.823	1.845	1.836	1.840	1.838	1.840	1.851	1.831
C(RH) def / °	90.06	89.98	89.98	89.98	90.01	90.01	90.10	90.09
X-C(RM) / Å	1.856	1.879	1.872	1.874	1.872	1.874	1.880	1.860
C(RM) def / °	89.94	90.02	90.02	90.02	89.99	89.99	89.90	89.91
X-C(M) / Å	3.361	3.417	3.399	3.402	3.397	3.400	3.409	3.372
C(M) def / °	89.25	90.31	90.14	90.18	89.92	89.92	89.07	89.08
X-H(R) / Å	2.918	2.935	2.923	2.932	2.929	2.932	2.943	2.911
H(R) def / °	88.05	88.55	88.28	88.39	88.32	88.29	87.93	87.94
Th-C(H) / Å	2.701	2.801	2.756	2.763	2.752	2.752	2.746	2.719
Th-C(C) / Å	2.721	2.824	2.781	2.787	2.774	2.775	2.761	2.734
C(RM)-C(RH) / Å	1.408	1.425	1.420	1.422	1.420	1.421	1.428	1.413
C(RM)-C(M) / Å	1.505	1.538	1.527	1.528	1.525	1.526	1.530	1.513
C(RH)-H(R) / Å	1.098	1.091	1.088	1.094	1.093	1.094	1.096	1.084
H(M)-H(M) / Å	2.864	3.265	3.139	3.151	3.084	3.082	2.902	2.880

Figure 4.17: Definition of the geometric variables for substituted actinocenes of the type An(TMCOT)$_2$. Due to the D_{4h} structure the 8 membered rings have two sets of symmetry inequivalent carbon atoms. These lie in two planes between which the centroid point X is considered to be equidistant. C(RM) is a ring carbon atom bearing a methyl group. C(M) is the methyl-carbon atom. C(RM)-def is the angle subtended by the X-C(RM) distance and the An-X distance. C(RH) is a ring carbon bearing a hydrogen atom. H(R) is a hydrogen atom bound directly to the C_8 ring. C(RH)-def is the angle subtended by the X-C(RH) distance and the An-X distance. Angles $< 90°$ indicate that the atom lies below the plane through the ring centroid perpendicular to the An-X distance. H(M)-H(M) is the closest approach of the methyl-hydrogen atoms on opposite rings.

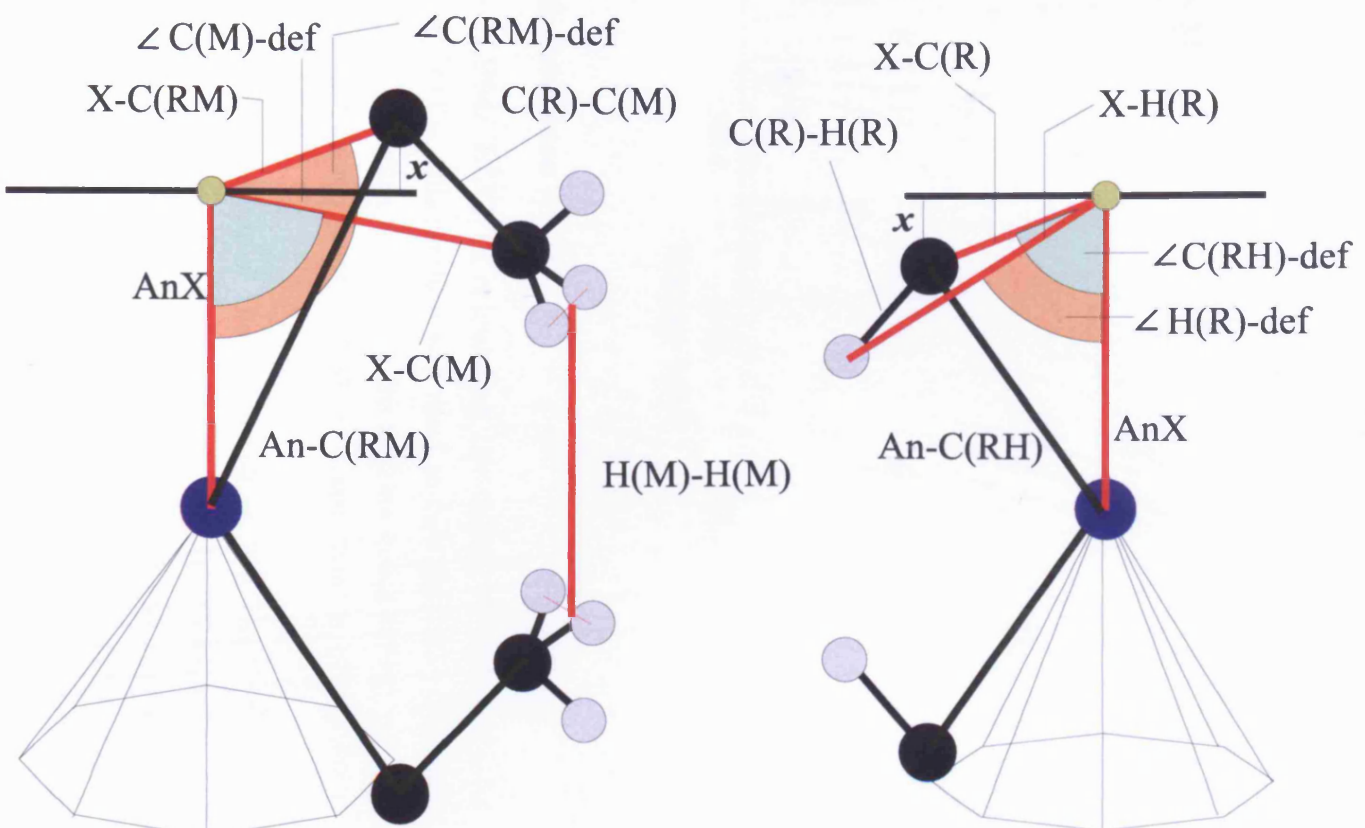

Figure 4.18: Theoretical electronic excitation spectrum for Th(TMCOT)$_2$ from a TD-DFT calculation using LB94 at the BLYP geometry.

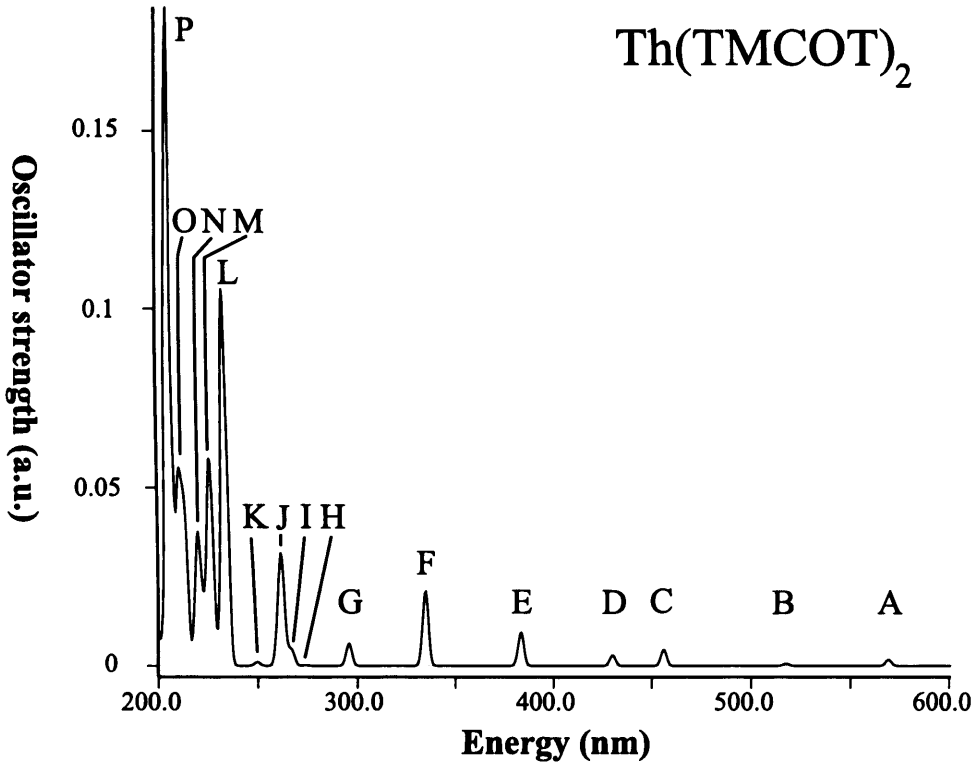

4.5.1.2 Electronic structure

Due to the success of LB94//BLYP in calculating the energy of the first electronic transition of Th(COT)$_2$, this method was used to calculate the electronic spectrum for Th(TMCOT)$_2$ (figure 4.18). The transitions contributing towards the dominant excitations are shown in figure 4.19, and are given in tabular form in table 4.11.

In comparison with the spectrum of thorocene (figure 4.7, page 160) it is observed that the first band occurs at a lower energy. This is attributed to the smaller HOMO-LUMO gap, because of the destabilisation of the ring orbitals by the substituents, such that they are a better energy match with the metal orbitals. It is also observed that the number of bands observed has increased. This can be accounted for by the reduction in symmetry from D_{8h} to D_{4h} caused by the addition of the methyl groups to the rings.

Bands A-D in Th(TMCOT)$_2$ have essentially the same character as bands A&B in Th(COT)$_2$, however, the (formerly $7e_{2g}$) orbital from which these transitions originate has been split into two components by the reduction in symmetry.

This has resulted in doubling the number of excitations. The reduction in the HOMO-LUMO gap (from 2 eV to 1.6 eV) coupled with the splitting of the $10b_{2g}$ and $8b_{1g}$ orbitals ($\approx$ 0.5 eV) has caused bands A&C to be substantially red-shifted compared with the equivalent in Th(COT)$_2$. The reason for these bands now comprising excitations with essentially a single transition, compared with the 2:3 ratios seen for Th(COT)$_2$ is not understood.

Band E&F are equivalent to band C in thorocene. These excitations are based on transitions between orbitals which have both been split by the reduction in symmetry, however only two bands, not four, result from this single band, because the $b_{1g}\rightarrow b_{1u}$ and $b_{2g}\rightarrow b_{2u}$ transitions are not dipole active. Bands G&H have the character of band D in Th(COT)$_2$, however, band H has a very small oscillator strength. Band K comprises two excitations which match bands F&G in Th(COT)$_2$, however, the remainder of the excitations which make up the Th(TMCOT)$_2$ spectrum are made up of many transitions, and do not have obvious analogous excitations in the spectrum of Th(COT)$_2$. The additional complexity in the spectrum of Th(TMCOT)$_2$ can be accounted for by the reduction in symmetry, which has both increased the density of states (due to the aforementioned splitting), but has also caused more transitions to be dipole active since $e_{1g/u}$ and $e_{1g/u}$ orbitals both become $e_{g/u}$ in Th(TMCOT)$_2$.[e] Therefore the number of transitions which can contribute towards an excitation has increased.

The experimental band at 480 nm could be assigned to either bands B (518 nm) or C (456 nm), however the experimental band falls virtually between these. If the bands in the spectrum were sufficiently broad, then perhaps the experimental assignment is a larger band at the average position of B&C. In any case, band A (569 nm) was not observed experimentally, perhaps due to its low energy and small oscillator strength.

[e] $e_{1g} \otimes e_{3u} = b_{1u} \oplus b_{2u} \oplus e_{2u}$ in D_{8h} and such is dipole inactive. In D_{4h} the descent in symmetry causes these irreps to become e_g and e_u, since $e_g \otimes e_u = a_{1u} \oplus a_{2u} \oplus b_{1u} \oplus b_{2u}$ it is now dipole active.

Table 4.11: Tabulated electronic excitation data for Th(TMCOT)$_2$ calculated with LB94, at the BLYP geometry using ADF. Details of the interpretation of these data may be found in section 4.3.2.1. These data are presented as a spectrum in figure 4.18, and are overlayed on a MO diagram in figure 4.19.

Feature on Spectrum	Excitation				Transition			
	Transition Symmetry	Energy eV	λ nm	f	From	To	%	Character
A	1 E_u	2.18	569	$6.32\text{x}10^{-3}$	$10b_{2g}$	$19e_u$	89.6	Rπ→M-f
					$8b_{1g}$	$19e_u$	7.9	Rπ→M-f
B	2 E_u	2.40	518	$2.27\text{x}10^{-3}$	$10b_{2g}$	$20e_u$	95.9	Rπ→M-f
C	3 E_u	2.72	456	$1.66\text{x}10^{-2}$	$8b_{1g}$	$19e_u$	76.7	Rπ→M-f
					$8b_{1g}$	$20e_u$	14.1	Rπ→M-f
					$10b_{2g}$	$29e_u$	6.6	Rπ→M-f
D	4 E_u	2.88	430	$1.09\text{x}10^{-2}$	$8b_{1g}$	$20e_u$	85.3	Rπ→M-f
					$8b_{1g}$	$19e_u$	11.1	Rπ→M-f
E	1 A_{2u}	3.24	383	$3.40\text{x}10^{-2}$	$10b_{2g}$	$9b_{1u}$	91.4	Rπ→M-f
					$8b_{1g}$	$7b_{2u}$	7.3	Rπ→M-f
F	2 A_{2u}	3.71	335	$7.65\text{x}10^{-2}$	$8b_{1g}$	$7b_{2u}$	89.0	Rπ→M-f
					$10b_{2g}$	$9b_{1u}$	5.9	Rπ→M-f
G	5 E_u	4.19	296	$2.26\text{x}10^{-2}$	$8b_{1u}$	$15e_g$	73.2	Rπ→Rπ
					$10b_{2g}$	$21e_u$	22.7	Rπ→Rπ
H	6 E_u	4.53	274	$6.31\text{x}10^{-4}$	$6b_{2u}$	$15e_g$	62.8	Rπ→Rπ
					$10b_{2g}$	$21e_u$	29.5	Rπ→Rπ
I1	3 A_{2u}	4.65	267	$1.43\text{x}10^{-2}$	$8b_{1u}$	$11b_{2g}$	40.3	Rπ→Rπ
					$14e_g$	$19e_u$	50.7	Rπ→M-f
					$6b_{2u}$	$9b_{1g}$	7.3	Rπ→Rπ
I2	7 E_u	4.69	264	$9.03\text{x}10^{-3}$	$14e_g$	$16a_{2u}$	89.1	Rπ→M-f
J1	8 E_u	4.74	262	$8.52\text{x}10^{-2}$	$8b_{1g}$	$21e_u$	39.1	Rπ→Rπ
					$10b_{2g}$	$21e_u$	30.3	Rπ→Rπ
					$8b_{1u}$	$15e_g$	10.1	Rπ→Rπ
					$14e_g$	$16a_{2u}$	10.1	Rπ→M-f
					$6b_{2u}$	$15e_g$	6.8	Rπ→Rπ
J2	4 A_{2u}	4.76	260	$3.93\text{x}10^{-2}$	$8b_{1u}$	$11b_{2g}$	43.2	Rπ→Rπ
					$14e_g$	$19e_u$	48.5	Rπ→M-f
					$6b_{2u}$	$9b_{1g}$	5.0	Rπ→Rπ
K1	9 E_u	4.97	250	$3.50\text{x}10^{-3}$	$18e_u$	$19a_{1g}$	97.6	Rπ→M-d
K2	5 A_{2u}	4.98	249	$4.17\text{x}10^{-4}$	$14e_g$	$20e_{1u}$	95.9	Rπ→M-f
L1	6 A_{2u}	5.29	234	$6.79\text{x}10^{-2}$	$13e_g$	$19e_u$	69.7	Rσ→M-f
					$6b_{2u}$	$9b_{1g}$	21.2	Rπ→Rπ
L2	11 E_u	5.32	233	$2.10\text{x}10^{-1}$	$10b_{2g}$	$22e_u$	45.3	Rπ→Rσ
					$8b_{1g}$	$21e_u$	24.9	Rπ→Rπ
					$6b_{2u}$	$15e_g$	8.3	Rπ→Rπ
					$14e_g$	$7b_{2u}$	5.7	Rπ→Rπ
L3	7 A_{2u}	5.33	233	$1.25\text{x}10^{-1}$	$6b_{2u}$	$9b_{1g}$	43.4	Rπ→Rπ
					$13e_g$	$19e_u$	30.0	Rσ→M-f
					$8b_{1u}$	$12b_{2g}$	13.3	Rπ→Rσ
M1	$12E_u$	5.46	227	$4.93\text{x}10^{-2}$	$7b_{1g}$	$19e_u$	67.4	Rσ→M-f

Continued on next page

Continued from previous page

Feature on Spectrum	Excitation				Transition			
	Transition Symmetry	Energy eV	λ nm	f	From	To	%	Character
					$10b_{2g}$	$22e_u$	20.0	Rπ→Rσ
M2	13 E_u	5.49	226	$9.89\text{x}10^{-2}$	$8b_{1u}$	$16e_g$	48.7	Rπ→Rσ
					$10b_{2g}$	$22e_u$	16.8	Rπ→Rσ
					$7b_{1g}$	$19e_u$	10.2	Rσ→M-f
					$14e_g$	$7b_{2u}$	7.4	Rπ→M-f
					$14e_g$	$9b_{1u}$	6.2	Rπ→M-f
M3	14 E_u	5.50	225	$8.34\text{x}10^{-2}$	$8b_{1u}$	$16e_g$	47.4	Rπ→Rσ
					$7b_{1g}$	$19e_u$	21.1	Rσ→M-f
					$10b_{2g}$	$22e_u$	12.7	Rπ→Rσ
N1	$9A_{2u}$	5.58	222.3	$3.75\text{x}10^{-2}$	$8b_{1u}$	$12b_{2g}$	54.5	Rπ→Rσ
					$18a_{1g}$	$16a_{2u}$	53.4	Rπ→M-f
N2	10 A_{2u}	5.64	220	$1.15\text{x}10^{-1}$	$18a_{1g}$	$16a_{2u}$	53.4	Rπ→M-f
					$8b_{1u}$	$12b_{2g}$	19.8	Rπ→Rσ
					$15a_{2u}$	$19a_{1g}$	17.1	Rπ→M-d
					$6b_{2u}$	$9b_{1g}$	5.0	Rπ→Rπ
O1	$11A_{2u}$	5.80	214	$3.73\text{x}10^{-2}$	$15a_{2u}$	$19a_{1g}$	59.0	Rπ→M-d
					$6b_{2u}$	$10b_{1g}$	32.1	Rπ→Rσ
O2	19 E_u	5.81	213	$1.08\text{x}10^{-1}$	$8b_{1g}$	$22e_u$	20.8	Rπ→Rσ
					$6b_{2u}$	$16e_g$	20.3	Rπ→Rσ
					$14e_g$	$9b_{1u}$	19.5	Rπ→M-f
					$18a_{1g}$	$20e_u$	14.5	Rπ→M-f
					$14e_g$	$7b_{2u}$	7.8	Rπ→M-f
					$9b_{2g}$	$20e_u$	6.1	Rσ→M-f
O3	12 A_{2u}	5.89	210	$1.68\text{x}10^{-1}$	$6b_{2u}$	$10b_{1g}$	63.8	Rπ→Rσ
					$15a_{2u}$	$19a_{1g}$	18.7	Rπ→M-d
					$8b_{1u}$	$12b_{2g}$	5.0	Rπ→Rσ
P	24 E_u	6.03	206	$6.66\text{x}10^{-1}$	$14e_g$	$9b_{1u}$	14.2	Rπ→M-f
					$14e_g$	$7b_{2u}$	13.1	Rπ→M-f
					$8b_{1g}$	$22e_u$	10.9	Rπ→Rσ
					$9b_{2g}$	$20e_u$	8.5	Rσ→M-f
					$6b_{2u}$	$16e_g$	8.3	Rπ→Rσ
					$8b_{1g}$	$21e_u$	7.5	Rπ→Rπ
					$18a_{1g}$	$20e_u$	6.0	Rπ→M-f

Figure 4.19: MO diagram from an LB94 calculation at the BLYP geometry for $Th(TMCOT)_2$, calculated with ADF. The half arrows indicate the HOMO. Overlayed on the diagram are the calculated excitations using TD-DFT; details of how to interpret these data are given in section 4.3.2.1. Table 4.11 gives this information in numerical form.

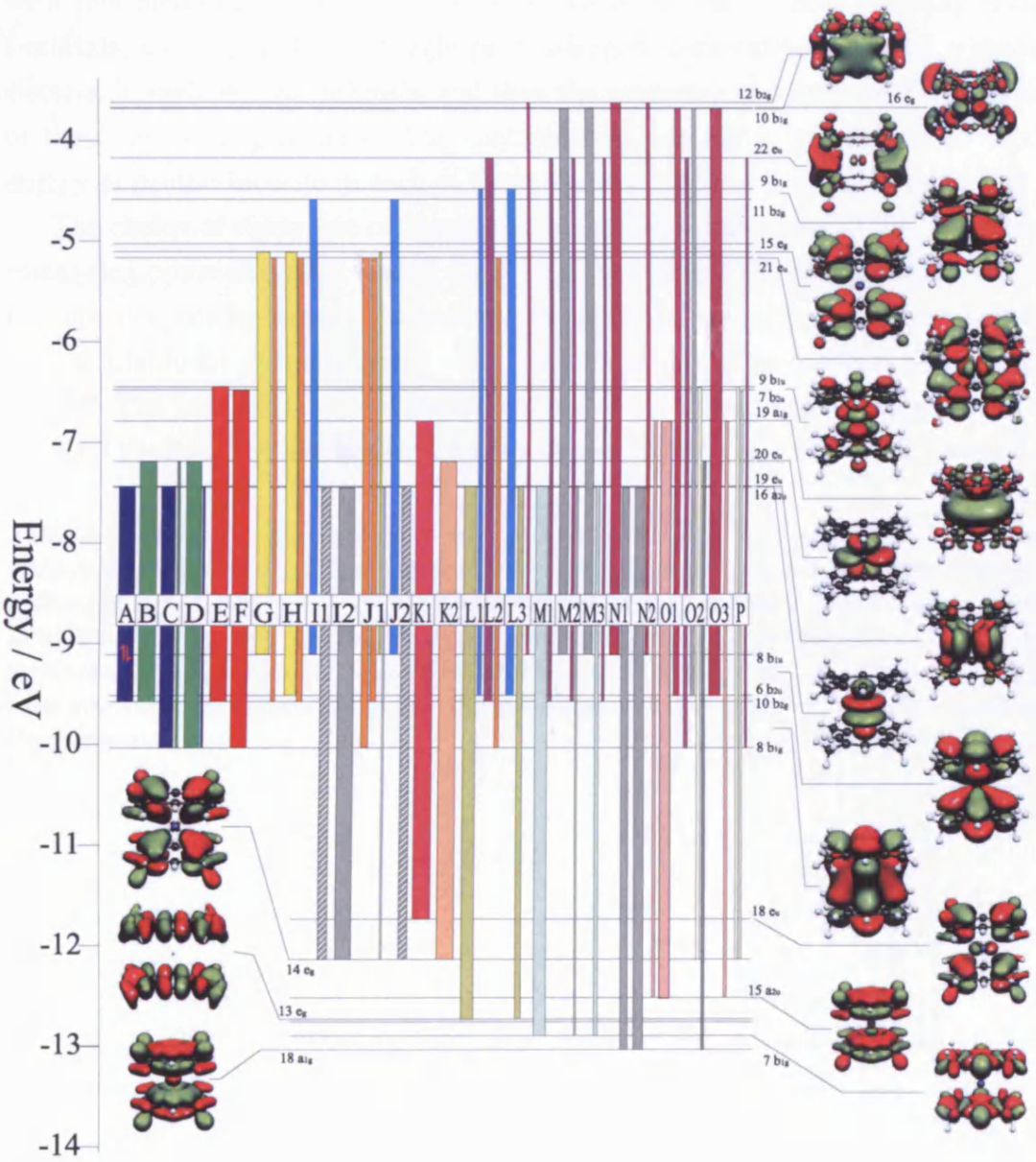

4.5.2 Protactinocene - Pa(COT)$_2$

4.5.2.1 Geometric structure

Because of the close energetic spacing of the f-orbitals, it is possible that Pa(COT)$_2$ has a multiconfigurational g.s. wavefunction. However, due to the size of the system, a multiconfigurational approach would be extremely difficult to execute. Instead, DFT was used, initially with a smearing factor, which allows the partial occupation of orbitals in a limited energy range. The geometry was optimised with this method, giving an electronic configuration with three partially filled f-orbitals, a_{2u}, e_{1u} and e_{3u}. Single point energies were calculated with a single electron in each of these orbitals, and then the geometry was optimised with each of these new configurations. The configuration, molecular geometry and total energy of protactinocene in each of these electronic states is given in table 4.12.

The choice of electronic configuration makes little difference (0.027 Å) to the metal-ring centroid distance, with the X^2A_{2u} state giving the best agreement with the smeared configuration. Unfortunately there are no structural experimental data available for protactinocene - the closest is a partial powder diffraction pattern.[146] The best estimate for the metal-ring centroid distance in protactinocene (1.964 Å) is from the average of the uranocene (1.924 Å) and thorocene (2.004 Å)

Table 4.12: The optimised geometry of Pa(COT)$_2$ with BLYP, in a number of different electronic configurations. The smeared electronic structure has the following configuration ($11a_{2u}^{0.27} + 5e_{3u}^{0.46} + 11e_{1u}^{0.27}$). The definition of the geometric parameters is given in figure 4.6. The total binding energy is given relative to the lowest energy optimised structure X^2A_{2u} for each optimised geometry, and for single point calculations with each electronic configuration at the optimised geometry calculated with the smeared electronic structure.

	Configuration			
	Smeared	X^2A_{2u}	A^2E_{1u}	B^2E_{3u}
Pa-X / Å	2.056	2.056	2.064	2.037
X-C / Å	1.857	1.857	1.857	1.858
X-H / Å	2.946	2.946	2.946	2.946
Pa-X-H / °	88.24	88.24	88.42	88.13
Pa-C / Å	2.770	2.770	2.776	2.757
C-C / Å	1.421	1.421	1.421	1.422
C-H / Å	1.091	1.091	1.091	1.091
H def / °	85.24	85.24	85.73	84.95
E(SP) / kJ mol^{-1}	-	-0.14	+35.14	+36.61
E(OPT) / kJ mol^{-1}	+28.5	0 (-19120.63)	+36.01	+34.85

experimental distances obtained from x-ray diffraction studies.[170] BLYP is seen to over-estimate the metal-ring distance by ≈ 0.1 Å if the lowest energy structure ($^2A_{2u}$) is considered, however this represents a shortening of the metal-ring distance of 0.05 Å compared with the BLYP result for thorocene (table 4.2), which matches the expected contraction from the experimental data (0.04 Å) fairly well.

4.5.2.2 Electronic structure

Unfortunately due to the limitations of the TD-DFT code in ADF, it is not possible to calculate excitations from smeared electronic configurations, or those with single electrons in degenerate orbitals, and so the only configuration from which excitations can be calculated is the X^2A_{2u} state, which fortunately is found to be the g.s. The optimised geometry with this electronic symmetry is lower in energy than the minimum energy structure in any other configuration, including the smeared one (table 4.12).

It is found that none of the electronic configurations resulting from the above calculations are *aufbau*. The result of moving the electron to the LUMO of the non-*aufbau* configuration is to destabilise that orbital, while stabilising the orbital from which the electron was removed, such that the new configuration remains non-*aufbau*. This is taken to indicate that the system would benefit from a multi-configurational treatment.

The choice of the A^2E_{1u} or B^2E_{3u} electronic configuration, where there is a single electron in a degenerate set of orbitals should lead to a Jahn-Teller distortion, in order to remove this degeneracy. This should lower the symmetry and alter the selection rules, resulting in more allowed transitions. Given this extra level of complexity (for which the requirement is uncertain), the general problems with performing such a calculation, and the generally accepted viewpoint that the species studied are highly symmetrical, it seems sensible to perform TD-DFT calculations from only the X^2A_{2u} ground state. With the "paucity"[156] of experimental data available for these species, and the extreme sensitivity of the energy of the excitations to the choice of method, it is thought unlikely that the choice of one state over another would significantly alter the conclusions from the study.[f]

The spectrum from an LB94 calculation at the BLYP optimised geometry with an X^2A_{2u} configuration is given in figure 4.20, the transitions making up the dominant excitations are shown in figure 4.21, and tabulated in table 4.13. As expected, the removal of the α/β degeneracy in the open-shell calculation results

[f]Non *aufbau* electronic configurations have been used before to successfully account for experimental results,[172] so it is not felt that the use of a non-*aufbau* electronic configuration in this study is a problem.

Table 4.13: Tabulated electronic excitation data for $Pa(COT)_2$ calculated with LB94, at the BLYP geometry using ADF. Details of the interpretation of these data may be found in section 4.3.2.1. These data are presented as a spectrum in figure 4.20, and are overlayed on a MO diagram in figure 4.21.

Feature on Spectrum	Excitation							
	Transition Symmetry	Energy eV	λ nm	f	Transition From	To	%	Character
A	1 A_{2u}	1.65	751	$1.01\text{x}10^{-2}$	$\alpha 11a_{2u}$	$\alpha 14a_{1g}$	99.5	M-f→M-d
B	1 E_{1u}	1.67	743	$9.50\text{x}10^{-4}$	$\alpha 7e_{2g}$	$\alpha 5e_{3u}$	80.4	Rπ→M-f
					$\alpha 7e_{2g}$	$\beta 5e_{3u}$	19.5	Rπ→M-f
C	2 E_{1u}	1.99	623	$1.03\text{x}10^{-2}$	$\beta 7e_{2g}$	$\beta 5e_{3u}$	79.3	Rπ→M-f
					$\alpha 7e_{2g}$	$\alpha 5e_{3u}$	18.9	Rπ→M-f
D	3 E_{1u}	2.53	490	$2.34\text{x}10^{-3}$	$\alpha 7e_{2g}$	$\alpha 11e_{1u}$	97.2	Rπ→M-f
E	4 E_{1u}	1.79	445	$3.52\text{x}10^{-3}$	$\beta 7e_{2g}$	$\beta 11e_{1u}$	97.7	Rπ→M-f
F	2 A_{2u}	2.84	437	$7.48\text{x}10^{-3}$	$\alpha 7e_{2g}$	$\alpha 6e_{2u}$	64.2	Rπ→M-f
					$\beta 7e_{2g}$	$\beta 6e_{2u}$	35.4	Rπ→M-f
G	4 A_{2u}	3.37	368	$1.85\text{x}10^{-1}$	$\beta 7e_{2g}$	$\beta 6e_{2u}$	62.1	Rπ→M-f
					$\alpha 7e_{2g}$	$\alpha 6e_{2u}$	33.2	Rπ→M-f
H1	5 A_{2u}	4.34	285	$1.30\text{x}10^{-4}$	$\alpha 3e_{3g}$	$\alpha 5e_{3u}$	99.9	Rσ→M-f
H2	5 E_{1u}	4.39	282	$3.64\text{x}10^{-3}$	$\alpha 11a_{2u}$	$\alpha 8e_{1g}$	99.5	M-f→Rσ
H3	6 E_{1u}	4.48	277	$3.90\text{x}10^{-4}$	$\beta 5e_{2u}$	$\beta 4e_{3g}$	50.9	Rπ→Rπ
					$\alpha 5e_{2u}$	$\alpha 4e_{3g}$	38.8	Rπ→Rπ
					$\alpha 7e_{2g}$	$\alpha 6e_{3u}$	5.9	Rπ→Rπ
I	7 E_{1u}	4.79	259	$8.04\text{x}10^{-3}$	$\alpha 5e_{2u}$	$\alpha 4e_{3g}$	32.5	Rπ→Rπ
					$\beta 7e_{2g}$	$\beta 6e_{3u}$	28.2	Rπ→Rπ
					$\beta 5e_{2u}$	$\beta 4e_{3g}$	27.3	Rπ→Rπ
					$\alpha 7e_{2g}$	$\alpha 6e_{3u}$	11.3	Rπ→Rπ
J	8 A_{2u}	5.17	240	$2.68\text{x}10^{-3}$	$\alpha 5e_{2u}$	$\alpha 8e_{2g}$	54.1	Rπ→Rπ
					$\beta 5e_{2u}$	$\beta 8e_{2g}$	37.4	Rπ→Rπ
					$\alpha 7e_{1g}$	$\alpha 11e_{1u}$	8.1	Rπ→M-f
K1	12 E_{1u}	5.41	229	$3.29\text{x}10^{-2}$	$\alpha 7e_{1g}$	$\alpha 6e_{2u}$	80.9	Rπ→M-f
					$\alpha 7e_{2g}$	$\alpha 6e_{3u}$	8.0	Rπ→Rπ
K2	9 A_{2u}	5.42	229	$5.81\text{x}10^{-3}$	$\beta 7e_{1g}$	$\beta 11e_{1u}$	95.6	Rπ→M-f
L	14 E_{1u}	5.59	222	$3.50\text{x}10^{-2}$	$\beta 7e_{1g}$	$\beta 6e_{2u}$	66.3	Rπ→M-f
					$\alpha 11a_{2u}$	$\alpha 9e_{1g}$	13.0	M-f→Rσ
					$\beta 7e_{2g}$	$\beta 6e_{3u}$	5.2	Rπ→Rπ
M1	10 A_{2u}	5.85	212	$2.37\text{x}10^{-1}$	$\alpha 11a_{2u}$	$\alpha 16a_{1g}$	41.5	M-f→Rσ
					$\beta 5e_{2u}$	$\beta 8e_{2g}$	28.7	Rπ→Rπ
					$\alpha 5e_{2u}$	$\alpha 8e_{2g}$	21.0	Rπ→Rπ
M2	11 A_{2u}	5.90	210	$2.08\text{x}10^{-1}$	$\alpha 11a_{2u}$	$\alpha 16a_{1g}$	57.6	M-f→Rσ
					$\beta 5e_{2u}$	$\beta 8e_{2g}$	17.9	Rπ→Rπ
					$\alpha 5e_{2u}$	$\alpha 8e_{2g}$	14.7	Rπ→Rπ
N1	$24E_{1u}$	6.06	205	$9.22\text{x}10^{-3}$	$\beta 6e_{2g}$	$\beta 11e_{1u}$	78.3	Rσ→M-f
					$\alpha 7e_{2g}$	$\alpha 12e_{1u}$	16.2	Rπ→Rσ
N2	$12A_{2u}$	6.13	202	$6.56\text{x}10^{-2}$	$\alpha 6e_{2g}$	$\alpha 6e_{2u}$	90.1	Rσ→M-f

Figure 4.20: Theoretical electronic excitation spectrum for $Pa(COT)_2$ calculated using TD-DFT using LB94 at the BLYP geometry.

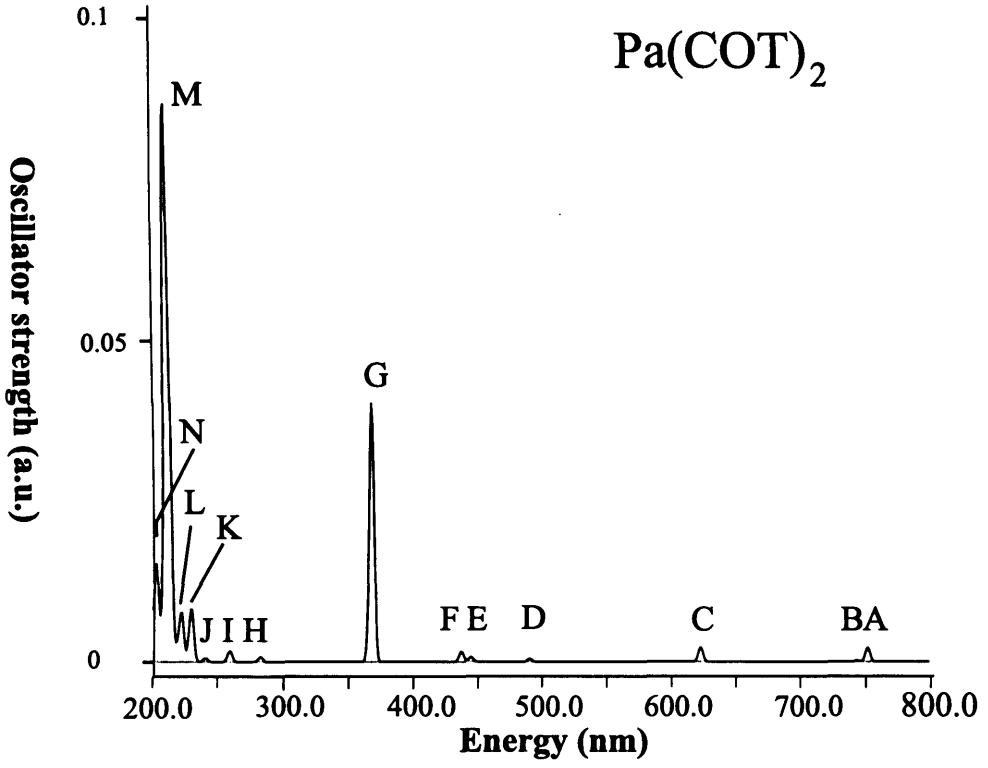

in more bands. While it is not, of course, possible to promote an electron to the $\alpha f_{a_{2u}}$-orbital which contains the unpaired electron, it is now possible to promote this electron to a variety of vacant orbitals. It might therefore be expected that the spectrum of protactinocene would be significantly affected by excitations that are based on transitions of this single f-electron.

Although the prediction that the first transition should occur at longer wavelengths than for thorocene is correct, it is not simply a result of a smaller HOMO-LUMO gap caused by the better energy match between the ring and metal orbitals. The molecular orbital structure for protactinocene is more complex than that for thorocene. To a first approximation the MO structure has three regions, compared with two regions for thorocene; the lower region (bulk occupied) contains the ring-based orbitals, and is fully occupied. The central region comprises the MOs with significant metal-f and d_{z^2} character, one of which contains the single unpaired electron. The third region is higher in energy, and contains the unoccupied ring-based orbitals (bulk vacant). These regions are shown in figure 4.22. Four different types of transition are therefore expected - from the bulk

Figure 4.21: MO diagram from an LB94 calculation at the BLYP geometry for $Pa(COT)_2$. The half arrows indicate the HOMO of the bulk occupied region, and the unpaired α electron. Overlayed on the diagram are the calculated excitations using TD-DFT; details of how to interpret these data are given in section 4.3.2.1. Table 4.13 gives this information in numerical form.

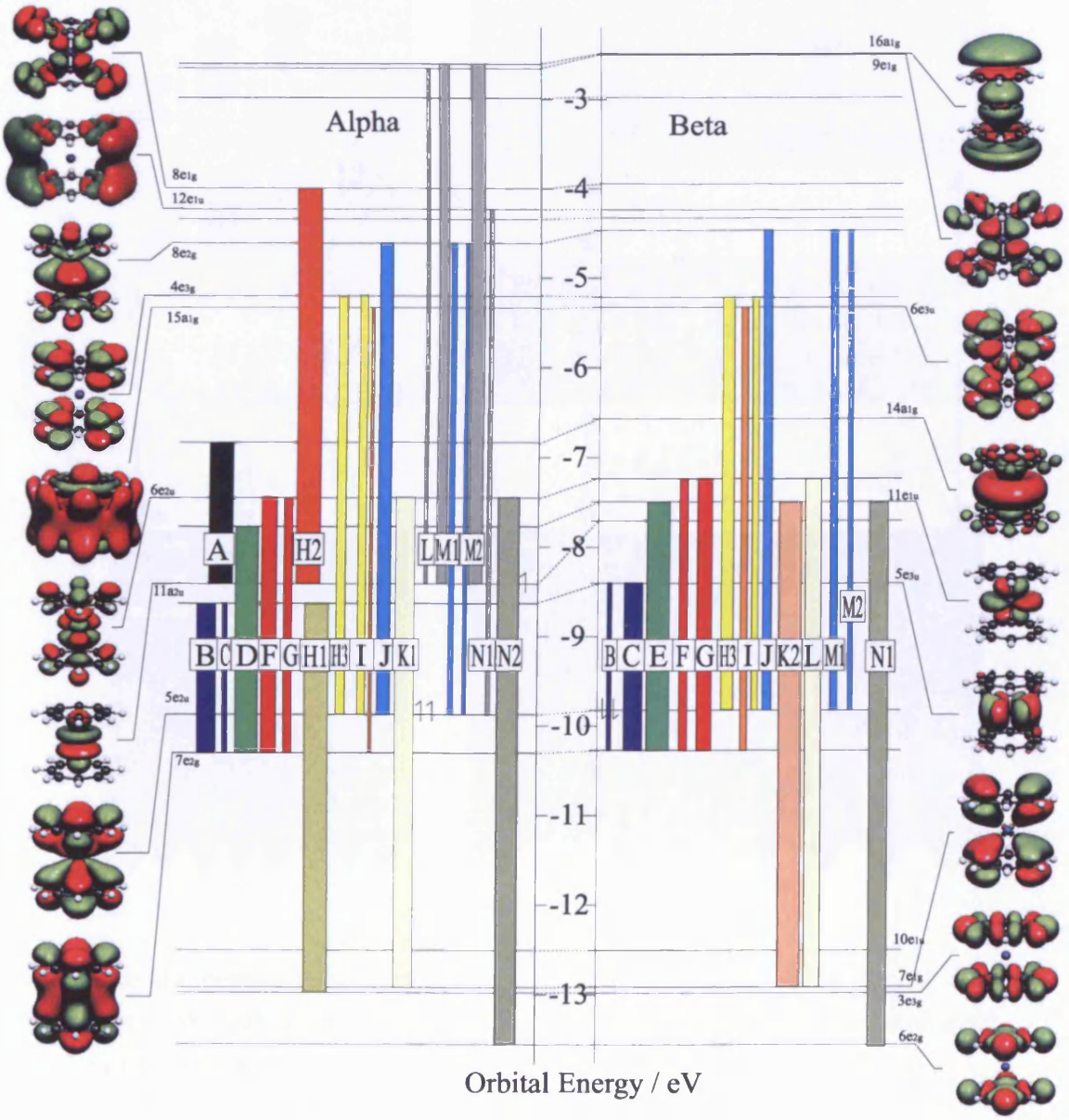

Figure 4.22: Schematic representation of the MO diagram of $Th(COT)_2$, $Th(TMCOT)_2$, $Pa(COT)_2$ and $Pa(TMCOT)_2$, showing the division of the MOs into regions.

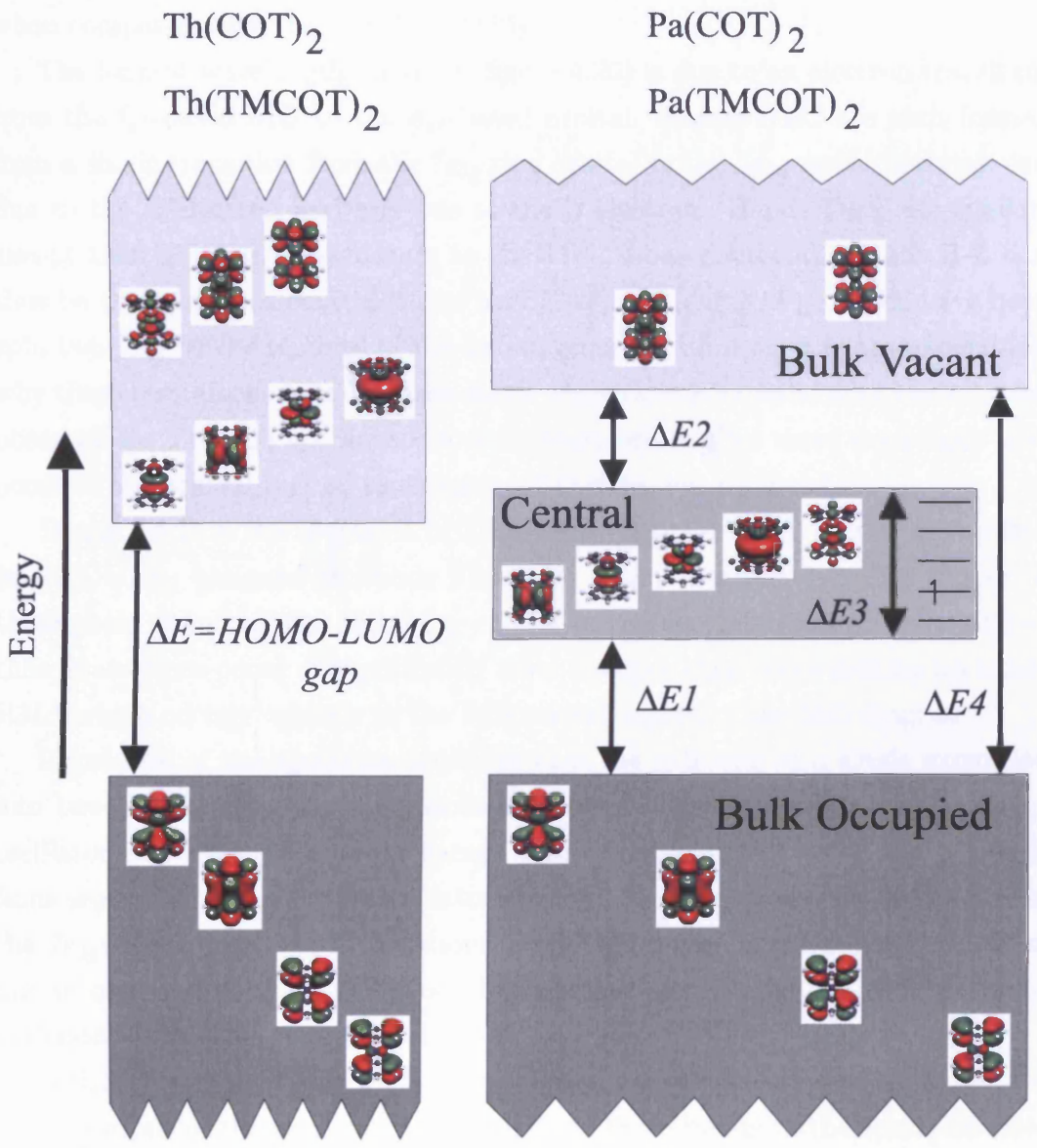

occupied to the central region, from the bulk occupied to the bulk vacant, and for the α-orbitals only, from the occupied orbital in the central region to another orbital in the central region, or to the bulk vacant region.

One might expect that the energetic positioning of the central region in the MO diagram will affect the resulting spectrum significantly; more stable orbitals, closer to the occupied ring orbitals (i.e. small ΔE_1) will favour LMCT transitions at low energies, while if this region is less stable and thus closer to the vacant

orbitals (i.e. small ΔE_2), MLCT bands will be favoured at lower energies. However transitions to, from, or within this central region will occur at lower energies than transitions from the bulk occupied to bulk vacant region (across ΔE_4), and this explains the significant red-shifting of the theoretical spectrum (figure 4.20) when compared with that for $Th(COT)_2$.

The longest wavelength band (A, figure 4.20) is due to an electron transition from the f_{z^3}-based MO to the d_{z^2}-based orbital. Bands B&C are each formed from a single transition from the $7e_{2g}$ ring orbital to the $5e_{3u}$ metal f-orbital, one due to the α electron and one due to the β electron. Bands D&E are similar, except that the transition occurs to the $11e_{1u}$ f-based orbital. Bands B-E can thus be thought of as equivalents of bands A&B in $Th(COT)_2$, which have been split two-fold by the removal of the α/β degeneracy, however it is not understood why these excitations now comprise single transitions compared with the 2:3 ratio observed for $Th(COT)_2$. Since the destination orbitals for these transitions now occur in the central region, significant red-shifting has occurred.

Bands C&D in the spectrum of $Th(COT)_2$ (figure 4.7) are each split two-fold in $Pa(COT)_2$, assigned to bands F&G and H3&I respectively. The former of these pairs populates the metal $f_{e_{2u}}$ orbital in the central group of MOs, and so these transitions occur at significantly lower energies than those making up bands H3&I which occupy orbitals in the bulk vacant region of the MO diagram.

Inspection of the spectrum indicates that the splitting of a single excitation into two components does not necessarily result in excitations with equivalent oscillator strengths. The lower energy component, dominated by the α transitions seems to have a lower oscillator strength, a phenomenon most obvious in the $7e_{2g} \rightarrow 6e_{2u}$ dominated excitations F&G, where the lower energy excitation has an oscillator strength 25x that of the higher energy component G. It is not understood why this should be the case.

Although we might have expected the spectrum of $Pa(COT)_2$ to be dominated by transitions of the unpaired f-electron, only three bands in the spectrum have substantial $f_{a_{2u}}$-character - A,H&M. The first two of these are very weak, but occur at low enough energies to be well resolved. The third band, M occurs at short wavelengths, and so is less well resolved. The increase in the number of significant bands with $\lambda > 250$ nm has increased from four to nine. However only two of these are due to first order effects of the f-electron (i.e. transitions of this f-electron). The rest of the complexity is due to the open-shell structure of $Pa(COT)_2$ - due to the unpaired electron. This may be considered a secondary effect of the single f-electron.

Table 4.14: Optimised geometries for Pa(TMCOT)$_2$ calculated with BLYP at a variety of electronic configurations. The smeared electronic structure has the following configuration ($11a_{2u}^{0.25}$ + $19e_u^{0.47}$ + $20e_u^{0.28}$). The definition of the geometric parameters is given in figure 4.17. The total binding energy is given relative to the most stable structure X^2A_{2u} for each optimised geometry, and for single point calculations with each electronic configuration at the optimised geometry of the smeared electronic structure.

	Configuration			
	Smeared	X^2A_{2u}	A^2E_u	B^2E_u
Pa-X / Å	2.059	2.074	2.050	2.066
X-C(RH) / Å	1.844	1.842	1.844	1.845
C(RH) def / °	89.98	89.99	89.96	89.99
X-C(RM) / Å	1.878	1.877	1.880	1.878
C(RM) def / °	90.02	90.01	90.04	90.01
X-C(M) / Å	3.416	3.415	3.417	3.416
C(M) def / °	90.17	90.10	90.34	90.33
X-H(R) / Å	2.934	2.932	2.933	2.934
H(R) def / °	88.41	88.39	88.29	88.58
Pa-C(RH) / Å	2.764	2.774	2.756	2.769
Pa-C(RC) / Å	2.787	2.797	2.783	2.793
C(RH)-C(RM) / Å	1.425	1.424	1.425	1.425
C(RM)-C(M) / Å	1.537	1.538	1.537	1.538
C(RH)-H(R) / Å	1.091	1.092	1.091	1.091
H(M)-H(M)/ Å	3.145	3.165	3.151	3.182
E(SP) / H	-	-0.81	+19.89	+32.06
E(OPT) / H	+25.23	0 (-31145.32)	+19.28	+32.37

LMCT bands H1&K2 have analogous bands in thorocene (E&F respectively), however, only one component of each of these transitions has a significant oscillator strength. The other component of these transitions is likely to be hidden behind another band in the 200-250 nm part of the spectrum, which is not well resolved due to the reciprocal scale. Band N1&N2 are the two components resulting from band J1 in Th(COT)$_2$, again with LMCT character. The remainder of the bands have a fairly complex structure, comprising many transitions, some of which are not observed for Th(COT)$_2$ or Th(TMCOT)$_2$ in the energy range studied.

4.5.3 Substituted protactinocene - Pa(TMCOT)$_2$

4.5.3.1 Geometric structure

Table 4.14 gives the optimised structures of Pa(TMCOT)$_2$ with BLYP in a number of different electronic configurations. The X^2A_{2u} state is again found to be

Table 4.15: Energy separations from figure 4.22 for Pa(COT)$_2$ and Pa(TMCOT)$_2$.

Energy	Pa(COT)$_2$		Pa(TMCOT)$_2$	
eV	α	β	α	β
ΔE_1	1.24	1.42	1.01	1.18
ΔE_2	1.19	1.25	1.35	1.11
ΔE_3	1.80	1.84	1.63	1.64
ΔE_4	4.55	4.50	3.99	3.94

the g.s.; however, as in Pa(COT)$_2$, this electronic configuration is found to be non-*aufbau*. The metal-ring centroid distance is found to be similar to that in Pa(COT)$_2$ if the smeared structure is used (table 4.12); if the X^2A_{2u} state is considered, a small increase is seen (0.018 Å), however in some states a small contraction is observed e.g. 0.014 Å when the A states are compared. When the X^2A_{2u} state is compared with Th(TMCOT)$_2$, a slightly larger contraction is observed in the metal-ring centroid (0.034 Å), just slightly smaller than the contraction observed in An(COT)$_2$ of 0.05 Å when replacing thorium with protactinium. As with Th(TMCOT)$_2$, the C_8 ring is essentially planar; however, the carbon atoms of the methyl group now lie above the ring plane, although the alteration is not significant. The hydrogen atoms lie below the ring plane (i.e. pointing in towards the opposite ring).

4.5.3.2 Electronic structure

The spectrum from an LB94 calculation at the BLYP optimised geometry of the X^2A_{2u} state is given in figure 4.23, and the transitions making up the dominant excitations are shown in figure 4.24, and tabulated in table 4.16. The spectrum has more bands than that for the unsubstituted analogue, and this increase in complexity can be explained by the effect of the descent of symmetry (as observed for thorocene on addition of the methyl groups), combined with the effect of the open-shell electronic structure on the MOs. The spectrum has been red-shifted when compared with Pa(COT)$_2$. This is explained by the reduction of the range of energies of the MOs as observed by the general reduction in ΔE_{1-4} upon substitution of the COT rings with methyl groups (see table 4.15).

Unlike for Pa(COT)$_2$, where the lowest energy band is due to a transition of the single metal-f electron within the central region of orbitals, the low energy band in Pa(TMCOT)$_2$ has LMCT character. This LMCT transition ($10b_{2g} \rightarrow 19e_u$) is one component of the $\alpha\pi_{7e_{2g}}$ ring to metal $f_{5e_{3u}}$ transition which has been split

Figure 4.23: Theoretical electronic excitation spectrum for Pa(TMCOT)$_2$ from a TD-DFT calculation using LB94 at the BLYP geometry.

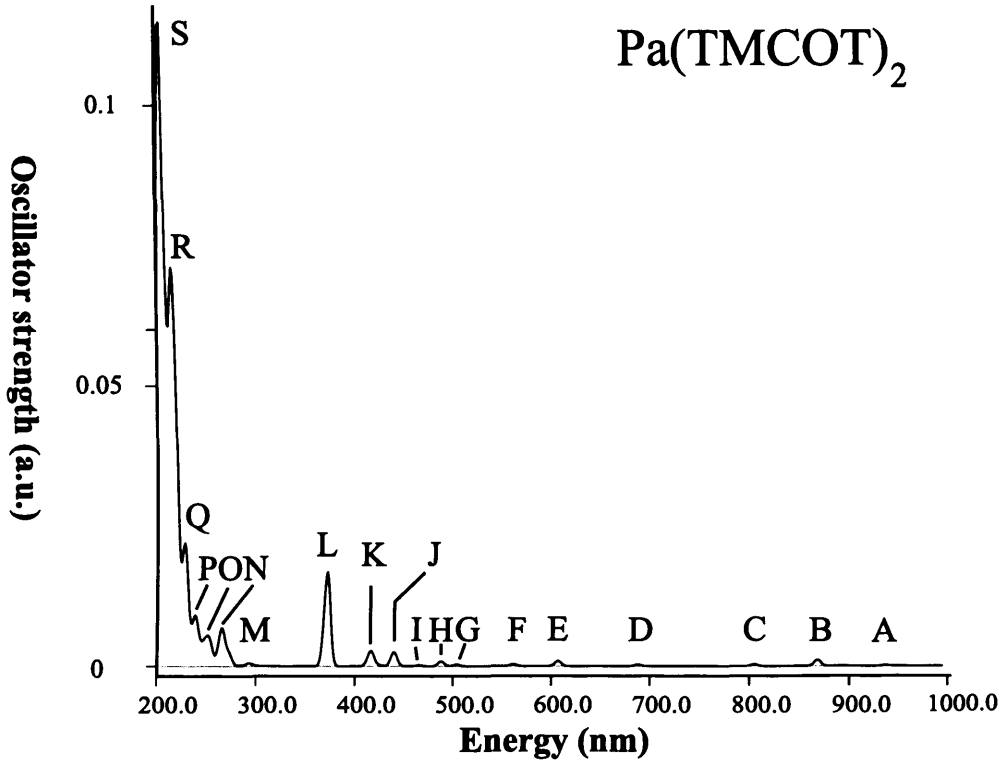

two-fold by the descent in symmetry of the origin MO. Band B is the equivalent of band A in Pa(COT)$_2$, and has been red-shifted by 117 nm. The reduction in ΔE_3 which effects the energy of f→d transition is $\approx$ 0.2 eV when comparing Pa(TMCOT)$_2$ with Pa(COT)$_2$ (thus explaining the bathochromic shift), but this is comparable with the contraction in ΔE_1, which affects the energy of the LMCT band. This, coupled with the splitting of the formerly $7e_{2g}$ level causes the LMCT band to be of lower energy than the Mf→d transition.[g]

Bands A,C,D&E are components of bands B&C in Pa(COT)$_2$ while bands F,G&I are components of bands D&E. This represents a two-fold splitting, although the fourth component from bands B&C has a very small oscillator strength and occurs at 425.83 nm, an extremely small component of band K, and thus is not tabulated or shown diagrammatically. Bands F&G in Pa(COT)$_2$ are affected by the splitting of both the origin and destination MOs, and the dipole active

[g]Because neither of the discussed transitions are between the frontier orbitals of the regions which are separated by the energies in table 4.15, these energies alone cannot be used to explain the reversal in the characters of the bands in the spectra; they do not take into account that the splitting of the orbitals has moved the origin of the LMCT closer in energy to the HOMO.

components contribute towards excitations H,J,K1,K2&L.

Five bands in the spectrum, B,K,P&S have MLCT character, however the bands > 300nm are very small, with the other two contributing to the large absorption between 200 and 300nm. The remaining excitations which make up the spectrum are fairly complex, including many component transitions, of which a number are not seen in the spectra of the other species investigated.

It was expected that the extra complexity of the spectrum compared with $Th(TMCOT)_2$ was due to transitions of the f-electron from the $16a_{2u}$ MO, however the majority of the bands in the spectrum are those that appear in $Th(COT)_2$, and hence $Th(TMCOT)_2$, except that have they been split into components by both the second order (open-shell) effects caused by the un-paired electron, and by the reduced symmetry of the ligand field.

The experimental data for $Pa(TMCOT)_2$ consist of a band at 380 nm with a shoulder at 490 nm. This suggests that the first band is quite wide, since the shoulder occurs at 490 nm, however, the actual spectrum is not available. It is clear that the lowest energy allowed transition (A, 936 nm), cannot be the first measured band at 380 nm, because the spectrum is unlikely to be recorded at such high wavelengths.[h] It is also unlikely that the theoretical spectrum is offset by 500 nm! In accordance with Occum's razor,[i] I suggest that the first measured experimental band is theoretical band L calculated at 372 nm, while the shoulder at 490 nm is likely to be band H calculated at 489 nm. The higher energy bands have perhaps been missed due to their low oscillator strengths. If the spectrum is broadened sufficiently such that band H becomes a shoulder on band L, then bands I,J&K would occur under the resulting band envelope, thus increasing the intensity of the shoulder. This assignment would also resolve the problems discussed before, where the 490 nm band was assigned to an f-electron transition and 380 nm to the *same* low energy transition as observed for $Th(TMCOT)_2$; this band has not been blue shifted, when we expected it to be red shifted, it is apparently not even the same band!

[h]Any band at 936 nm would occur in the infra-red region of the electromagnetic spectrum where vibrational transitions dominate. Thus if the spectrum were recorded in this region, the band would probably be confused for a vibrational transition.

[i]Occum's razor is a principle attributed to the 14^{th} century logician William of Ockham and states that given two explanations of a phenomenon, one should adopt the simpler explanation, or that which makes the fewest assumptions.

Table 4.16: Tabulated electronic excitation data for Pa(TMCOT)$_2$ calculated with LB94, at the BLYP geometry using ADF. Details of the interpretation of these data may be found in section 4.3.2.1. These data are presented as a spectrum in figure 4.23, and are overlayed on a MO diagram in figure 4.24.

Feature on Spectrum	Excitation				Transition			
	Transition Symmetry	Energy eV	λ nm	f	From	To	%	Character
A	$1E_u$	1.32	936	$1.07\text{x}10^{-3}$	$\alpha 10b_{2g}$	$\alpha 19e_u$	93.6	Rπ→M-f
					$\beta 10b_{2g}$	$\beta 19e_u$	5.1	Rπ→M-f
B	$1A_{2u}$	1.43	868	$8.78\text{x}10^{-3}$	$\alpha 16a_{2u}$	$\alpha 19a_{1g}$	99.6	M-f→M-d
C	$2E_u$	1.54	806	$2.47\text{x}10^{-3}$	$\beta 10b_{2g}$	$\beta 19e_u$	88.6	Rπ→M-f
					$\alpha 8b_{1g}$	$\alpha 19e_u$	6.4	Rπ→M-f
D	$3E_u$	1.80	689	$2.18\text{x}10^{-3}$	$\alpha 8b_{1g}$	$\alpha 19e_u$	82.9	Rπ→M-f
					$\beta 8b_{1g}$	$\beta 19e_u$	12.5	Rπ→M-f
E	$4E_u$	2.04	607	$7.22\text{x}10^{-3}$	$\beta 8b_{1g}$	$\beta 19e_u$	83.0	Rπ→M-f
					$\alpha 8b_{1g}$	$\alpha 19e_u$	9.1	Rπ→M-f
F	$5E_u$	2.21	562	$2.76\text{x}10^{-3}$	$\alpha 10b_{2g}$	$\alpha 20e_u$	96.1	Rπ→M-f
G	$6E_u$	2.46	505	$2.38\text{x}10^{-3}$	$\beta 10b_{2g}$	$\beta 20e_u$	98.3	Rπ→M-f
H	$2A_{2u}$	2.54	489	$6.97\text{x}10^{-3}$	$\alpha 10b_{2g}$	$\alpha 9b_{1u}$	77.5	Rπ→M-f
					$\beta 10b_{2g}$	$\beta 9b_{1u}$	21.3	Rπ→M-f
I	$7E_u$	2.66	466	$1.30\text{x}10^{-3}$	$\alpha 8b_{1g}$	$\alpha 20e_u$	98.4	Rπ→M-f
J	$3A_{2u}$	2.82	440	$2.00\text{x}10^{-2}$	$\beta 10b_{2g}$	$\beta 9b_{1u}$	62.9	Rπ→M-f
					$\alpha 8b_{1g}$	$\alpha 7b_{2u}$	21.8	Rπ→M-f
					$\alpha 10b_{2g}$	$\alpha 9b_{1u}$	14.1	Rπ→M-f
K1	$4A_{2u}$	2.97	417	$1.38\text{x}10^{-2}$	$\alpha 8b_{1g}$	$\alpha 7b_{2u}$	43.4	Rπ→M-f
					$\alpha 16a_{2u}$	$\alpha 20a_{1g}$	24.3	M-f→Rσ
					$\beta 8b_{1g}$	$\beta 7b_{2u}$	23.4	Rπ→M-f
					$\beta 10b_{2g}$	$\beta 9b_{1u}$	6.5	Rπ→M-f
K2	$5A_{2u}$	2.98	415	$9.03\text{x}10^{-3}$	$\alpha 16a_{2u}$	$\alpha 20a_{1g}$	75.4	M-f→Rσ
					$\alpha 8b_{1g}$	$\alpha 7b_{2u}$	11.0	Rπ→M-f
					$\beta 8b_{1g}$	$\beta 7b_{2u}$	10.2	Rπ→M-f
L	$6A_{2u}$	3.33	372	$1.34\text{x}10^{-1}$	$\beta 8b_{1g}$	$\beta 7b_{2u}$	64.0	Rπ→M-f
					$\alpha 8b_{1g}$	$\alpha 7b_{2u}$	22.1	Rπ→M-f
					$\beta 10b_{2g}$	$\beta 9b_{1u}$	5.9	Rπ→M-f
M	$11E_u$	4.22	294	$4.60\text{x}10^{-3}$	$\beta 10b_{2g}$	$\beta 21e_u$	39.3	Rπ→Rπ
					$\beta 8b_{1u}$	$\beta 15e_g$	32.0	Rπ→Rπ
					$\alpha 8b_{1u}$	$\alpha 15e_g$	24.7	Rπ→Rπ
N1	$15E_u$	4.54	273	$1.73\text{x}10^{-2}$	$\alpha 6b_{2u}$	$\alpha 15e_g$	34.5	Rπ→Rπ
					$\beta 6b_{2u}$	$\beta 15e_g$	21.7	Rπ→Rπ
					$\alpha 10b_{2g}$	$\alpha 21e_u$	14.6	Rπ→Rπ
					$\beta 10b_{2g}$	$\beta 21e_u$	13.8	Rπ→Rπ
					$\alpha 8b_{1u}$	$\alpha 15e_g$	6.0	Rπ→Rπ
N2	$17E_u$	4.66	266	$4.98\text{x}10^{-2}$	$\beta 8b_{1g}$	$\beta 21e_u$	35.6	Rπ→Rπ
					$\alpha 8b_{1g}$	$\alpha 21e_u$	11.7	Rπ→Rπ
					$\alpha 10b_{2g}$	$\alpha 21e_u$	10.9	Rπ→Rπ
					$\beta 10b_{2g}$	$\beta 21e_u$	9.7	Rπ→Rπ
					$\beta 6b_{2u}$	$\beta 15e_g$	8.3	Rπ→Rπ

Continued on next page

Continued from previous page

Feature on Spectrum	Excitation				Transition			
	Transition Symmetry	Energy eV	λ nm	f	From	To	%	Character
					$\alpha 8b_{1u}$	$\alpha 15e_g$	6.5	Rπ→Rπ
					$\alpha 6b_{2u}$	$\alpha 15e_g$	6.3	Rπ→Rπ
					$\beta 8b_{1u}$	$\beta 15e_g$	5.2	Rπ→Rπ
O1	$20E_u$	4.82	257	$3.65\text{x}10^{-3}$	$\alpha 18a_{1g}$	$\alpha 19e_u$	72.6	Rπ→M-f
					$\alpha 9b_{2g}$	$\alpha 19e_u$	18.1	Rσ→M-f
					$\beta 14e_g$	$\beta 16a_{2u}$	6.8	Rπ→M-f
O2	$15A_{2u}$	4.89	253	$3.29\text{x}10^{-2}$	$\beta 8b_{1u}$	$\beta 11b_{2g}$	52.7	Rπ→Rπ
					$\alpha 8b_{1u}$	$\alpha 11b_{2g}$	28.4	Rπ→Rπ
					$\alpha 6b_{2u}$	$\alpha 9b_{1g}$	8.7	Rπ→Rπ
O3	$23E_u$	4.99	248	$2.25\text{x}10^{-2}$	$\alpha 14e_g$	$\alpha 7b_{2u}$	79.3	Rπ→Rπ
					$\alpha 8b_{1g}$	$\alpha 21e_u$	7.8	Rπ→Rπ
O4	$24E_u$	5.04	246	$3.95\text{x}10^{-3}$	$\beta 18a_{1g}$	$\beta 19e_u$	71.3	Rπ→M-f
					$\alpha 14e_g$	$\alpha 9b_{1u}$	21.8	Rπ→M-f
P1	$28E_u$	5.16	240	$1.97\text{x}10^{-2}$	$\alpha 16a_{2u}$	$\alpha 17e_g$	75.7	M-f→Rσ
					$\beta 14e_g$	$\beta 7b_{2u}$	10.9	Rπ→M-f
					$\beta 14e_g$	$\beta 9b_{1u}$	5.2	Rπ→M-f
P2	$29E_u$	5.20	238	$5.02\text{x}10^{-2}$	$\beta 14e_g$	$\beta 7b_{2u}$	48.7	Rπ→M-f
					$\alpha 16a_{2u}$	$\alpha 17e_g$	21.4	M-f→Rσ
					$\beta 14e_g$	$\beta 9b_{1u}$	10.1	Rπ→M-f
Q1	$31E_u$	5.37	231	$2.05\text{x}10^{-2}$	$\beta 18e_u$	$\beta 19a_{1g}$	72.3	Rπ→M-d
					$\alpha 10b_{2g}$	$\alpha 22e_u$	9.8	Rπ→Rσ
Q2	$19A_{2u}$	5.43	228	$1.41\text{x}10^{-1}$	$\beta 6b_{2u}$	$\beta 9b_{1g}$	38.3	Rπ→Rπ
					$\alpha 6b_{2u}$	$\alpha 9b_{1g}$	26.5	Rπ→Rπ
					$\beta 8b_{1u}$	$\beta 12b_{2g}$	14.9	Rπ→Rπ
					$\alpha 8b_{1u}$	$\alpha 12b_{2g}$	7.1	Rπ→Rπ
R1	$39E_u$	5.63	220	$3.55\text{x}10^{-2}$	$\alpha 13e_g$	$\alpha 7b_{2u}$	62.2	Rσ→M-f
					$\beta 8b_{1u}$	$\beta 16e_g$	14.1	Rπ→Rσ
					$\alpha 8b_{1u}$	$\alpha 16e_g$	5.4	Rπ→Rσ
R2	$40E_u$	5.65	219	$7.48\text{x}10^{-2}$	$\alpha 18a_{1g}$	$\alpha 20e_u$	22.7	Rπ→M-f
					$\alpha 13e_g$	$\alpha 7b_{2u}$	21.2	Rσ→M-f
					$\alpha 9b_{2g}$	$\alpha 20e_u$	16.9	Rσ→M-f
					$\alpha 13e_g$	$\alpha 9b_{1u}$	9.1	Rσ→M-f
					$\beta 8b_{1u}$	$\beta 16e_g$	6.8	Rπ→Rσ
R3	$22A_{2u}$	5.69	218	$1.06\text{x}10^{-1}$	$\alpha 8b_{1u}$	$\alpha 12b_{2g}$	40.1	Rπ→Rπ
					$\beta 8b_{1u}$	$\beta 12b_{2g}$	29.0	Rπ→Rπ
					$\beta 18a_{1g}$	$\beta 16a_{2u}$	6.0	Rπ→M-f
R4	$44E_u$	5.75	216	$2.58\text{x}10^{-1}$	$\beta 7b_{1g}$	$\beta 20e_u$	36.6	Rσ→M-f
					$\alpha 9b_{2g}$	$\alpha 20e_u$	7.3	Rσ→M-f
					$\alpha 18a_{1g}$	$\alpha 20e_u$	6.6	Rπ→M-f
R5	$45E_u$	5.80	214	$1.33\text{x}10^{-1}$	$\beta 7b_{1g}$	$\beta 20e_u$	59.7	Rσ→M-f
					$\beta 8b_{1g}$	$\beta 22e_u$	8.8	Rπ→Rσ
					$\alpha 16a_{2u}$	$\alpha 18e_g$	7.5	M-f→Rσ
S1	$50E_u$	5.93	209	$7.65\text{x}10^{-2}$	$\beta 18a_{1g}$	$\beta 20e_u$	35.6	Rπ→M-f
					$\beta 9b_{2g}$	$\beta 20e_u$	22.8	Rσ→M-f

Continued on next page

Continued from previous page

Feature on Spectrum	Excitation				Transition			
	Transition Symmetry	Energy eV	λ nm	f	From	To	%	Character
					$\alpha 16a_{2u}$	$\alpha 18e_g$	11.1	Rπ→Rσ
					$\beta 13e_g$	$\beta 9b_{1u}$	11.0	Rσ→M-f
					$\alpha 8b_{1g}$	$\alpha 22e_u$	6.4	Rπ→Rπ
S2	$28A_{2u}$	5.96	208	$7.59\text{x}10^{-2}$	$\beta 6b_{2u}$	$\beta 10b_{1g}$	32.2	Rπ→Rπ
					$\alpha 15a_{2u}$	$\alpha 19a_{1g}$	18.6	Rπ→M-d
					$\alpha 6b_{2u}$	$\alpha 10b_{1g}$	16.4	Rπ→Rπ
					$\beta 7b_{1g}$	$\beta 7b_{2u}$	7.1	Rσ→M-f
					$\alpha 9b_{2g}$	$\alpha 9b_{1u}$	6.5	Rπ→M-f
					$\beta 15a_{2u}$	$\beta 19a_{1g}$	6.3	Rπ→M-d
S3	$53E_u$	6.01	206	$1.80\text{x}10^{-1}$	$\beta 6b_{2u}$	$\beta 16e_g$	40.4	Rπ→Rσ
					$\alpha 6b_{2u}$	$\alpha 16e_g$	16.4	Rπ→Rσ
					$\alpha 16a_{2u}$	$\alpha 18e_g$	12.8	M-f→Rσ
					$\beta 18a_{1g}$	$\beta 20e_u$	9.0	Rπ→M-f
					$\beta 9b_{2g}$	$\beta 20e_u$	7.4	Rσ→M-f
S4	$54E_u$	6.05	205	$5.60\text{x}10^{-1}$	$\alpha 6b_{2u}$	$\alpha 16e_g$	20.2	Rπ→Rσ
					$\beta 6b_{2u}$	$\beta 16e_g$	18.3	Rπ→Rσ
					$\beta 9b_{2g}$	$\beta 20e_u$	8.9	Rσ→M-f
					$\beta 18a_{1g}$	$\beta 20e_u$	7.0	Rπ→M-f
S5	$33A_{2u}$	6.17	201	$8.37\text{x}10^{-2}$	$\beta 15a_{2u}$	$\beta 19a_{1g}$	70.1	Rπ→M-d
					$\alpha 16a_{2u}$	$\alpha 23a_{1g}$	7.8	Rπ→M-d
					$\beta 9b_{2g}$	$\beta 9b_{1u}$	5.2	Rσ→M-f

Figure 4.24: MO diagram from an LB94 calculation at the BLYP geometry for $Pa(TMCOT)_2$. The half arrows indicate the HOMO of the bulk occupied region, and the unpaired α electron. Overlayed on the diagram are the calculated excitations using TD-DFT; details of how to interpret these data are given in section 4.3.2.1. Table 4.16 gives this information in numerical form.

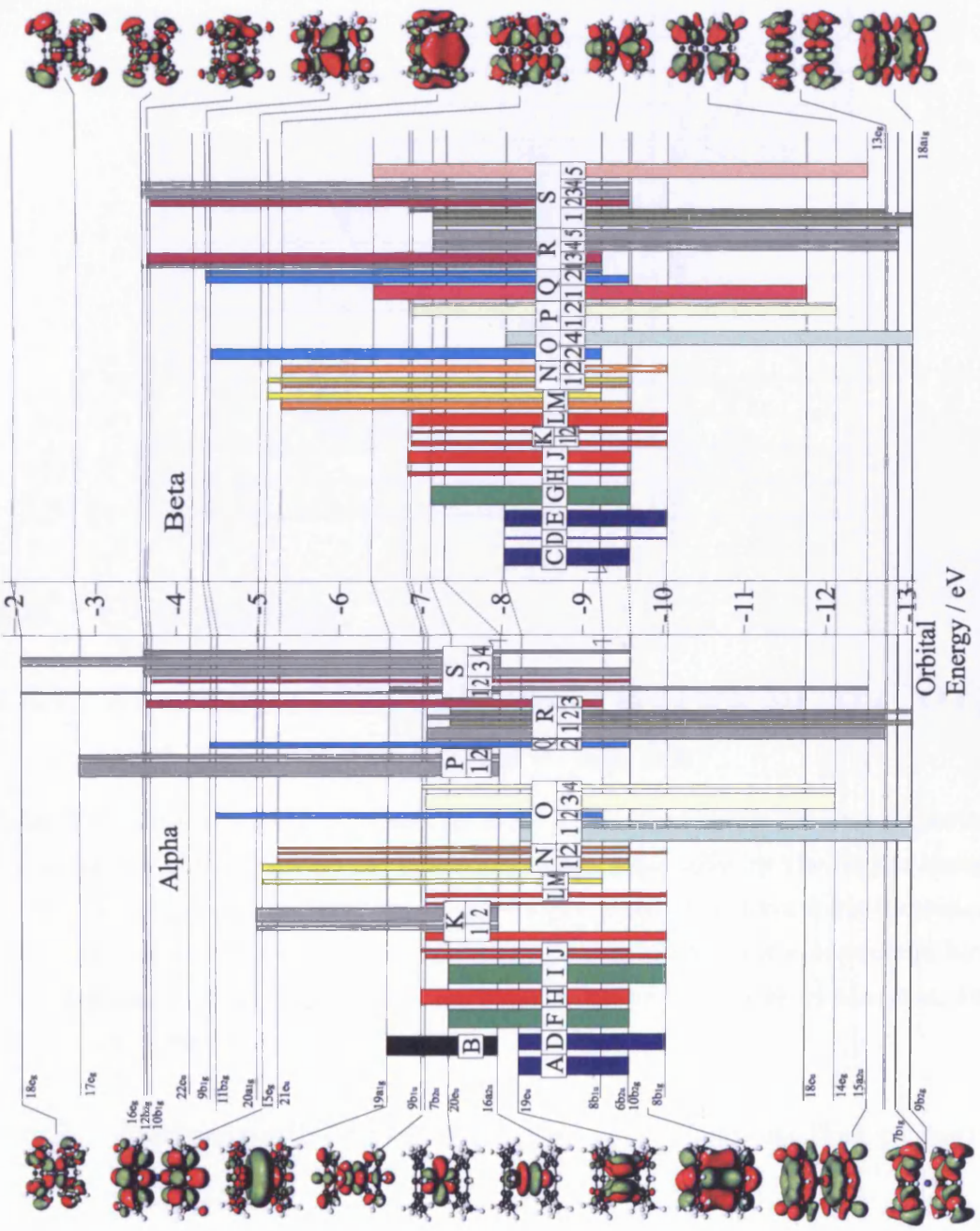

Table 4.17: Excitations which have equivalent character in the spectra are indicated here. An excitation has only been considered if it is has approximately the same breakdown into component transitions. Some transitions which are not dominated by a single transition, and have significant mixed character have not been considered. More information on these mixed bands can be obtained by the colour coded transitions on the MO diagrams, figures 4.8, 4.19, 4.21 and 4.24.

$Th(COT)_2$	$Th(TMCOT)_2$	$Pa(COT)_2$	$Pa(TMCOT)_2$
A,B	A,C	B, C	A, C, D, E
A,B	B,D	D, E	F, G, I
C	E,F	F, G	H, J, K1, L
D	G, H, J1	H3, I	M, N1, N2
E	L1	H1	-
F	K2	K2	-
G	K1	-	Q1
H	I1, J2, L3	J, M1, M2	O2, Q2
J1	-	N1, N2	-
J2	L2	-	-
-	M1	-	O1, O4
-	N1, O3	-	R3, S2
-	-	K1, L	O3, P2
-	-	A	B

4.6 Conclusions

4.6.1 Summary of LB94 electronic spectra for $An(COT)_2$ and $An(TMCOT)_2$ (An = Th, Pa)

Table 4.17 summarises the equivalence of the excitations in the electronic spectra. For some bands there are no obvious equivalents, especially for the higher energy section of the spectra, however, the lower energy excitations have fairly consistent character and are split in a predictable way. Some of the split components have small oscillator strengths, and are hidden behind more intense excitations, and are thus not listed in table 4.17.

4.6.2 Assignment of the experimental data in the present study

The band at 450 nm for $Th(COT)_2$ is assigned to either LMCT bands A (469 nm) or B (442 nm) in figure 4.7 (page 160), which populate the f-based e_{1u} and

e_{3u} levels from the HOMO-1 (e_{2g}) ring orbital. The experimental band at 480 nm for $Th(TMCOT)_2$ is likely to be either band B (518 nm) or C (456 nm) (figure 4.18), which are two split components of bands A&B in $Th(COT)_2$, and thus also have LMCT character. Band A (569 nm) for $Th(TMCOT)_2$ appears to be missing from the experimental spectrum, perhaps due to low oscillator strength, or poor resolution.

For $Pa(TMCOT)_2$, the band at 380 nm is assigned to band L (372 nm), while the shoulder at 490 nm is assigned to band H at 489 nm (figure 4.24). Both these bands populate the split components of the formally e_{2u} metal f-orbitals, from split components of the (formally HOMO-1) ring orbitals. Although they are LMCT transitions, the character is not the same as the excitations assigned to the experimental bands of the thorium species. A number of calculated bands are not reported in the experimental spectrum for $Pa(TMCOT)_2$ (bands A-G), however, these all have small oscillator strengths, or occur outside visible wavelengths.

This assignment is fairly consistent with that proposed by consideration of the MO diagram for thorocene. This theoretical study assigns all of the experimentally observed bands to LMCT transitions; none of the experimental bands are assigned to transitions of the outer f^1 electron in the Pa system. The experimental band in $Th(TMCOT)_2$ does indeed originate from the first observed band in $Th(COT)_2$, shifted to longer wavelengths by the effects of the methyl groups. The effect of the methyl substitution of the rings was not envisaged to cause a band (A, figure 4.19) at wavelengths significantly shorter than the first recorded band in the spectrum,[146] however this effect does not result in an alteration of the assignment of the first recorded experimental band (B/C); the band assigned to the experiment, and the aforementioned shorter wavelength band have the same character.

The extra complexity of the $Pa(TMCOT)_2$ electronic structure compared with that for $Th(COT)_2$ accounts for the difficulty in assigning the bands in the pre-calculation analysis, although it was clear that a discrepancy existed in the experimental data at this stage. The prediction that the $Pa(TMCOT)_2$ data are inconsistent with those for the thorium species is also born out by the theoretical data; indeed the experimentally observed bands, although having LMCT character, are not related to the experimental bands reported for $Th(COT)_2$ or $Th(TMCOT)_2$. The extra complexity has two effects. Firstly, the MO structure of $Pa(TMCOT)_2$ is substantially different from that of the thorium species, with a central region containing the f-antibonding orbitals in which the electron population is predicted to be non-*aufbau*. This allows the possibility that the lowest

energy transition can either be from the f^1 outer configuration to a higher lying orbital, or from the bulk occupied region to the first unoccupied orbital in the central region (which is lower in energy than that containing the f-electron). For $Pa(COT)_2$ the lowest energy transition is of the former kind mentioned above, but for $Pa(TMCOT)_2$ it is the latter kind. Secondly, it was not envisaged that transitions would occur at such low energies. All of the bands in $Pa(TMCOT)_2$ (A & C-E) which originate from the lowest energy transition in $Th(COT)_2$, and the lowest energy transition from the f^1 configuration (B), occur at higher wavelengths than the experimental band, with band A occurring in the infra-red, with λ >900 nm. On reflection, it is unsurprising that these bands are not reported, and that the incomparability with the experimental data should have resulted.

4.6.3 Comparison with past assignments of the experimental data

The study of Rösch and Streitwieser assigns the lowest band in the spectrum of thorocene to a LMCT transition from the $\pi_{e_{2g}}$ to the $f_{e_{3u}}$ orbital.[153] Dolg *et al.* assign this band to the $\pi_{e_{2u}} \rightarrow d_{a_{1g}}$ transition, with a rather closer agreement of the energy to experiment.[158] The assignment from the present study agrees more closely with the character of the transition of Rösch and Streitwieser, since bands A & B for thorocene both have some character of this transition. The band of Dolg *et al.* is not dipole active in a non-SO treatment of the system, such as the present study.

Solar *et al.* suggest that the maximum in the spectrum of $Pa(TMCOT)_2$ (380 nm) will occur at 365 nm for $Pa(COT)_2$.[146] Chang *et al.* assign this estimated band to the $\pi \rightarrow$d transition, although the character of this transition is unclear.[159] Kaltsoyannis and Bursten assign this band to either a MLCT from the metal $f(\sigma + \pi + \phi)$ based orbital to the ring-ϕ antibonding orbitals, or to a LMCT from the ring based $\delta_{e_{2g}}$ orbital to the aforementioned lying f-levels. The shoulder in the $Pa(TMCOT)_2$ spectrum is assigned on the same principle to a second LMCT transition, from the ring $\delta_{e_{2u}}$ orbitals, again to low lying M-f orbitals. The study of $Pa(COT)_2$ by Li and Bursten[156] also used the assumption of Solar *et al.*.[146] Li and Bursten assign the predicted band at 365 nm to a MLCT band from the outer $(f_{e3u})^1$ configuration to the e_{2g} antibonding orbital. On the same basis, they assign the shoulder at 490 nm to a LMCT transition ($e_{2u} \rightarrow 6d_{z^2}$) occurring at 430-435 nm for $Pa(COT)_2$.

The present study assigns the features in the experimental spectrum of $Pa(TMCOT)_2$ to LMCT transitions. The study of Kaltsoyannis and Bursten[157] also

proposed that LMCT transitions could be responsible for both features of the experimental spectrum, however, the character is not the same as those in the present study. The study of Li and Bursten assigns the spectrum by using a LMCT and a MLCT transition. The character of the LMCT is different from that assigned in the present study where it would not be dipole active.

The use by Li and Bursten of the assumption made by Solar *et al.*[146] is supported by the present study; the excitations assigned to the spectrum of $Pa(TMCOT)_2$ (L, 372 nm and H, 489 nm, figure 4.23) do have the same character as bands F (437 nm) and G (368 nm) in the $Pa(COT)_2$ spectrum (figure 4.20), except that they have undergone a bathochromic shift.

4.6.4 The effect of errors on the assignment

The spectra predicted with LB94 for $Pa(COT)_2$, and the substituted species, all have bands at lower energies (longer wavelengths) than the lowest energy band reported for these species in the literature. However, these bands all have small oscillator strengths, and it seems reasonable to assume that they were too weak, or at too long a wavelength to be observed when the spectra were recorded.

The other functionals investigated tended to give spectra that were more contracted to higher energies, and although they might not have predicted so many unobserved bands for $Th(TMCOT)_2$ and $Pa(TMCOT)_2$, they would also have failed to give a reasonable spectrum for $Th(COT)_2$, one failing to account for the lowest energy band from experiment. In short, the use of LB94 seems to be justified, and seems to produce sensible assignments for the experimental bands, including the expected bathochromic shift due to the substitution of the COT rings.

This study ignores an imporant effect of relativity which is present in systems such as these with heavy atoms - that of spin-orbit (SO) coupling. The studies of Kaltsoyannis & Bursten and Li & Bursten both include the effects of SO coupling, but they calculated the excitations using Slater's transition state method. This study uses the more advanced technique of TD-DFT (which allows for configuration mixing), but since we do not have access to any codes which allow this type of calculation to be performed with the inclusion of SO coupling (although efforts are being made to develop such codes, for instance by Gao *et al.*),[173] I have used the scalar relativistic approximation.

The following discussion attempts to judge the magnitude of the effects of SO coupling on the energy of the excitations, and then to compare it with the other sources of error in this study, such as the effects of basis set, geometry and

choice of functional. A comparison of these quantities should indicate whether the exclusion of SO effects will be likely to significantly alter the findings of this study.

The effects of SO coupling will be the largest for the f-orbitals, because they feel the effects of the nuclear charge more strongly, while the interactions with the ligand field will be at their smallest due to their contracted nature. Edelstein and Kot,[174] in their review of the Pa^{4+} ion, give the energy range of the splitting in the f-orbitals as 1 eV for the ion as a dopant in a Cs_2ZnCl_6 crystal; the effects of the crystal field were estimated to be approximately 0.25 eV. One would expect the SO interaction to be quenched in a molecular environment when compared with an isolated atom, however the degree to which the SO interaction is already quenched within the crystal is not clear.

A SO calculation using BLYP with ADF at the scalar relativistic optimised geometry for protactinocene has been used to gauge the magnitude of SO coupling the molecular environment. Unfortunately due to limitations with ADF it is necessary to run such calculations without symmetry, which makes analysis of the results quite difficult. However, since the f-orbitals do not mix strongly with the ligand orbitals, and because we do not expect the SO coupling to alter the basic MO structure, we can just use the energy separation between the ring and metal based orbitals (the HOMO-LUMO gap in thorocene) as an indication of the extra splitting due to SO effects over and above the effects of the ligand field. This energy separation has been reduced by 0.13 eV on the inclusion of SO coupling, and so we can estimate the extra splitting to be in the order of 0.13 eV. This represents a significant quenching compared with the Pa^{4+} in the crystalline environment.

Since the only experimental data for the actinocene complexes studied here are bands at $\approx$ 400 nm, the effects of the SO splitting will be considered on this range of the spectrum, an alteration of 0.13 eV in the excitation energy equates to a shift of $\approx$ 40 nm on the wavelength. In comparison, the effect of an alteration to the metal ring-centroid distance are estimated to be 3.5 $eV\text{Å}^{-1}$. This figure has been calculated by noting the effect on the lowest energy excitation when the metal ring-centroid is varied with a constant ring geometry (figure 4.25). The accuracy with which the geometry is determined should lead to an error in the excitation energy of the same order of magnitude as the effects of SO coupling.

The effect of the basis set on the excitation energy is difficult to estimate from these calculations. This has been judged by comparing the B3LYP calculations from Gaussian with ADF. These calculations used basis sets of similar quality,

Figure 4.25: Variation of the first five excitation energies with the metal-ring centroid distance calculated with LB94 at the BLYP geometry using ADF. The rings are fixed at the BLYP fully optimised geometry. Red lines indicate excitations of E_{1u} symmetry, while black lines indicate transitions of A_{2u} symmetry

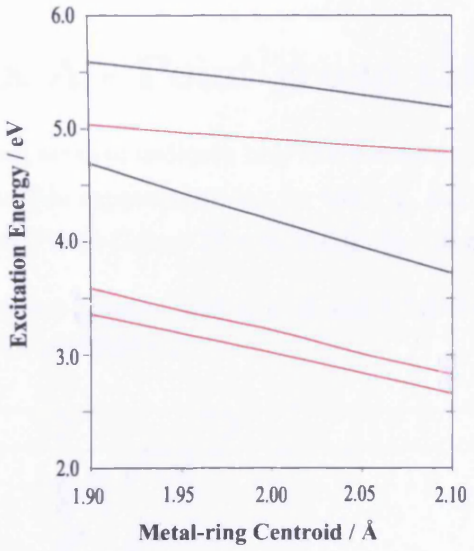

however a variation of approximately 7 nm in the energy of the long wavelength bands was observed. This difference is taken to be an indication of the error in the wavelength caused by basis set effects. In a study of the electronic spectra of uranium complexes by Ingram and Kaltsoyannis a variety of different basis sets were used for the TD-DFT calculations. They concluded that the size of the basis set made little difference to their results.[175]

The largest factor affecting the excitation energies is the choice of functional. This is seen to make a difference of as much as 100 nm if the extremes of the first excitation energies are considered - LB94//BLYP and SAOP//VWN. This variation in the excitation energy is far larger than the effects of SO coupling, and so it is felt that the effects of the latter can be safely neglected considering this and the other errors discussed.

The logical extension to the study of these system would be to include the effects of SO coupling with TD-DFT. However, with the available experimental data it is felt that such a study would lead to conclusions which are no more valuable than those from this study. It is felt that neither the present assignment, nor the past assignments of the experimental data can really be confirmed for correctness until a more comprehensive experimental study of these systems has been undertaken, such as full UV-vis spectra which resolves some fine structure.

Chapter 5

Appendices

5.1 Appendix A - Point group tables

The tables in the following section indicate how the cartesian tensors and atomic basis functions span the irreducible representations for the D_{4h} and D_{8h} point groups. This information is taken from *Point-Group Theory Tables by Altmann and Hertzig*.[176]

Table 5.1: How the cartesian tensors and s, p, d and f functions span the irreducible representations of the D_{4h} point group.

D_{4h}	0	1	2	3
A_{1g}	1		x^2+y^2, z^2	
A_{2g}		R_z		
B_{1g}			x^2-y^2	
B_{2g}			xy	
E_g		(R_x, R_y)	(xz, yz)	
A_{1u}				
A_{2u}		z		$(x^2+y^2)z, z^3$
B_{1u}				xyz
B_{2u}				$z(x^2-y^2)$
E_u		(x, y)		$\{x(x^2+y^2), y(x^2+y^2)\}, (xz^2, yz^2),$ $\{x(x^2-3y^2), y(3x^2-y^2)\}$

Table 5.2: How the cartesian tensors and s, p, d and f functions span the irreducible representations of the D_{8h} point group.

D_{8h}	0	1	2	3
A_{1g}	1		x^2+y^2, z^2	
A_{2g}		R_z		
B_{1g}				
B_{2g}				
E_{1g}		(R_x, R_y)	(xz, yz)	
E_{2g}			(xy, x^2-y^2)	
E_{3g}				
A_{1u}				
A_{2u}		z		$(x^2+y^2)z, z^3$
B_{1u}				
B_{2u}				
E_{1u}		(x, y)		$\{x(x^2+y^2), y(x^2+y^2)\}, (xz^2, yz^2)$
E_{2u}				$\{xyz, z(x^2-y^2)\}$
E_{3u}				$\{x(x^2-3y^2), y(3x^2-y^2)\}$

Table 5.3: Descent in symmetry for the irreducible representations of D_{8h} under the D_{4h} point group.

D_{8h}	D_{4h}
A_{1g}	A_{1g}
A_{2g}	A_{2g}
B_{1g}	A_{1g}
B_{2g}	A_{2g}
E_{1g}	E_g
E_{2g}	$B_{1g} \oplus B_{2g}$
E_{3g}	E_g
A_{1u}	A_{1u}
A_{2u}	A_{2u}
B_{1u}	A_{1u}
B_{2u}	A_{2u}
E_{1u}	E_u
E_{2u}	$B_{1u} \oplus B_{2u}$
E_{3u}	E_u

Bibliography

[1] P. O. Widmark, B. O. Roos Eds. European Summerschool in Quantum Chemistry 2005 Course Book. Lund University, 2005.

[2] F. Jensen. Introduction to Computational Chemistry - Second Edition. John Wiley and Sons, 2007.

[3] P. W. Atkins. Physical Chemistry 3^{rd} edition. Oxford University Press Inc.

[4] C. J. Cramer. Essentials of Computational Chemistry - Theories and Models. John Wiley and Sons, 2002.

[5] C. Møller, M. S. Plesset. *Phys. Rev.* **46**, 1934, 618–622.

[6] A. Szabo, N. S. Ostlund. Modern Quantum Chemistry - Introduction to Advanced Electronic Structure Theory. Dover Publications Inc., 1996.

[7] D. Cramer, Z. He. *J. Phys. Chem.* **100**, 1996, 6173–6188.

[8] F. Coester, H. Kümmel. *Nucl. Phys.* **17**, 1960, 477–485.

[9] An Introduction to Coupled Cluster Theory for Computational Chemists by T. D. Crawford and H. F. Schaefer III. Reviews in Computational Chemistry, volume 14, editors K. B. Lipkowitz and D. B. Boyd. Wiley-VCH, 2000.

[10] T. J. Lee, P. R. Taylor. *Int. J. Quant. Chem. S* **23**, 1989, 199–207.

[11] Gaussian 98 (Revision A.11), M. J. Frisch, G. W. Trucks, H. B. Schlegel, G. E. Scuseria, M. A. Robb, J. R. Cheeseman, V. G. Zakrzewski, J. A. Montgomery, Jr., R. E. Stratmann, J. C. Burant, S. Dapprich, J. M. Millam, A. D. Daniels, K. N. Kudin, M. C. Strain, O. Farkas, J. Tomasi, V. Barone, M. Cossi, R. Cammi, B. Mennucci, C. Pomelli, C. Adamo, S. Clifford, J. Ochterski, G. A. Petersson, P. Y. Ayala, Q. Cui, K. Morokuma, P. Salvador, J. J. Dannenberg, D. K. Malick, A. D. Rabuck, K. Raghavachari, J. B. Foresman, J. Cioslowski, J. V. Ortiz, A. G. Baboul, B. B. Stefanov, G. Liu, A. Liashenko, P. Piskorz, I. Komaromi, R. Gomperts, R. L. Martin, D. J. Fox, T. Keith, M. A. Al-Laham, C. Y. Peng, A. Nanayakkara, M. Challacombe, P. M. W. Gill, B. Johnson, W. Chen, M. W. Wong, J. L. Andres, C. Gonzalez, M. Head-Gordon, E. S. Replogle, and J. A. Pople, Gaussian, Inc., Pittsburgh PA, 2001.

[12] Gaussian 03, Revision C.02, M. J. Frisch, G. W. Trucks, H. B. Schlegel, G. E. Scuseria, M. A. Robb, J. R. Cheeseman, J. A. Montgomery, Jr., T. Vreven, K. N. Kudin, J. C. Burant, J. M. Millam, S. S. Iyengar, J. Tomasi, V. Barone, B. Mennucci, M. Cossi, G. Scalmani, N. Rega, G. A. Petersson, H. Nakatsuji, M. Hada, M. Ehara, K. Toyota, R. Fukuda, J. Hasegawa, M. Ishida, T. Nakajima, Y. Honda, O. Kitao, H. Nakai, M.

Klene, X. Li, J. E. Knox, H. P. Hratchian, J. B. Cross, V. Bakken, C. Adamo, J. Jaramillo, R. Gomperts, R. E. Stratmann, O. Yazyev, A. J. Austin, R. Cammi, C. Pomelli, J. W. Ochterski, P. Y. Ayala, K. Morokuma, G. A. Voth, P. Salvador, J. J. Dannenberg, V. G. Zakrzewski, S. Dapprich, A. D. Daniels, M. C. Strain, O. Farkas, D. K. Malick, A. D. Rabuck, K. Raghavachari, J. B. Foresman, J. V. Ortiz, Q. Cui, A. G. Baboul, S. Clifford, J. Cioslowski, B. B. Stefanov, G. Liu, A. Liashenko, P. Piskorz, I. Komaromi, R. L. Martin, D. J. Fox, T. Keith, M. A. Al-Laham, C. Y. Peng, A. Nanayakkara, M. Challacombe, P. M. W. Gill, B. Johnson, W. Chen, M. W. Wong, C. Gonzalez, and J. A. Pople, Gaussian, Inc., Wallingford CT, 2004.

[13] J. C. Rienstra-Kiracofe, W. D. Allen, H. F. Schaefer III. *J. Phys. Chem. A.* **104**, 2000, 9823–9840.

[14] D. Jayatilaka, T. J. Lee. *J. Chem. Phys.* **98**, 1993, 9734–9747.

[15] J. Peiró-García, I. Nebot-Gil. *Chem. Phys. Chem.* **4**, 2003, 843–847.

[16] J. Peiró-García, I. Nebot-Gil. *J. Comp. Chem.* **24**, 2003, 1657–1663.

[17] M. Martíanez-Ávila, J. Peiró-García, V. M. Ramírez-Ramírez, I. Nebot-Gil. *Chem. Phys. Lett.* **370**, 2003, 313–318.

[18] P. Hohenberg, W. Kohn. *Phys. Rev. B.* **136**, 1964, 864–871.

[19] W. Kohn, L. J. Sham. *Phys. Rev. A.* **140**, 1965, 1133–1138.

[20] W. Koch, M. C. Holthausen. A Chemist's Guide to Density Functional Theory. Wiley-VCH, 2001.

[21] J. P. Perdew, K. Burke, M. Ernzerhof. *Phys. Rev. Lett.* **77**, 1996, 3865–3868.

[22] P. J. Stephens, F. J. Devlin, C. F. Chabalowski, M. J. Frish. *J. Phys. Chem.* **98**, 1994, 11623–11627.

[23] J. Baker, P. Pulay. *J. Comput. Chem.* **24**, 2003, 1184–1191.

[24] D. L. Clark, J. C. Gordon, P. J. Hay, R. Poli. *Organometallics* **24**, 2005, 5747–5758.

[25] M.A.L. Marques and E.K.U. Gross, in: A Primer in Density Functional Theory, C. Fiolhais, F. Nogueira and M.A.L. Marques, ed., Springer Lecture Notes in Physics **620**, 2003, 144-184. Also available at http://www.physik.fu-berlin.de/~ag-gross/articles/pdf/MG03.pdf.

[26] C. O. Almbladh, U. von Barth. *Phys. Rev. B.* **31**, 1985, 3231–3244.

[27] A Guided Tour of Time-dependent Density Functional Theory, K. Burke and E.K.U. Gross, in: Density Functionals: Theory and Applications, D. Joubert, ed., Springer Lecture Notes in Physics **500**, 1998, 116-146. Also available at http://www.physik.fu-berlin.de/~ag-gross/articles/pdf/BG98.pdf.

[28] The ADF manual is available at http://www.scm.com/Doc/Doc2007.01 /ADF/Welcome.html.

[29] P. R. T. Schipper, O. V. Gritsenko, S. J. A. van Gisbergen, E. J. Baerends. *J. Chem. Phys.* **112**, 2000, 1344–1352.

[30] R. van Leeuwen, E. J. Baerends. *Phys. Rev. A.* **49**, 1994, 2421–2431.

[31] M. E. Casida, C. Jamorski, K. C. Casida, D. R. Salahub. *J. Chem. Phys.* **108**, 1998, 4439–4449.

[32] M. E. Casida, D. R. Salahub. *J. Chem. Phys.* **113**, 2000, 8918–8935.

[33] M. E. Casida, K. C. Casida, D. R. Salahub. *Int. J. Quantum Chem.* **70**, 1998, 933–941.

[34] G. Menconi, N. Kaltsoyannis. *Chem. Phys. Lett.* **415**, 2005, 64–68.

[35] J. Sun, K. Ruedenberg. *J. Phys. Chem.* **101**, 1994, 2157–2167.

[36] C. Y. Peng, P. Y. Ayala, H. B. Schlegel, M. J. Frisch. *J. Comp. Chem.* **17**, 1994, 49–56.

[37] C. Y. Peng, H. B. Schlegel. *Israel J. Chem.* **33**, 1993, 449–454.

[38] Gaussian 03 User's Reference, A. Frisch, M. J. Frisch and G. W. Trucks, Gaussian Inc., Carnegie, PA, 2003. Also available at http://www.gaussian.com.

[39] Molpro Users Manual Version 2006.1, University College Cardiff Consultants Limited, Cardiff, 2006. Also available at http://www.molpro.net/.

[40] A. C. F. Santos, C. A. Lucas, G. G. B. de Souza. *Chem. Phys.* **282**, 2002, 315–326.

[41] N. Tafadar, N. Kaltsoyannis, S. D. Price. *Int. J. Mass. Spectrom.* **192**, 1999, 205–214.

[42] P. Champkin, N. Kaltsoyannis, S. D. Price. *J. Electron Spectrosc. Relat. Phenom.* **105**, 1999, 21–28.

[43] C. S. S. O'Connor, S. D. Price. *Int. J. Mass. Spectrom.* **184**, 1999, 11–23.

[44] K. K. Baeck, Y. Joo. *Chem. Phys. Lett.* **337**, 2001, 190–198.

[45] K. K. Baeck, H. Choi, S. Iwata. *J. Chem. Phys. A* **103**, 1999, 6772–6777.

[46] K. K. Irikura, R. D. Johnson III, J. W. Hudgens. *J. Chem. Phys. A* **104**, 2000, 3800–3805.

[47] C. Q. Jiao, R. Nagpal, P. Haaland. *Chem. Phys. Lett.* **265**, 1997, 239–243.

[48] K. K. Baeck, R. J. Bartlett. *J. Chem. Phys.* **106**, 1997, 4604–4617.

[49] C. W. Bauschlicher Jr, A. Ricca. *J. Phys. Chem. A* **103**, 1999, 4313–4318.

[50] M. H. F. Bettega. *Phys. Rev. A* **62**, 2000, 024701.

[51] C. Tav, P. G. Datskos, L. A. Pinnaduwage. *J. Appl. Phys.* **84**, 1998, 5805–5807.

[52] N. A. Love, S. D. Price. *Int. J. Mass. Spectrom.* **233**, 2004, 145–153.

[53] L. H. Thomas, N. Kaltsoyannis. *Phys. Chem. Chem. Phys.* **8**, 2006, 1271–1281.

[54] S. D. Price. *J. Chem. Soc., Faraday Trans.* **93**, 1997, 2451–2460.

[55] R. D. Verma. *J. Mol. Spectrosc.* **169**, 1995, 295–301.

[56] N. Kaltsoyannis, S. D. Price. *Chem. Phys. Lett.* **313**, 1999, 679–684.

[57] MOLPRO, version 2006.1, a package of ab initio programs, H.-J. Werner, P. J. Knowles, R. Lindh, F. R. Manby, M. Schtz, P. Celani, T. Korona, G. Rauhut, R. D. Amos, A. Bernhardsson, A. Berning, D. L. Cooper, M. J. O. Deegan, A. J. Dobbyn, F. Eckert, C. Hampel and G. Hetzer, A. W. Lloyd, S. J. McNicholas, W. Meyer and M. E. Mura, A. Nicklass, P. Palmieri, R. Pitzer, U. Schumann, H. Stoll, A. J. Stone, R. Tarroni and T. Thorsteinsson , see http://www.molpro.net.

[58] The NIST Scientific and Technical Databases can be found at: http://www.nist.gov/srd/.

[59] P. L. Pauson, T. J. Kealy. *Nature* **168**, 1951, 1039–1040.

[60] S. A. Miller, J. A. Tebboth, J. F. Tremaine. *J. Chem. Soc.* , 1952, 632–635.

[61] E. Fischer, W. Pfab. *Z. Naturforsch., B:* **7**, 1952, 377–379.

[62] G. Wilkinson, M. Rosenblum, M. C. Whiting, R. B. Woodward. *J. Am. Chem. Soc.* **74**, 1952, 2125–2126.

[63] H. P. Lüthi. *J. Mol. Struct. (Theochem)* **388**, 1996, 299–304.

[64] H. P. Lüthi, P. E. M. Siegbahn, J. Almlöf. *J. Phys. Chem.* **89**, 1985, 2156–2161.

[65] H. P. Lüthi, J. Ammeter, J. Almlöf, K. Korsell. *Chem. Phys. Lett.* **69**, 1980, 540–542.

[66] H. Koch, P. Jørgensen, T. Helgaker. *J. Chem. Phys.* **104**, 1996, 9528–9530.

[67] S. Coriani, A. Haaland, T. Helgaker, P. Jørgensen. *Chem. Phys. Chem.* **7**, 2006, 245–249.

[68] C. Park, J. Almlöf. *J. Chem. Phys.* **95**, 1991, 1829–1833.

[69] K. Pierloot, B. J. Persson, B. O. Roos. *J. Phys. Chem.* **99**, 1995, 3465–3472.

[70] T. E. Taylor, M. B. Hall. *Chem. Phys. Lett.* **114**, 1985, 338–342.

[71] K. Ishimura, M. Hada, H. Nakatsuji. *J. Chem. Phys.* **117**, 2002, 6533–6537.

[72] N. Rösch, H. Jörg. *J. Chem. Phys.* **84**, 1986, 5967–5968.

[73] H. P. Lüthi, P. E. M. Siegbahn, J. J. Almlöf, J. K. Faegri, A. Heiberg. *Chem. Phys. Lett.* **111**, 1984, 1–6.

[74] B. Delley, M. Wrinn, H. P. Lüthi. *J. Chem. Phys.* **100**, 1994, 5785–5791.

[75] M. J. Mayor-López, H. P. Lüthi, H. Koch, P. Y. Morgantini, J. Weber. *J. Chem. Phys.* **113**, 2000, 8009–8014.

[76] Z.-F. Xu, Y. Xie, W.-L. Feng, H. F. Schaefer, III. *J. Phys. Chem. A* **107**, 2003, 2716–2729.

[77] W. Klopper, H. P. Lüthi. *Chem. Phys. Lett.* **262**, 1996, 546–552.

[78] M. S. Gordon, M. W. Schmidt, G. M. Chaban, K. R. Glaesemann, W. J. Stevens, C. Gonzalez. *J. Chem. Phys.* **110**, 1999, 4199–4207.

[79] I. M. B. Nielsen, C. L. Janssen. *Chem. Phys. Lett.* **310**, 1999, 568–576.

[80] J. Aguilera-Iparraguirre, W. Klopper. *J. Chem. Theory Comput.* **3**, 2007, 139–145.

[81] A. Mansergas, J. M. Anglada. *J. Phys. Chem. A* **111**, 2007, 976–981.

[82] J. Demaison, A. G. Császár, I. Kleiner, H. Møllendal. *J. Phys. Chem. A* **111**, 2007, 2574–2586.

[83] J. Demaison, H. Herman, J. Liévin, H. D. Rudolph. *J. Phys. Chem. A* **111**, 2007, 2602–2609.

[84] X. Zhang, A. T. Maccarone, M. R. Nimlos, S. Kato, V. M. Bierbaum, G. B. Ellison, B. Ruscic, A. C. Simmonett, W. D. Allen, H. F. Schaefer III. *J. Chem. Phys.* **126**, 2007, 044312.

[85] K. A. Peterson, D. Figgen, M. Dolg, H. Stoll. *J. Chem. Phys.* **126**, 2007, 124101.

[86] N. Strickland, J. N. Harvey. *J. Phys. Chem. B* **111**, 2007, 841–852.

[87] H. Cho, L. Andrews. *Organometallics* **26**, 2007, 633–643.

[88] C. Puzzarini. *J. Molec. Spect.* **242**, 2007, 70–75.

[89] G. Cazzoli, C. Puzzarini, A. Baldacci, A. Baldan. *J. Molec. Spect.* **241**, 2007, 112–115.

[90] M. Bühl, H. Kabrede. *J. Chem. Theory Comput.* **2**, 2006, 1282–1290.

[91] W. J. Pietro, W. J. Hehre. *J. Comp. Chem.* **4**, 1983, 241–251.

[92] J. Demuynck, A. Strich, A. Veillard. *Nouv. J. Chem.* **1**, 1977, 217–228.

[93] B. J. Persson, B. O. Roos, K. Pierloot. *J. Chem. Phys.* **101**, 1994, 6810–6821.

[94] C. Sosa, J. Andzelm, B. C. Elkin, E. Wimmer, K. D. Dobbs, D. A. Dixon. *J. Phys. Chem.* **96**, 1992, 6630–6636.

[95] A. Matveev, M. Staufer, M. Mayer, N. Rösch. *Int. J. Quant. Chem.* **75**, 1999, 863–873.

[96] J. Li, G. Schreckenbach, T. Ziegler. *J. Am. Chem. Soc.* **117**, 1995, 486–494.

[97] L. A. Barnes, M. Rosi, C. W. Bauschlicher, Jr. *J. Chem. Phys.* **94**, 1991, 2031–2039.

[98] B. Beagley, D. G. Schmidling. *J. Mol. Struct.* **22**, 1974, 466–468.

[99] U. Radius, F. M. Bickelhaupt, A. W. Ehlers, N. Goldberg, R. Hoffmann. *Inorg. Chem.* **37**, 1998, 1080–1090.

[100] E. S. Apostolova, A. P. Tikhonov, O. A. Sendyurev. *Russ. J. Coord. Chem.* **28**, 2002, 38–45.

[101] B. W. McClelland, A. G. Robiette, L. Hedberg, K. Hedberg. *Inorg. Chem.* **40**, 2001, 1358–1362.

[102] J. N. Harvey, M. Aschi. *Faraday Discuss.* **124**, 2003, 129–143.

[103] S. Villaume, C. Daniel, A. Strich, S. A. Perera, R. J. Bartlett. *J. Chem. Phys.* **122**, 2005, 044313.

[104] G. J. O. Beran, S. R. Gwaltney, M. Head-Gordon. *Phys. Chem. Chem. Phys.* **5**, 2003, 2488–2493.

[105] D. C. Graham, G. J. O. Beran, M. Head-Gordon, G. Christian, R. Stranger, B. F. Yates. *J. Phys. Chem. A* **109**, 2005, 6762–6772.

[106] P. Bouř. *J. Comp. Chem.* **21**, 2000, 8–16.

[107] MOLPRO, version 2002.6, a package of ab initio programs written by H.-J. Werner, P. J. Knowles, M. Schtz, R. Lindh, P. Celani, T. Korona, G. Rauhut, F. R. Manby, R. D. Amos, A. Bernhardsson, A. Berning, D. L. Cooper, M. J. O. Deegan, A. J. Dobbyn, F. Eckert, C. Hampel, G. Hetzer, A. W. Lloyd, S. J. McNicholas, W. Meyer, M. E. Mura, A. Nickla, P. Palmieri, R. Pitzer, U. Schumann, H. Stoll, A. J. Stone R. Tarroni, and T. Thorsteinsson.

[108] R. Lindh, U. Ryu, B. Liu. *J. Chem. Phys.* **95**, 1991, 5889–5897.

[109] R. Lindh. *Theor. Chim. Acta* **85**, 1993, 423–440.

[110] T. Busch, A. Degli Esposti, H. J. Werner. *J. Chem. Phys.* **94**, 1991, 6708–6715.

[111] A. El Azhary, G. Rauhut, P. Pulay, H. J. Werner. *J. Chem. Phys.* **108**, 1998, 5185–5193.

[112] H. J. Werner, P. J. Knowles. *J. Chem. Phys.* **82**, 1985, 5053–5065.

[113] P. J. Knowles, H. J. Werner. *Chem. Phys. Lett.* **115**, 1985, 259–267.

[114] H. J. Werner, P. J. Knowles. *J. Chem. Phys.* **89**, 1988, 5803–5814.

[115] P. J. Knowles, H. J. Werner. *Chem. Phys. Lett.* **145**, 1988, 514–522.

[116] C. Hampel, K. A. Peterson, H. J. Werner. *Chem. Phys. Lett.* **190**, 1992, 1–12.

[117] M. J. O. Deegan, P. J. Knowles. *Chem. Phys. Lett.* **227**, 1994, 321–326.

[118] F. Eckert, P. Pulay, H. J. Werner. *J. Comp. Chem.* **18**, 1997, 1473–1483.

[119] J. C. Slater. *Phys. Rev.* **81**, 1951, 385–390.

[120] S. H. Vosko, L. Wilk, M. Nusair. *Can. J. Phys.* **58**, 1980, 1200–1211.

[121] A. D. Becke. *Phys. Rev. A.* **38**, 1988, 3098–3100.

[122] C. T. Lee, W. T. Yang, R. G. Parr. *Phys. Rev. B.* **37**, 1988, 785–789.

[123] B. Miehlich, A. Savin, H. Stoll, H. Preuss. *Chem. Phys. Lett.* **157**, 1989, 200–206.

[124] J. P. Perdew. *Phys. Rev. B.* **38**, 1986, 8822–8824.

[125] C. Adamo, V. Barone. *J. Chem. Phys.* **110**, 1999, 6158–6170.

[126] J. P. Perdew, J. A. Chevary, S. H. Vosko, K. A. Jackson, M. R. Pederson, D. J. Singh, C. Fiolhais. *Phys. Rev. B.* **46**, 1992, 6671–6687.

[127] A. D. Becke. *J. Chem. Phys.* **107**, 1997, 8554–8560.

[128] F. A. Hamprecht, A. J. Cohen, D. J. Tozer, N. C. Handy. *J. Chem. Phys.* **109**, 1998, 6264–6271.

[129] Personal communication with Professor Peter Knowles, University of Cardiff, by email.

[130] Personal communication with Dr. Jeremy Harvey, University of Bristol, by email.

[131] G. te Velde, F. Bickelhaupt, S. J. A. van Gisbergen, C. F. Guerra, E. J. Baerends, J. Snijders, T. Ziegler. *J. Comput. Chem.* **22**, 2001, 931–967.

[132] C. F. Guerra, J. G. Snijders, G. te Velde, E. J. Baerends. *Theor. Chem. Acc.* **99**, 1998, 391–403.

[133] ADF2006.01, SCM, Theoretical Chemistry, Vrije Universiteit, Amsterdam, The Netherlands, http://www.scm.com E.J. Baerends, J. Autschbach, A. Brces, F.M. Bickelhaupt, C. Bo, P.M. Boerrigter, L. Cavallo, D.P. Chong, L. Deng, R.M. Dickson, D.E. Ellis, M. van Faassen, L. Fan, T.H. Fischer, C. Fonseca Guerra, S.J.A. van Gisbergen, J.A. Groeneveld, O.V. Gritsenko, M. Grning, F.E. Harris, P. van den Hoek, C.R. Jacob, H. Jacobsen, L. Jensen, G. van Kessel, F. Kootstra, E. van Lenthe, D.A. McCormack, A. Michalak, J. Neugebauer, V.P. Osinga, S. Patchkovskii, P.H.T. Philipsen, D. Post, C.C. Pye, W. Ravenek, P. Ros, P.R.T. Schipper, G. Schreckenbach, J.G. Snijders, M. Sol, M. Swart, D. Swerhone, G. te Velde, P. Vernooijs, L. Versluis, L. Visscher, O. Visser, F. Wang, T.A. Wesolowski, E. van Wezenbeek, G. Wiesenekker, S.K. Wolff, T.K. Woo, A.L. Yakovlev, and T. Ziegler.

[134] A. Haaland. *Topp. Curr. Chem.* **53**, 1975, 19–21.

[135] For details of Molden visualisation package, please visit http://www.cmbi.kun.nl/ ~schaft/molden.html.

[136] F. A. Cotton. Chemical Applications of Group Theory. John Wiley and Sons Inc, 1971.

[137] G. Menconi, N. Kaltsoyannis. *Organometallics* **24**, 2005, 1189–1197.

[138] J. C. Green, N. Kaltsoyannis, K. H. Sze, M. MacDonald. *J. Am. Chem. Soc.* **116**, 1994, 1994–2004.

[139] J. G. Brennan, G. Cooper, J. C. Green, N. Kaltsoyannis, M. A. MacDonald, M. P. Payne, C. M. Redfern, K. H. Sze. *Chem. Phys.* **164**, 1992, 271–281.

[140] M. Hargittai, N. Y. Subbotina, M. Kolonits, A. G. Gershikov. *J. Chem. Phys.* **94**, 1991, 7278–7286.

[141] A. Streitwieser, Jr., U. Müller-Westerhoff. *J. Am. Chem. Soc.* **90**, 1968, 7364–7364.

[142] A. Streitwieser, Jr., N. Yoshida. *J. Am. Chem. Soc.* **91**, 1969, 7528–7528.

[143] D. F. Stark, T. C. Parsons, A. Streitwieser, Jr., N. Edelstein. *Inorg. Chem.* **13**, 1974, 1307–1308.

[144] N. N. Greenwood, A. Earnshaw. Chemistry of the Elements. Reed Educational and Professional Publishing Ltd., Oxford., 1997.

[145] N. Kaltsoyannis, P. Scott. The f-elements. Oxford University Press Inc., New York, 1999.

[146] J. P. Solar, H. P. G. Burghard, R. H. Banks, A. Streitwieser, Jr., D. Brown. *Inorg. Chem.* **19**, 1980, 2186–2188.

[147] P. W. Roesky. *Eur. J. Inorg. Chem.* , 2001, 1653–1660.

[148] C. Levanda, A. Streitwieser, Jr. *Inorg. Chem.* **20**, 1981, 656–659.

[149] P. M. Boerrigter, E. J. Baerends, J. G. Snijders. *Chem. Phys.* **122**, 1988, 357–374.

[150] J. P. Clark, G. C. Green. *J. Chem. Soc. Dalton Trans.* , 1977, 505–508.

[151] A. Rosa, G. Ricciardi, O. Gritsenko, E. J. Baerends. *Structure and Bonding* **112**, 2004, 49–115.

[152] M. Dolg, P. Fulde. *Chem. Eur. J.* **4**, 1998, 200–204.

[153] N. Rösch, A. Streitwieser, Jr. *J. Am. Chem. Soc.* **105**, 1983, 7237–7240.

[154] J. G. Brennan, J. C. Green, C. M. Redfern. *J. Am. Chem. Soc.* **111**, 1989, 2373–2377.

[155] R. G. Hayes, N. Edelstein. *J. Am. Chem. Soc.* **94**, 1972, 8688–8691.

[156] J. Li, B. E. Bursten. *J. Am. Chem. Soc.* **120**, 1998, 11456–11466.

[157] N. Kaltsoyannis, B. E. Bursten. *J. Organometallic Chem.* **528**, 1997, 19–33.

[158] M. Dolg, P. Fulde, H. Stoll, H. Preuss, A. Chang, R. M. Pitzer. *Chem. Phys.* **195**, 1995, 71–82.

[159] A. H. H. Chang, K. Zhao, W. C. Ermler, R. M. Pitzer. *J. Alloys Compd.* **213**, 1994, 191–195.

[160] N. C. Handy, A. J. Cohen. *Mol. Phys.* **99**, 2001, 403–412.

[161] T. W. Keal, D. J. Tozer. *J. Chem. Phys.* **119**, 2003, 3015–3024.

[162] M. Grüning, O. V. Gritsenko, S. J. A. van Gisbergen, E. J. Baerends. *J. Chem. Phys.* **114**, 2001, 652–660.

[163] M. J. Frisch, G. W. Trucks, H. B. Schlegel, G. E. Scuseria, M. A. Robb, J. R. Cheeseman, J. A. Montgomery, Jr., T. Vreven, K. N. Kudin, J. C. Burant, J. M. Millam, S. S. Iyengar, J. Tomasi, V. Barone, B. Mennucci, M. Cossi, G. Scalmani, N. Rega, G. A. Petersson, H. Nakatsuji, M. Hada, M. Ehara, K. Toyota, R. Fukuda, J. Hasegawa, M. Ishida, T. Nakajima, Y. Honda, O. Kitao, H. Nakai, M. Klene, X. Li, J. E. Knox, H. P. Hratchian, J. B. Cross, V. Bakken, C. Adamo, J. Jaramillo, R. Gomperts, R. E. Stratmann, O. Yazyev, A. J. Austin, R. Cammi, C. Pomelli, J. W. Ochterski, P. Y. Ayala, K. Morokuma, G. A. Voth, P. Salvador, J. J. Dannenberg, V. G. Zakrzewski, S. Dapprich, A. D. Daniels, M. C. Strain, O. Farkas, D. K. Malick, A. D. Rabuck, K. Raghavachari, J. B. Foresman, J. V. Ortiz, Q. Cui, A. G. Baboul, S. Clifford, J. Cioslowski, B. B. Stefanov, G. Liu, A. Liashenko, P. Piskorz, I. Komaromi, R. L. Martin, D. J. Fox, T. Keith, M. A. Al-Laham, C. Y. Peng, A. Nanayakkara, M. Challacombe, P. M. W. Gill, B. Johnson, W. Chen, M. W. Wong, C. Gonzalez, J. A. Pople. "Gaussian 03, Revision D.01". Gaussian, Inc., Wallingford, CT, 2004.

[164] W. Kuchle, M. Dolg, H. Stoll, H. Preuss. *J. Chem. Phys.* **100**, 1994, 7535–7542.

[165] X. Y. Cao, M. Dolg, H. Stoll. *J. Chem. Phys.* **118**, 2003, 487–496.

[166] The molekel visualisation package is available at http://www.cscs.ch/molekel/.

[167] ADF-Spectra is a visualisation package which is part of the ADF suite of programs.

[168] R. Dennington II, T. Keith, J. Millam, K. Eppinnett, W. L. Hovell, R. Gilliland. "Gaussview version 3.09". Semichem, Inc., Shawnee Mission, KS, 2003.

[169] N. M. O'Boyle, GaussSum 2.0, 2006. Available at http://gausssum.sf.net.

[170] A. Adveef, K. N. Raymond, K. O. Hodgson, A. Zalkin. *Inorg. Chem.* **11**, 1972, 1083–1088.

[171] K. O. Hodgson, K. N. Raymond. *Inorg. Chem.* **12**, 1973, 458–466.

[172] F. G. N. Cloke, J. C. Green, N. Kaltsoyannis. *Organometallics* **23**, 2004, 832–835.

[173] J. Gao, W. Liu, B. Song, C. Liu. *J. Chem. Phys.* **121**, 2004, 6658–6666.

[174] N. M. Edelstein, W. K. Kot. *J. Alloys Compd.* **193**, 1993, 82–87.

[175] K. Ingram and N. Kaltsoyannis pgs 258-260 in Recent Advances in Actinide Science, I. May, R. and N. Bryan Eds. The Royal Society of Chemistry, Cambridge, 2006.

[176] S. L. Altmann, P. Herzig. Point-Group Theory Tables. Oxford University Press, 1994.